REPORT DOCUMENTATION PAGE

Form Approved
OMB No. 0704-0188

Public reporting burden for this collection of information is estimated to average 1 hour per response, including the time for reviewing instructions, searching existing data sources, gathering and maintaining the data needed, and completing and reviewing the collection of information. Send comments regarding this burden estimate or any other aspect of this collection of information, including suggestions for reducing this burden, to Washington Headquarters Services, Directorate for information Operations and Reports, 1215 Jefferson Davis Highway, Suite 1204, Arlington, VA 22202-4302, and to the Office of management and Budget, Paperwork Reduction Project (0704-0188) Washington, DC 20503.

1. AGENCY USE ONLY (Leave Blank)	2. REPORT DATE May 1993	3. REPORT TYPE AND DATES COVERED Final

4. TITLE AND SUBTITLE Fatigue Crack Retardation in PM Aluminum Alloys AA8022 and AA5091	5. FUNDING NUMBERS

6. AUTHORS
Gary Harper Bray

7. PERFORMING ORGANIZATION NAME(S) AND ADDRESS(ES)
University of Virginia

AFRL-SR-BL-TR-98-

N

0008

9. SPONSORING/MONITORING AGENCY NAME(S) AND ADDRESS(ES)
AFOSR/NI
110 Duncan Avenue, Room B-115
Bolling Air Force Base, DC 20332-8080

AGENCY REPORT NUMBER

11. SUPPLEMENTARY NOTES

12a. DISTRIBUTION AVAILABILITY STATEMENT Approved for Public Release	12b. DISTRIBUTION CODE

13. ABSTRACT *(Maximum 200 words)*
See attached.

DTIC QUALITY INSPECTED 2

14. SUBJECT TERMS

19980115 229

15. NUMBER OF PAGES

16. PRICE CODE

17. SECURITY CLASSIFICATION OF REPORT Unclassified	18. SECURITY CLASSIFICATION OF THIS PAGE Unclassified	19. SECURITY CLASSIFICATION OF ABSTRACT Unclassified	20. LIMITATION OF ABSTRACT UL

Standard Form 298 (Rev. 2-89)
Prescribed by ANSI Std. 239.18
Designed using WordPerfect 6.1, AFOSR/XPP, Oct 96

Fatigue Crack Retardation in PM Aluminum

Alloys AA8022 and AA5091

A Dissertation

Presented to

the Faculty of the School of Engineering

and Applied Science

University of Virginia

In Partial Fulfillment

of the Requirements for the Degree

Doctor of Philosophy (Materials Science and Engineering)

by

Gary Harper Bray

May 1993

Approval Sheet

This dissertation is submitted in partial fulfillment of the requirements

for the degree of

Doctor of Philosophy (Materials Science and Engineering)

Gary H. Bray

Gary Harper Bray

This dissertation has been read and approved by the examining committee:

Edgar A. Starke, Jr. (dissertation advisor)

Richard P. Gangloff (committee chairman)

Heinz G.F. Wilsdorf

Doris Kuhlmann-Wilsdorf

John M. Duva

Accepted for the School of Engineering and Applied Science:

Edgar A. Starke, Jr.
Dean, School of Engineering and Applied Science

May 1993

Abstract

An important goal of fatigue research is the prediction of fatigue crack propagation rate under service loading conditions. Intermittent high peak tensile loads can cause crack retardation in subsequent load cycles. The mechanisms responsible for crack retardation must be characterized in each alloy or class of alloys so that appropriate predictive models can be developed and utilized. The objective of this investigation was to identify the mechanisms responsible for crack retardation in PM aluminum alloys AA8022 and AA5091 using an elastic-plastic fracture mechanics approach.

The results of single tensile overload tests and computer simulations with FASTRAN, a plasticity-induced closure model, indicate that plasticity-induced closure is the primary cause of retardation in AA8022 at both low and high R in air at room temperature. Both plasticity and roughness-induced closure contribute to crack retardation in AA5091.

The relative contributions of the surface and interior region to crack retardation were determined by performing surface removal experiments and examining crack front profiles at various positions through the affected zone. The results of these experiments indicate that the plasticity-induced closure mechanism is through-thickness in nature. However, the magnitude of the retardation effect is greater in the surface regions than in the interior region.

The effect of an overload was significantly reduced by subsequent elevated temperature exposure. This behavior results from reductions in

plastic strain and compressive residual stresses ahead of the crack tip. These changes significantly reduce the contribution of closure mechanisms to crack retardation.

Acknowledgments

I would like to thank my first advisor, Dr. H.G.F Wilsdorf, who provided me with an opportunity to work on an Air Force contract investigating the fatigue crack propagation characteristics of powder metallurgy aluminum alloys. Many ideas developed while working on this contract were utilized in this investigation.

I also thank my second advisor, Dr. E.A. Starke, for giving me direction and keeping me focused, as well as for his technical expertise in the area of fatigue. I greatly appreciate his many kind words of support and encouragement.

I would like to thank the other members of my committee, Dr. D. Kuhlmann-Wilsdorf, Dr. J.M. Duva, and Dr. R.P. Gangloff for their suggestions in improving the manuscript. I especially thank Dr. Gangloff for his careful reading of the manuscript and his technical suggestions, but also for catching many typos, grammatical errors, incorrect references, etc. that were completely invisible to me due to my overfamiliarity with the manuscript.

I am very grateful to Dr. J.C. Newman of NASA Langley for providing me with a copy of his FASTRAN-II computer program and for helpful discussions on using the program, and for technical discussions on crack closure, constraint, and other aspects of fatigue crack growth. The FASTRAN-II program was an extremely valuable tool in this investigation and shed a great deal of light on the results.

I dedicate this dissertation to my dear wife, Susan, who sacrificed the most over the past five years, but always supported me with her love and encouragement and never complained. I am so happy to once again be a full-time husband and father to her and our beautiful son, Samuel.

Table of Contents

List of Figures

x

List of Tables

List of Symbols

a_{aff}	affected distance
a_{min}	increment of crack extension at $(da/dN_{min}$
Δa	increment of crack extension
α	constraint factor in FASTRAN model
b	Burger's vector
B	specimen thickness
C	Paris Law constant
CTOD	crack tip opening displacement
ΔCTOD	crack tip opening displacement range
d	grain diameter
da/dN	crack growth rate
$(da/dN)_B$	baseline crack growth rate
$(da/dN)_{min}$	minimum crack growth rate following overload
ϵ_{yy}	tensile strain normal to crack plane
ϵ_{zz}	tensile strain in through-thickness direction
$\Delta\epsilon_p$	cyclic plastic strain range
$\Delta\epsilon_t$	total cyclic strain range
ϵ_m	mean strain
E	Young's modulus
G	shear modulus
K_{min}	minimum applied stress intensity factor
K_{max}	maximum applied stress intensity factor
ΔK	applied stress intensity factor range= K_{max}-K_{min}
ΔK_B	baseline stress intensity factor range
K_{ol}	maximum stress intensity factor in overload cycle
K_{ul}	minimum stress intensity factor in the underload cycle
ΔK_{ul}	K_{max}-K_{ul}
K_{cl}, K_{op}	stress intensity factor at closure
ΔK_{eff}	effective stress intensity factor range= K_{max}-K_{cl}
k_1, k_2	Mode I and Mode II stress intensity factors at crack tip of deflected crack
ΔK_{notch}	equivalent stress intensity factor at blunted crack
ΔK_{th}	threshold stress intensity factor

K_I	Mode I stress intensity factor
K_{III}	Mode III stress intensity factor
N_d	number of delay cycles from overload
n	Paris Law coefficient
OLR	overload ratio$= K_{ol}/K_{max}$
ULR*	underload ratio$= \Delta K_{ul}/\Delta K_B$
P_{cl}	closure load
P_{max}	maximum load
ρ	blunted crack tip root radius
R	baseline stress ratio$= K_{min}/K_{max}$
R_{eff}	effective stress ratio$= K_{cl}/K_{max}$
r_p	monotonic of forward plastic zone size in crack plane
Δr_p	cyclic or reversed plastic zone size in crack plane
S_{op}	crack opening stress
S_{tt}	stress needed to produce tensile yielding ahead of crack tip
ΔS_{eff}	effective stress range
σ_{yy}	tensile stress normal to crack plane (y=0)
σ_y	2% offset yield strength
σ_o	flow stress
τ_o	shear flow stress
τ_p	lattice friction or Peierl-Nabarro stress
τ_{gb}	strength increase due to grain boundaries
τ_{disp}	strength increase due to dispersoids
τ_{loop}	Orowan or looping stress
τ_b	bowing stress
τ_{LR}	long range stress from accumulation of dislocation loops
τ_{im}	image stress from differences in elastic-plastic behavior of matrix and dispersoid
x	distance ahead of crack tip

1. Introduction

An important goal of fatigue research is the ability to predict the rate of fatigue crack propagation in engineering structures under service loading conditions. This goal is becoming increasingly important as emphasis is placed on making safer and more durable structures while at the same time reducing weight and energy consumption through the use of more efficient designs and lighter, often less fatigue resistant materials. One current example is the increasing substitution of aluminum for steel in automobiles in order to decrease weight and improve fuel efficiency. A second example is the substitution of high temperature aluminum alloys for titanium in engine and structural components exposed to elevated temperatures in order to reduce weight, and improve performance and fuel efficiency of commercial and military aircraft.

The service loading conditions experienced by structures can be placed into one of three categories schematically shown in Figure 1.1: (1) constant amplitude loading, (2) narrow band variable amplitude loading, or (3) broad band variable amplitude loading. The fatigue life of structures subjected to constant amplitude loading in benign environments can be predicted by integration of the crack growth rate equation:

$$\frac{da}{dN} = f(\Delta K, R) \tag{1.1}$$

obtained from constant amplitude fatigue crack growth (FCGR) tests on laboratory test specimens, provided the loads and stress intensity factor solutions for the structural components are known. The fatigue life of

Constant Amplitude Loading

Narrow Band Variable Amplitude Loading

Broad Band Variable Amplitude Loading

GUST LOADS (RANDOM)

GROUND-AIR-GROUND
TRANSITION (DETERMINISTIC)
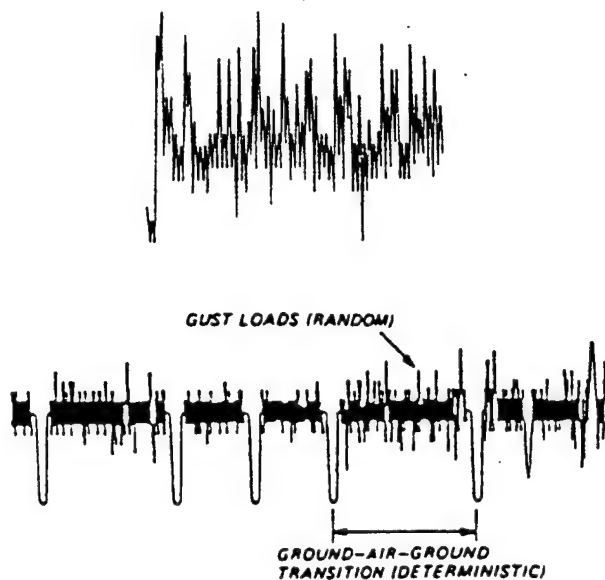
Figure 1.1.   Three classes of service loading conditions.

structures subjected to narrow band variable amplitude loading or slowly varying loads can be obtained utilizing the same crack growth rate equation by employing a cycle-by-cycle integration:

$$a = a_o + \sum_{i=1}^{N} \Delta a_i \qquad (1.2)$$

where Δa_i = da/dN from the constant amplitude FCGR curve for the ΔK and stress ratio R of the ith cycle. However, this method is inadequate under broad band variable amplitude loading, because under this type of loading the crack growth rate depends not only on the loads in the current cycle, but also the loads in previous cycles (i.e., the load history). For example, intermittent high peak tensile loads or overloads can cause fatigue cracks in metals to decelerate or even arrest during subsequent load cycles [1]. This behavior is known as crack retardation. When crack retardation occurs the use of Equation 1.2 to predict fatigue life yields an overly conservative prediction possibly leading to over design of the structural component increasing weight and reducing fuel efficiency or leading to more frequent inspections than necessary increasing maintenance cost. The mechanisms responsible for crack retardation must be understood before computer models can be developed that are capable of predicting fatigue life of structures subjected to broad band variable amplitude loading.

Several mechanisms have been proposed to contribute to crack retardation effects including: (1) crack tip strain hardening [2], (2) crack tip blunting [3], (3) crack tip branching and secondary cracking [4,5], (4) compressive residual stresses [6], (5) roughness-induced closure [4,7], and (6) plasticity-induced closure [1]. Which of these

mechanisms are dominant in a given alloy may be significantly influenced by its microstructure and the magnitude of the applied loads. If this is the case, it is unlikely that a computer model based on a single mechanism will be capable of predicting fatigue life for all alloys and loading conditions. Therefore, it is important to identify the dominant mechanism or mechanisms in each alloy or class of alloys so that appropriate computer models can be developed and utilized.

The closure mechanisms are capable of explaining many retardation phenomena including: (1) inititial acceleration immediately following an overload, (2) delayed retardation, and (3) a reduction in the magnitude of the retardation effect when the tensile overload is followed by a compressive underload leading many investigators to conclude that closure mechanisms are primarily responsible for crack retardation. However, these investigators disagree whether plasticity-induced or roughness-induced closure is the dominant mechanisms. They also disagree whether crack retardation is controlled by the surface region or whether it is through-thickness in nature.

Other investigators point out that measured post-overload closure levels are not always consistent with post-overload crack growth rates and in some cases there is no increase in measured post-overload closure levels. These and other discrepancies have led these investigators to conclude that the compressive residual stresses or crack tip blunting is primarily responsible for crack retardation. Critics of these mechanisms suggest that these mechanisms are due to the use of methods which are too insensitive to measure closure levels

following overloads. Few previous studies have considered the contribution of the intrinsic material response to an overload.

The objective of this investigation was to identify the mechanisms responsible for crack retardation effects in two recently developed powder metallurgy (PM) aluminum alloys, AA8022 (Al-6Fe-1.3Si-0.6V) and AA5091 (Al-4Mg-1.3Li-1.1C-0.4O) over a wide range of loading conditions. AA8022 was designed as a lightweight replacement for ingot metallurgy (IM) titanium alloys in elevated temperature applications and is produced using rapid solidification and powder metallurgy (RS/PM) techniques. AA5091 was designed as a lightweight substitute for 7000 series IM aluminum alloys and is produced by mechanical alloying (MA). Both alloys exhibit a sub-micron grain size and a distribution of fine dispersoids.

Three current areas of disagreement in the literature were also considered: (1) What is the role of compressive residual compressive stresses in crack retardation?; (2) Why does the magnitude of the retardation increase with decreasing baseline ΔK?; and (3) Is retardation strictly a surface phenomenon or is it through-thickness in nature?

Single tensile overloads were applied to both alloys at R=0.1 and 0.6 over a wide range of overload conditions. The possible contributions of each of the above mechanisms was considered on the basis of elastic-plastic fracture mechanics. The results of the experiments were compared to predictions from FASTRAN, a plasticity-induced closure model. The ability or inability of this program to predict the experimental behavior was used as an indicator of whether plasticity-induced closure was contributing to retardation. The three-dimensional

nature of crack retardation was examined by performing surface removal experiments and examining crack fron profiles at various positions through the affected zone. Possible contributions to crack retardation resulting from the intrinsic material response to an overload, such as crack tip strain hardening, were evaluated by performing overstrain experiments on low cycle fatigue specimens.

2. Background

2.1. Nomenclature

The nomenclature used in the literature to describe test conditions and material response in crack retardation studies varies widely. A 100% overload in some studies means that the maximum load was doubled in the overload cycle while in others it means that the load range was doubled in the overload cycle. The material response is often expressed in terms of the number of delay cycles. However, in some studies this refers to the total number of cycles over which crack growth rates are affected by an overload, while in others it refers to the difference in the number of cycles needed to propagate the crack through the affected region following an overload and the number of cycles required to propagate the crack this distance under constant amplitude loading conditions. Similar double meanings can be found for other parameters. For this reason this initial background section will be devoted to clearly defining the nomenclature used in the current investigation.

The parameters used to define the test conditions are shown schematically in Figure 2.1. The baseline stress intensity factor range, $\Delta K_B = K_{max} - K_{min}$, and baseline stress ratio, R, are the applied ΔK and stress ratio prior to the overload and after the overload. The magnitude of the overloads and underloads was expressed using the nomenclature of Davidson et al. [8]. The overload ratio, OLR, is the ratio of the maximum stress intensity factor, K_{ol}, in the overload cycle to the maximum stress intensity factor, K_{max}, under baseline loading conditions. The underload

ratio, ULR*, is the ratio of the underload stress intensity factor range, $\Delta K_{ul} = K_{max} - K_{ul}$, to ΔK_B.

The parameters used to describe the response to an overload or overload/underload combination are shown schematically in Figure 2.2(a) and (b). The baseline crack growth rate, $(da/dN)_B$, is the steady state crack growth rate prior to the overload. The affected distance, a_{aff}, is the increment of crack extension following the overload during which crack growth rates are not equal to the baseline growth rate. The number of delay cycles, N_d, is the difference between the number of cycles required to reach a_{aff} following an overload and the number of cycles that would be required to grow this distance at the baseline growth rate. The minimum growth rate following an overload is designated $(da/dN)_{min}$. The increment of crack extension at which the minimum crack growth rate occurs is designated a_{min}.

2.2. Review of Fatigue Crack Propagation Fundamentals

Crack retardation phenomena and the mechanisms proposed to explain these phenomena cannot be understood without a basic understanding of fatigue crack propagation under constant amplitude loading conditions. The purpose of this section is to provide a review of the current understanding in this area.
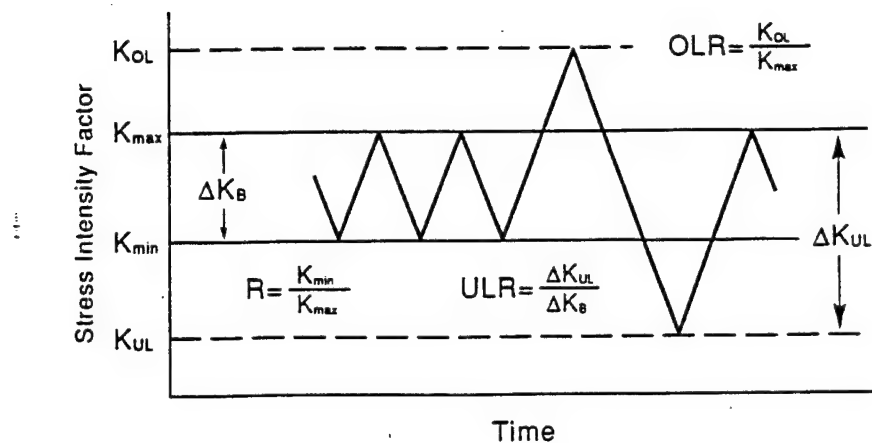
Figure 2.1.   Parameters used to define overload test conditions (after Davidson et al. [8]).
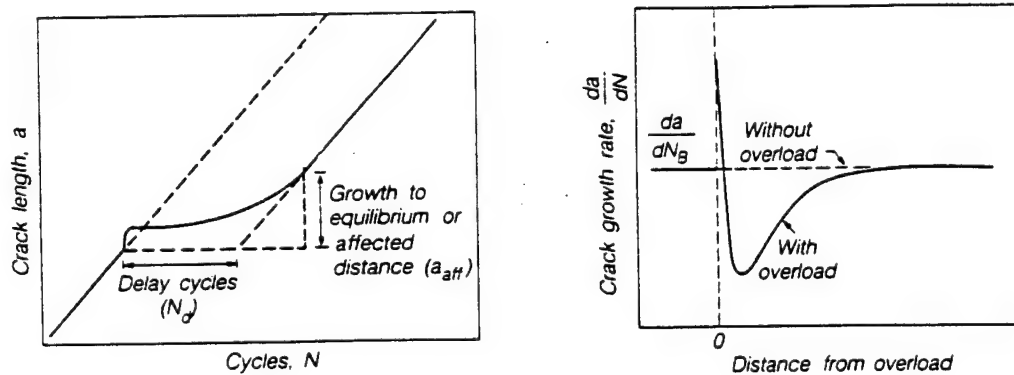
Figure 2.2.   Parameters used to describe the response to an overload (after Rao and Ritchie [7]).

2.2.1. Stress and Strain Distributions and Plastic Zones

The fundamental cause of fatigue crack propagation is cyclic plastic strain at the crack tip. However, crack tip strains are confined to a small region and exhibit steep gradients making their experimental measurement and direct correlation with fatigue crack growth extremely difficult. Paris, Gomez, and Anderson [9] were the first to realize that there was a relationship between fatigue crack growth rates and the linear elastic stress intensity factor range $\Delta K = K_{max} - K_{min}$. At intermediate crack growth rates this relationship has the form:

$$da/dN = C(\Delta K)^n \qquad (2.1)$$

which is commonly called the Paris equation. ΔK is easily calculated if the crack length, applied loads, and K solution for the specimen geometry are known. The implicit result of their work is that ΔK is related to the cyclic stress and cyclic plastic strain at the crack tip.

The stress distribution ahead of the crack tip in the crack plane (y=0) for a linear elastic material under monotonic Mode I (i.e., tensile) loading is shown in Figure 2.3(a). The stress distribution for an applied stress intensity factor K_{max} is described by:

$$\sigma_{yy} = \frac{1}{\sqrt{x}} K_{max} f_{yy} \qquad (2.2)$$

The characteristic feature of the distribution is the inverse square root character of the crack tip singularity. The strain distribution exhibits

this same form since it is related to the stress through the linear compliance tensor.

The linear elastic solution predicts an infinite stress and strain as the crack tip is approached. This cannot occur in an elastic-plastic material which can support a stress only equivalent to its flow stress, σ_o. The stress distribution ahead of the crack tip for an elastic-plastic material is shown in Figure 2.3(b). Yielding occurs at the crack tip forming a zone of plastic deformation. Irwin [10] estimated that the full width of this plastic zone in the crack plane is given by:

$$ r_p = \frac{1}{\pi}\left(\frac{K_{max}}{\sigma_o}\right)^2 \qquad (2.3) $$

where σ_o is the flow stress. For plane-stress conditions ($\sigma_{zz}=0$) the monotonic tensile yield stress, σ_y, is usually substituted for the flow stress. For fully plane-strain conditions ($\epsilon_{zz}=0$) the flow stress is elevated to $3\sigma_y$ due to the hydrostatic stresses resulting from constraint of the surrounding elastic material. However, Irwin argued that fully plane-strain conditions do not exists throughout the plastic zone and that a more reasonable value for the flow stress is $1.73\sigma_y$. The substitution of σ_y and $1.73\sigma_y$ for σ_o in Equation 2.3 gives the following equations for the plastic zone width in the crack plane (y=0) under plane stress and plane strain conditions, respectively:

$$ r_p = \frac{1}{\pi}\left(\frac{K_{max}}{\sigma_y}\right)^2 = 0.318\left(\frac{K_{max}}{\sigma_y}\right)^2 \qquad (2.4) $$
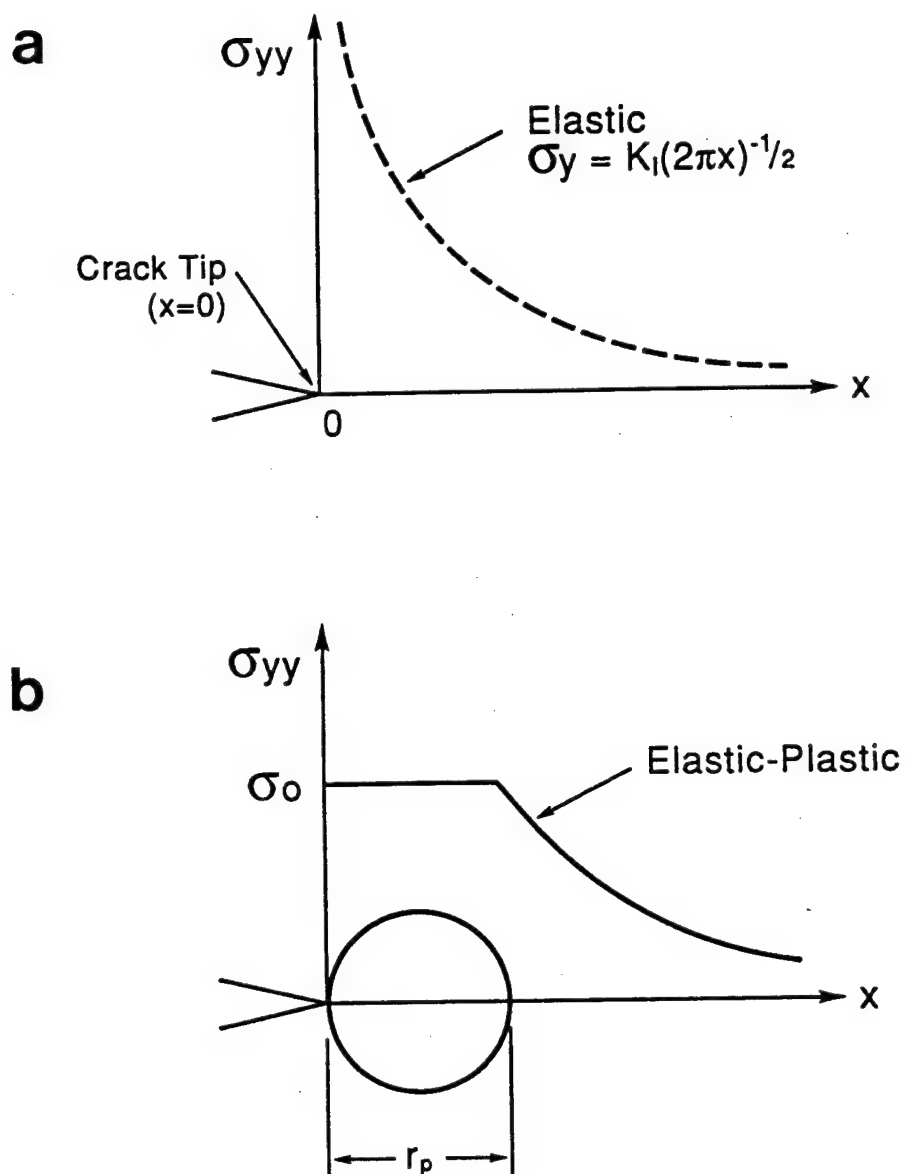
Figure 2.3. Stress distribution ahead of a crack tip in: (a) a linear elastic material; (b) an elastic-plastic material.

$$r_p = \frac{1}{3\pi}\left(\frac{K_{max}}{\sigma_y}\right)^2 = 0.106\left(\frac{K_{max}}{\sigma_y}\right)^2 \qquad (2.5)$$

More sophisticated methods employing von Mises and Tresca yield criteria or numerical analysis methods have generated other estimates of plastic zone sizes. Generalizing Equations 2.4 and 2.5 to:

$$r_p = \beta\left(\frac{Kmax}{\sigma_y}\right)^2 \qquad (2.6)$$

the range of β from these analyses is β= 0.159-0.382 for plane stress and β=0.035-0.106 for plane strain conditions.

The above analyses were for a homogeneous, isotropic, elastic-perfectly plastic materials. The plastic zone sizes are smaller than that given by the above relationships in strain hardening materials. McClung [11] estimates plastic zone sizes in high strain hardening materials are 70-80% of those in elastic-perfectly plastic materials. The stress state in a material is predominantly plane stress when the calculated plane-stress plastic zone width, r_p, is on the order of the material thickness, and predominantly plane strain when the plane-stress plastic zone width is less than one-eighth of the specimen thickness. However, plane stress conditions exist at the surface even in thick materials as shown in Figure 2.4.

Plastic zone sizes have been measured experimentally by numerous techniques including etching, microhardness, and selected area electron channeling. Many of these studies were reviewed by Lankford et al. [12]. The size of the plastic zones varied linearly with $(K/\sigma_y)^2$ in agreement with the analytical predictions. The average β from surface

measurements was 0.1. Predominantly, plane stress conditions exist at the surface. This average value is below the range of analytical predictions. This discrepancy may be partly due to the fact that the average was obtained from large number of steel and nickel alloys which typically exhibit a high degree of strain hardening. The average β for the high strength aluminum alloys in these studies was 0.28 which lay within the range of analytical predictions. High strength aluminum alloys typically exhibit a low degree of strain hardening so their behavior more closely resemble the elastic-perfectly plastic material on which the analytical predictions are based. The average β from interior measurements was 0.06. Predominantly, plane strain conditions exist in the specimen interior. This value is consistent with the analytical predictions for plane strain.

The stress, σ_{yy}, within the plastic zone is essentially constant as shown in Figure 2.3(b). The stress distribution ahead of the plastic zone is given by the linear elastic stress distribution shifted ahead of the crack by a distance equal to one half the plastic zone width. In contrast, the strain, ϵ_{yy}, in the plastic zone is not constant. An analysis by Rice [3] of the simpler anti-plane shearing case (Mode III) indicated that shear strain, γ_{yz}, in the plastic zone had a $1/x$ singularity beginning at the crack tip, instead of the $1/\sqrt{x}$ singularity predicted for a linear elastic material. More sophisticated analyses of the Mode I case such as those of Hutchinson, and Rice and Rosengren reviewed by Nicoletto [13] indicate that the tensile strain, ϵ_{yy}, in Mode I loading also exhibits a $1/x$ singularity in an elastic-perfectly plastic material.

The effect of increasing applied K_{max} on the stress and strain distribution is shown in Figure 2.5. For stress, the distance ahead of the crack tip where σ_{yy} is essentially constant increases (i.e., the plastic zone size increases) and the distribution outside the plastic zone broadens. For strain, the distribution broadens beginning at the crack tip. There is one salient difference between the effect increasing K_{max} has on the stress and strain distributions. σ_{yy} remains constant in the plastic zone regardless of the applied K_{max}. ϵ_{yy}, on the other hand, increases at any given point inside the plastic zone with increasing K_{max}.

The stress and strain distributions under fatigue loading in an elastic-perfectly plastic material were analyzed by Rice [3]. His analysis is shown schematically in Figure 2.6. The stresses and strains ahead of a virgin crack (i.e., no prior loading) at zero load are equal to zero. The stress state after the initial loading to K_{max} is that for a monotonically loaded crack shown in Figure 2.6(a). Plastic flow (i.e., tensile yielding) has occurred within the monotonic or forward plastic zone. Subsequent unloading by an amount ΔK to K_{min} produces reversed plastic flow (i.e., compressive yielding) at the crack tip, which begins with the first increment of load reduction assuming that crack tip rounding by plastic deformation is negligible. This creates a new reversed plastic zone of compressively yielded material embedded within the monotonic plastic zone. Rice proposed that the changes in stresses, strains and displacements due to the load reversal are given by a solution identical to that for the original monotonic loading but with K_{max} replaced with ΔK and the flow stress replaced by $2\sigma_o$. The resulting stress distribution is shown in Figure 2.6(b). The stress distribution at
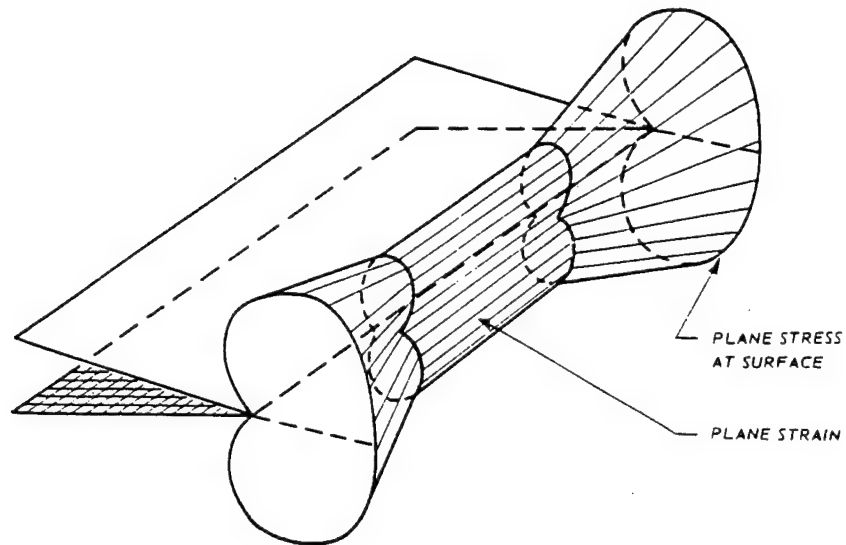
Figure 2.4.   Variation in plastic zone size across thickness in a plate of intermediate thickness (from Ewalds and Wanhill [10]).
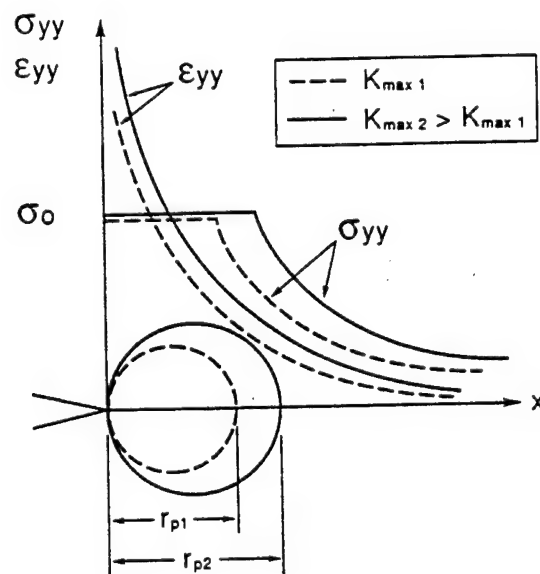
Figure 2.5.   Effect of increasing K_{max} on the stress and strain distribution ahead of a crack tip.

K_{min} shown in Figure 2.6(c) is obtained by adding the stress distribution from ΔK to the stress distribution from K_{max} using the principle of superposition. For subsequent cycles the stress distribution varies between that at K_{max} in Figure 2.6(a) to that at K_{min} in Figure 2.6(c).

A more intuitive understanding of the formation of the reversed plastic zone and the stress state at K_{min} can be obtained from the explanation of Broek [14] which is paraphrased as follows and illustrated schematically in Figure 2.7. Consider a virgin crack subjected to constant amplitude fatigue loading at R=0. Before the loading starts at point A, imagine a dashed circle at the crack tip indicating the material that will go undergo plastic deformation in the forward plastic zone (Figure 2.7(a)). The plate is then loaded to B and the material within the dashed circle is permanently deformed (Figure 2.7(b)). Now this material is removed and set aside (Figure 2.7(c)). The crack is then unloaded to zero. Since all the material is elastic, the plastic zone having been removed, all stresses, strains, and displacements are equal to zero. Thus, the hole at the crack tip (Figure 2.7(d)) is equal in size to the dashed circle in Figure 2.7(a). However, the plastic zone is permanently deformed making it larger than the hole. In order to return it to the hole at zero load it must be squeezed back to near original size by applying a compressive stress. The squeezing is accomplished by the elastic material which surrounds the small plastic zone. The squeezing produces some compressive yielding in the forward plastic zone to form the reversed plastic zone. Thus, after unloading tozero load there is a residual compressive stress equal to the flow stress in the reversed plastic zone as shown in Figure 2.7(e). This is
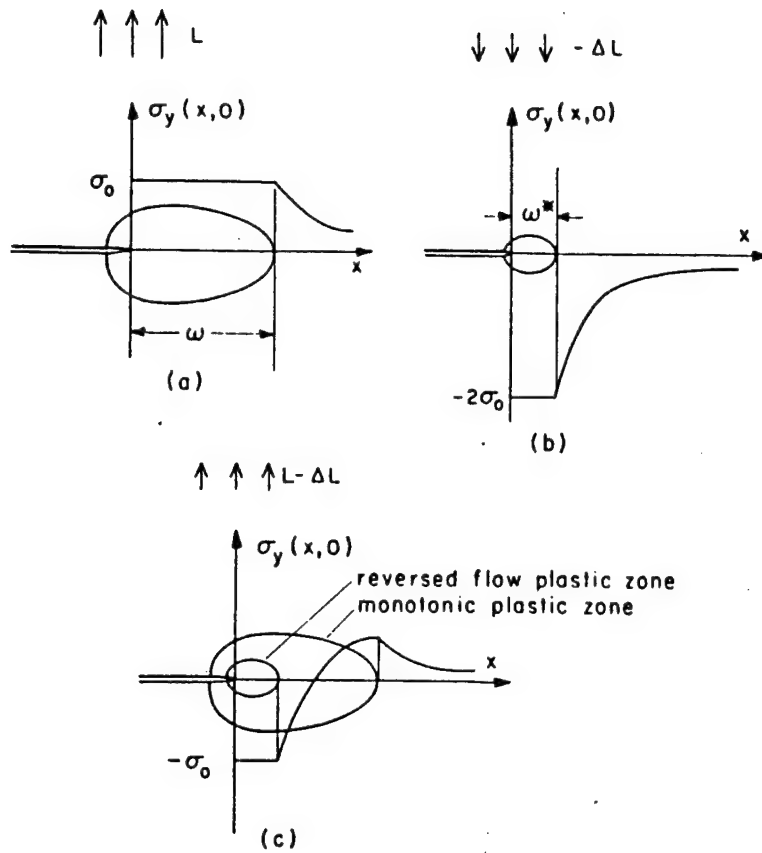
Figure 2.6.   Schematic illustrating the Rice analysis for stress distribution under cyclic loading: (a) stress distribution at K_{max}; (c) stress distribution at K_{min} (after Rice [3]).
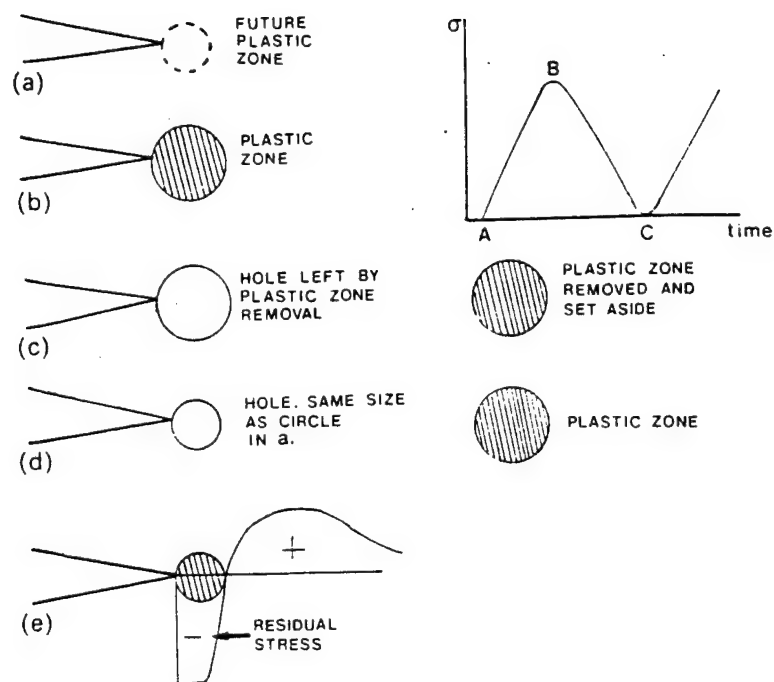
Figure 2.7. Schematic illustrating formation of reversed plastic zone: (a) load at A; (b) load at B; (c) load at B, plastic zone removed; (d) load at C, plastic zone still out; and (e) load at C, plastic zone back in (from Broek [14]).

balanced by a residual tensile stress outside the plastic zone in order to satisfy stress equilibrium requirements.

The size of the reverse plastic zone, Δr_p, was estimated by Rice [3] by substituting ΔK for K_{max} and $2\sigma_y$ for σ_y. These substitutions into Equation 2.6 yields:

$$\Delta r_p = \frac{1}{4}\beta\left(\frac{\Delta K}{\sigma_y}\right)^2 = \beta'\left(\frac{\Delta K}{\sigma_y}\right)^2 \qquad (2.7)$$

This equation shows that the coefficient β' for the reverse plastic zone is one fourth that for the forward plastic zone. The analysis indicates this holds under both plane stress and plane strain conditions. The equation predicts that when the stress ratio ($R=K_{min}/K_{max}$) is zero (i.e., $K_{min}=0$, $\Delta K=K_{max}$) the reversed plastic zone is one fourth the size of the forward plastic zone. However, at higher R the relative size of the reverse plastic zone decreases. For example, at R=0.6 the reverse plastic zone is only 1/11 of the forward plastic zone. The reverse plastic zone is of greater significance in constant amplitude fatigue crack growth than the forward plastic zone because it is within this zone that cyclic plastic strain occurs.

The Rice analysis [3] indicates that the cyclic variations in stress and strain during constant amplitude fatigue loading depend only on the stress intensity factor range ΔK and are independent of K_{max}. A greater understanding of the variations within the reversed plastic zone according to the Rice analysis, and the effects of changes in ΔK and K_{max} can be obtained by considering several stress-strain histories of an element within the reversed zone which are shown schematically in Figure 2.8.
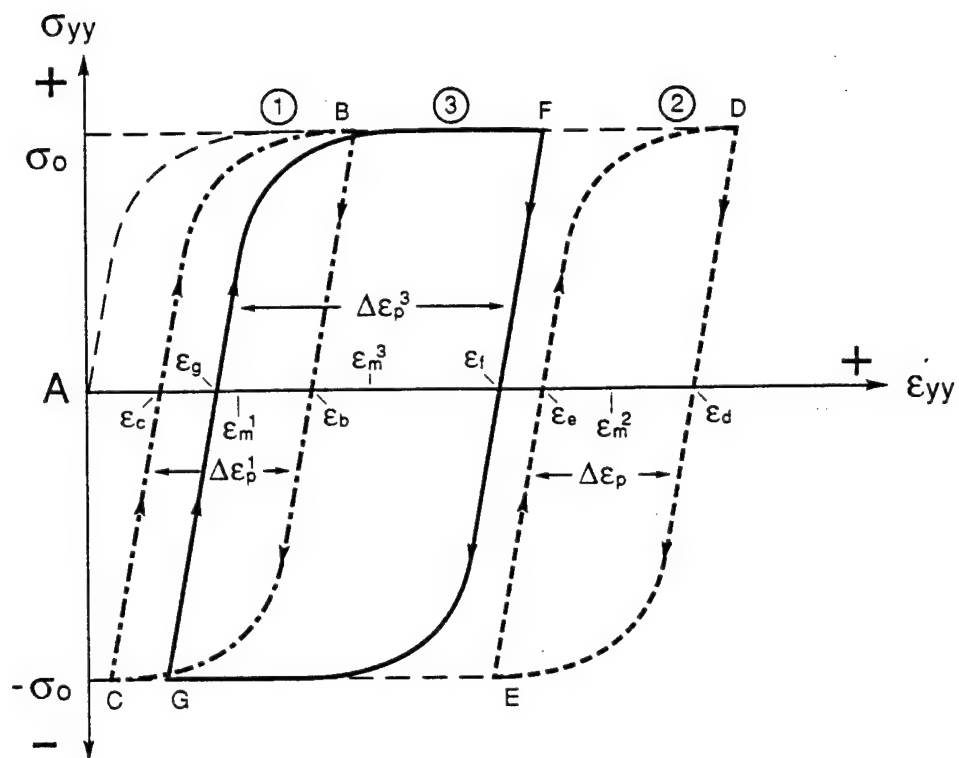
Figure 2.8. Schematic showing effect of ΔK and K_{max} on stress-strain history of element at the crack tip: (1) ΔK_1 at R=0; (2) ΔK_1 at R=0.6; (3) $\Delta K_2 > \Delta K_1$ at R=0.

First, consider a crack which will be subjected to stress intensity factor range ΔK_1 at R=0. Assume the crack has no previous load history, the material does not cyclically harden or soften and does not exhibit a Bauschinger effect. The stress and strain in the element prior to load application are zero (point A) and no plastic zone has formed. On loading to K_{max1} the stress and strain within the element are now defined by point B and the forward plastic zone has formed. On unloading to K_{min1} (i.e., zero load in this case) the reversed plastic zone forms. The material within the element is squeezed almost back to its original shape reducing the strain within the element to almost zero (point C). In subsequent cycles the element experiences the hysteresis loop defined by endpoints CB. The element is subjected to a stress range from $-\sigma_o$ to σ_o (R_σ=-1) and a plastic strain range $\Delta\epsilon_1$ from $\epsilon_c \approx 0$ to ϵ_b around a mean strain ϵ_{m1} ($R_\epsilon \approx 0$). The strain in the reverse plastic zone is always positive relative to the initial strain ϵ=0 ahead of the virgin crack.

Next, consider a crack subjected to the same stress intensity factor range, ΔK_1 but at R=0.6. The crack is subjected to loading between K_{max2} and $K_{min2} \neq 0$. On initial loading from zero load to K_{max2} the stress-strain state within the element goes from point A to point D. On unloading to K_{min2} the element yields in compression but the strain returns to only point E because the crack is not fully unloaded to zero. In subsequent cycles the element experiences the hysteresis loop defined by enpoints ED. The element still experiences the same stress range ($-\sigma_o$ to σ_o) as in the previous case. The element is subjected to a plastic strain range $\Delta\epsilon_2$ from ϵ_e to ϵ_d around a mean strain ϵ_{m2} ($R_\epsilon \approx 0.6$).

According to the analysis of Rice, the plastic strain range $\Delta\epsilon_2$ is equal to $\Delta\epsilon_1$ in the previous case. Thus, the only effect of increasing R while holding ΔK constant is to increase the mean strain the element experiences.

Finally, consider a crack subjected to a higher stress intensity factor range ΔK_2 at R=0. The crack is subjected to loading from K_{min1}=0 to K_{max2}. On initial loading from zero load the stress-strain state within the element goes from point A to point F. On unloading to K_{min1} (i.e., zero load) the strain returns to point G. The residual strain at zero load is higher than for the first case. In subsequent cycles the element experiences the hysteresis loop defined by endpoints GF. The stress range remains the same as in the other two cases. The plastic strain range $\Delta\epsilon_3$ varies from ϵ_r to ϵ_d around a mean strain ϵ_{m3} (R_ϵ=0). Thus, the effect of increasing ΔK while holding R=0 is to increase the plastic strain range and the mean strain experienced by the element, and to increase the residual strain at zero load.

The Rice analysis relates the cyclic plastic strain range to ΔK and provides a theoretical basis for understanding the Paris equation (Equation 2.1). The relationship between ΔK and cyclic plastic strain range has been confirmed experimentally by Davidson and Lankford in aluminum alloy 7075-T6 [15]. Using a stereoimaging technique they obtained the following relationship:

$$\Delta\epsilon_p = 2.8E{-}04(\Delta K)^{2.7} \tag{2.8}$$

The cyclic plastic strain range can also be related to the crack tip opening displacement range (ΔCTOD) and the reverse plastic zone

size [15]. This is not surprising since both ΔCTOD and reverse plastic zone size are a function of ΔK.

According to the Rice analysis the cyclic plastic strain range depends only on ΔK and is independent of K_{max}. This implies that fatigue crack growth rates should be independent of the applied stress ratio (R). However, in most alloys crack growth rates increase with increasing R. This behavior can be explained on the basis of crack closure effects.

2.2.2. Crack Closure

Rice [3] estimated that crack closure (i.e., contact of the crack surfaces behind the crack tip) occurred at a compressive load of approximately 5% of the maximum tensile load. He hypothesized that once crack closure occurred the remaining portion of a tension-compression load cycle below the closure level did not contribute significantly to cyclic plastic strain and fatigue crack growth. This view of crack closure ended in 1970 when Elber [16] proved experimentally that cracks under zero-tension loading (R=0) are fully closed at positive tensile loads prior to reaching zero load. He concluded that crack closure at a positive load was a consequence of residual tensile plastic deformations in the wake of the propagating crack. The residual deformation is what remains of the crack tip plastic zones through which the crack has progressed. Elber maintained the idea of Rice that the portion of the load cycle below the closure level should not contribute significantly to cyclic plastic strain and fatigue

crack growth and defined an effective stress intensity factor range $\Delta K_{eff} = K_{max} - K_{cl}$ where K_{cl} is the stress intensity factor at the crack closure load.

Therefore, the effect of crack closure is to reduce the crack driving force from the applied ΔK to some lower ΔK_{eff}. Elber revised the Paris equation (Equation 2.1) to account for closure as follows:

$$da/dN = C(\Delta K_{eff})^n \tag{2.9}$$

Alternatively, crack closure can be accounted for by incorporating an effective stress ratio, $R_{eff} = K_{cl}/K_{max}$, into the Paris equation as follows:

$$da/dN = C(\Delta K_{eff})^n = C(K_{max}(1 - R_{eff}))^n \tag{2.10}$$

Crack closure resulting from residual tensile strains in the crack wake is now commonly referred to as plasticity-induced closure. This closure mechanism has been studied by numerous investigators employing simple analytical models based on the Dugdale-Barenblatt method or utilizing finite element methods. McClung and Davidson [17] used finite element methods to examine crack profiles of stationary cracks and fatigue cracks. The crack profiles at maximum load are shown in Figure 2.9. The COD of the fatigue crack is significantly lower than the COD of the elastic-plastic stationary crack. McClung and Davidson believe two factors contribute to this difference. Their calculations indicate that approximately 60% of the difference is due to the residual tensile deformations in the crack wake. They believe the remaining 40% results from the compressive residual stresses ahead of the crack tip at zero load. The lower COD of the fatigue crack
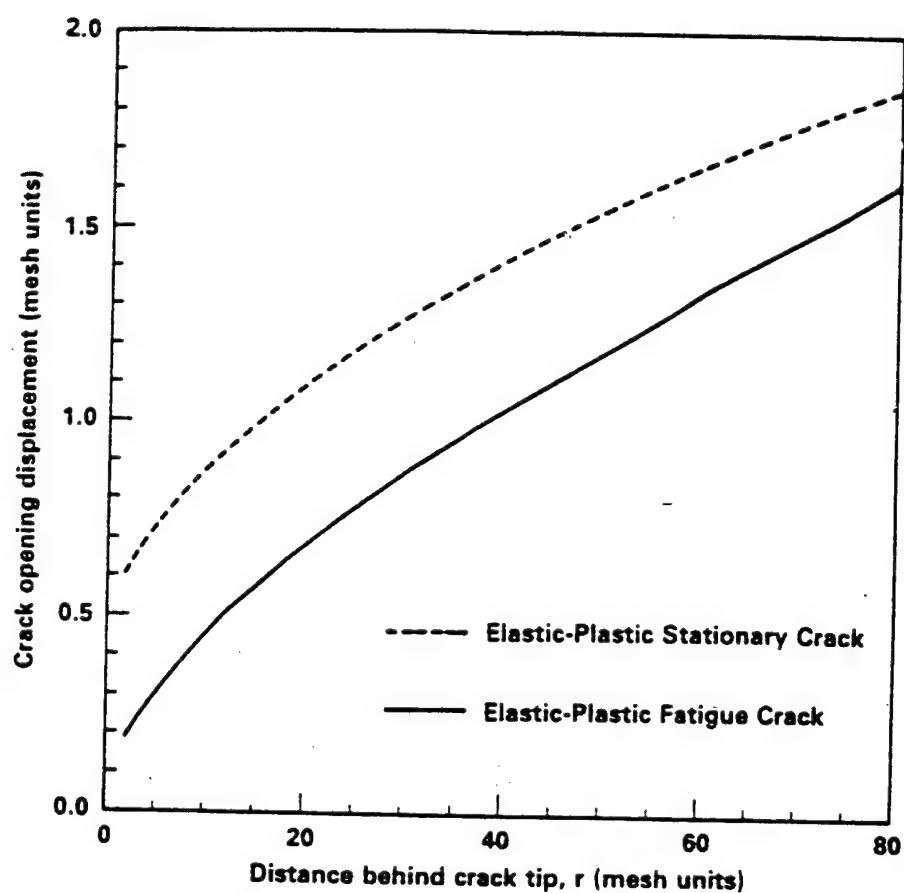
Figure 2.9. Comparison of crack opening displacements of stationary crack (i.e, non-propagating) and fatigue crack at K_{max} (from McClung and Davidson [17]).

resulting from these two factors leads to crack closure prior to zero load.

Newman [18] used a modified Dugdale-Barenblatt model to investigate the effects of crack closure on the stress and strain distributions at a fatigue crack tip. The results are shown in Figure 2.10. The stress distribution at K_{max} is nearly identical to that for a stationary crack as shown in Figure 2.10(a). However, the stress distribution at K_{min} is significantly altered by crack closure as shown in Figure 2.10(b). First, the reverse plastic zone size is significantly smaller than that for a stationary crack. This occurs because the amount of reversed plastic flow during the unloading portion of the load cycle is limited by crack closure. Once closure begins the stress singularity at the crack tip which is driving reverse plastic flow moves behind and away from the crack tip as the crack faces zip together, and the ability of the singularity to produce reversed plastic flow in front of the crack tip diminishes. Second, crack closure produces compressive contact stresses in the crack wake. These stresses are a maximum right at the crack tip and decay to zero further behind the crack tip. During the loading portion of the load cycle the contact stresses must be overcome by the applied load before the crack tip opens and forward plastic flow commences in front of the crack tip. The stress intensity factor at the point of their elimination corresponds to K_{cl}.

McClung [11] employed finite element methods to investigate the effects of closure on reversed plastic sizes. The reverse plastic zone was only 0.16 as large as the forward plastic zone size in a material

(a) Maximum stress

(b) Minimum stress
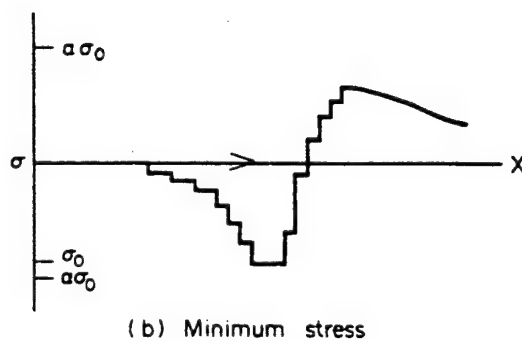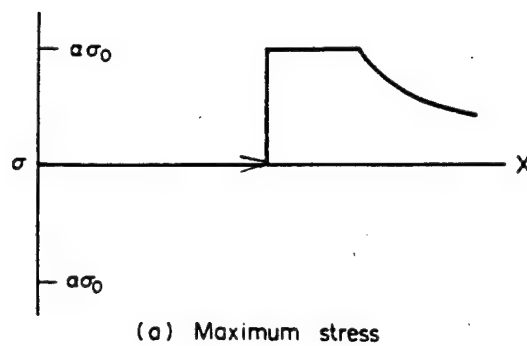
Figure 2.10. Stress distribution at a fatigue crack tip (arrowhead) with crack closure: (a) at K_{max}; and (b) at K_{min} (from Newman [18]).

with properties typical of aluminum when the analysis accounted for crack closure. This is significantly smaller than Rice's approximation of 0.25 for a stationary crack.

The effect of crack closure on the deformation history of a crack tip element at R=0 was studied by Fuhring and Seeger [19] using an analysis based on the Dugdale-Barenblatt method. The results are shown in Figure 2.11(a). On initial loading the crack tip element is deformed to point A. In the case of a stationary crack, unloading causes reverse plastic flow over the entire strain range and the deformation is partially reversed to point B. On the second load cycle, forward plastic flow commences immediately and the element is deformed to point A. Thus, an element at a stationary crack is deformed from point B to point A in each load cycle. In the case of a fatigue crack, reverse plastic flow essentially stops at K_{cl} and deformation is only reversed to point C. In reality, a small amount of plastic flow continues below K_{cl} as the stress singularity moves away from the crack tip. On loading, forward plastic flow commences when the stress intensity factor exceeds K_{cl}. Thus, an element at a fatigue crack is deformed only from point C to point A in each load cycle. The corresponding stress-strain histories of elements at a stationary and fatigue crack are compared in Figure 2.11(b). The stress range and the maximum strain are virtually identical in both cases. The cyclic strain range is smaller and the mean strain is larger for the fatigue crack due to crack closure.

The effect of applied stress ratio (R) on plasticity-induced closure levels has been considered in several analytical studies [18,20,21,22]. The results of Newman's study [18] which is typical of the others is
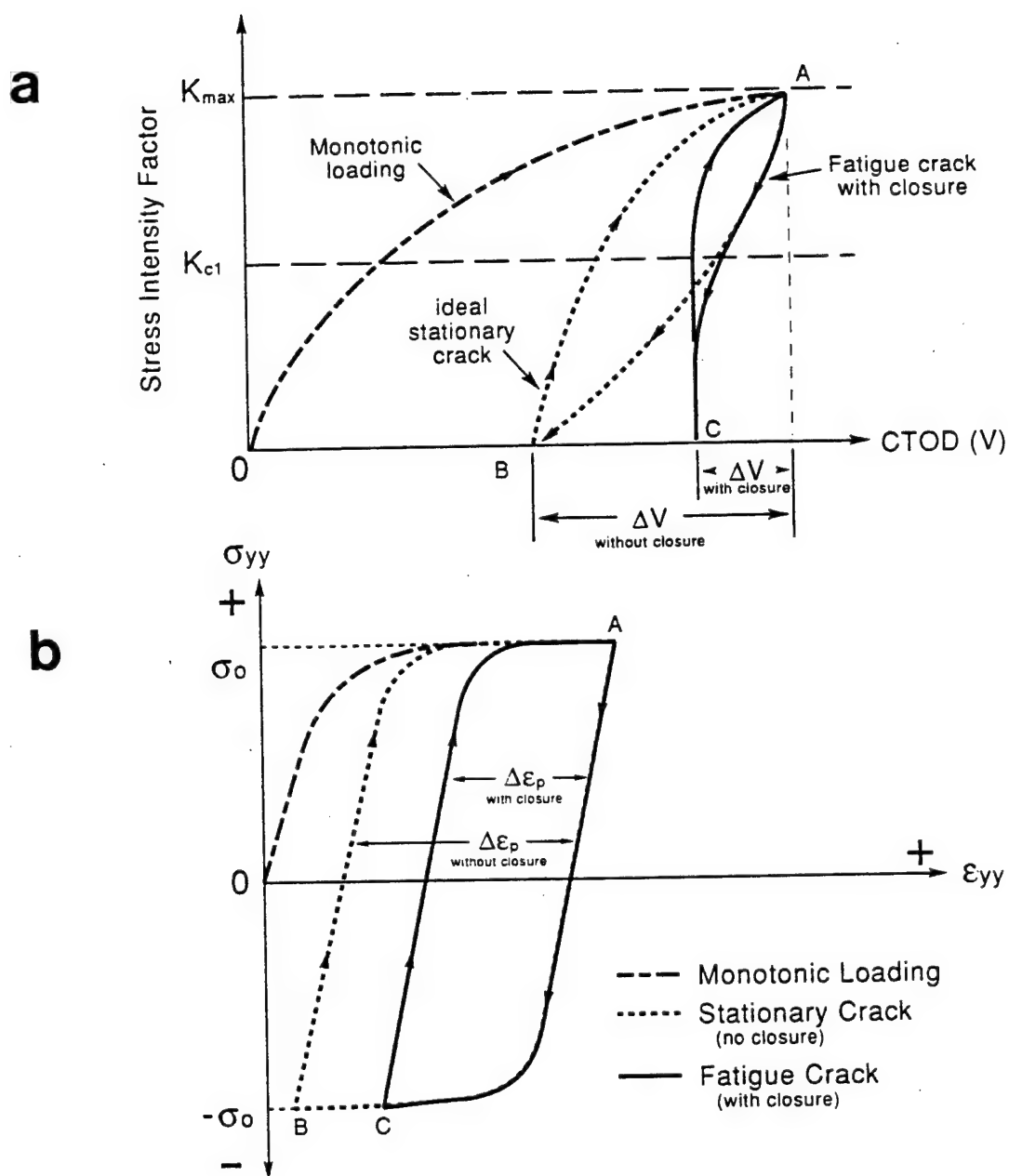
Figure 2.11. Comparison of (a) deformation history (after Fuhring and Seeger [19]; and (b) stress-strain history of element ahead of stationary crack and fatigue crack with closure.

shown in Figure 2.12. The results indicate closure levels in terms of R_{eff} increase with increasing applied R. However, the closure effects actually diminish with increasing applied R, because R_{eff} increases less rapidly than applied R. Closure ceases to occur at high applied R where R_{eff} becomes equal to applied R. The applied R at which the two first become equal is often referred to as the critical stress ratio, R_{cr}. Above R_{cr}, K_{cl} is equal to K_{min} and ΔK_{eff} is equal to the applied ΔK.

An increase in R_{eff} with increasing applied R is also supported by several experimental studies. Bray in [23] investigated the effects of R ratio on closure levels in several PM alloys, including AA5091 (Al-4Mg-1.3Li) and Al-12Fe-1V-2Si. The latter alloy is similar to AA8022 but contains a higher volume fraction of dispersoids. The closure levels were calculated indirectly from the equation:

$$K_{cl} = K(R)_{max} - \Delta K_{eff} \tag{2.11}$$

where $K(R)_{max}$ was the maximum applied K for an applied $R \leq 0.6$ for a given crack growth rate and ΔK_{eff} was the applied ΔK at R=0.7 for the same crack growth rate. The crack growth rate used in this study (da/dN=2.5E-7 mm/cycle) was in the near threshold region. Under these conditions the crack front was predominantly under a state of plane-strain. The closure levels in terms of R_{eff} ($K_{cl}/K(R)_{max}$) increased with increasing applied R and asymptotically approached the $R_{eff}=R_{app}$ line as shown in Figure 2.13(a). There was fairly good agreement between the behavior observed and that predicted by Newman for plane-strain conditions. The increase in closure levels is more dramatically illustrated in Figure 2.13(b) which shows K_{cl} as a function of applied R.
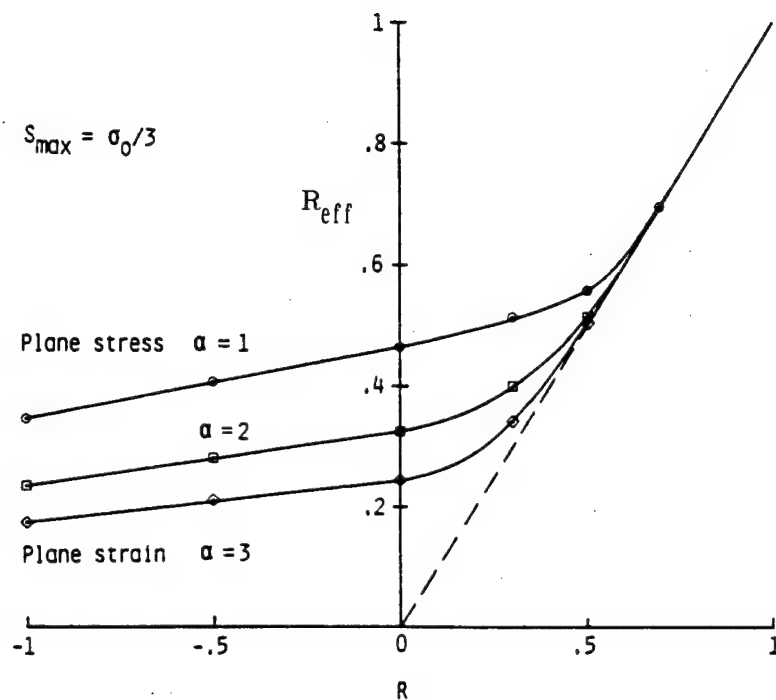
Figure 2.12. Normalized crack opening stress ($R_{eff}=K_{cl}/K_{max}$) as function of applied stress ratio under constant amplitude loading conditions for plane-stress ($a=1$) and plane-strain ($a=3$) (from Newman [18]).
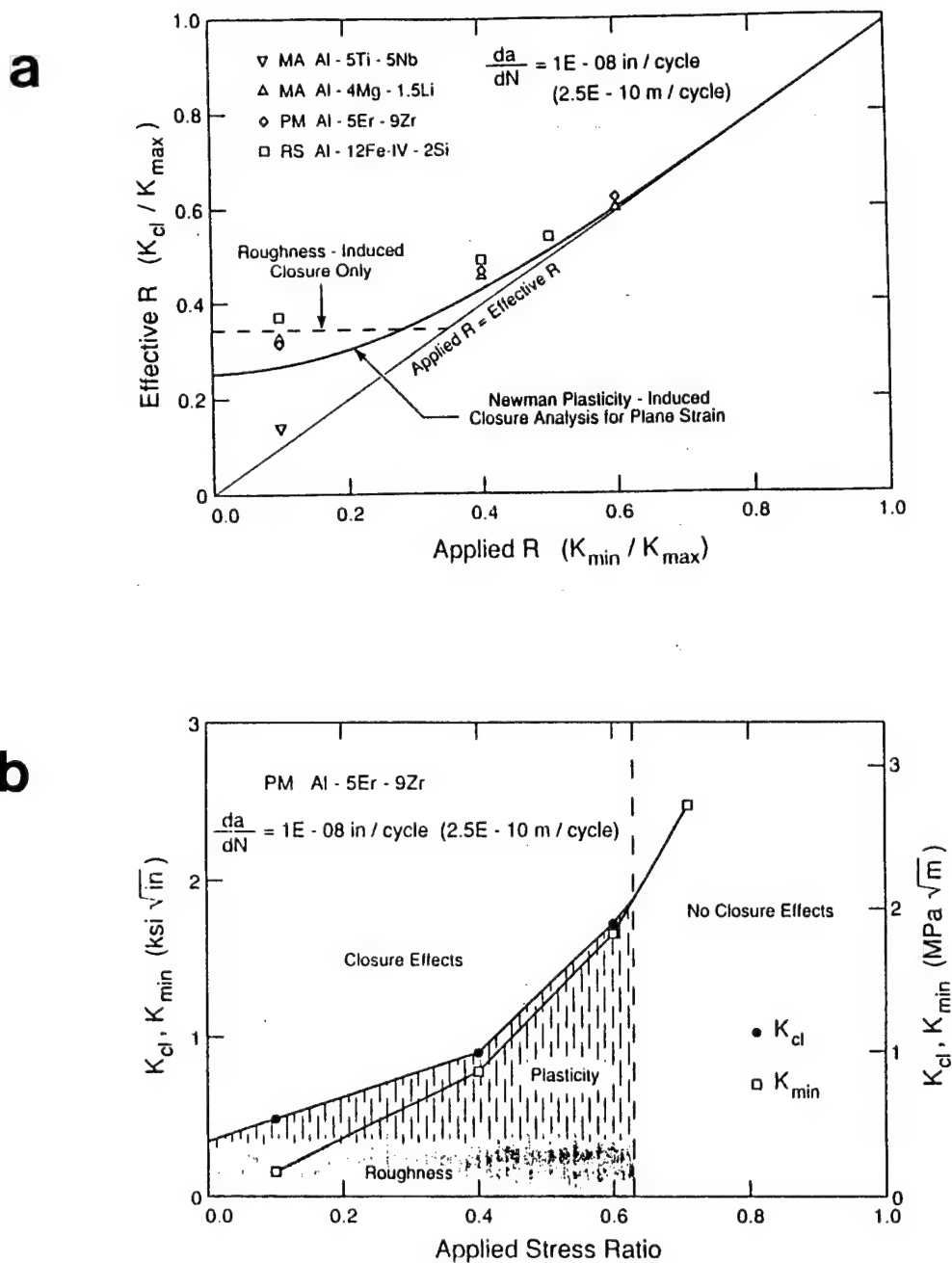
Figure 2.13. Crack closure level as function of applied stress ratio in several PM aluminum alloys in terms of: (a) R_{eff}; and (b) K_{cl}.

An increase in R_{eff} with increasing R was also observed by Hudak and Davidson [24] in PM aluminum alloy AA7091 using an SEM or an optical microscope to determine the load at which the crack tip closed, and by Gray and Mackenzie [25] in titanium alloy IMI 685 using Moire' interferometry to measure closure levels.

Newman [18] and numerous other investigators have also considered the effect of stress state on closure levels. The studies indicate that R_{eff} is significantly higher under plane stress ($\alpha=1$) than plane strain ($\alpha=3$) as shown in Figure 2.12. McClung [26] used a finite element model to study stress and strain distributions at a fatigue crack tip at R=0 under plane stress and plane strain. He found that the stress and strain distributions under plane strain were similar to those under plane stress with the following notable exceptions. The magnitude of the tensile plastic strains ahead of and behind the crack tip are not as large. The forward plastic zone is smaller and the magnitude of the residual compressive stresses are larger due to triaxial constraint. The contact stresses behind the crack tip decay much more rapidly (i.e., the crack is closed behind the tip over a much smaller distance). The smaller tensile plastic strain in the crack wake and the smaller closure distance are primarily responsible for the lower closure levels under plane strain.

Chermahini et al. [27] used a finite element model to investigate the variation in closure level across the crack front of a straight through-thickness crack in a 38 mm thick material. K_{cl} was approximately 34% of K_{max} in the interior region and 56% of K_{max} in the surface region. These differences are a reflection of the plane strain

conditions in the specimen interior and the plane stress conditions at the material surface.

The effect of stress state on closure levels predicted analytically is supported by several experimental studies. Ewalds and Furnee [28] examined the effect of surface removal on closure levels at R=0.1 in 2024-T3. There was a large decrease in closure levels following removal of 2 mm from the surface of each side of the M(T) specimen. This depth corresponded to the average width of the shear lips. After the first removal fatigue crack closure levels did not change significantly. The authors concluded that closure levels were higher in the plane stress surface region than in the plane strain interior region. Dawicke et al. [29] used near tip strain gages to measure closure levels at R=0.1 in 2024-T3 at an applied $\Delta K= 13.8$ MPa$\sqrt{m}$. The R_{eff} measured in the interior was 0.19 compared to an R_{eff} of 0.38 in the surface region.

McEvily [30] and many other researchers believe that plasticity-induced closure cannot occur under plane strain conditions on the basis of the following argument: The residual plastic stretch in the crack wake responsible for plasticity-induced closure requires a source of material. The source of material under plane stress conditions is the lateral contraction of the specimen in the through-thickness direction. This is not a possible source of material under plane-strain conditions because in this case there is no lateral contraction ($\epsilon_z = 0$). Therefore, plasticity-induced closure is not possible under plane-strain conditions.

However, recent analytical studies by McClung et al. [26] and Sehitoglu and Sun [31] using finite element methods indicate that the

residual plastic stretch in plane strain results from a transfer of material in the in-plane transverse direction (x-direction).

Not all experimental results are consistent with the analytical models of plasticity-induced closure. Closure levels in the near threshold region at low R are often much higher than those predicted for plasticity-induced closure, and closure levels often depend not only on applied R, but also on applied ΔK. Two additional closure mechanisms have been identified that can explain these behaviors, oxide-induced and roughness-induced closure.

Oxide-induced closure is closure resulting from corrosion deposits (i.e., oxide layer or corrosion debris) within the crack. Oxide-induced closure is promoted by: (1) small crack tip opening displacements (CTOD) such as those in the near threshold region, (2) moist environments such as moist air or water, (3) low stress ratios which result in repeated contact of the fracture surfaces, (4) rough fracture surfaces which promote relative sliding and rubbing between mating crack surfaces, and (5) low strength materials where the base metal is soft enough to undergo considerable fretting damage [32].

Roughness-induced closure results from the mismatch of fracture surface roughness due to combined Mode I-Mode II displacements which produce interference of the fatigue crack surfaces while still in tensile loading. The roughness is due to crack path meandering that has microstructural origins (i.e., it would not occur in a perfectly homogeneous isotropic continuum). The roughness has a hill-to-valley correspondence and Mode II displacements are necessary for interference to occur. In comparison, plasticity and oxide-induced

closure do not require Mode II displacements and do not have microstructural origins (i.e., they would occur in a perfectly homogeneous isotropic continuum). Roughness-induced closure is promoted by those factors which increase surface roughness and promote Mode II displacements. These include: (1) a small plastic zone size at the crack tip (i.e., typically less than a grain diameter), (2) microstructures with coherent, shearable precipitates which promote coarse, planar slip, and (3) crack deflection mechanisms. Roughness-induced closure is also enhanced at low R and low ΔK where CTOD is smaller than the size of the surface asperities [32].

Numerous experimental studies [e.g., 33, 34, 35] have demonstrated that when crack closure is accounted for by using the modified Paris equation (Equation 2.9) fatigue crack growth curves at different applied R essentially collapse onto a single curve. This indicates that crack closure is primarily responsible for the effect of applied R on fatigue crack growth rates. However, it should be noted that environmental effects and static failure mechanisms can also contribute to stress ratio effects especially at low and high ΔK, respectively.

To summarize, fatigue crack growth is a consequence of cyclic plastic strain at the crack tip. The cyclic plastic strain range is related to ΔK_{eff}, which is the effective stress intensity factor range experienced by the crack tip after accounting for crack closure effects. The fatigue crack growth rate increases with increasing cyclic plastic strain range and, therefore, increasing ΔK_{eff}. The fatigue crack growth rate is related to ΔK_{eff} through the modified Paris equation (Equation 2.9 or Equation 2.10).

2.3. Fatigue Crack Retardation

2.3.1. Typical Behavior

Most investigations of fatigue crack retardation have focused on the effects of single tensile overloads in ingot metallurgy (IM) alloys. The typical response of an IM aluminum alloy to a single overload is shown in Figure 2.14. There is an initial acceleration of crack growth rates over a small distance followed by a rapid decline to some minimum value, and then a more gradual increase to the baseline crack growth rate. Since the minimum crack growth rate does not occur immediately after the overload this type of response is called delayed retardation. There are several factors that affect the retardation behavior which is typically characterized in terms of the number of delay cycles N_d, the minimum crack growth rate, $(da/dN)_{min}$, and the affected distance, a_{aff}. N_d typically increases with increasing overload magnitude as a result of a lower minimum crack growth rate and a larger a_{aff} as shown in Figure 2.15 [7]. N_d and a_{aff} typically have a minimum value at some intermediate value of baseline ΔK and then increase with decreasing ΔK toward threshold or increasing ΔK toward fast fracture as shown in Figure 2.16 [36]. N_d generally increases as material thickness decreases as shown in Figure 2.17 [37]. N_d usually increases as the baseline stress ratio increases [38]. N_d increases with decreasing yield strength. N_d is often reduced when a single tensile overload is followed by a compressive underload [39].
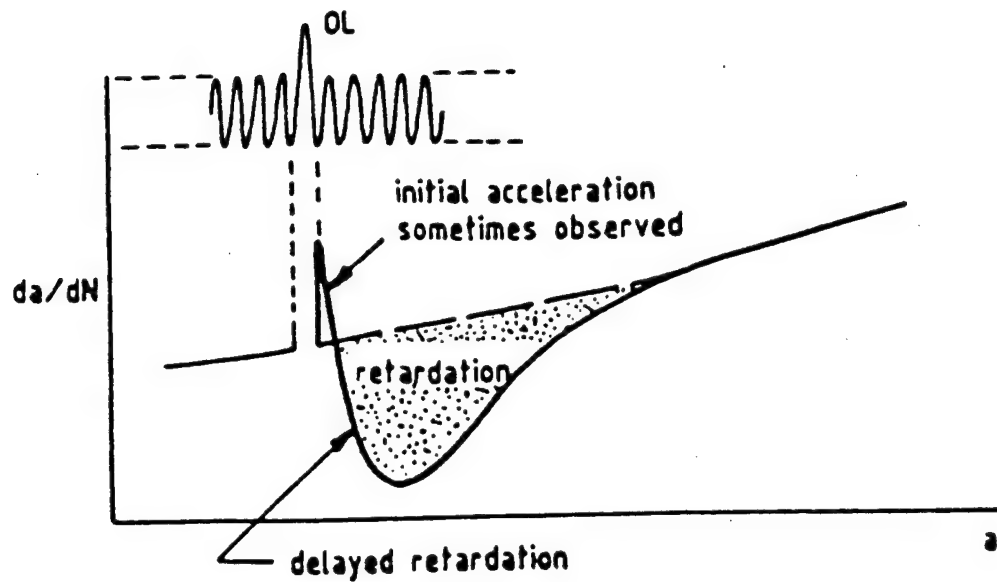
Figure 2.14. Typical response of an IM alloy to a single tensile overload.
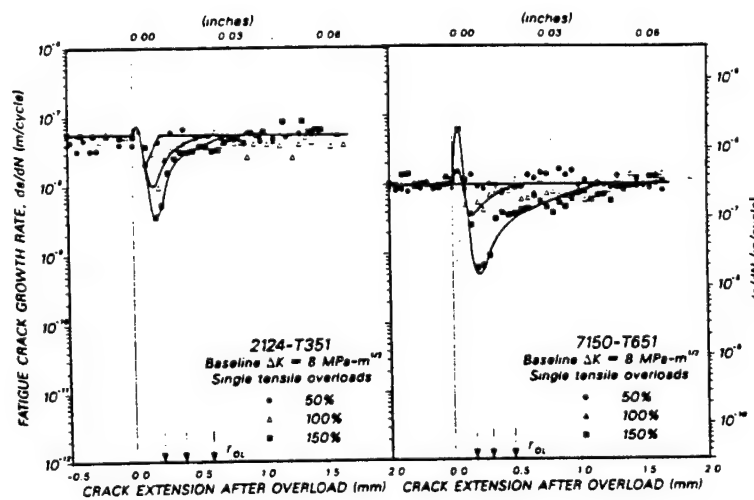
Figure 2.15. Effect of increasing overload magnitude on response of IM 2124-T351 and 7150-T651 (from Rao and Ritchie [7]).
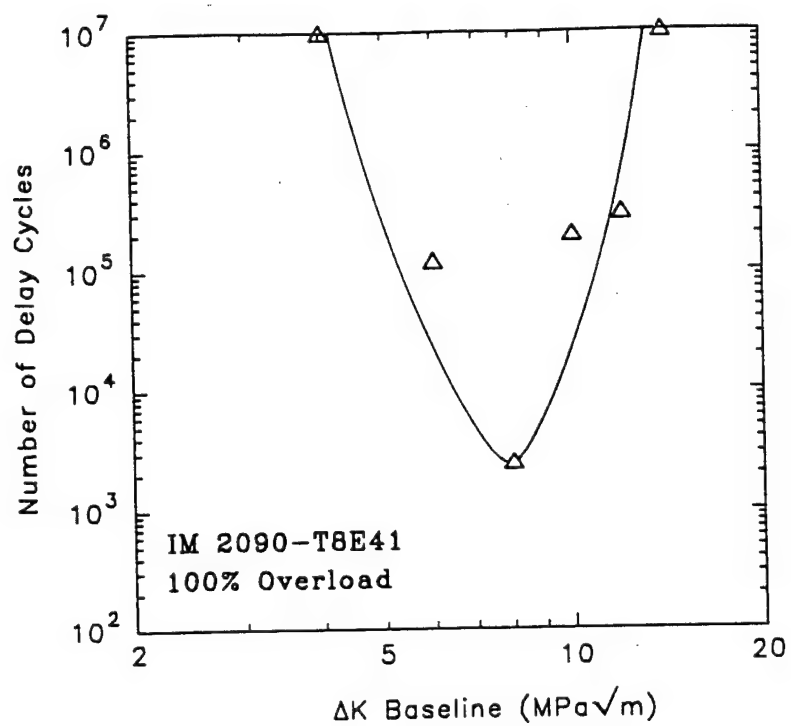
Figure 2.16. Number of delay cycles as a function of ΔK_B in IM 2090-T8E41 (after Rao and Ritchie [7]).

Only a few investigations have examined crack retardation in PM alloys [8,38,40,41]. These investigations indicate that post-overload behavior in PM alloys is quite similar to that in IM alloys. However, there are two notable differences. First, for a given overload condition, N_d in a PM alloy is typically smaller than N_d in an IM alloy with a similar yield strength [38,40]. Second, an increase in baseline stress ratio produces a larger increase in N_d in PM alloys than in IM alloys [38].

2.3.2. Proposed Retardation Mechanisms

Any mechanism proposed to explain retardation effects must reduce the cyclic plastic strain range or ΔK_{eff} experienced by the material at the crack tip. The following mechanisms have been proposed to contribute to retardation:

(1) Crack tip strain hardening

(2) Crack tip blunting

(3) Crack deflection/branching

(4) Secondary cracking

(5) Compressive residual stresses

(6) Plasticity-induced closure

(7) Roughness-induced closure

In this section the means by which each of these mechanisms reduces the cyclic plastic strain range will be examined. Then, experimental support for and against each mechanism will be considered.

a. Crack Tip Strain Hardening - The mechanism by which crack tip strain hardening reduces the cyclic plastic strain range is illustrated schematically in Figure 2.18. The crack tip element experiences the hysteresis loop defined by ABCD under baseline conditions prior to the overload. The cyclic plastic strain range is C-A. The overload increases the strain to point E. This strain is not totally reversible on unloading to the baseline minimum load resulting in a residual strain of magnitude H-A. The flow stress at point E is greater than that at point B as a result of strain hardening. Assuming strain hardening is isotropic, the compressive stress at point G is also greater than that at point D. Under baseline conditions after the overload, the crack tip element experiences the hysteresis loop defined by HIJG. The cyclic plastic strain range after the overload, J-H, is less than that prior to the overload, C-A, because of the higher flow stress after the overload. The crack must grow beyond this region of strain hardened material or cyclic softening of this material must occur before the crack resumes propagating at the baseline rate. This mechanism differs from all the others with the possible exception of the compressive residual stress mechanism because the cyclic plastic strain range is reduced because of a change in intrinsic material properties rather than through a reduction in ΔK_{eff}.

Knott and Pickard [2] used this mechanism to explain differences in the number of delay cycles in an underaged and overaged Al-Zn-Mg alloy. The tests were performed on thick specimens at a stress ratio of R=0.5 in order to minimize closure effects. The number of delay cycles
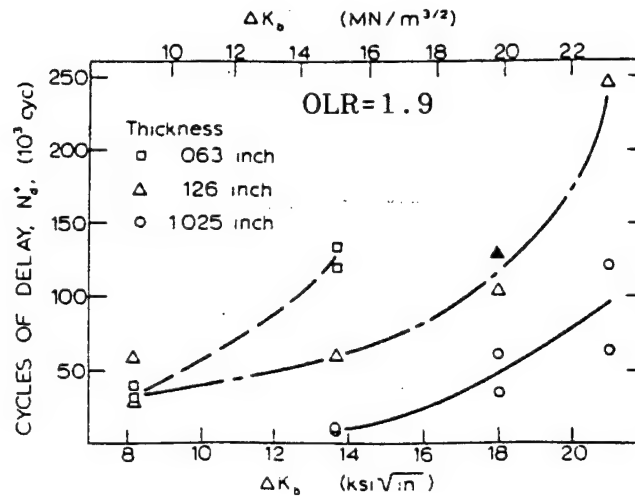
Figure 2.17. Effect of specimen thickness on the number of delay cycles in IM 2024-T3 (from Mills and Hertzberg [37]).
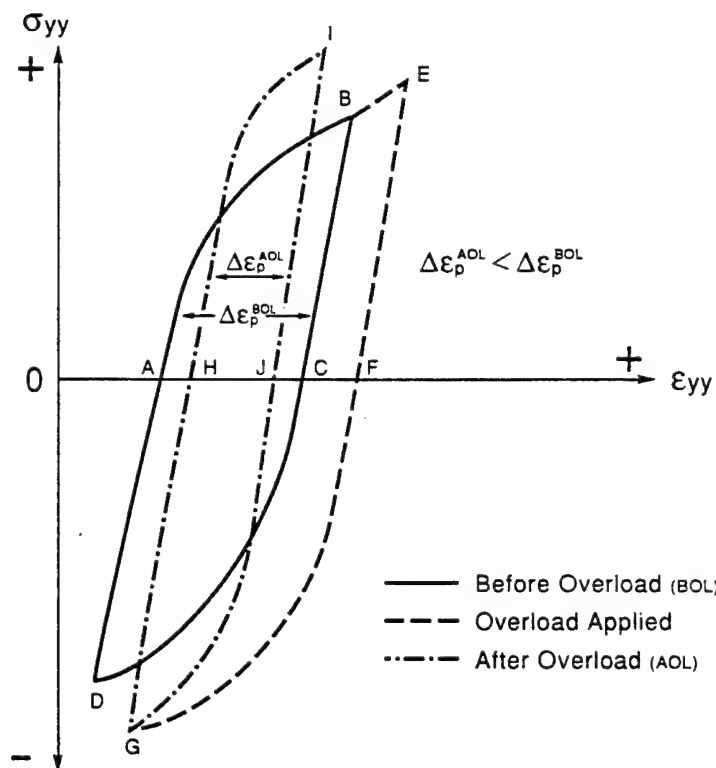
Figure 2.18. Schematic of crack tip strain hardening mechanism.

was greater in the underaged material which exhibited greater work hardening than the overaged material.

Fleck [41] believes this mechanism is only of secondary importance and cites the following evidence to support his position: (1) The model predicts immediate retardation which is inconsistent with the delayed retardation observed in both IM and PM alloys. (2) Cracks have been observed to grow faster in pre-strained IM Ti-6Al-4V, IM 2024-T3, and SAE 1010 steel than in unstrained material, presumably because strain hardening leads to increased crack growth rates by reducing ductility. (3) The application of a compressive overload following a tensile overload which should further strain harden the material and cause greater delay, instead reduces subsequent retardation.

b. **Crack Tip Blunting** - There is an increase in plastic strain ahead of a crack tip as a result of an overload. The increase in plastic strain occurs because the plastic strain resulting from the maximum load of the overload is not totally reversible on unloading. This increase in plastic strain produces crack tip blunting. The blunting reduces the cyclic plastic strain range at the crack tip. Proponents of the crack tip blunting mechanism believe that the reduction in cyclic plastic strain range is significant to produce a reduction in crack growth rates or even crack arrest. In the latter case they contend that a finite number of cycles is required to reinitiate the crack before it can continue to propagate.

Rice [3] performed calculations in order to assess the effects of crack tip blunting on cyclic plastic strain range. He considered these

calculations to be rough approximations, but felt they were qualitatively correct. His analysis for stress and strain distributions at a fatigue crack previously discussed in Section 2.2.1. assumed that the crack tip of a fatigue crack is infinitely sharp, and the resulting stress concentration is infinite. In fact, crack tip opening displacement is finite and plastic flow at the crack tip does not occur immediately upon loading and unloading, but rather is preceded by small amount of elastic loading or unloading. Rice estimated that under constant amplitude loading the material at the crack tip behaved plastically over approximately 95% of the load range. This suggests that under baseline loading conditions the assumption of a finite crack tip and immediate plastic flow is reasonable. Rice estimated that in one case the cyclic plastic strain range at the crack tip under baseline loading conditions was approximately $\Delta\epsilon_p=0.69$. However, when an overload of twice the baseline maximum load was applied, the calculated cyclic plastic strain range under subsequent baseline conditions decreased to $\Delta\epsilon_p=0.22$, and when an overload of five times the baseline maximum load was applied, the calculated cyclic plastic strain range decreased to $\Delta\epsilon_p=0.04$. Rice's calculations suggests that crack tip blunting can have a significant effect on crack growth rates following an overload.

However, a more recent experimental study conducted by Taylor et al. [42] indicates that extremely high overloads are necessary to produce significant retardation by this mechanism. In this study, blunted cracks were produced in A533B pressure vessel steel by applying overloads and stress relieving. In this manner, root radii of up to 60 μm could be obtained in this tough steel without initiating unstable cracking. The

crack growth rates out of the blunted crack tip were equal or greater than that under constant amplitude loading conditions except for the largest root radii which did produce a reduction in growth rates. For example, for ΔK_B=5 MPa√m at R=0.3 a root radius of 20 μm was needed to retard crack growth. The overload stress intensity needed to produce this root radius was 80 MPa√m which corresponds to an overload of magnitude OLR=11. Taylor et al. estimated the equivalent stress intensity of a notch or blunted crack in terms of its root radius, ρ, and the stress intensity, ΔK, of a sharp crack of the same length as follows:

$$\Delta K_{notch} = \sigma_y \left[\left(\frac{\Delta K}{\sigma_y} \right)^2 - \frac{\rho}{0.08} \right]^{1/2}$$
(2.12)

This equation was derived assuming plane strain conditions and that a notch or blunted crack and a sharp crack having equal reversed plastic zone size (i.e., equal cyclic plastic strain range) should have equivalent ΔK.

Fleck [41] cites the following additional evidence that suggests this mechanism is of secondary importance under typical overload conditions: (1) This mechanism predicts immediate retardation which is inconsistent with the delayed retardation typically observed in IM and PM alloys. (2) The affected distance typically observed in IM and PM alloys is on the order of the overload plastic zone size. The affected distance predicted by this mechanism is approximately 2% of the overload plastic zone size. Suresh [4] points out that crack branching along the intense shear bands caused by the overload often occurs which would render this mechanism ineffective. Suresh also points out

that severe blunting following an overload can eliminate crack closure which existed prior to the overload. He believes this effect is responsible for the initial increase in crack growth rates that is often observed following an overload.

c. Crack Deflection/Branching and Secondary Cracking - Crack tip deflection/branching and secondary cracking are proposed to cause retardation following a tensile overload by reducing the effective stress intensity range, ΔK_{eff}, at the crack tip. A reduction in ΔK_{eff} corresponds to a reduction in cyclic plastic strain range.

Crack deflection or branching are often observed along the intense shear bands that form during the overload cycle [e.g.,7,43] producing either deflected or branched crack geometries which are shown schematically in Figure 2.19(a) and (b). Suresh [4] analytically determined the effects of these geometries on the effective crack driving force defined as:

$$k=(k_1^2+k_2^2)^{1/2} \qquad (2.13)$$

where k_1 and k_2 are the Mode I and Mode II stress intensity factors at the tip of the deflected or branched crack. Using a crack deflection angle of 45° which is typical of post-overload deflection, k_1 and k_2 were found to be 0.8 K_1 and 0.3 K_1, respectively for a deflected crack and 0.6 K_1 and 0.3 K_1, respectively, for a branched crack where K_1 is the stress intensity factor of the main crack. Substituting these values into equation 2.14 yields an effective stress intensity ratio of 0.85 K_1 for a

kinked crack and 0.65 K_1 for a forked crack. Thus, crack deflection reduces the crack driving force by 15% and crack branching by 35%.

Secondary cracking refers to microcracks or fissures that are not connected to the main crack. This type of cracking is most common in brittle materials such as ceramics or metal matrix composites. However, secondary cracking can also occur in ductile metals when they contain large, brittle constituent phases for example. Rose [44] calculated the effects of microcracks on the stress intensity factor at the main crack tip. The stress intensity factor increased or decreased depending on the position of the microcracks. For example, for the geometry schematically shown in Figure 2.19(c) the stress intensity factor of the main crack increased when $\theta < 70°$ and decreased when $\theta > 70°$.

There is general agreement among investigators that crack branching and secondary cracking can contribute to retardation effects. However, most feel this mechanism is of secondary importance because it fails to predict the delayed retardation that is typically observed. The extent to which it does contribute is heavily influenced by alloy microstructure. Bucci et al. [5] observed greater retardation in low purity 7075-T6 than in high purity 7075-T6. They attributed this to crack branching and secondary cracking in the low purity material associated with large constituent particles. Rao and Ritchie [7] observed greater retardation in aluminum-lithium alloy 2090-T8, than in 2124-T3 or 7150-T6. They partially attributed this to greater crack deflection in 2090-T8. This alloy deforms by planar slip which promotes crack branching, while 2124-T3 and 7150-T6 deform more homogeneously.
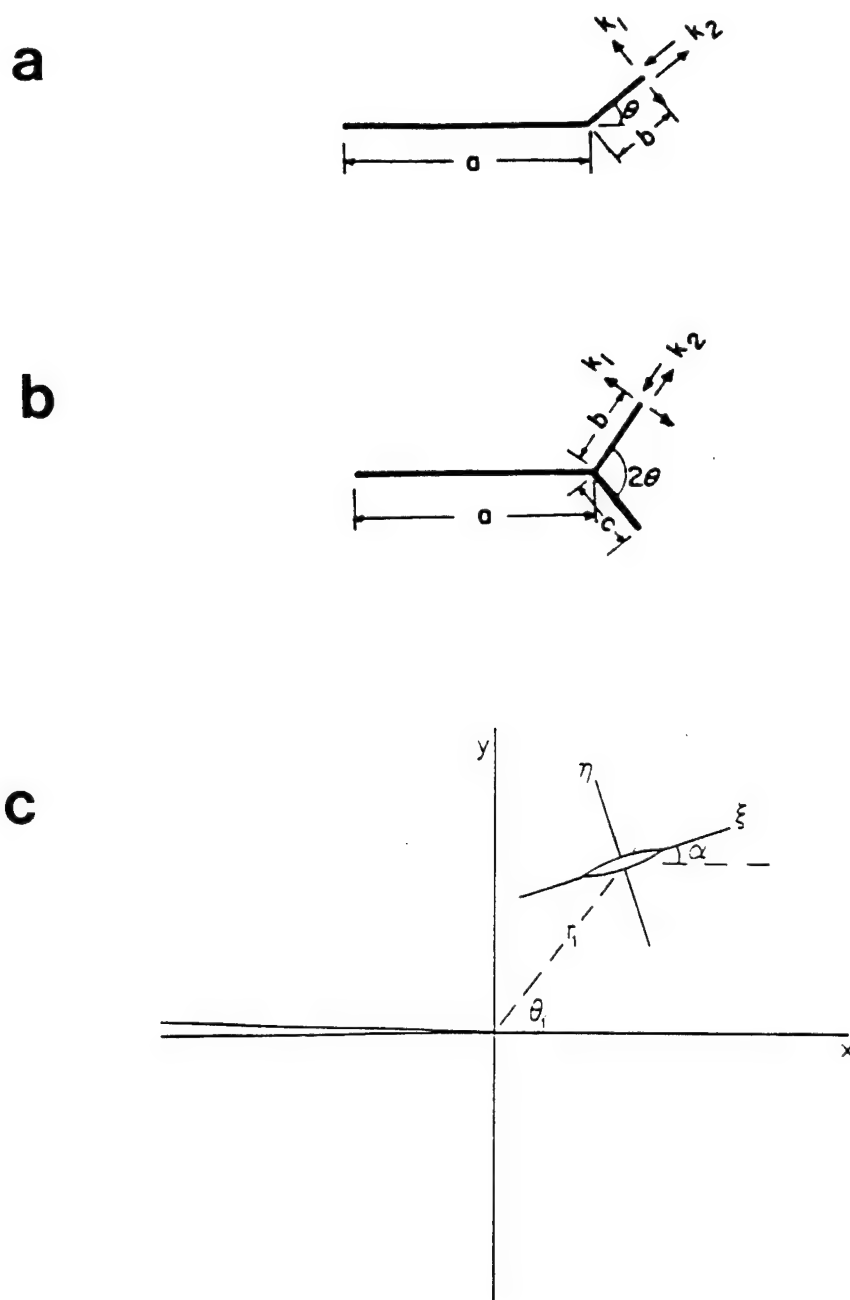
Figure 2.19. Schematics showing: (a) crack deflection; (b) crack branching; and (c) secondary cracking ((a) and (b) from Suresh [4] and (c) from Rose [44]).

d. Residual Stresses at the Crack Tip - Wheeler [6] proposed the first retardation mechanism based on residual compressive stresses. He believed that the enlarged zone of residual compressive stresses ahead of the crack tip resulting from the overload causes retardation by reducing K_{max} under subsequent baseline cycling.

More recently, Sun and Sehitoglu [31,45] employed a CRAY supercomputer and finite element methods to investigate the effects of the residual compressive stresses ahead of fatigue cracks. Their analysis indicates that the stress needed to produce tensile yielding ahead of a fatigue crack, which they designated S_{tt}, exceeds the crack opening stress, S_{op}, needed to eliminate contact stresses in the crack wake. The discrepancy in S_{tt} and S_{op} was the consequence of a finite crack tip radius and compressive residual stresses ahead of the crack tip. These results suggest that both crack closure behind the crack tip and compressive residual stresses ahead of the crack tip influence the cyclic plastic strain range experienced by the crack tip. The relative contributions of the crack closure and compressive residual stresses to S_{tt} depended on stress level, stress ratio and stress state. The compressive residual stress component of S_{tt} was larger in plane strain than in plane stress, and decreased with increasing applied stress and increasing stress ratio as shown in Figure 2.20. This analysis was for constant amplitude loading conditions. However, assuming this analysis is correct, it is reasonable to believe that S_{tt} would increase following an overload, since overloads enlarge the region of compressive residual stresses ahead of the crack tip. This would reduce the cyclic plastic strain range ahead of the crack tip and cause crack retardation.
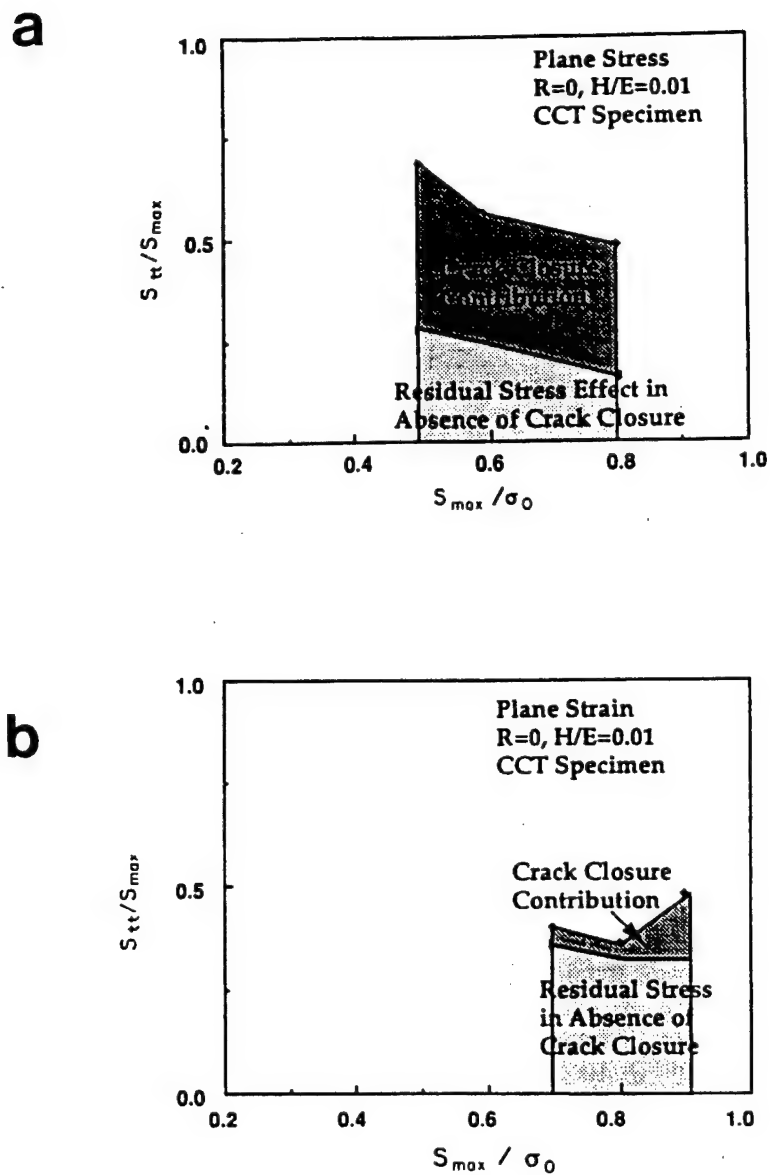
Figure 2.20. Crack closure contribution to S_{tt} and the residual stress effect on S_{tt} in the absence of crack closure: (a) plane stress; and (b) plane strain (from Sun and Sehitoglu [45]).

Drew et al. [46] investigated the role of compressive residual stresses in retardation by stress relieving C-Mn structural steels after tensile overloads. Stress relieving completely eliminated retardation leading the investigators to conclude that residual compressive stresses are the main cause of retardation following overloads. The elimination of retardation effects by stress relieving was also observed by Damri and Knott [47] in structural steel and by Ling and Schijve [48] in IM aluminum alloy 2024-T3. However, an experimental study by Blazewicz reported in [41] suggests that the contribution of compressive residual stresses ahead of the crack tip to crack retardation is small. In this study impressions were made in 2024-T3 sheet with a ball indenter to induce compressive residual stress fields. There was only a slight reduction in growth rates when the crack was grown into the region of high residual compressive stresses between impressions.

Schijve [39] other critics of the Wheeler mechanism point out that this model is not physically reasonable since K_{min} should also be reduced by compressive residual stresses by an amount equal to the reduction in K_{max} producing no net change in ΔK_{eff}. Fleck [41] raises several other objections to this mechanism: (1) The model predicts the retardation effect is immediate since the maximum residual compressive stresses exists immediately after an overload, when, in reality, delayed retardation typically occurs. (2) Crack growth rates typically remain retarded after the crack has propagated well beyond the overload reversed plastic zone. (3) Mean stress relaxation occurs in the reversed plastic zone ahead of an advancing crack tip. Thus, the crack

tip experiences fully reversed loading regardless of the sign or magnitude of any residual stress field.

Brown and Weertman [49] disagree that delayed retardation rules out the residual compressive stress mechanism. They contend that in addition to increasing the residual compressive stress ahead of the crack tip, the overload heavily strains the region nearest the crack tip. During the delay, the crack is traversing this heavily damaged region which is less resistant to fatigue propagation. The growth rate reaches its minimum value when this effect diminishes and the retardation effect is dominated by the compressive residual stresses.

e. **Plasticity-Induced Closure** - Elber [1] first proposed that plasticity-induced closure can cause crack retardation following tensile overloads. The mechanism by which this occurs can be explained by considering the changes in the stress and strain distributions resulting from an overload. The stress and strain distribution immediately before and immediately after an overload are shown schematically in Figures 2.21(a) and (b). The overload produces an increase in plastic strain ahead of the crack tip, and the region of plastic strain is expanded, now corresponding in size to the monotonic overload plastic zone from K_{ol}. The increase in plastic strain occurs because the plastic strain due to the overload is not totally reversible on unloading. This has been verified experimentally by Lankford and Davidson [50] using the stereoimaging technique and by Nicoletto [51,52] using Moire interferometry. The increase in plastic strain causes crack tip blunting since the plastic strains in the crack wake remain unchanged. The zone

of residual compressive stresses ahead of the crack is enlarged due to the increased plastic zone size resulting from the overload, but the magnitude of these stresses remains unchanged in a non-strain hardening material. This has been confirmed experimentally by Davidson and Hudak [53]. The contact stresses behind the crack tip are reduced as a result of crack tip blunting.

The reduction in contact stresses behind the crack tip produce a corresponding decrease in K_{cl} and an increase in ΔK_{eff} which can cause the crack to accelerate. However, this acceleration is temporary, because as the crack grows into the overload plastic zone the increased plastic strain in this region leads to increased residual tensile deformations in the wake of the crack as shown in Figure 2.21(c). The increased residual tensile deformations, coupled with the larger zone of compressive residual stresses, in front of the crack produce higher contact stresses in the crack wake and a concurrent increase in K_{cl} to a level greater than that which existed prior to the overload. The corresponding decrease in ΔK_{eff} to a value less than the baseline ΔK_{eff} initiates the retardation effect. Closure levels remain higher than baseline levels until the crack grows beyond the overload plastic zone. The effect of crack closure on the cyclic plastic strain range was shown previously in Figure 2.11.

Unlike the previous mechanisms, this mechanism is consistent with all of the following retardation phenomena: (1) initial acceleration immediately following overload, (2) delayed retardation, (3) increasing N_d with decreasing thickness, (4) increasing N_d with decreasing yield strength, and (5) a reduction in N_d when a tensile overload is followed
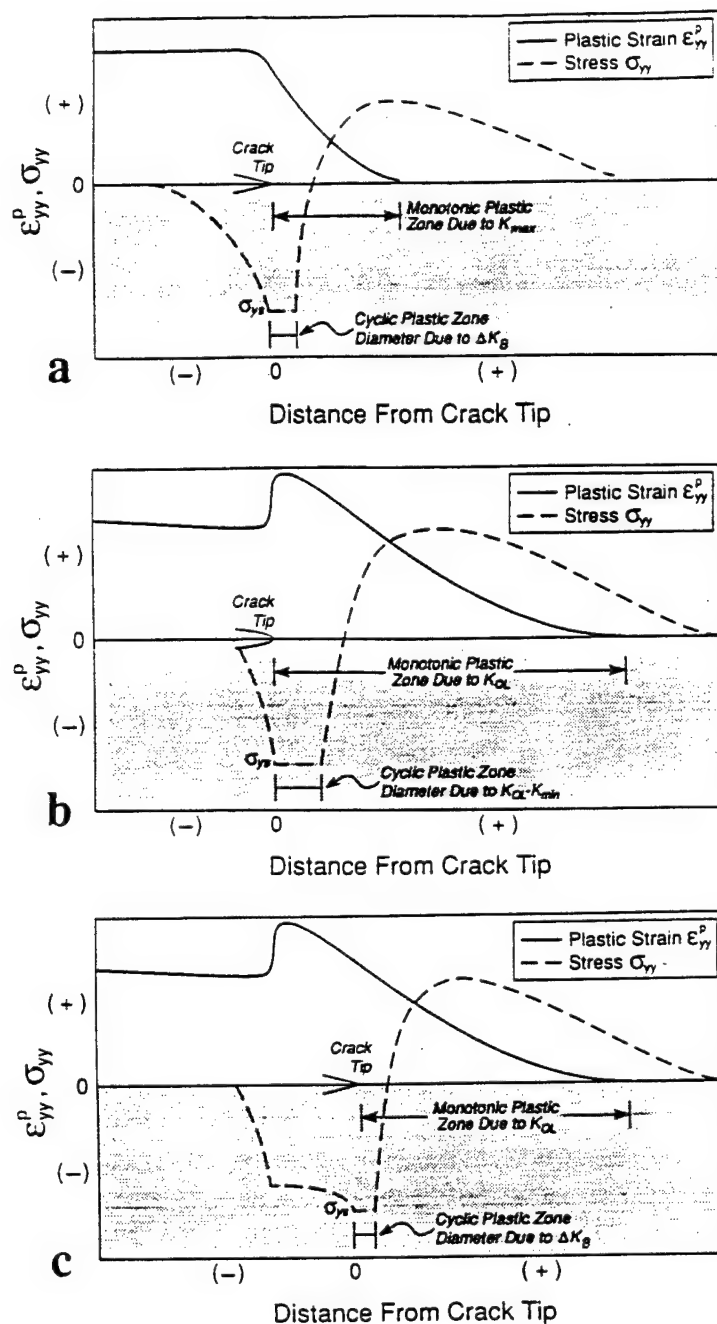
Figure 2.21. Schematics showing stress and strain distribution: (a) immediately before overload; (b) immediately after overload; and (c) after the crack has propagated into the overload plastic zone.

by a compressive underload. According to this mechanism, the initial acceleration occurs because the level of closure is reduced immediately after the overload due to crack tip blunting. The delayed retardation occurs because an increase in closure levels can only occur after the crack propagates for some distance into the overload plastic zone. N_d increases with decreasing thickness because closure levels are higher under plane stress conditions than under plane strain. N_d increases with decreasing yield strength because the overload plastic zone size is inversely proportional to σ_y^2. A reduction in N_d occurs when a tensile overload is followed by a compressive underload because the underload reduces the plastic strain in the overload plastic zone.

Many experimental studies also indicate that crack closure is a primary cause of retardation. Trebules et al. [54] removed the fatigue crack wake in 2024-T3 after applying a tensile overload and allowing the crack to propagate some distance into the overload plastic zone. The crack growth rate immediately assumed the baseline value after removal of the wake consistent with closure mechanisms. Nayeb-Hashemi, McClintock, and Ritchie [55] demonstrated that no retardation occurred following overloads under Mode III loading conditions. In Mode III loading there is no crack closure.

Many investigators have measured increased closure levels following overloads consistent with this mechanism. For example, Dawicke et al. [29] used near-tip strain gages on IM aluminum alloy 2024-T3 to measure closure levels following an overload of magnitude of OLR=2.6 at R=0.1, ΔK_B=13.8 MPa$\sqrt{m}$. Closure levels increased from a baseline value of R_{eff}=0.38 to a maximum R_{eff}=0.68 after the overload.

Reynolds [40] used near-tip strain gages to measure closure levels in IM aluminum alloy 2618-T651 following overloads of magnitude of OLR=2.0 at R=0.1, ΔK_B=8.8 MPa√m. The results are shown in Figure 2.22. Closure levels increased rapidly from a baseline closure level of R_{eff}=0.46 to a maximum closure level of R_{eff}=0.88 and then gradually returned to baseline levels. There was good correspondence between post-overload growth rates and closure levels.

However, in other studies, no increase in closure levels was observed and often there is poor correspondence between post-overload growth rates and closure levels. In a recent cooperative test program conducted by NASA [56], participants used both far-field and near-tip methods to measure closure levels in 2024-T3 following overloads of magnitude OLR=2.0 at R=0.1, ΔK_B=6 and 20 MPa√m. In the low ΔK tests, none of the methods showed a systematic increase in the closure level even though the cracks showed a large drop in growth rate or even arrested. In the high ΔK tests all methods showed an increase in closure levels although the changes were not very pronounced in some cases and did not coincide with the observed growth rates. Brown and Weertman [49] applied overloads of magnitude OLR=1.8 at R=0.05 to thin (2.5 mm) and thick (5.7 mm) 7050 sheet. Closure measurements were made with a front-face COD gage. An increase in closure levels was measured in the thin product following an overload, but the minimum growth rate and maximum closure level did not correspond. No increase in closure levels was observed in the thick specimens. This led Brown and Weertman to conclude that compressive residual stresses rather than closure are primarily responsible for the retardation.

Some investigators [4,43,57] argue that the plasticity-induced closure is primarily a plane stress effect and cannot contribute to retardation at low ΔK_B where the stress state is predominantly plane-strain. Suresh and Vasudevan [43] argue that this mechanism cannot account for retardation in cases where a_{aff} is larger than the overload plastic zone size. Fleck [41] disagrees and has proposed that even after the crack has grown beyond the overload plastic zone, the contact of the residual plastic humps can prevent the crack tip from closing and reduce ΔK_{eff}. This mechanism which Fleck calls *discontinuous closure* is shown schematically in Figure 2.23. Suresh also suggests that the plasticity-induced closure mechanism cannot explain the crystallographic or striationless mode of crack advance which often follows an overload in IM alloys. This mode is typical of crack advance under near threshold conditions.

f. **Roughness-Induced Closure** - Several investigators [4,56,57,7] have concluded that roughness-induced closure is primarily responsible for closure at low ΔK_B. The mechanism they have proposed is illustrated schematically in Figure 2.24. Residual compressive stresses and crack deflection along shear bands reduce ΔK_{eff} at the post-overload crack tip to near threshold levels. This reduction in ΔK_{eff} causes the crack to propagate by Stage I crystallographic cracking. The increase in surface roughness associated with this mode enhances roughness-induced closure and causes crack retardation. The retardation is delayed since the crack must propagate into the overload plastic zone before closure levels can increase. As the retarded crack grows away from the zone of
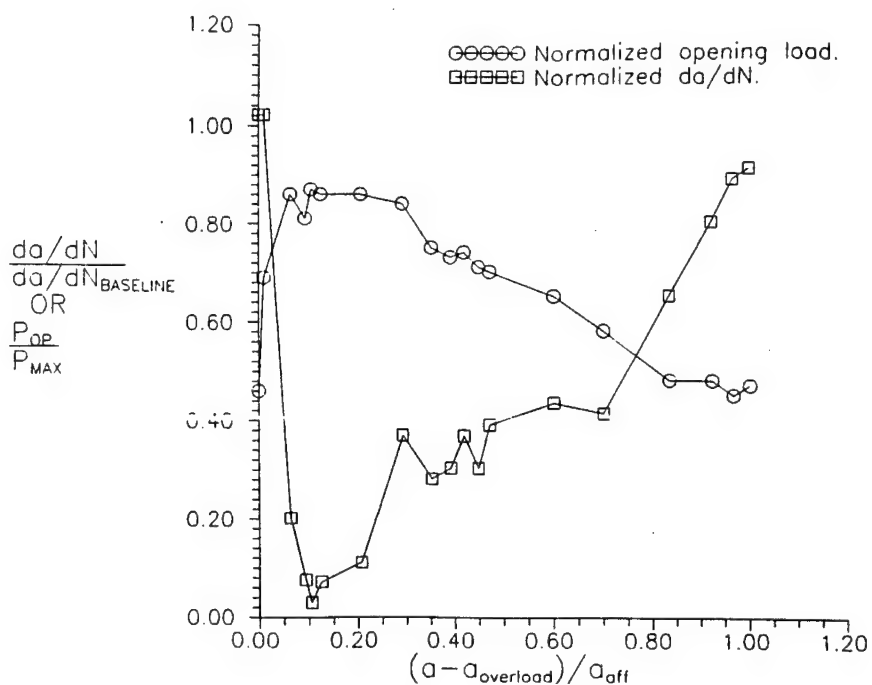
Figure 2.22. Crack growth rates and closure levels in IM 2618-T651 following overload of magnitude OLR=2.0 at ΔK_B= 8.8 MPa$\sqrt{m}$ (from Reynolds [40]).
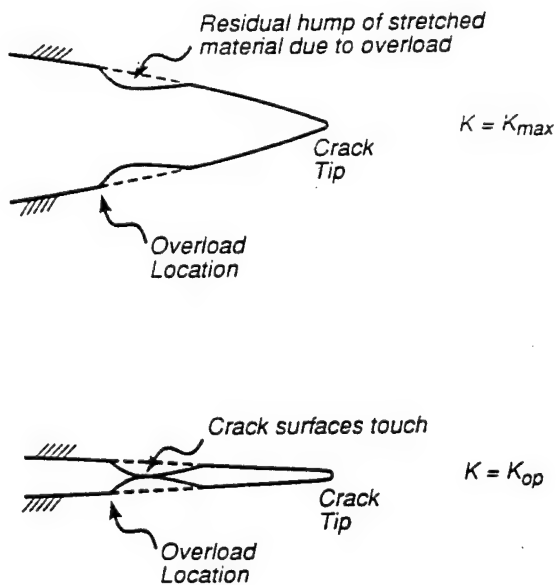
Figure 2.23. Schematic showing the phenomenon of discontinuous closure (after Fleck [41]).
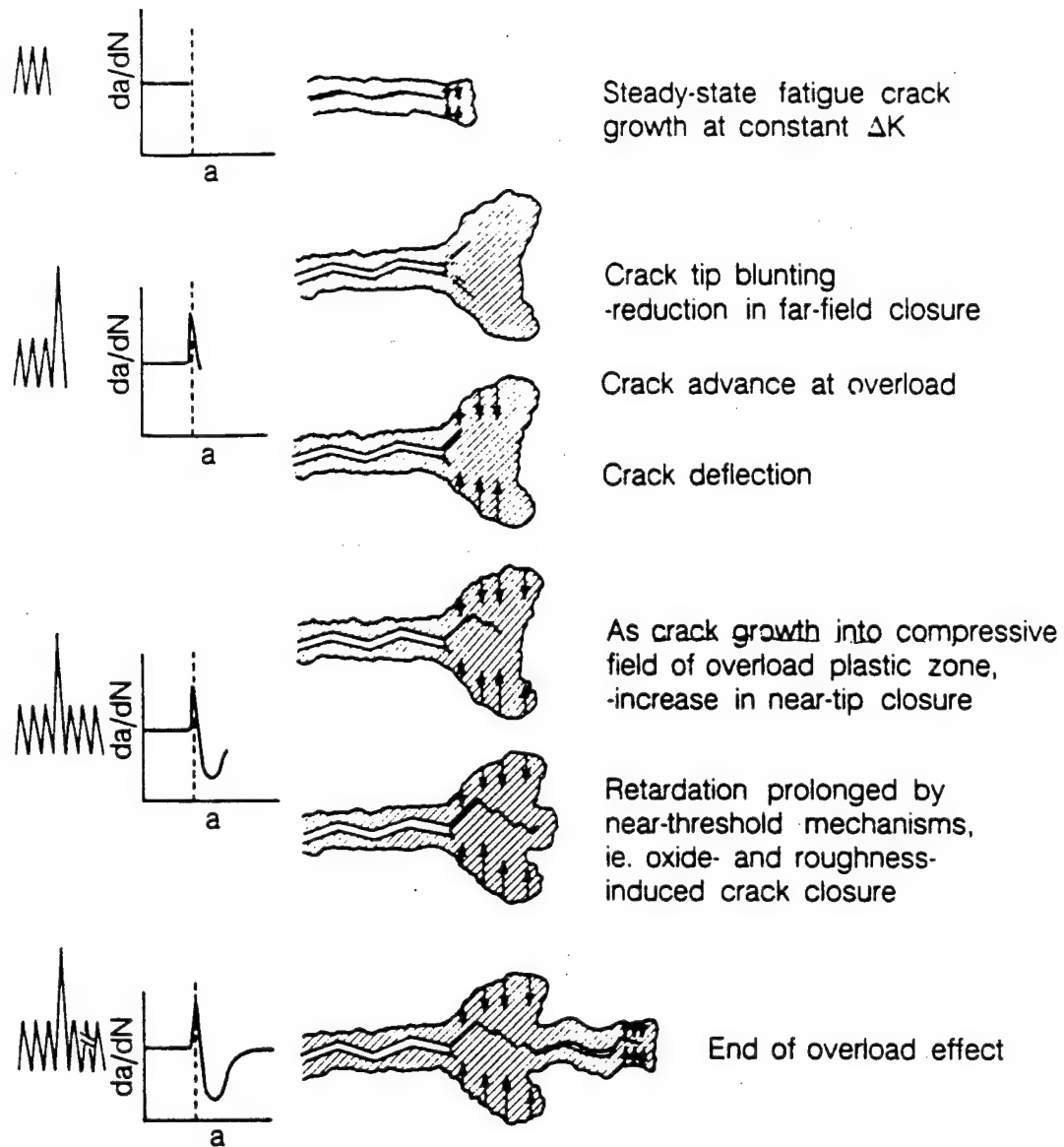
Figure 2.24. Schematic showing roughness–induced closure mechanism for crack retardation (from Rao and Ritchie [7]).

residual stresses and crack branching, ΔK_{eff} progressively increases, Stage II crack propagation gradually resumes, and growth rates assume pre-overload values. The roughness-induced closure does not initiate retardation, but prolongs it well beyond the overload plastic zone, and is the primary cause of the delay.

This mechanism has been invoked to explain crack retardation at low baseline ΔK in IM aluminum alloys 2090 [7], 2020, and 7075 [56] and IM titanium alloy IMI 550 [57]. These alloys all exhibited crack deflection and Stage I crystallographic propagation consistent with this mechanism. This mechanism is supported by observations of crack deflection and Stage I cracking following overloads in many alloy systems. Fleck [41] argues that crystallographic Stage I cracking is a consequence of a reduction in ΔK_{eff} to near threshold levels as a result of plasticity-induced closure rather than the cause of crack growth retardation.

2.3.3. Current Areas of Disagreement and Confusion

The above discussion on retardation mechanisms points out some of the many disagreements that currently exist regarding crack retardation mechanisms. This section highlights several of the areas where disagreements and confusion currently exists. The current study will examine these issues.

a. The role of residual compressive stresses- Most investigators now believe that closure mechanisms are primarily responsible for the

retardation effect at low stress ratios. Closure mechanisms are capable of explaining most, if not all, retardation phenomena and there is a great deal of experimental support for these mechanisms. However, a significant number of investigators believe that compressive residual stresses rather than closure mechanisms are the primary cause of crack retardation. This issue is somewhat confused by the fact that crack closure is due to the combined action of residual plastic deformation in the crack wake and compressive residual stresses ahead of the crack tip as explained previously in Section 2.2.2. Thus, both the increase in residual tensile deformations in the crack wake as the crack propagates into the overload plastic zone and the enlargement in the zone of compressive residual stresses ahead of the crack tip should contribute to higher closure levels following an overload and a reduction in ΔK_{eff} (i.e., the cyclic plastic strain range). However, this is not the mechanism by which the proponents of the residual compressive stress mechanism believe that residual compressive stresses cause retardation. They contend that compressive residual stresses can produce crack retardation in the complete absence of any crack closure effects.

The main argument utilized by the proponents of the compressive residual stress mechanism against closure mechanisms is that measured post-overload closure levels are not always consistent with crack growth rates. Thus, proponents of closure mechanisms must be able to explain these inconsistencies. Fleck [41] suggests that these discrepancies may be due to the use of methods which are too insensitive to measure closure levels following overloads. Near-tip methods are generally more sensitive than far-field methods. Dexter et al [8] proposed that the

discrepancy between crack growth rates and closure levels occurs because growth rates are controlled by the average through-thickness closure level, but closure measurements reflect the higher closure levels in the plane-stress surface region.

The primary argument used against the compressive residual stress mechanism is that compressive residual stresses reduce both K_{max} and K_{min} following an overload and therefore produce no change in ΔK_{eff} and the cyclic plastic strain range. Thus, the proponents of this mechanism must demonstrate that compressive residual stresses by themselves are capable of producing a reduction in ΔK_{eff} and/or the cyclic plastic strain range in the absence of crack closure effects. This has not been demonstrated experimentally, but the finite element study of Sun and Sehitoglu [44] discussed previously in Section 2.3.2.d. suggests that it is possible. The greatest experimental support for this mechanism seems to be the fact that stress relieving following an overload significantly reduces the retardation effect.

b. Mechanisms of crack retardation at high stress ratios- Crack closure effects decrease with increasing stress ratio under constant amplitude loading conditions as discussed previously in Section 2.2.2. Thus, if crack closure mechanisms are the primary cause of retardation, it is reasonable to believe that retardation effects should greatly diminish with increasing baseline stress ratio. However, results from the limited number of studies which have investigated retardation at high stress ratios suggest that this is not the case.

Brown and Weertman [48] applied tensile overloads of OLR=1.8 to IM aluminum alloy 7050-T76 at R=0.05 and 0.5. The reduction in growth rates was approximately the same at both stress ratios. Closure levels measured by a COD gage positioned at the center-line of the M(T) specimen increased following the overloads at R=0.05, but no closure was measured at R=0.5 either before or after the overload. The similarities between R=0.05 and 0.5 led Brown and Weertman to conclude that the compressive residual stress mechanism is primarily responsible for retardation at both low and high baseline stress ratios. Turner et al. [58] applied tensile overloads of magnitude OLR=1.23 to 1.5 IM aluminum alloy 7475-T73 at R=0.7, ΔK_B= 6.0 MPa$\sqrt{m}$. The number of delay cycles was significant ranging from 6600 to 15100. An Elber CTOD gage located one-half the specimen thickness behind the crack tip detected no closure either before or after the overloads. They attributed the retardation to the crack tip blunting mechanism. Kleek and Nicholas [38] applied tensile overloads of magnitude OLR=1.8 to IM aluminum alloy 7475-T73 and PM aluminum alloy CW67-T7. The minimum growth rate following an overload in PM CW67 was half the baseline rate at R=0.1, but at R=0.33 the minimum growth rate was ten times slower than the baseline rate. The minimum growth rate in IM 7475 was one tenth the baseline rate at both R=0.1 and 0.33.

These studies indicate that the magnitude of the retardation effect at high stress ratios is as great as that at low stress ratios if not greater. This result and the absence of an increase in measured closure levels following an overload seems to suggests that compressive residual stresses, crack tip blunting or some other mechanism must be

the primary cause of retardation at high stress ratios. However, an increase in closure levels following an overload at high stress ratio has been observed in at least one study. Bertel et al. [59] applied tensile overloads of magnitude OLR=1.5 to IM aluminum alloy 2124-T351 under baseline conditions of R=0.5, ΔK_B =12.0 MPa√m. Crack growth rates decreased by a factor of ten following an overload. Closure measured by a COD gage at the crack tip increased following the overload. ΔK_{eff} calculated from these measurements correlated well with observe crack growth rates indicating that a closure mechanism was responsible for the reduction in growth rates.

c. **The "U"-shaped curve**- The number of delay cycles following a tensile overload typically increases from a minimum at an intermediate baseline ΔK with decreasing ΔK_B toward threshold and increasing ΔK_B approaching unstable fracture [7,36,57,60]. This behavior results in a characteristic "U"-shaped curve when N_d for a given overload ratio is plotted against ΔK_B. Two explanations have been proposed to explain this behavior. Rao and Ritchie [7] propose that the roughness-induced closure mechanism and the plasticity-induced closure mechanism combine to produce the "U"-shaped curve. They believe that the increase in N_d as ΔK_B approaches threshold is primarily due to the roughness-induced closure mechanism. They contend that the increase in N_d occurs because roughness-induced closure effects are greatest at low ΔK_B where CTOD is small. They argue that plasticity-induced closure cannot explain the increase in N_d with decreasing ΔK_B toward threshold because the increase in plastic strain and the size of the overload plastic zone

decreases with decreasing ΔK_B. McEvily and Yang [60] disagree and hypothesize that the increase in N_d is due to the high sensitivity of crack growth rates to small changes in ΔK_{eff} at low ΔK_B. Both Rao and Ritchie and McEvily and Yang agree that the increase in N_d with increasing ΔK_B toward unstable fracture is primarily due to plasticity-induced closure.

d. Three-dimensional nature of crack retardation- There is currently disagreement over whether crack retardation is primarily a surface effect or if it is through thickness in nature. Several studies have shown that when the surface regions of the test specimen are removed following an overload the retardation effect is significantly reduced, indicating that the surface region is primarily responsible for retardation. Rao and Ritchie [7] examined the effects of surface removal following overloads of magnitude OLR=2.0 in IM aluminum alloy 2090-T8E41 at R=0.1, ΔK_B= 4.0 and 12.0 MPa√m. The retardation effect was significantly reduced but not eliminated. They explained this behavior on the basis of roughness-induced closure. According to their mechanism crack deflection at the specimen surface enhances roughness-induced closure effects in the surface region by increasing asperity wedging as the crack deviates back to the original crack plane. Removal of this region produces a reduction in the retardation effect. This mechanism was supported by the crack profiles exhibited by 2090. The profiles exhibited significant crack deflection at the specimen surface at the point of the overload, while at mid-thickness there was no deflection.

McEvily and Yang [60] examined the effects of surface removal following overloads of magnitude OLR=2.0 in IM aluminum alloy 6061-T6 at $\Delta K_B = 8.0$ MPa$\sqrt{m}$. 1.5 mm was machined from each surface after the crack growth rate had reached its minimum value following the overload. After machining the crack growth rate increased immediately by an order of magnitude, indicating that the plane stress surface regions were primarily responsible for retardation. They explained this behavior on the basis of a plasticity-induced closure mechanism. According to this mechanism retardation is entirely due to plasticity-induced closure in the plane-stress surface region. The closure level in this region increases following an overload due to increased residual tensile deformation in the crack wake resulting from lateral contraction in the through-thickness direction. The closure level in the interior region actually decreases because the stretched material at the surface serves as a wedge to hold the interior surfaces apart. Although the closure level in the interior decreases, the crack growth in this region is restrained by the surface regions resulting in crack retardation across the entire crack front.

This mechanism was supported by post-overload compliance curves. These curves exhibited a single closure level prior to an overload and immediately after an overload. McEvily and Yang believed this to be the closure level in both the interior and surface regions under constant amplitude loading conditions. However, at the minimum growth rate following an overload the compliance curve exhibited two closure levels. McEvily and Yang interpreted the upper closure level to be the closure level in the plane-stress surface region and the lower

closure level to be the closure level in the plane-strain interior region. The upper closure level was significantly higher than the baseline value and the lower closure level slightly less than the baseline value. Surface removal eliminated the upper closure level and the lower opening level returned to its baseline value.

However, other proponents of the plasticity-induced closure mechanism believe that this mechanism operates in both the surface and interior regions of the specimen. Dawicke et al. [29] used near tip strain gages on 2024-T3 to measure closure levels following an overload of magnitude OLR=1.6 at R=0.1, ΔK_B= 13.8 MPa$\sqrt{m}$ in 10 mm thick 2024-T3. The normalized closure levels (K_{cl}/K_{max}) increased from 0.19 and 0.38, in the interior and surface regions, respectively, to 0.25 and 0.68 as a result of the overload. Fleck [41] used an Elber gage to measure surface response and a push-rod assembly in the specimen interior to measure interior response following an overload of magnitude OLR=2.0 at R=0.05, ΔK_B= 25 MPa$\sqrt{m}$ in 24 mm thick BS4360 50B structural steel. K_{cl}/K_{max} increased from approximately 0.24 and 0.33 in the interior and surface regions, respectively, to a maximum of 0.52 and 0.81 as a result of the overload. Fleck also measured residual displacements on the fatigue crack surfaces resulting from the overload using a surface analyzer which had a resolution of approximately 1 μm. There was a residual plastic hump across the entire width of the specimen indicating that plasticity-induced closure produced retardation in both the plane-stress surface regions and plane-strain interior regions.

2.4. The FASTRAN-II Fatigue Crack Growth Program

The FASTRAN-II fatigue crack growth program is utilized in the current study to predict the behavior of AA8022 and AA5091 following single tensile overloads and overload/underload combinations. This program was developed by Dr. J.C. Newman of NASA-Langley [18] and is a two-dimensional model based on the Dugdale model modified to account for plasticity-induced closure arising from residual plastic deformation in the wake of the crack. The ability or inability of this program to predict the experimentally observed retardation behavior in AA8022 and AA5091 will provide an additional indicator of whether the plasticity-induced closure mechanism is contributing to retardation in these alloys.

The Dugdale or Dugdale-Barenblatt model [10, 19] assumes that all plastic deformation in the plastic zone ahead of a crack subjected to a remote stress S is concentrated in a strip of material ahead of the crack. The material in the plastic zone carries a stress equal to the yield stress, σ_{ys}, while the elastic material beyond the plastic zone carries a lower stress. Dugdale assumed that because of the plastic zone, the effective crack length was longer than the physical crack length. The plastic zone size, crack opening displacements and stress intensity factor at the crack tip are obtained by the principle of superposition. The elastic solution for a crack subjected to a traction stress, σ_{ys}, in the crack plane (y=0) over the increment Δa obtained by subtracting the effective crack length from the physical crack length is subtracted from the elastic solution for a crack in a finite-width plate subjected to a remote uniform stress, S.

Newman [61] divided the plastic zone and crack wake into one-dimensional rigid perfectly plastic elements with a flow stress, σ_o, equal to the average of the yield and ultimate strength. The flow stress was defined in this way to account for the effects of strain hardening on plastic zone size and crack opening displacements to a first approximation. The bar elements are intact in the plastic zone and broken in the crack wake. The broken elements can carry compressive stresses only. The deformation state of all elements is monitored on a cycle-by-cycle basis. The deformation of the broken elements is compared with the elastic displacements of the crack wake. Compressive stresses or contact stresses arise when the length of the deformed broken elements is greater than the computed elastic displacements. The model is illustrated schematically at maximum and minimum load in Figure 2.25. The effective stress range for a given cycle is $\Delta S_{eff} = S_{max} - S_{op}$ where S_{op} is the stress where the crack opens and contact stresses are reduced to zero. ΔS_{eff} and the current crack length are used to calculate ΔK_{eff}. The crack growth increment for that cycle (i.e., $\Delta a = da/dN$ at ΔK_{eff}) is obtained from a user input da/dN vs. ΔK_{eff} curve. The crack is propagated that amount and the procedure is repeated.

The model uses a constraint factor, α, to account for the stress state at the crack tip. The constraint factor which is user defined can be varied from $\alpha=1$ to simulate plane stress conditions to $\alpha=3$ for plane strain conditions. The constraint factor elevates the tensile flow stress for the intact elements within the plastic zone to $\alpha\sigma_o$. The appropriate constraint factor to use for a given material and thickness is obtained by finding an α by trial and error that will correlate da/dN versus
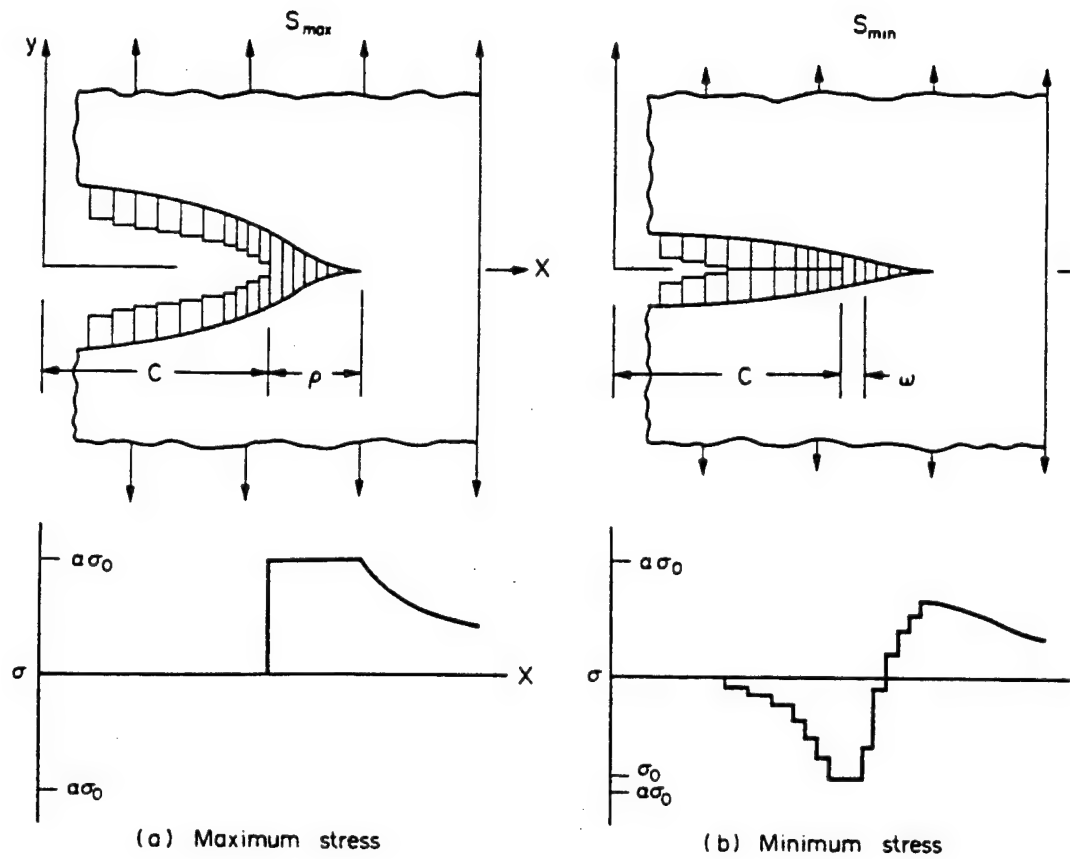
Figure 2.25. Schematic showing FASTRAN-II crack closure model under constant amplitude loading conditions (after Newman [18]).

ΔK_{eff} under constant amplitude loading over a wide range of stress ratios utilizing the equation:

$$\Delta K_{eff} = \left[\frac{\left(1 - \dfrac{S_o}{S_{max}}\right)}{(1-R)} \right] \Delta K \qquad (2.15)$$

where the quantity S_o/S_{max} is a function of a and stress ratio. The details of this method are contained in [62].

Several studies have demonstrated that the FASTRAN-II program, or its predecessors FASTRAN or FAST, provide reasonable predictions of fatigue life under constant amplitude, variable amplitude, and spectrum loading conditions. Newman [63] used FAST to predict fatigue life in IM aluminum alloy 2219-T851 for 18 constant amplitude tests, 49 variable amplitude tests and 13 spectrum load tests. The ratio of predicted to experimental lives ranged from 0.5 to 1.9 with an mean value of 0.97 and a standard deviation of 0.27. In a more recent study, Newman and Dawicke [64] used FASTRAN to predict the fatigue life of IM aluminum alloy 7475-T7351 under ten different variable amplitude loading histories. The mean value of the ratio of predicted to experimental lives was 0.95 with a standard deviation of 0.2.

Dexter et al. [8] compared FASTRAN predictions of crack opening behavior with experimental results from PM alloy 7091 obtained using stereoimaging techniques. They found that FASTRAN accurately predicted the relationship between the extent of closed crack and the applied load during the crack opening process under constant amplitude loading conditions. FASTRAN underpredicted the near tip closure measurements. The authors attributed this to the presence of other

closure mechanisms such as roughness and oxide-induced closure. FASTRAN also provided reasonable predictions of post-overload crack growth rates in terms of closure levels and crack growth rates. The Blom et al. [65] recently compared FASTRAN to a more sophisticated program based on a finite element model under plane strain conditions. There was good agreement between the models in terms of closure levels, crack surface displacements and stress distributions. However, one difference stood out. FASTRAN required a factor of a thousand less CPU time on a VAX computer than the FEM analysis required on a CYBER super-computer. In the current study FASTRAN-II was run on a IBM-compatible personal computer with an Intel 386DX microprocessor.

3. Experimental Procedures

3.1. Materials

Two AA5091 hand forgings were supplied by Inco Alloys International, Inc., Huntington, WV. The approximate size of the forgings was 26 mm X 135 mm X 220 mm. The two forgings were identified as #AL0153B122 and #AL0153B123. The composition of this material was given as Al-4.12Mg-1.3Li-1.28C-0.34O. Eight AA8022 hand forgings were supplied by Allied-Signal Inc., Morristown, NJ. The approximate size of the forgings was 10 mm X 75 mm X 120 mm. The forgings were produced from a 38 mm diameter extruded rod identified as #90B663-2. The forgings bore identification numbers RGF1208 through RGF1211 and RGF1329 through RGF1332. The lot chemistry of this material was not provided. The nominal composition of AA8022 is Al-6.5Fe-1.3Si-0.6V.

3.2. Microstructural Evaluation

Coarse microstructural features of AA5091 and AA8022 were investigated by light microscopy. Samples were prepared by electroetching as-received material in 3:1 methanol/nitric solution at -30°C.

Fine microstructural features of AA5091 and AA8022 were investigated by examining foils from as-received material in a transmission electron microscope (TEM). Foils were prepared from the

L-LT, L-ST, and LT-ST planes by electropolishing in 3:1 methanol nitric solution at -30°C. The foils were examined to characterize average grain size and aspect ratio, dispersoid size and distribution, and pre-existing dislocation structures. There was no distinction made between subgrain and grain boundaries in these measurements.

3.3. Mechanical Property Evaluation

The purpose of these tests was to characterize the monotonic and cyclic deformation behavior, and constant amplitude fatigue crack propagation resistance of AA5091 and AA8022. All mechanical property tests were performed on a 10 metric ton Materials Test System (MTS) electrohydraulic test machine.

3.3.1. Tensile Tests

Tensile tests were performed to examine the monotonic tensile behavior of AA5091 and AA8022 in the longitudinal orientation. Round specimens with a gage length of 25.4 mm and a gage diameter of 6.4 mm were tested in accordance with ASTM E8. The axial strain was monitored with an extensometer. The tests were performed in stroke control at a strain rate of 0.0005/s. Foils were excised from the LT-ST plane of the failed specimens and examined in the TEM.

3.3.2. Constant Amplitude Low Cycle Fatigue Tests

Constant amplitude low cycle fatigue (LCF) tests were performed
to determine the strain hardening/softening response of AA5091 and
AA8022 to cyclic plastic strain. The tests were conducted in accordance
with ASTM E606 on round specimens with a gage length of 12.7 mm and
a gage diameter of 5.1 mm. The tests were performed in strain control
using total axial strain amplitude as the controlling variable. The axial
strain was monitored with an extensometer. The strain rate was 0.005/s.
Separate specimens were cycled at total strain ranges of $\Delta\epsilon_t$=1, 2, and
4% until failure. Peak tensile and compressive stresses for all loops
were recorded by computer and/or strip chart recorder. Foils were
excised from the LT-ST plane of the specimens and examined in the TEM.

3.3.3. Constant Amplitude Fatigue Crack Propagation Tests

Tests were performed on AA5091 and AA8022 to evaluate their
fatigue crack propagation (FCP) resistance under constant amplitude
loading conditions. The tests were conducted in accordance with ASTM
E647 on compact tension (C(T)) specimens in the L-T orientation. The
specimen dimensions were thickness B=8 mm and width W=38.1 mm.
Fatigue crack growth rate (FCGR) curves were determined at stress
ratios of R=0.1 and 0.6 at a frequency of 10 Hz. The lower portion of
the each FCGR curve was obtained by the K-decreasing test method and
the upper part of each curve by the constant load (increasing K) test
method. The normalized K- gradient in the K-decreasing tests was –

0.1/mm. The tests were computer controlled using Fracture Technology Associates' software program FCGR2-Steady State Fatigue Crack Growth Rates Using Compliance.

The crack length measurements were made by the compliance method. The software program calculates crack length continuously from digitized load-displacement data obtained from a front-face COD gage and adjust the load automatically to obtain the desired ΔK. The program obtains the slope of the compliance curve from a linear regression of the load-displacement pairs within a window of the load range. When no crack closure is detected the window spans from 50 to 95% of the load range. If crack closure is detected above the lower limit, it is raised to eliminate load-displacement pairs below the opening load. The accuracy of the individual crack length measurements is improved by averaging the slopes from a number of compliance curves. The number of slopes averaged depends on the crack growth rate, varying from approximately 2000 in the near threshold region to 5 in the high ΔK region. The precision of the crack length measurements made by this method was approximately ± 0.003 mm. The average crack length, average ΔK, and cycle count are stored in a computer file after a user selected increment of crack extension. The program adjust the slope number to obtain approximately 10 individual crack length measurements within the selected storage interval. The stored average is the average of these individual measurements. The averages are used in the software analysis program to calculate the FCGR curve from the secant method. The storage increment selected in these tests was a/W=

0.005 (Δa=0.2 mm) at high and medium ΔK, and a/W= 0.002 (Δa=0.08 mm) in the near threshold region.

The software program also calculates crack closure levels continuously during the test [66]. The compliance curve is divided into 10 segments from minimum to maximum load. The slope of each segment is compared to the linear region of the load-displacement curve (i.e., above crack closure) and the slope segments which correspond to a deviation (offset) of 1, 2, 4, 8, and 16% from the linear region are identified. The mean load in each of these regions is taken as the closure load (P_{cl}) corresponding to that percent offset. The closure level is defined in terms of the effective stress ratio, $R_{eff}=P_{cl}/P_{max}$. The minimum closure level detectable by this procedure is approximately applied R plus 0.07. This procedure is performed only once every 20 compliance measurement sets. The computer program averages the closure levels over the user selected increment of crack extension and stores this information in the computer file with the other test information. A 1% offset was used in the current study to define the closure level.

The fatigue surfaces of the failed specimens were examined in the scanning electron microscope (SEM). The roughness of the fatigue surfaces was measured with a Surftest surface roughness analyzer.

3.4. Overload Experiments

The objective of these experiments was to characterize the effects of single tensile overloads and overload/underload combinations on the

fatigue crack propagation behavior of AA5091 and AA8022, and to determine the mechanisms responsible for these effects.

3.4.1. Low Cycle Fatigue Overstrain Tests

The purpose of the low cycle fatigue (LCF) overstrain tests was to determine the intrinsic material response to a strain history simulating that experienced by material at the crack tip of a long crack (i.e., crack length much greater than dimension of grain size or plastic zone) subjected to an overload. The intrinsic response is usually overshadowed by the mechanical response (e.g., residual stress fields, crack closure) in fatigue crack propagation overload tests making possible effects of the former on overload behavior difficult to ascertain. The specimen configuration and test methods were identical to those in the constant amplitude low cycle fatigue tests (see Sec. 3.3.2) except for the following. Specimens were cycled at $\Delta\epsilon_t$=2% for 20 cycles followed by the application of a tensile overstrain and/or compressive understrain. The specimen was then unloaded to zero load followed by additional cycling at $\Delta\epsilon_t$=2% around the new mean strain for approximately 100 additional cycles. This procedure was followed for a 2% tensile overstrain, a 2% compressive understrain, a 2% tensile overstrain followed by partial compressive understrain, and a 2% tensile overstrain followed by annealing at 350°C for 0.75 h.

3.4.2. Fatigue Crack Propagation Overload Tests

The purpose of the overload tests was to characterize the response of AA5091 and AA8022 to single tensile overloads and overload/underload combinations at R=0.1 and R=0.6 in terms of the number of delay cycles (N_d), the affected distance (a_{aff}), and post-overload fatigue crack growth rates and closure levels. The complete test matrix is shown in Table 3.1. A minimum of two tests were performed for each test condition in most cases. The specimen configuration and test methods were identical to that used in the constant amplitude fatigue crack growth tests (see Sec. 3.3.3) except for the following. The fatigue crack was propagated at the baseline ΔK until a steady state crack growth rate was achieved. The loads were adjusted continuously by the computer program to maintain a constant ΔK. A single tensile overload or overload/underload combination was applied manually at a frequency of approximately 0.1 Hz. After the overload the crack was propagated at the baseline ΔK until the steady state crack growth rate was achieved or for 1 million cycles in the case of crack arrest.

The storage interval for the average crack length and closure level typically used in these tests was a/W=0.002 (Δa=0.08 mm). A shorter storage interval was desired for both quantities in order to obtain a more accurate picture of the variation of crack length and closure level through the affected zone. However, choosing a shorter interval produced unacceptable precision of the individual crack length measurements due to averaging an insufficient number of slopes. This

Table 3.1. Overload Test Matrix

Test Type	Stress Ratio	OLR	ULR*	ΔK_B
Overload	0.1	2.00	---	1.75,2.25,3,4,6, 8,10,12
		2.50	---	4,5,6
		3.00	---	4,5,6,7,8
	0.6	1.44	---	1.75,2.25,3,4,5
		1.66	---	1.75,2.25,3,4,5
		2.00	---	1.75,2.25,3,4,5
Overload/ Underload	0.1	2.00	2.50	4.0
		2.50	2.50	4.0
		3.00	2.50	4.0
	0.6	1.44	2.50	4.0
		1.66	2.50	4.0
		2.00	2.50	4.0
Underload/ Overload	0.1	2.00	2.50	4.0
	0.6	1.66	2.50	4.0

problem was overcome by altering the program to store the individual crack length measurements and corresponding cycle count in a separate data file. Unfortunately, the program only calculates an individual closure level measurement for each storage increment. Thus, the calculated closure levels represent the average closure level over a crack growth increment of a/W=0.002 (Δa=0.08 mm). This increment is on the order of the affected distance in the low baseline ΔK tests so the variation in closure level through the affected zone could not be observed in these tests, only the average closure level through the zone.

Crack growth rates from (a,N) data pairs were computed using the seven-point incremental polynomial method of ASTM E647. This method fits a second-order polynomial curve to groups of seven crack length measurements, a_{i-3} to a_{i+3}. The crack growth rate at a_i is obtained from the derivative of the polynomial curve at that point. This method worked well except for the first few data pairs immediately before and after the overload due to the sharp discontinuity in the a vs. N curve resulting from the overload. The crack growth rates for these points were calculated manually using the secant method. The affected distance, a_{aff}, was taken as the point following the overload where a steady state crack growth rate was achieved. There was often uncertainty in this selection because the crack growth rate approaches the baseline rate in an asymptotic fashion. The number of delay cycles, N_d, was calculated as the difference between the actual number of post-overload cycles to reach the affected distance and the number of cycles it would have taken had the crack grown at the baseline rate. The

exact choice of a_{aff}, did not have a significant effect on the value of N_d obtained because most of the delay occurs well before the affected distance is reached. In short, the values of N_d obtained are significantly more precise than the values of a_{aff}.

The fatigue surfaces at the point of the overloads were examined in the SEM for evidence of crack branching, secondary cracking, rubbing, fretting products, surface roughness changes, unstable crack growth, or any other characteristics that might provide information about the retardation mechanisms in these alloys.

3.4.3. Crack Deflection Study

Crack profiles at the specimen surfaces at the positions of overloads were examined with a light microscope for all overload tests. The specimen surface was polished to a 1 µm finish with alumina powder prior to testing. Crack profiles were examined in order to determine the extent of crack deflection, crack branching, and/or secondary cracking resulting from the overload in the near surface region. The depth to which crack deflection and/or branching extended was determined for selected tests. This was accomplished by successively removing 0.12, 0.25, 0.50 mm, etc., from the nominal thickness and noting the depth at which crack deflection was no longer observed.

3.3.4. Surface Crack Retardation Study

The propagation of the crack through the affected zone was observed at the specimen surface for selected tests shown in Table 3.2. The purpose was to determine whether retardation at the surface was immediate (i.e., minimum growth rate occurred immediately) or delayed (i.e., minimum growth rate occurred after some increment of growth). This was primarily accomplished at R=0.1 by unloading the specimen to zero after some pre-selected increment of cycles, removing it from the test machine, and examining the crack tip region in a light microscope at magnifications up to 400X. At R=0.6 this method could not be used because unloading the specimen to zero significantly affected post-overload behavior. Instead acetate replicas were made in-situ while the specimen was held at the mean load and these were later examined in the light microscope.

Table 3.2. Crack Retardation Study Test Matrix

Test Type	Stress Ratio	OLR	ΔK_B
Overload	0.1	2.00 3.00	1.75,2.25,8.0 4.00
	0.6	1.66 2.00	2.25,4.0 2.25,4.0

3.4.5. Surface Removal Experiments

The purpose of the surface removal experiments was to elucidate the contribution of the interior region, if any, to the crack retardation

effect. An overload of magnitude OLR=2.0 was applied at ΔK_B= 2.25 MPa$\sqrt{m}$ and R=0.1. The specimen was removed from the test machine and 0.5 mm was removed from each surface by machining. The removal was accomplished in four to five passes in order to minimize specimen heating. Following the removal the test was continued at the former baseline ΔK. This test was performed on both alloys. An overload of magnitude of OLR=2.0 was applied at ΔK_B=10.0 MPa to AA5091 only. The amount of surface removal for this test was 1.0 mm. The post-overload behavior was compared to that in corresponding tests without surface removal. Surface removal tests could not be performed at R=0.6 because unloading the specimen for machining had a significant effect on post-overload behavior.

3.4.6. Crack Front Progression Experiments

The purpose of the crack front progression experiments was to determine the history of the crack front progression through the overload affected zone across the entire specimen thickness. This hopefully would provide information about the three-dimensional nature of the retardation effect. These experiments were performed for selected overload tests shown in Table 3.3. An overload was applied and the crack was allowed to grow some preselected distance through the overload affected zone. Then a second overload was applied in order to mark the position of the crack front. The specimen was then annealed for R=0.1 tests and unloaded to zero for R=0.6 tests to partially remove the effect of the overload. This procedure was performed for

preselected distances of approximately 0.05, 0.5, 1.0, 1.3, and 2 or 3 times the average selected distance determined in the overload tests (Sec. 3.4.2) in order to determine the shape of the crack front as it progresses through the overload affected zone. Following completion of the tests, the crack fronts were photographed in the SEM and then digitized to obtain an ASCII file.

Table 3.3. Crack Front Progression Test Matrix

Test Type	Stress Ratio	OLR	ΔK_B
Overload	0.1	2.00	4.0,8.0
	0.6	1.66	4.0

3.4.7. Elevated Temperature Exposure Experiments

The initial purpose of the elevated temperature exposure experiments was to investigate the contribution of residual compressive stresses to crack retardation in AA5091 and AA8022. This was accomplished by applying overloads of magnitude OLR=3.0 at ΔK_B=4.0 MPa$\sqrt{m}$, R=0.1 to AA8022 and AA5091 and an overload of OLR=2.0 at ΔK_B=10 MPa$\sqrt{m}$ to AA5091 at 25°C. The specimens were then exposed at temperatures of 100°C, 150°C, 225°C, 275°C, or 300°C for 1 h and slow cooled. Following exposure, the tests were continued under baseline loading conditions until baseline crack growth rates resumed. The temperatures and time selected do not produce grain growth or other major microstructural changes in these dispersion strengthened alloys and have essentially no effect on mechanical properties [67,68]. The

primary effect of this exposure is that the residual stresses in the material following exposure are limited to the yield strength at the exposure temperature.

3.4.8. Strain Gage Experiments

The purpose of the strain gage experiments was to qualitatively assess the effects of overloads and underloads on the residual strain at the crack tip. This experiment was performed for overloads of magnitude OLR=3.0 followed by an underload of magnitude ULR*=2.5 at R=0.1, ΔK_B=4.0 MPa$\sqrt{m}$, and an OLR=2.0 and ULR*=2.5 at R=0.6, ΔK_B=4.0 MPa$\sqrt{m}$. Micro-Measurements No. CEA-13-062UW-350 strain gages were applied approximately 1.5 mm ahead of the crack tip. The crack was then propagated under baseline conditions up to the edge of the strain gage grid. Strain readings were then taken in the following sequence: K_{min}, K_{max}, K_{ol}, K_{min}, K_{ul}, and at K_{min}. The readings determined in this manner are the average strain across the entire strain gage grid which had an area of approximately 1.5 X 3 mm.

3.4.9. FASTRAN Analysis

The FASTRAN-II program, previously described in detail in Section 2.4, is a fatigue crack growth program based on plasticity-induced closure. Thus, the ability or inability of this program to model or predict the trends observed in the fatigue crack propagation overload tests would provide an additional indicator of whether the plasticity-

induced closure mechanism is contributing to retardation in these alloys. The FASTRAN-II program was utilized in this investigation for this purpose. The program outputs the same information that was obtained in the experimental overload tests, i.e., crack length versus the number of cycles, crack growth rate, and closure levels. From this information the number of delay cycles and the affected distance can be determined in the same manner as in the experimental tests. Thus, direct comparison of all parameters in the experimental and simulated tests are possible.

The user inputs the monotonic tensile properties, the da/dN versus ΔK_{eff} curve, and the constraint factor, α which is equal to one for a state of plane stress and three for plane strain. The R=0.6 curve obtained for each alloy in the constant amplitude fatigue crack growth tests was utilized as the ΔK_{eff} curve. This was done on the basis of prior work with similar alloys [23] that indicated that crack closure effects are insignificant at this stress ratio under constant amplitude loading conditions. The constraint factor α was determined from the constant amplitude fatigue crack growth curves at R=0.1 and 0.6 curves by the method described previously in Section 2.4. The α obtained by this procedure was the value that yielded a ΔK_{eff} curve for R=0.1 that best corresponded to the R=0.6 curve. The α for both AA8022 and AA5091 was 2.4. This value indicates that the crack front was predominantly under a state of plane strain, which is consistent with the specimen thickness (B=8 mm) utilized in this investigation. The FASTRAN-II program predicts that the overload response is slightly dependent on crack length for a given ΔK_B and overload magnitude.

However, there was no indication of a crack length dependence in the experimental results. Therefore, in all FASTRAN simulations the crack length at the point of the overload was assumed to be 20 mm. This is approximately the midpoint of the range of crack lengths where overloads were applied in the experimental tests.

4. Results

4.1. Microstructure

The coarse microstructural features of AA8022 and AA5091 are shown in the optical micrographs of Figure 4.1. The only observable features were oxide particles. These oxide particles are the remnants of the surface oxide layer on the powder particles. The oxide layer forms as a result of the high reactivity of aluminum and oxygen, and is an inherent part of all aluminum powder particles. The surface oxide does not have a detrimental effect on the mechanical properties provided it is sufficiently broken up and distributed during consolidation and hot working [69]. The fairly good distribution of oxide particles exhibited by AA8022 and AA5091 and their good tensile elongation indicates that this was accomplished in the extrusion and forging operation. The grain structure and dispersoids in both alloys were too fine to be observed by optical microscopy.

The fine microstructural features of AA8022 are shown in the TEM micrograph of Figure 4.2. The average grain diameter in the L-LT plane was approximately 1.0 μm. There was no distinction made between grain and subgrain boundaries in these measurements. The grains were flattened as a consequence of the forging operation. The average aspect ratios L:LT:ST were approximately 2:2:1. The small grain size results from the pinning of the boundaries by the dispersoids. The $Al_{13}(Fe,V)_3Si$ dispersoids were spherical and had an average diameter of approximately 100 nm. The dispersoids were not
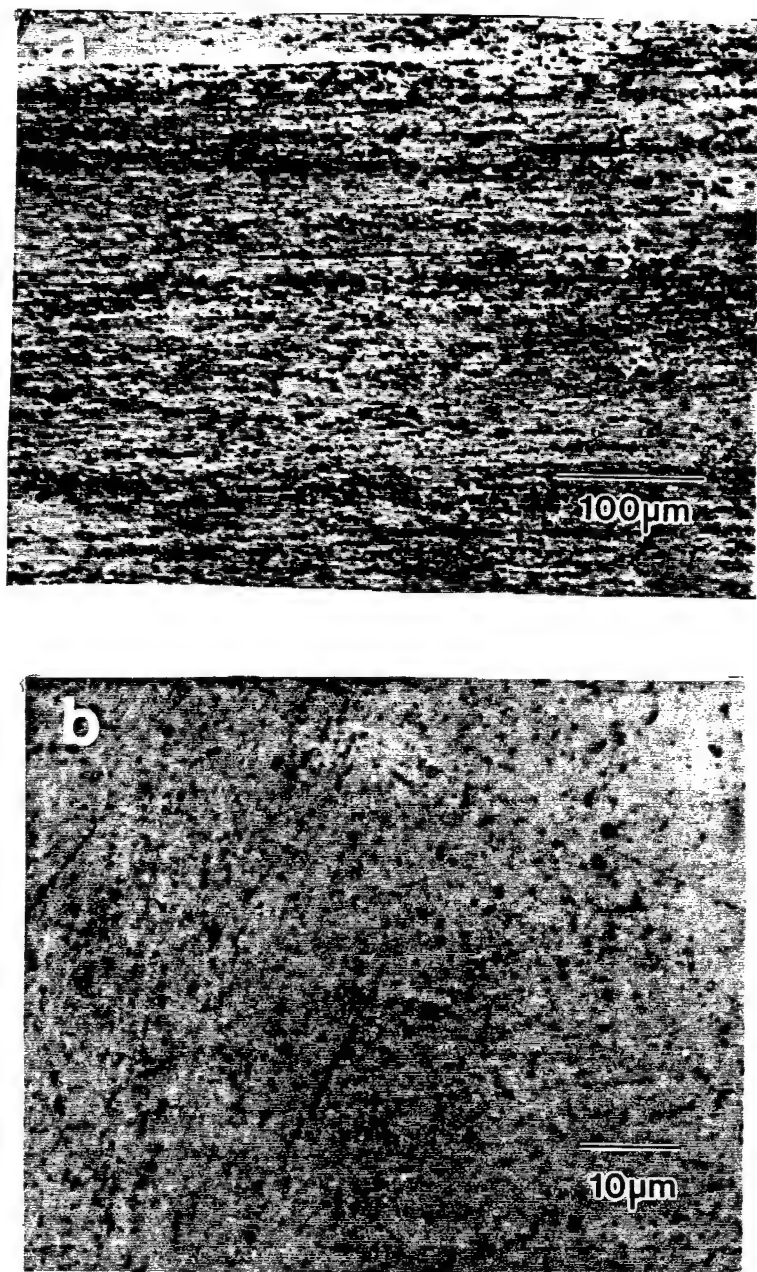
Figure 4.1. Optical micrograph in the L-LT plane: (a) AA8022; (b) AA5091.

uniformly distributed as shown in Figure 4.2(b). Roughly half lay along grain boundaries. The dispersoids within the grain interiors were usually clustered or lay together in strings. The volume percent of dispersoids in AA8022 is reportedly 16 percent [68]. The dislocation density within grains was relatively small. Those that were observed were usually associated with dispersoids.

The fine microstructural features of AA5091 are shown in Figure 4.3. The average grain diameter in the L-LT plane was approximately 0.6 µm with occasional grains as large as 2.5 µm. The grains were flattened by the forging operation and exhibited an average aspect ratio of 3:3:2. The oxide and carbide dispersoids in the AA5091 were significantly smaller than the $Al_{13}(Fe,V)_3Si$ dispersoids in AA8022 as shown in Figure 4.3(b). The carbides were cylindrically-shaped with average dimensions of 20 by 100 nm. Assuming all the oxygen and carbon is tied up in dispersoids the calculated volume percent of dispersoids in AA5091 is approximately 5 percent. As in AA8022, roughly half the dispersoids lay along grain boundaries. However, the dispersoids in the grain interiors were more uniformly distributed than in AA8022. The alloy contained no age hardening precipitates. The Mg and Li levels in AA5091 were selected to avoid precipitation. The dislocation density within the grains was greater than that observed in AA8022. The dislocations were primarily associated with dispersoids in regions adjacent to grain boundaries having a high density of dispersoids.
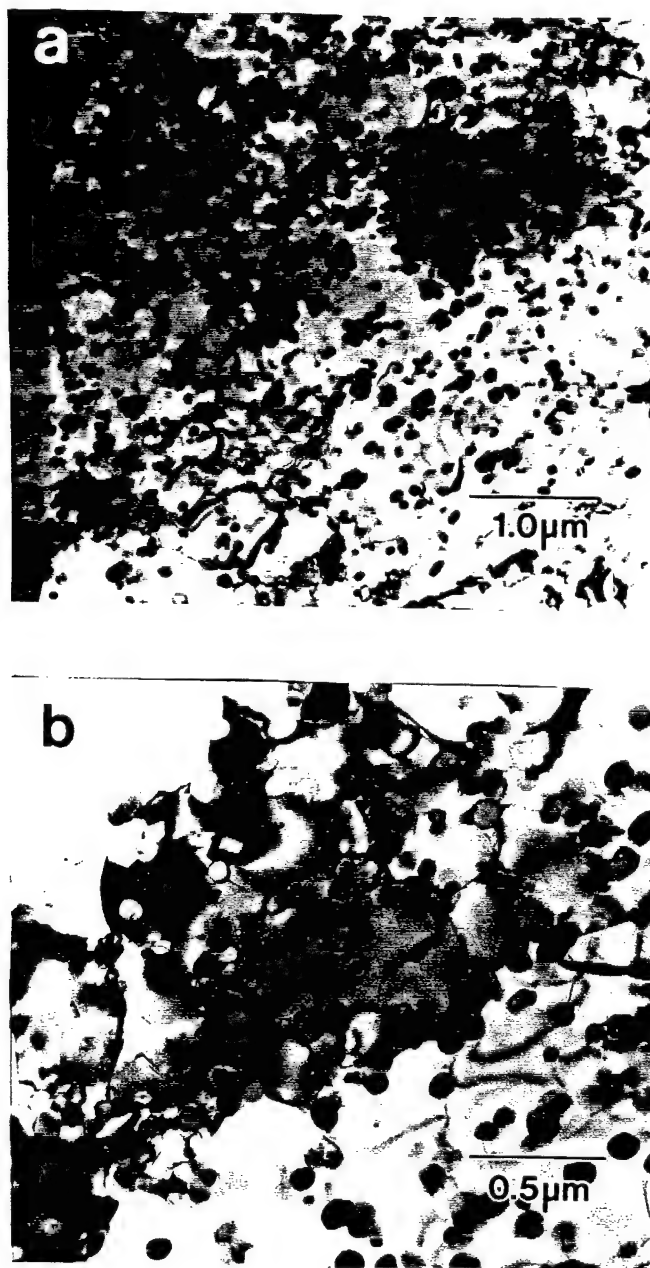
Figure 4.2.   TEM micrographs of as-received microstructure of AA8022.
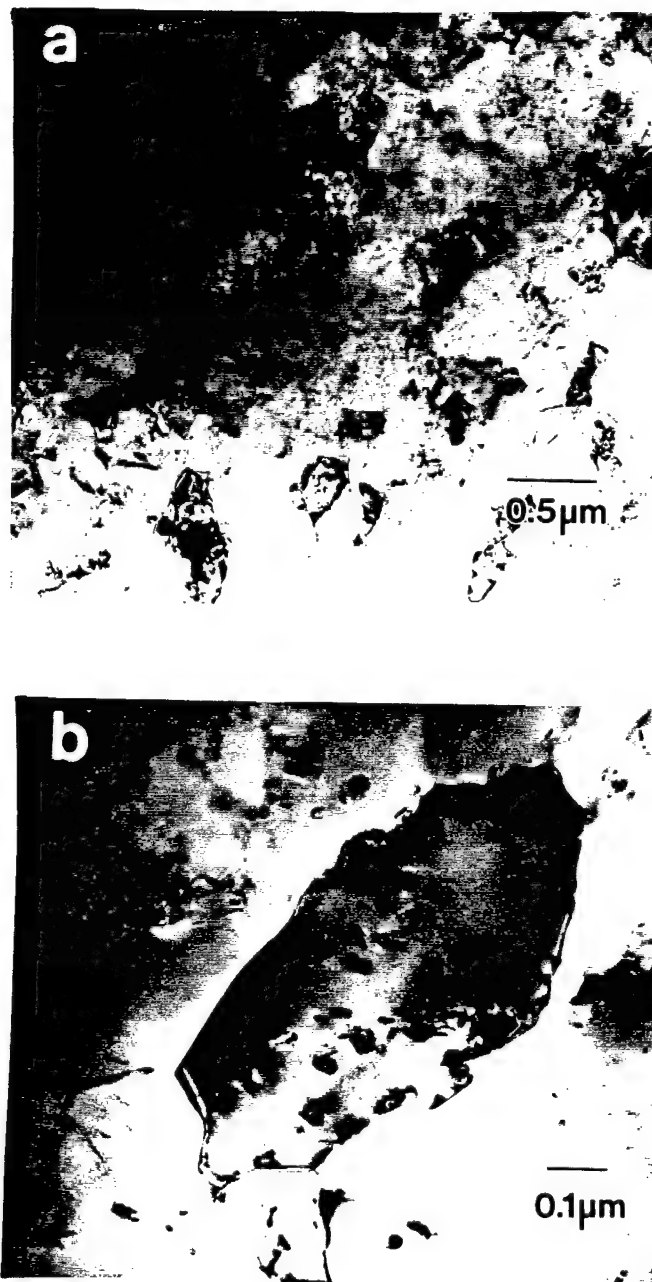
Figure 4.3.   TEM micrographs of as-received microstructure of AA5091.

4.2. Mechanical Behavior

4.2.1. Tensile

The longitudinal tensile properties of AA5091 and AA8022 are shown in Table 4.1. The yield and ultimate strengths of AA5091 are approximately 60% higher than those of AA8022. Neither alloy exhibited significant work hardening. The ratio of UTS/YS in both alloys was approximately 1.1 Both alloys exhibited good elongation to failure (ϵ_p^f) for their respective strength levels. Other aspects of the stress-strain behavior were significantly different. The plastic strain at the onset of necking (ϵ_p^N) was only 1.5% in AA8022 compared to 8.8% in AA5091. The good final elongation in AA8022 results from the large reduction in area (RA) prior to failure instead of a large amount of uniform elongation. AA5091 exhibited a yield point and serrated yielding. The yield point occurred at 515 MPa and 0.6% plastic strain. From 0.6% to 3.3% plastic strain, the flow stress was approximately constant at 510 MPa. The flow stress then slowly increased to UTS at the onset of necking. Serrated yielding was observed following the initial yield point and continued until specimen failure.

Table 4.1. Longitudinal Tensile Properties

Alloy	UTS(MPa)	YS(MPa)	ϵ_p^f(%)	ϵ_p^N(%)	RA(%)
AA5091	525	472	16	8	20
AA8022	328	292	23	1.5	73

The fracture toughness of AA8022 and AA5091 were not determined in the current study. The plane-strain fracture toughness, K_{Ic} reported by the alloy producers is 23.5 and 30 MPa√m for AA8022 and AA5091, respectively [67,68].

4.2.2. Deformation Characteristics

TEM micrographs from failed tensile specimens are shown in Figure 4.4. The AA8022 foil was from the necked region and had experienced approximately a 40% reduction in area. The AA5091 foil was from outside the necked region and had experienced approximately 9% strain. The density of dislocations had increased significantly in both alloys. The dislocations had interacted with each other and with the dispersoids. The distribution of dislocations was homogeneous within each grain. The dislocations were evenly distributed among the grains with two exceptions. Small grains and grains which contained few or no dispersoids often contained few or no dislocations. This is understandable since the probability of a dislocation-dislocation interaction or a dislocation-dispersoid interaction is greater in a large grain or a grain containing a large number of dispersoids, than in a small grain or a grain devoid of dispersoids. Slip in the small grains probably occurred by the motion of dislocations across the entire grain (i.e., grain boundaries were the sources and sinks of dislocations), thus, leaving no evidence of dislocation activity.

Figure 4.4. TEM micrographs of failed tensile specimens showing homogeneous deformation: (a) AA8022; and (b) AA5091.

4.2.3. Constant Amplitude Low Cycle Fatigue

The results of the constant amplitude low cycle fatigue tests are shown in Figures 4.5 and 4.6 for AA5091 and AA8022, respectively. Both alloys exhibited significant softening over the first few cycles in both tension and compression. For example, for a total strain range ($\Delta \epsilon_t$) of 2% the peak tensile stress decreased from 495 MPa to 445 MPa in AA5091 over the first eight cycles and from 335 MPa to 310 MPa in AA8022 over the first 10 cycles. After the initial softening, AA5091 began to gradually harden and continued to harden until the onset of failure. In contrast, AA8022 continued to soften until the onset of failure. Similar behavior was observed at all three total strain ranges.

4.2.4. Constant Amplitude Fatigue Crack Propagation

The results of the constant amplitude fatigue crack growth tests are shown in Figure 4.7. The fatigue crack resistance of AA8022 was slightly better than that of AA5091 at both R=0.1 and R=0.6. The fatigue crack growth resistance is similar to that observed in other fine-grained PM aluminum alloys. The fatigue crack growth resistance of both alloys at R=0.1 was inferior to that typically observed in IM aluminum alloys. The crack growth resistance at R=0.6 approached that observed in IM aluminum alloys.

The crack paths in these alloys, which are shown in Figure 4.8, were much straighter than those typically observed in IM alloys. There was no evidence of secondary cracking or crack branching. The fatigue

Figure 4.5.   Cyclic-stress response curves of AA5091 under constant amplitude loading: (a) peak tensile stress vs. load reversals; and (b) peak compressive stress vs. load reversals.
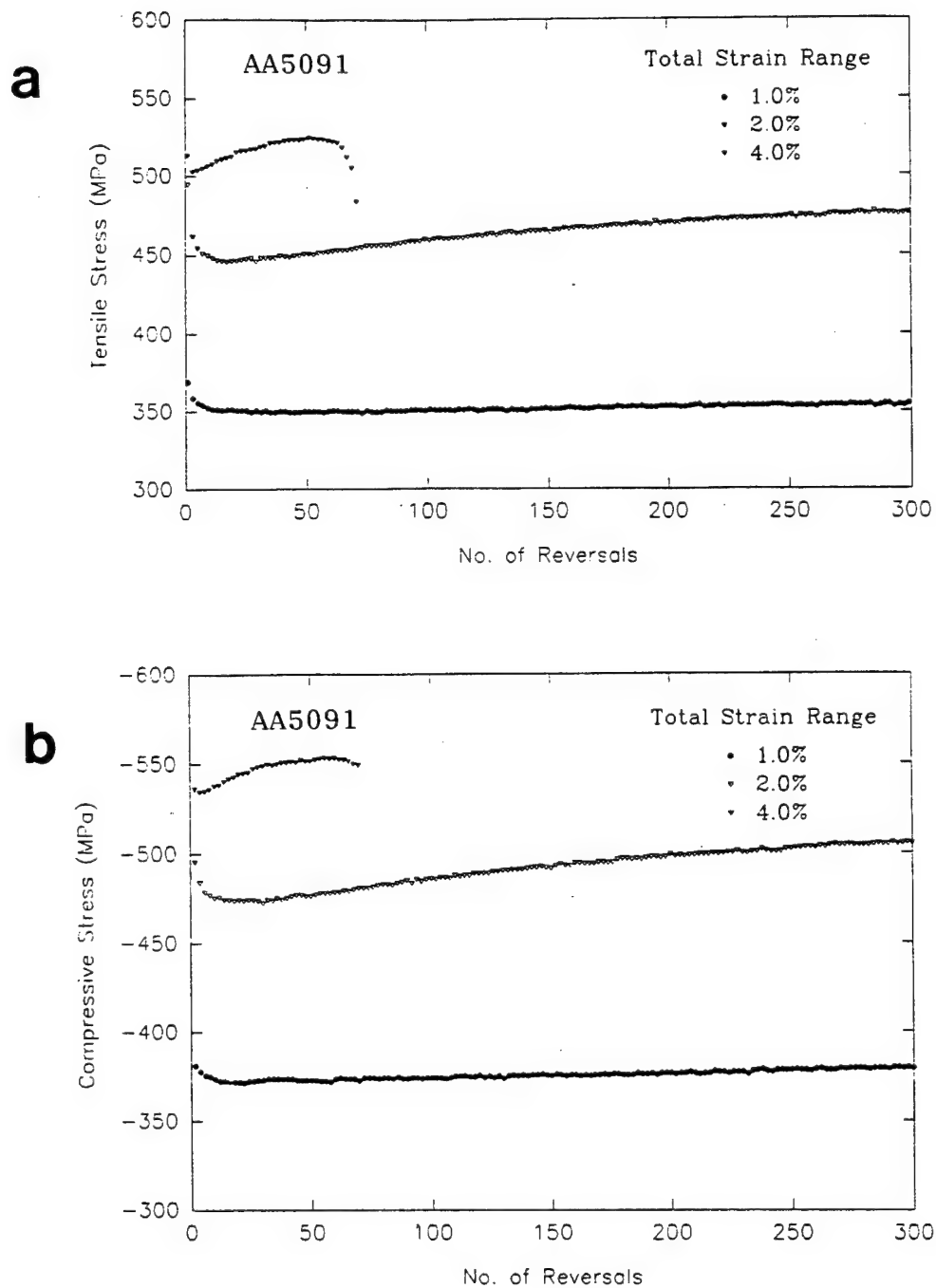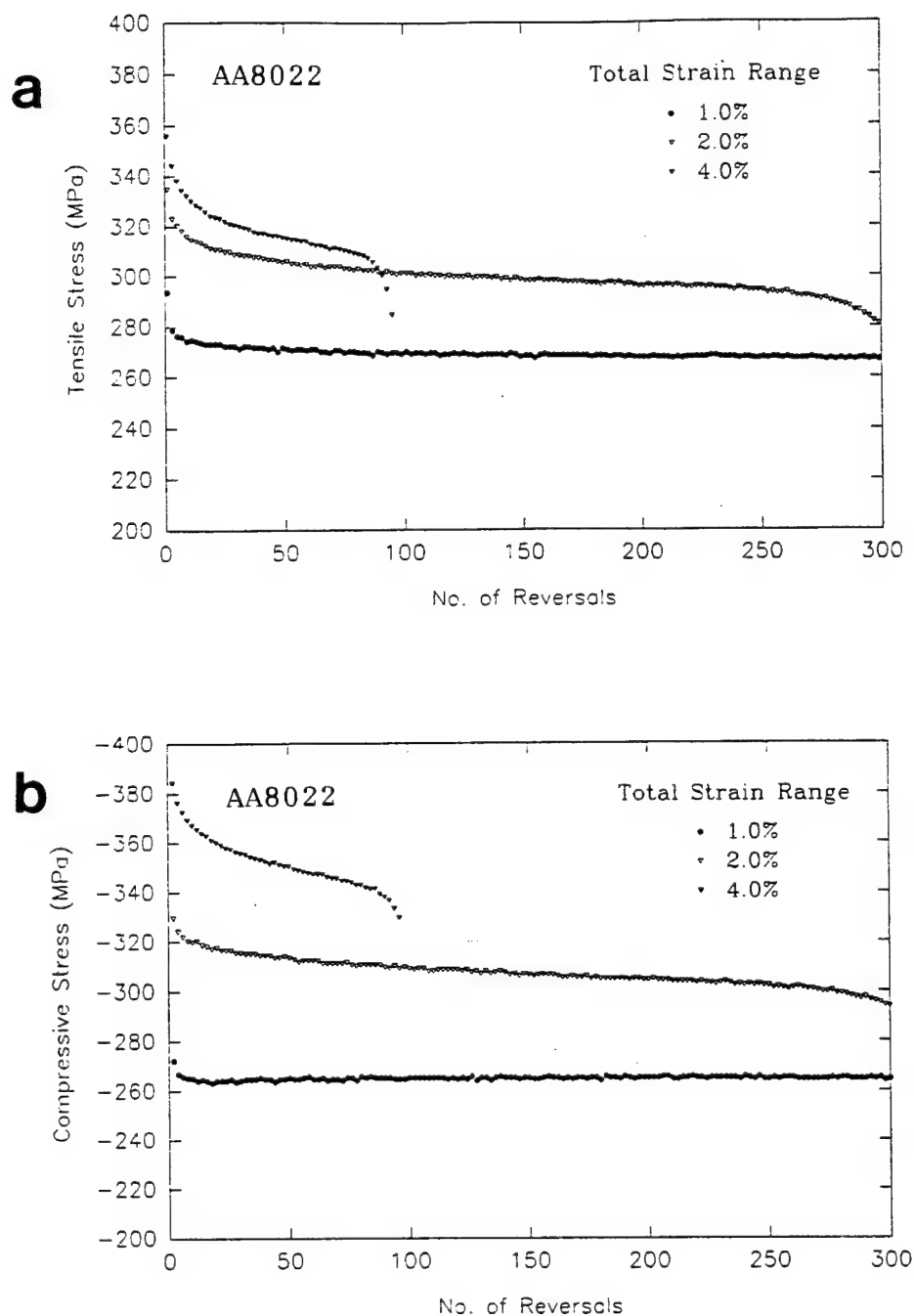
Figure 4.6. Cyclic-stress response curves of AA8022 under constant amplitude loading: (a) peak tensile stress vs. load reversals; and (b) peak compressive stress vs. load reversals.
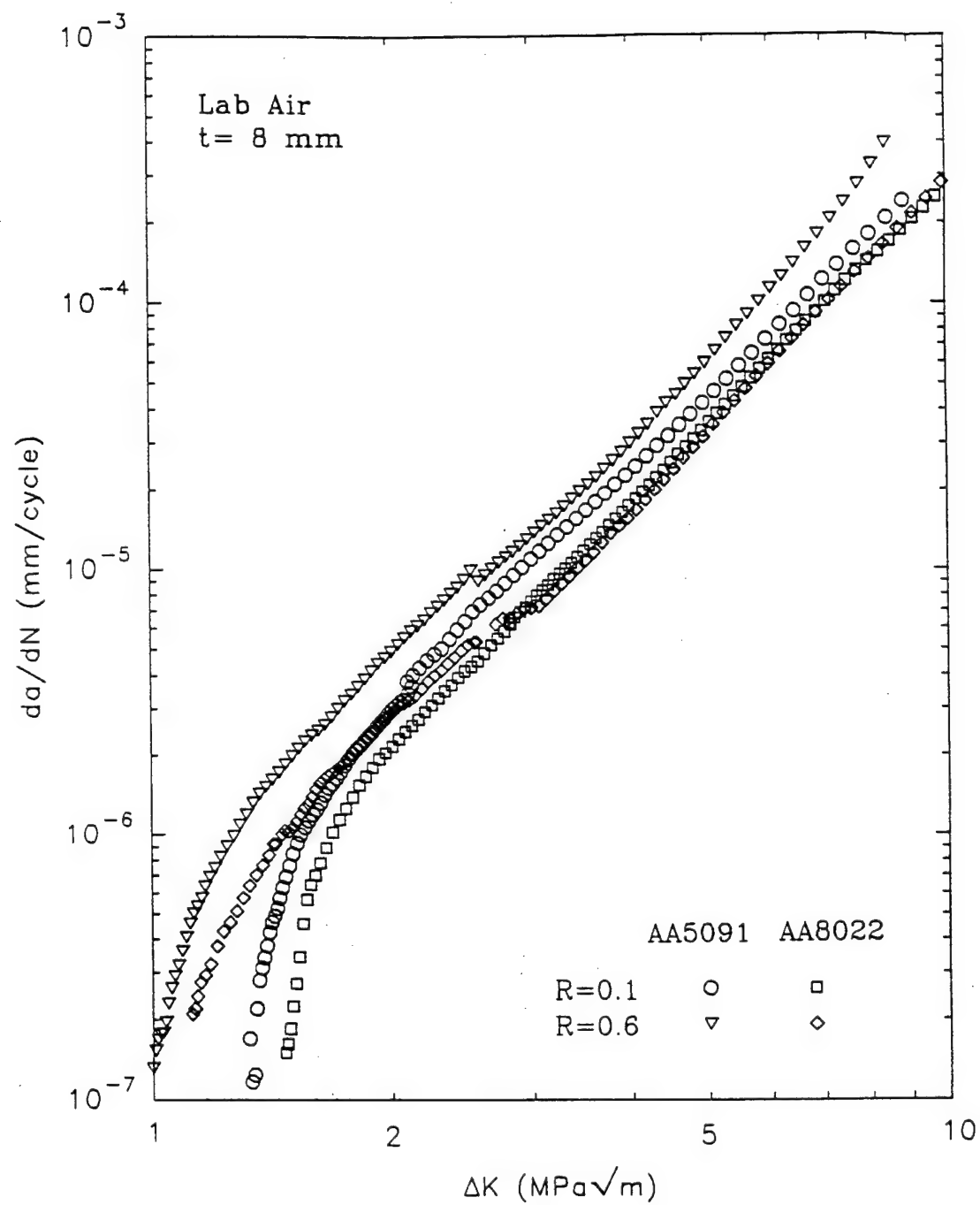
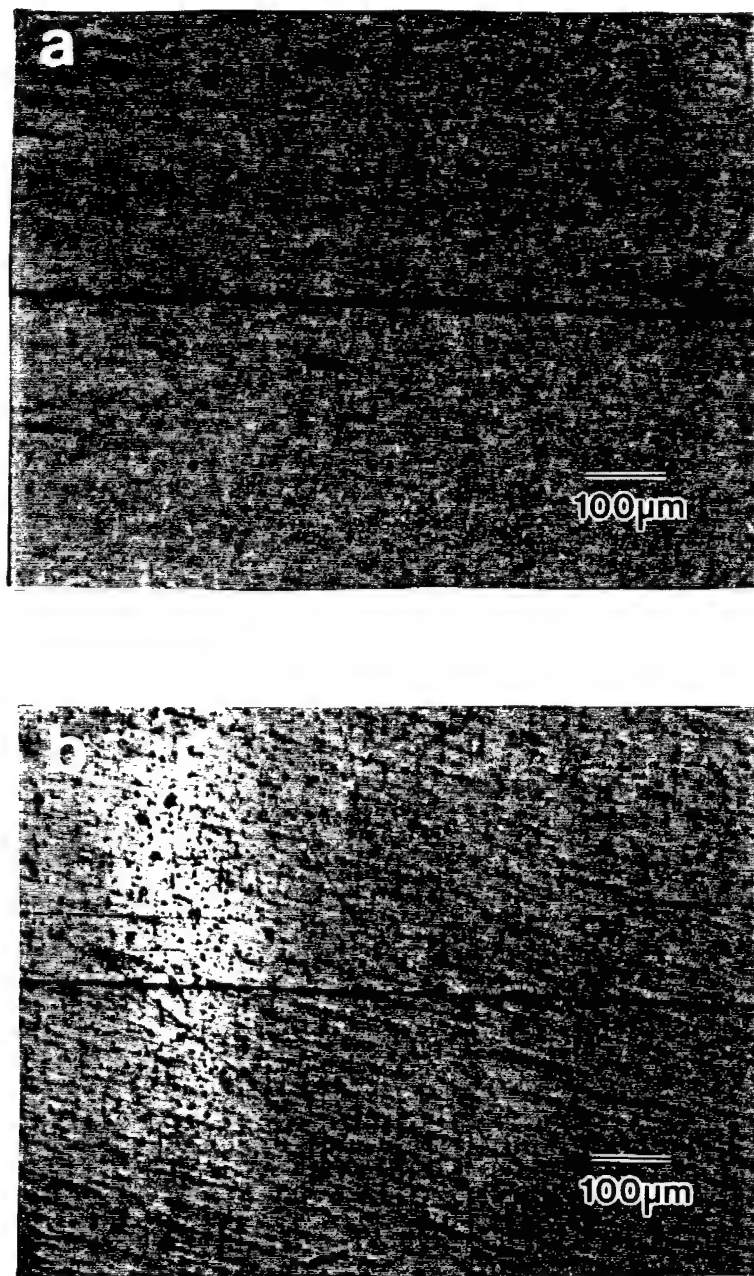Figure 4.7.   Constant amplitude FCGR curves for AA8022 and AA5091 at R=0.1 and 0.6.

Figure 4.8.   Crack profiles under constant amplitude loading conditions at
ΔK=4 MPa√m: (a) AA8022; and (b) AA5091.

crack surfaces at low and high ΔK are shown in Figure 4.9. The surface roughness decreased with decreasing ΔK (i.e., decreasing crack growthrate) and were very smooth in comparison to IM alloys over the entire ΔK range. There was no evidence in these alloys of a change to a crystallographic mode of cracking in the near threshold region like that which is often observed in IM alloys. This change in mode is usually accompanied by an increase in surface roughness.

The closure levels at R=0.1 in the near threshold region expressed in terms of the effective stress ratio ($R_{eff}=K_{cl}/K_{max}$) was approximately 0.3 in both alloys. Closure levels in IM alloys under these same conditions are typically 0.5 to 0.7. There was no closure detected at R=0.6 in either alloy.

4.3. Overload Results

4.3.1. Low Cycle Fatigue Overstrains

The effect of overstrains and understrains on the low cycle fatigue behavior of AA5091 are shown in Figure 4.10. The overstrain produced a residual plastic strain of 1.2% at zero load and the understrain a residual plastic strain of -1.2%. As a result of the overstrain, subsequent hysteresis loops shifted upward as indicated by an algebraic increase in both the peak tensile stress and peak compressive stress as shown in Figure 4.10(a). Similarly, the understrain shifted subsequent hysteresis loops downward as shown in Figure 4.10(b). The magnitude of the shift was approximately 90 MPa in both cases. The magnitude of the shift was
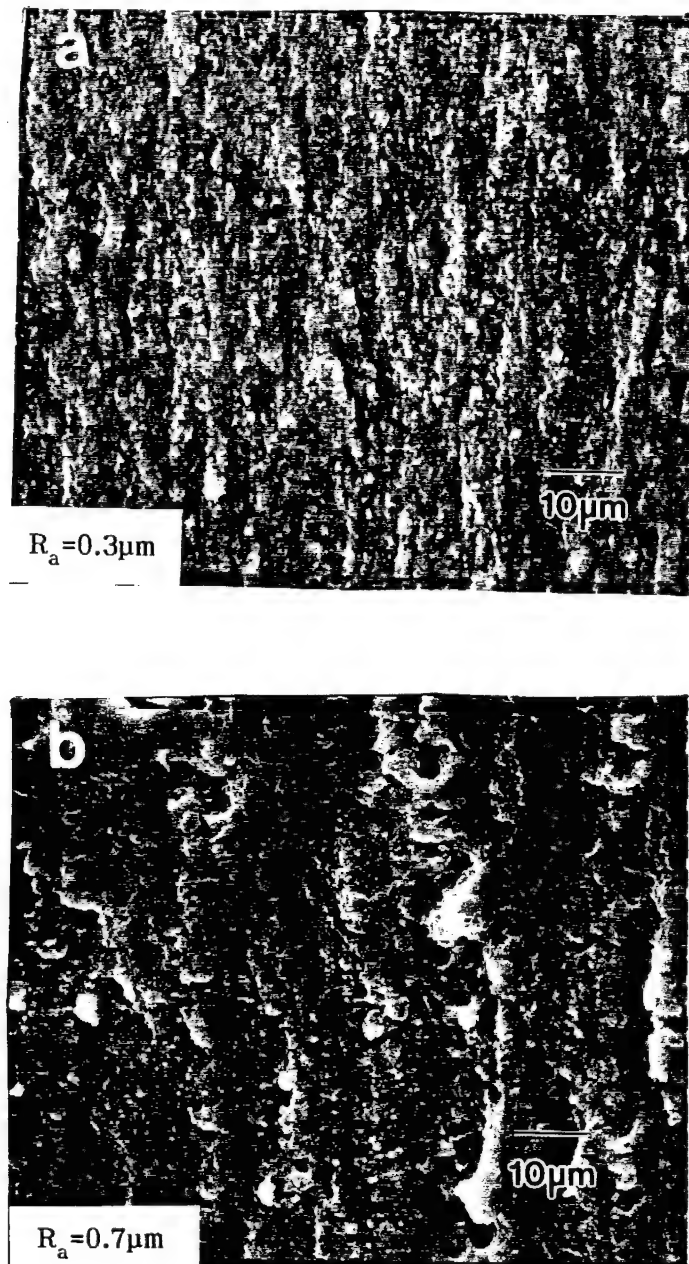
Figure 4.9. Fatigue crack surfaces and surface roughness of: (a) AA8022 at ΔK=1.5 MPa$\sqrt{m}$; (b) AA8022 at ΔK=10 MPa$\sqrt{m}$;
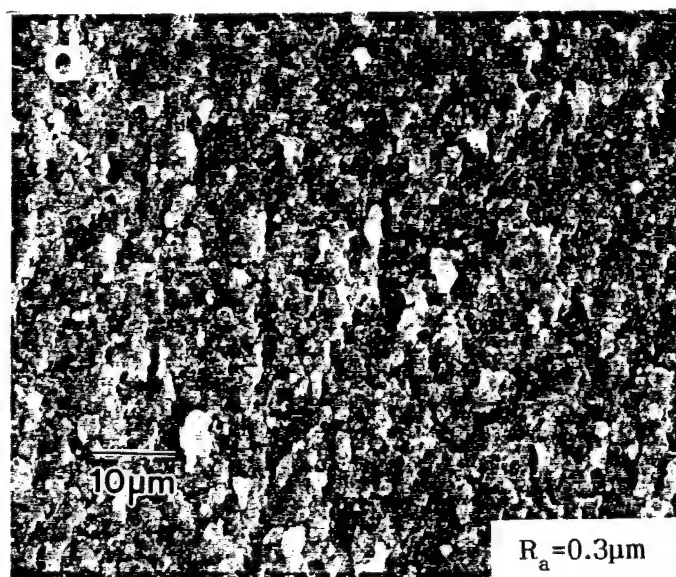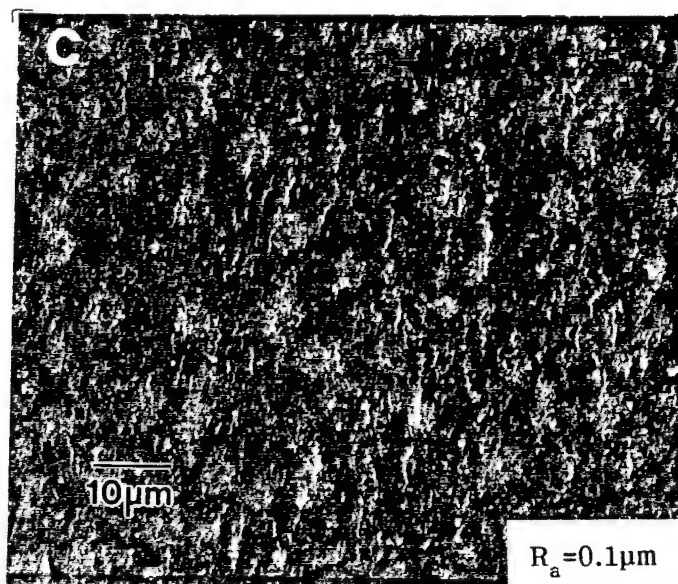
Figure 4.9 (cont'd).   (c) AA5091 at ΔK=1.5 MPa√m; (d) AA5091 at ΔK=10 MPa√m.

reduced to 45 MPa when the overstrain was followed by a partial understrain as shown in Figure 4.10(c). The overstrain decreased the stress range necessary to achieve a total strain range $\Delta\epsilon_t$=2% in subsequent cycles by 30 MPa.

Similar behavior was observed in AA8022 as shown in Figure 4.11. The overstrain produced a residual plastic strain of 1.6% and the understrain a residual plastic strain of -1.6%. As a result of the overstrain, subsequent hysteresis loops shifted upward, and the understrain shifted loops downward as shown in Figures 4.11(a) and (b), respectively. The magnitude of the shift was approximately 30 MPa in both cases. The shift was eliminated by the partial understrain as shown in Figure 4.11(c). The overstrain decreased the stress range necessary to achieve $\Delta\epsilon_t$=2% in subsequent cycles by 10 MPa.

The upward shift of the entire hysteresis loop following an overstrain indicates an overstrain produced kinematic (i.e., directional) hardening. The magnitude of the kinematic hardening was significantly reduced when the overstrain was followed by a partial understrain. The decrease in the stress range necessary to obtain a total strain range $\Delta\epsilon_t$=2% following an overstrain indicates the overstrain produced isotropic softening. The effects of an overstrain were eliminated after 100 cycles or less. The effects of an overstrain were also eliminated by annealing as shown in Figures 4.10(d) and 4.11(d). The cyclic response after annealing was similar to that in virgin material.

Figure 4.10. Stress-strain response of AA5091: (a) overstrain; (b) understrain (numbers indicate endpoints for cycle number);

Figure 4.10 (cont'd). (c) overstrain with partial understrain; and (d) overstrain followed by annealing (numbers indicate endpoint for cycle number).
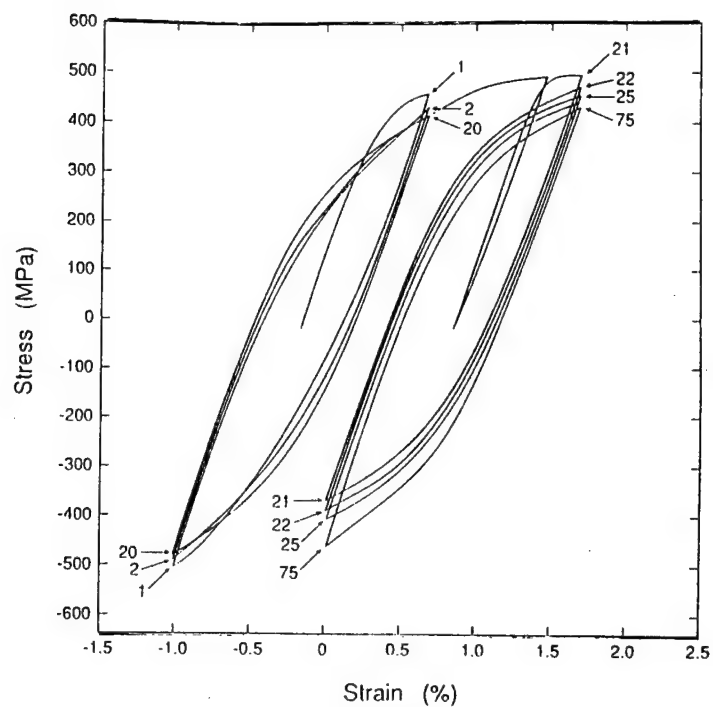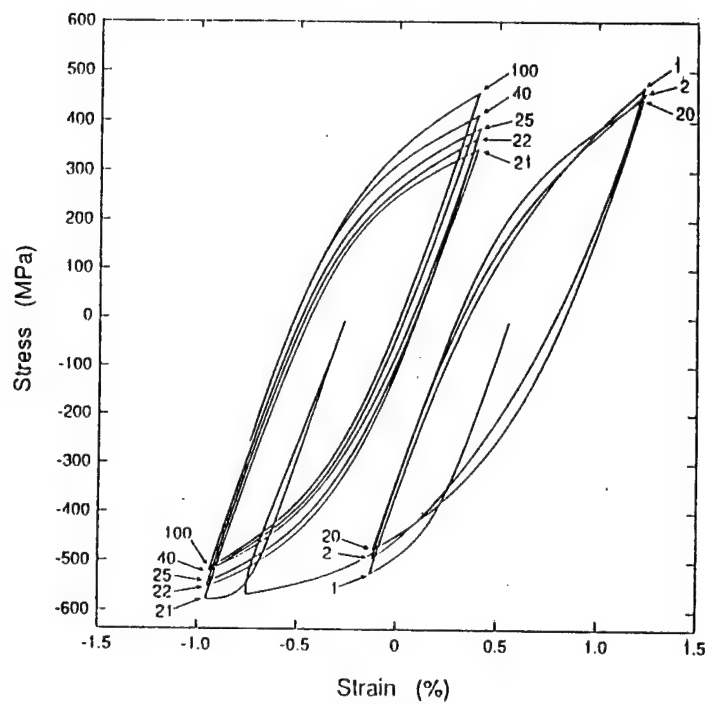
Figure 4.11. Stress-strain response of AA8022: (a) overstrain; (b) understrain (numbers indicate endpoint for cycle number);
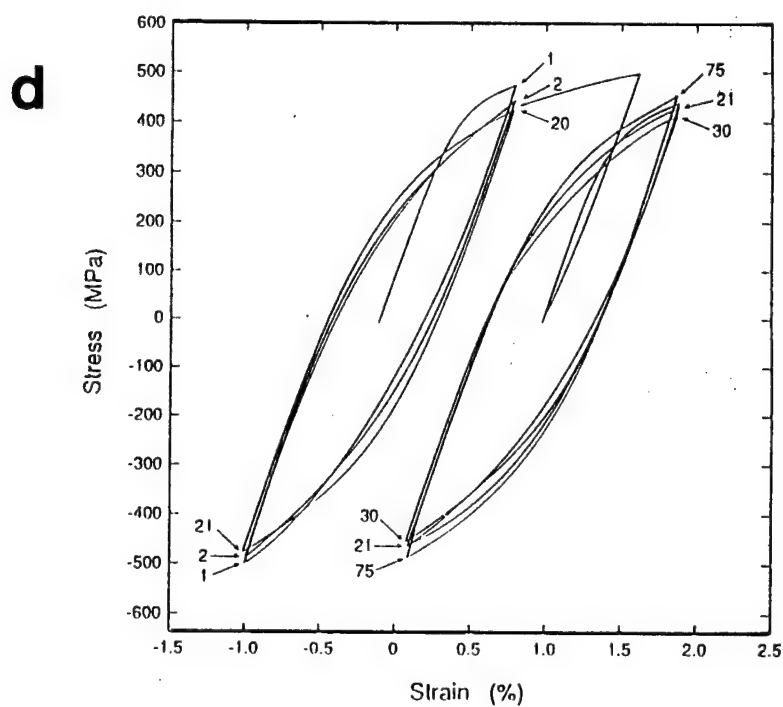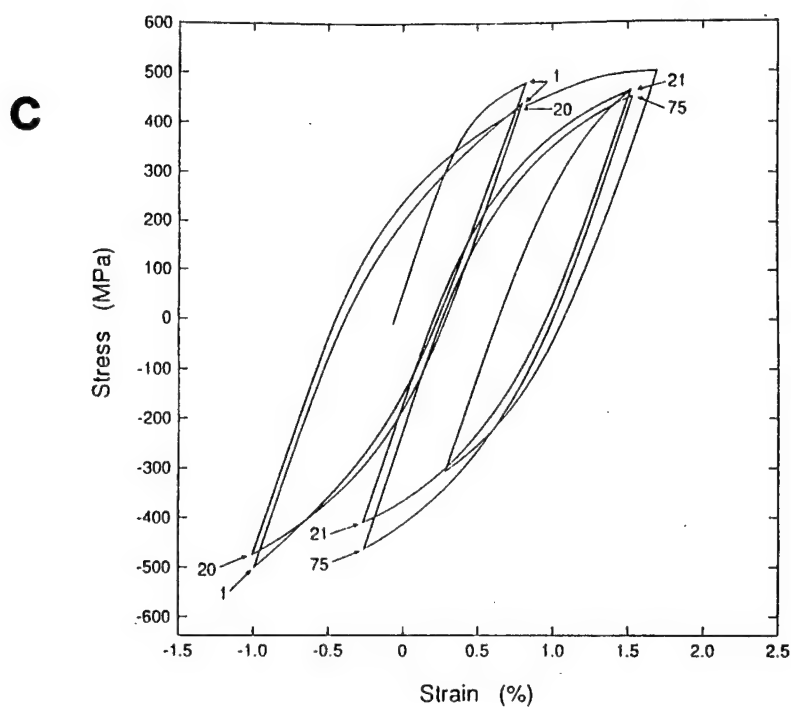
110
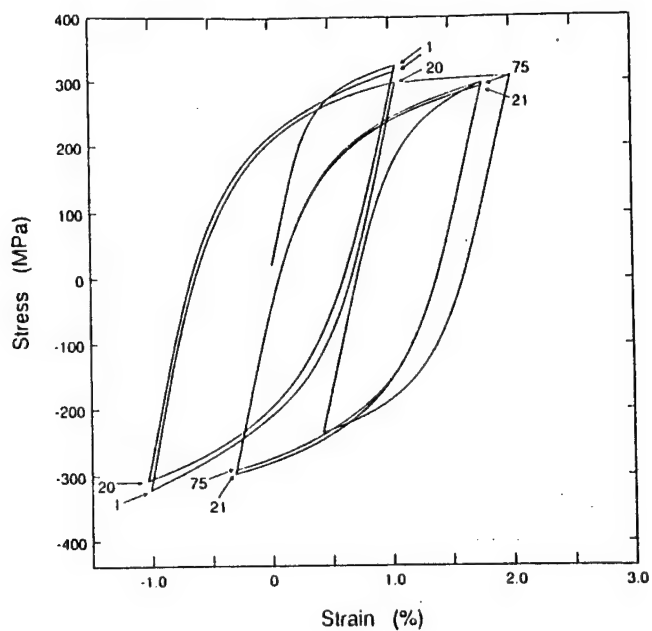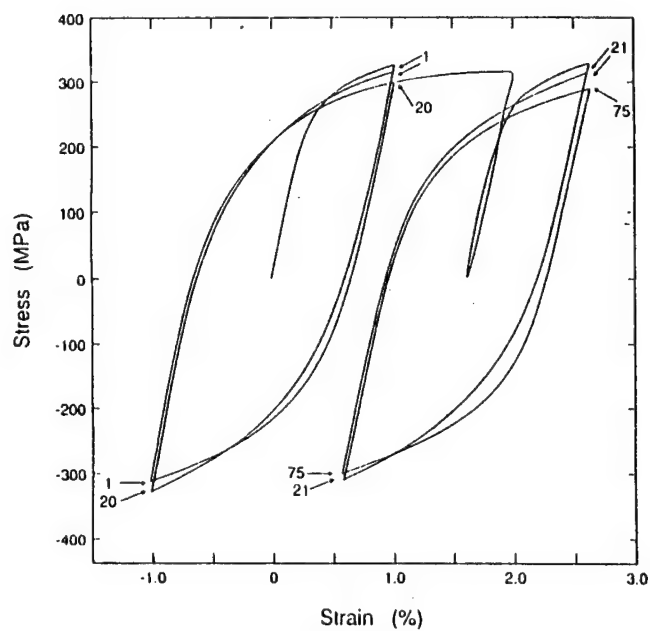
Figure 4.11 (cont'd). (c) overstrain with partial understrain; and (d) overstrain followed by annealing (numbers indicate endpoints for cycle number).
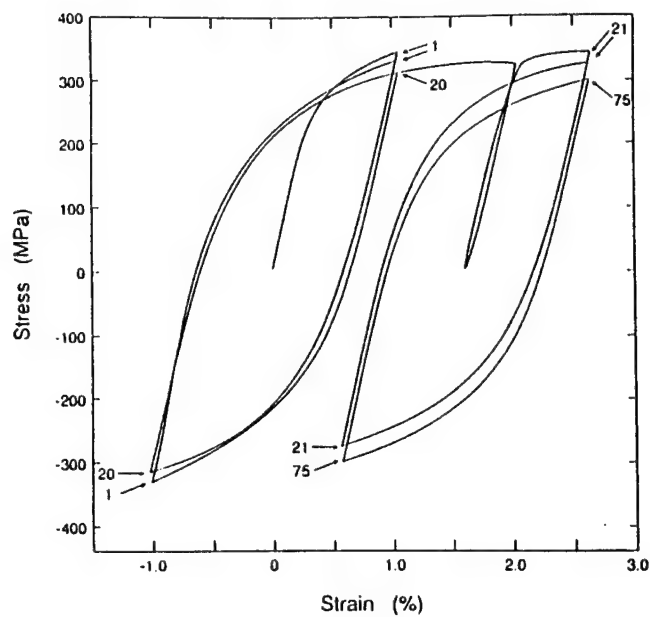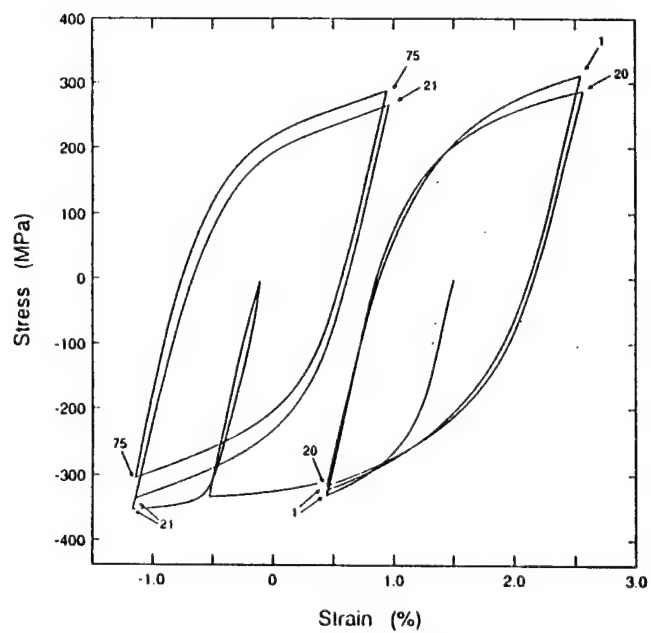
4.3.2. Fatigue Crack Propagation Overloads

The results of the single tensile overload tests at R=0.1 are shown in Figures 4.12 and 4.13 for AA8022 and AA5091, respectively. The number of delay cycles, N_d, in both alloys increased with decreasing ΔK_B for all three overload magnitudes except for OLR=3.0 in AA5091. The crack arrested (i.e., N_d>1 million) for OLR=3.0 over the entire range of ΔK_B except for two tests, one at ΔK_B=6.0 MPaΔm and the other at ΔK_B=8.0 MPa$\sqrt{m}$. The affected distance, a_{aff}, in both alloys decreased with decreasing ΔK_B except at OLR=2.0 where at the lowest ΔK_B, a_{aff} increased slightly. A_{aff} was approximately equal to or slightly greater than the overload plastic zone size calculated using Equation 2.3. N_d increased at a given ΔK_B with increasing overload magnitude. This occurred because of a decrease in the minimum growth rate, $(da/dN)_{min}$, and an increase in a_{aff} with increasing OLR as shown in Figure 4.14. The ΔK_B below which crack arrest occurred also increased with increasing OLR.

The behavior of AA8022 and AA5091 for OLR=2.0 is compared in Figures 4.15. N_d was approximately equivalent in the two alloys at low and high ΔK_B, but was significantly higher in AA8022 at medium ΔK_B. This behavior was a consequence of similarities and differences in $(da/dN)_{min}$ and a_{aff} at different ΔK_B. $(da/dN)_{min}$ and a_{aff} were virtually identical at low ΔK_B, as shown in Figure 4.16(a), so N_d was nearly equivalent. At medium ΔK_B, $(da/dN)_{min}$ was essentially identical, but AA8022 had a larger a_{aff} as shown in Figure 4.16(b), which resulted in a larger number of delay cycles. At high ΔK_B, $(da/dN)_{min}$ was significantly
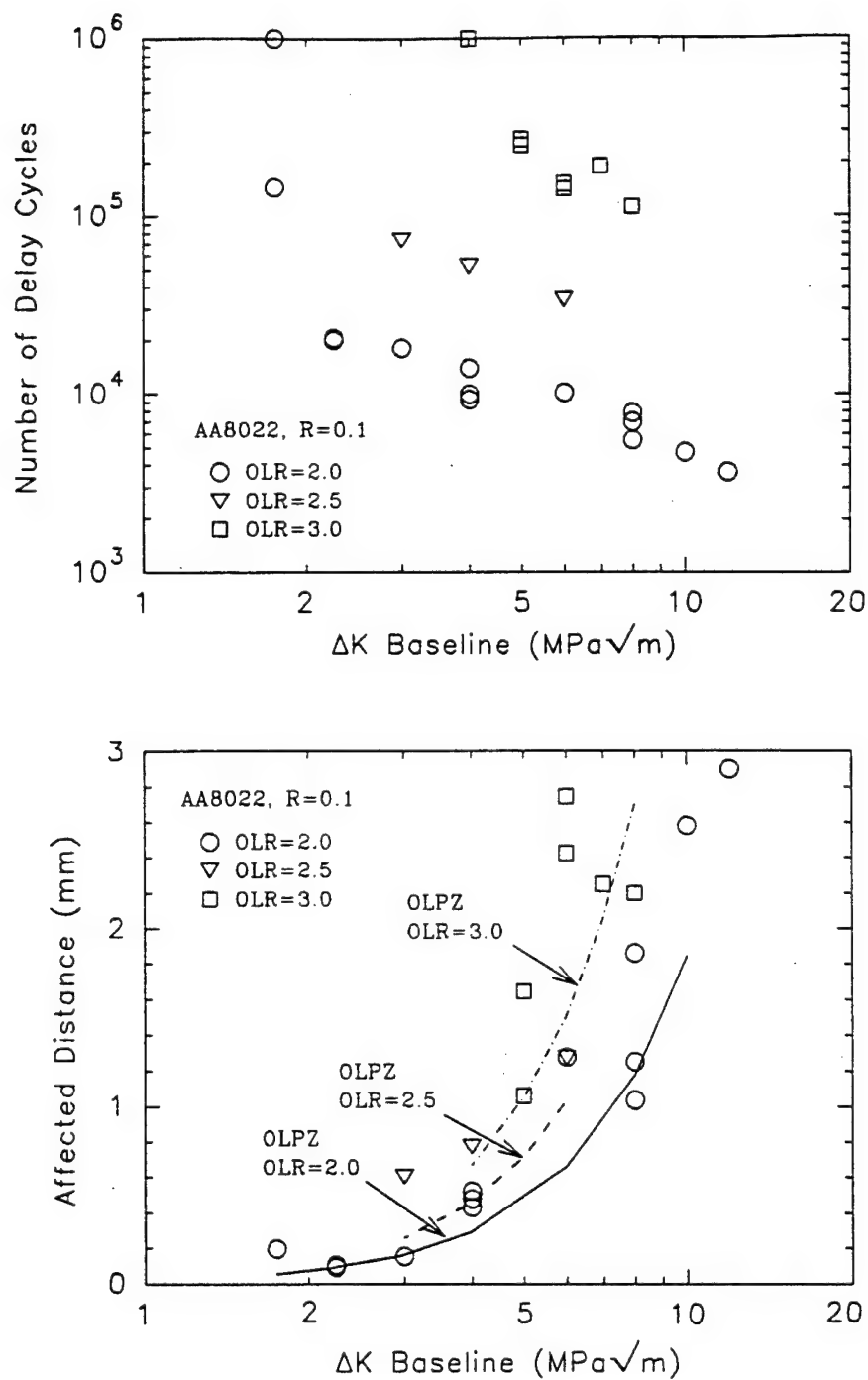
Figure 4.12. Magnitude of crack retardation in AA8022 at R=0.1 as a function of ΔK_B (OLPZ=calculated overload plastic zone size).
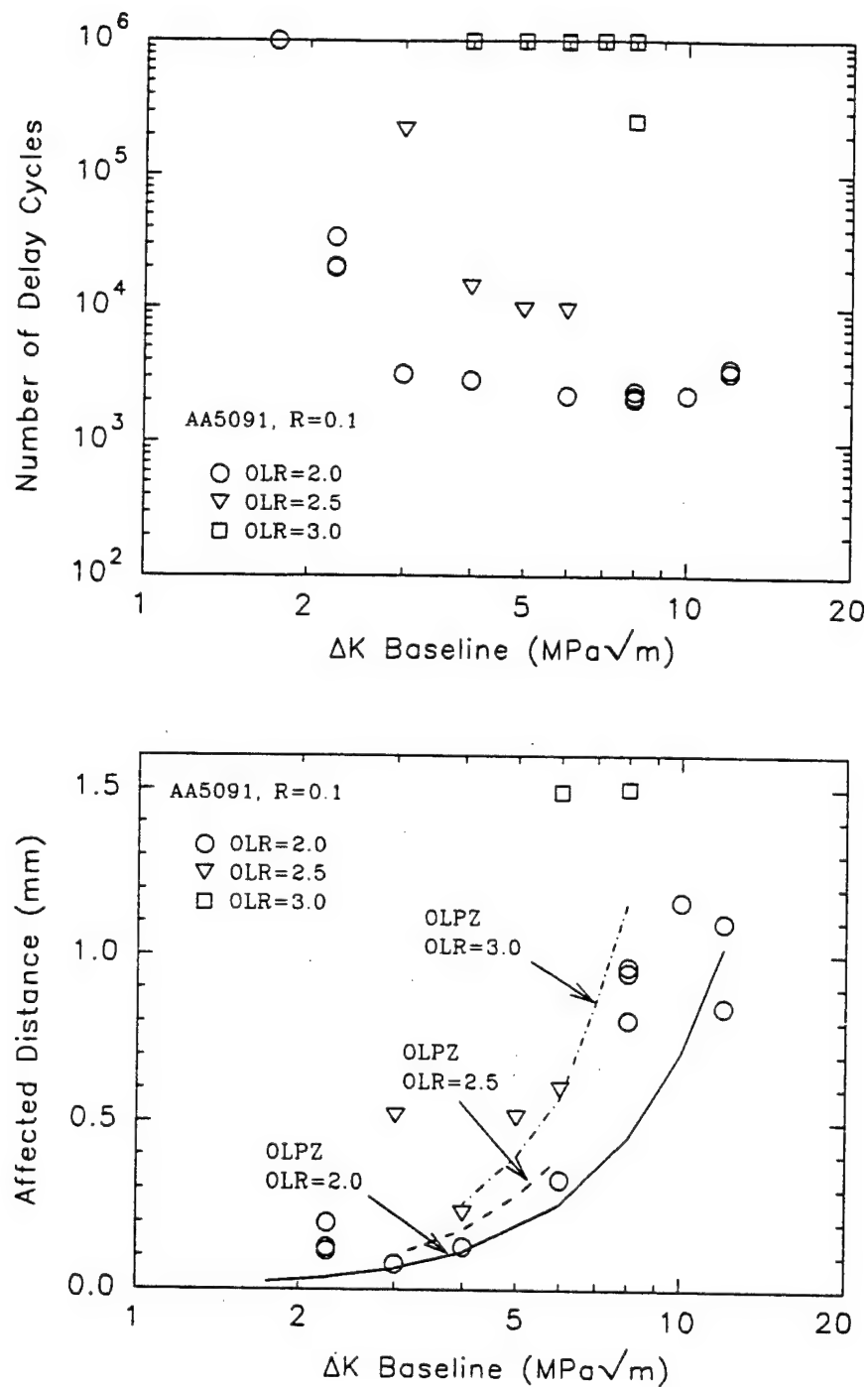
Figure 4.13. Magnitude of crack retardation in AA5091 at R=0.1 as a function of ΔK_B (OLPZ=calculated overload plastic zone size).
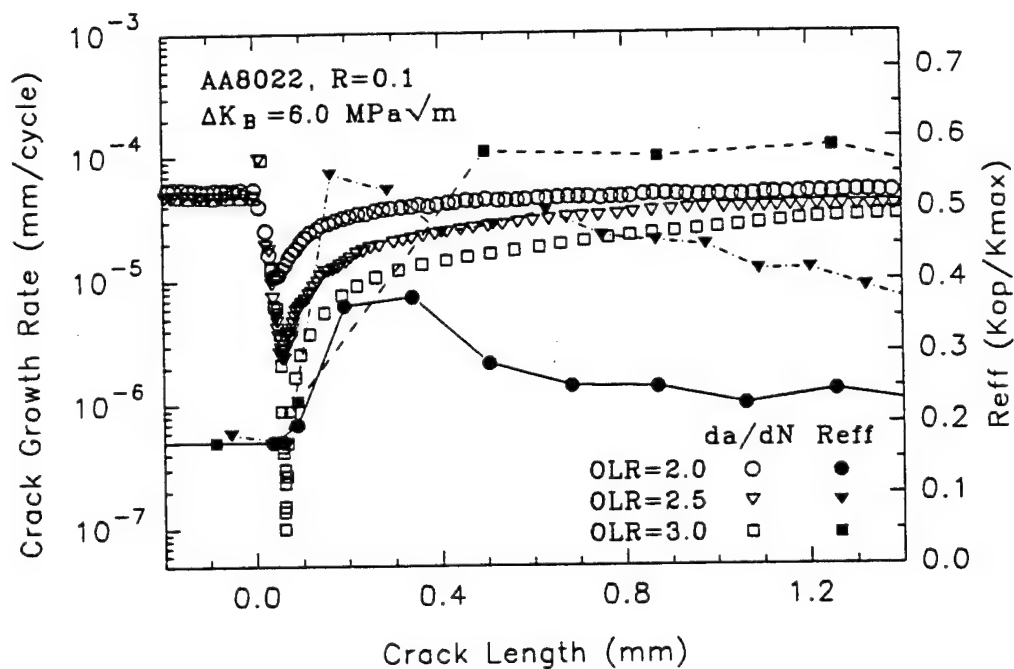
Figure 4.14. Effect of overload magnitude on overload response in AA8022 at ΔK_B=6 MPa√m, R=0.1.
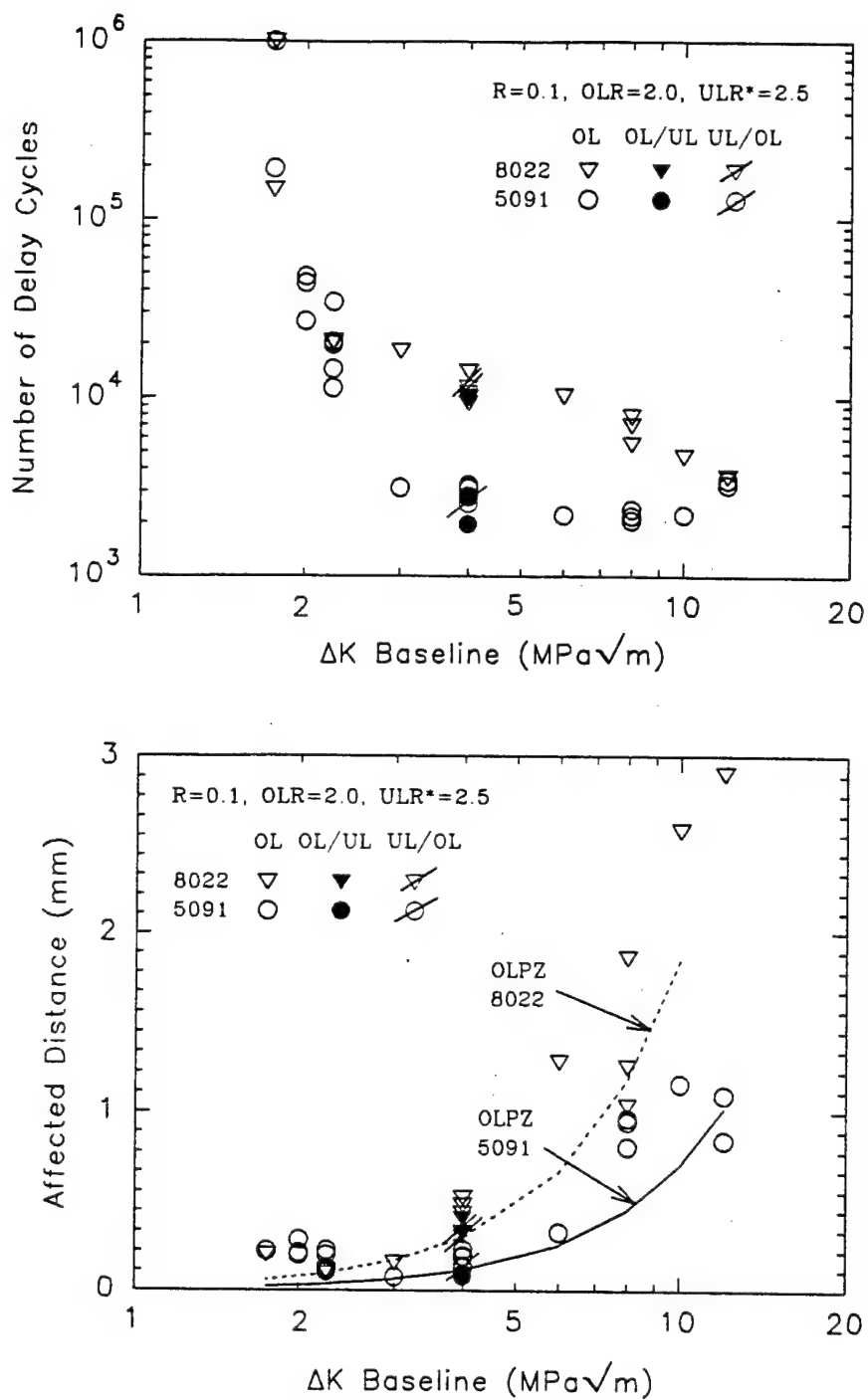
Figure 4.15. Comparison of retardation magnitude (OLR=2) in AA5091 and AA8022 at R=0.1 (OLPZ=calculated overload plastic zone size).

lower in AA5091, but this was offset by a larger a_{aff} in AA8022, as shown in Figure 4.16(c), so N_d was again approximately equivalent.

The behavior of the alloys for OLR=3.0 is compared in Figure 4.17. The alloys exhibited identical behavior at ΔK_B= 4.0 MPa√m (i.e., crack arrest), but N_d was significantly higher in AA5091 than in AA8022 at all other ΔK_B . This behavior was a consequence of either crack arrest or a significantly lower $(da/dN)_{min}$ in AA5091, as shown in Figure 4.18.

The effects of overload/underload and underload/overload combinations at R=0.1 are also shown in Figures 4.15 and 4.17. N_d following these combinations was nearly equivalent to that following single tensile overloads. This was a consequence of the minimum growth rate and a_{aff} being essentially the same in all three types of tests as shown for AA8022 in Figure 4.19.

The closure levels before and after overloads at R=0.1 were monitored with a front-face COD gage as described previously in Section 3.4.2. The measured closure levels did not significantly increase following an overload at low ΔK_B as shown in Figure 4.16(a). The closure levels increased more significantly as ΔK_B increased as shown in Figure 4.16(b) and (c). The maximum closure level typically occurred well after the minimum growth rate. The increment of crack growth over which closure levels were elevated was frequently greater than a_{aff}. The maximum closure level and the increment of crack growth over which closure levels were elevated typically increased with increasing overload magnitude as shown in Figure 4.14. There was no significant change in closure levels when crack arrest occurred following an overload. The increase in closure levels was typically larger in AA8022 than in AA5091 as shown in
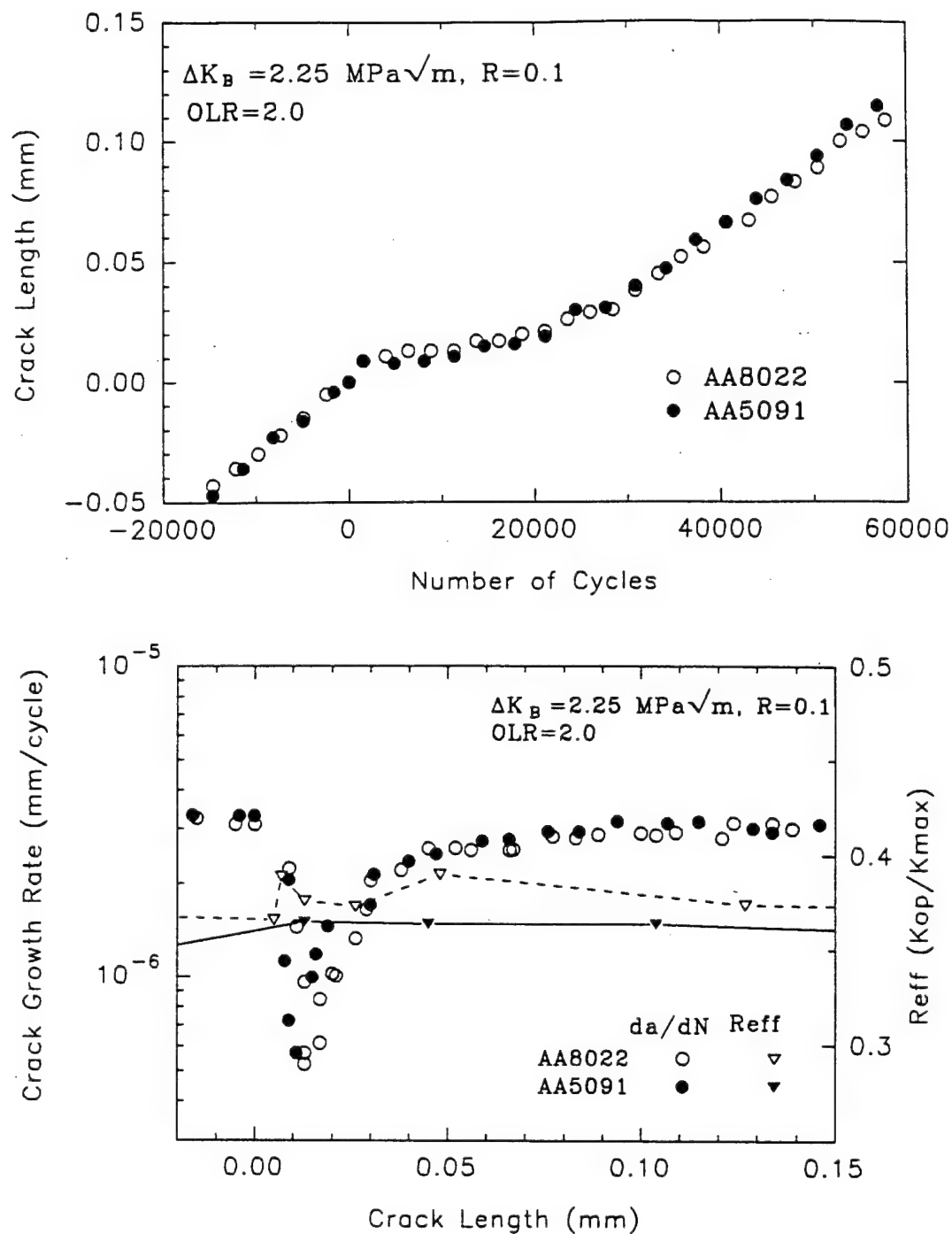
Figure 4.16. Comparison of overload response (OLR=2) in AA8022 and AA5091 at R=0.1: (a) ΔK_B=2.25 MPa$\sqrt{m}$;
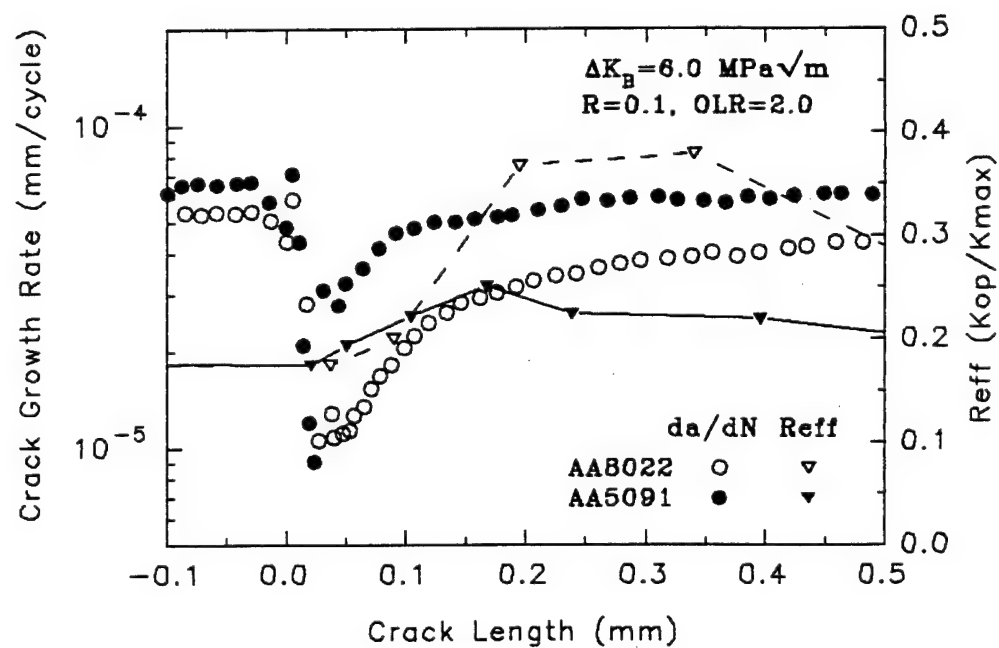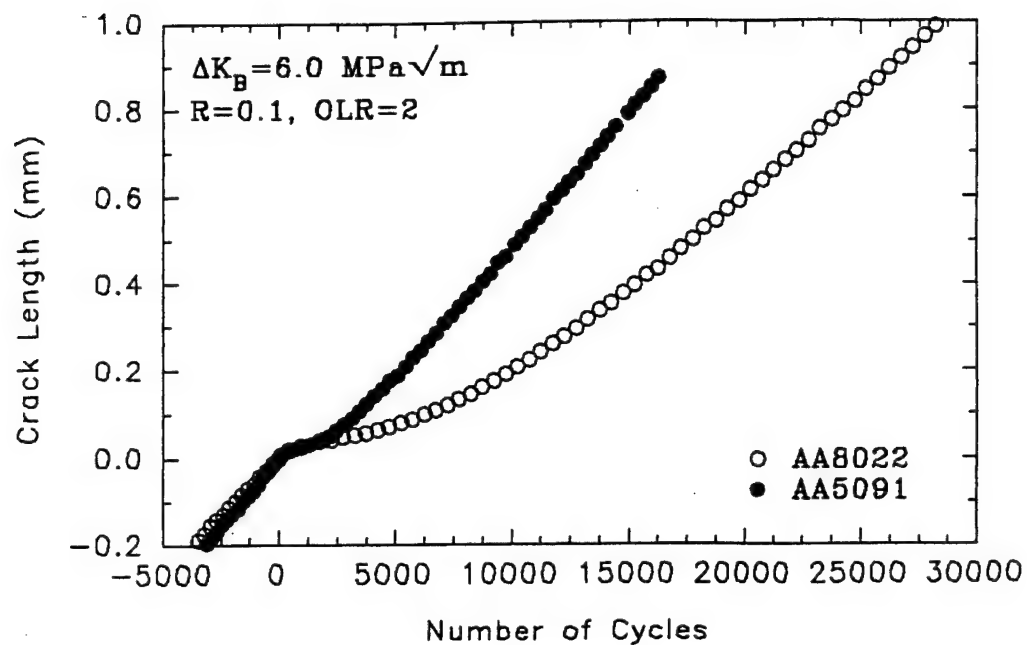
Figure 4.16 (cont'd). (b) $\Delta K_B = 6$ MPa$\sqrt{m}$;

Figure 4.16 (cont'd). (c) ΔK_B=12 MPa$\sqrt{m}$.

Figure 4.17. Comparison of retardation magnitude (OLR=3) in AA8022 and AA5091 at R=0.1 (OLPZ=calculated overload plastic zone size).

Figure 4.18. Comparison of overload response (OLR=3) in AA8022 and AA5091 at R=0.1, ΔK_B=6.0 MPa$\sqrt{m}$.
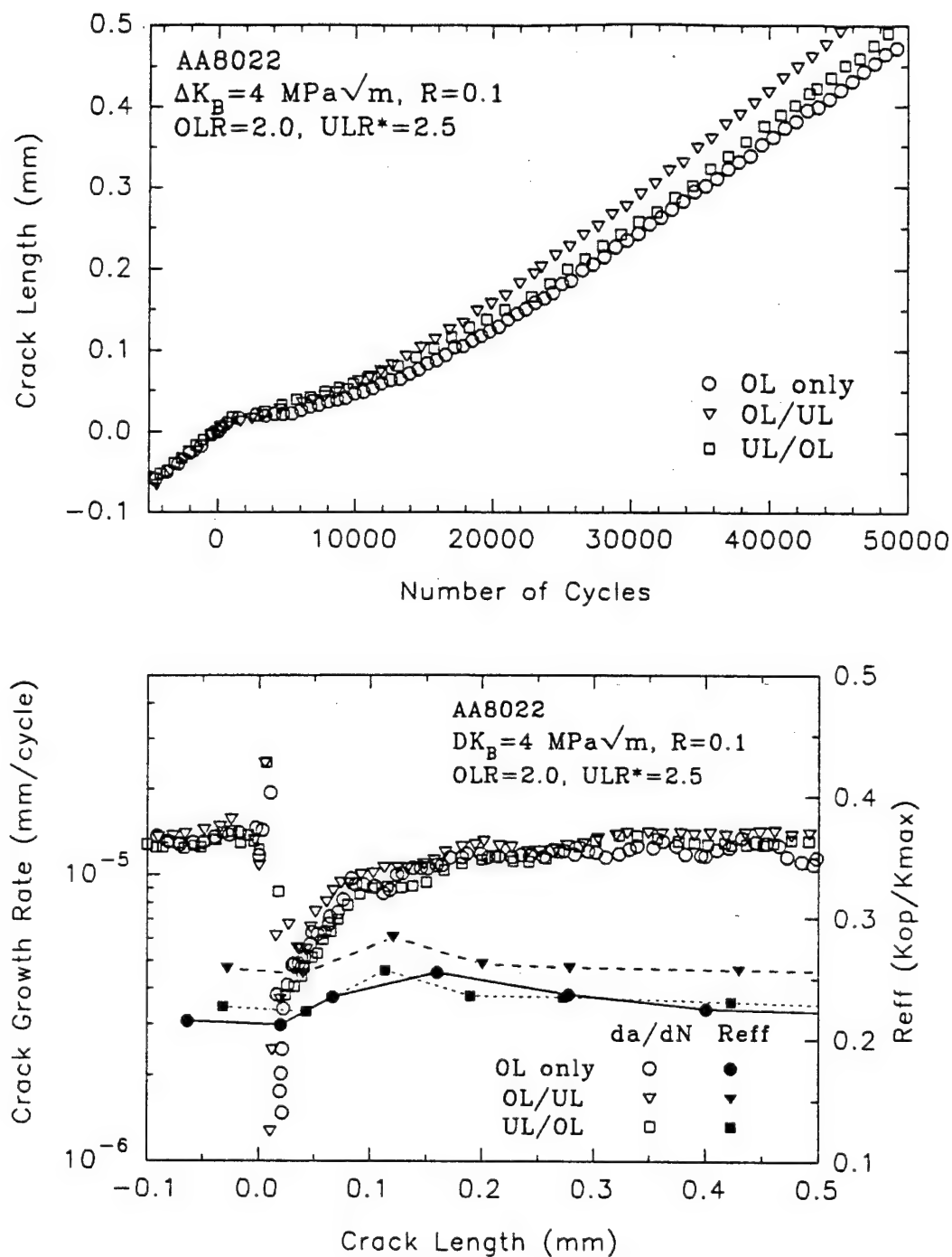
Figure 4.19. Effect of overload/underload combinations (OLR=2/ULR*=2.5) on the overload response of AA8022 at R=0.1.

Figure 4.16(a) and (b), and Figure 4.18. One notable exception was OLR=2.0 at high ΔK_B. In this case, the increase in closure levels was larger in AA5091 than in AA8022 as illustrated in Figure 4.16(c). The closure behavior following overload/underload and underload/overload combinations was nearly identical to that following single tensile overloads as shown in Figure 4.19.

The results of the single tensile overload tests at R=0.6 are shown in Figures 4.20 and 4.21 for AA8022 and AA5091, respectively. N_d increased with decreasing ΔK_B, except at OLR=2.0 where crack arrest occurred over the entire ΔK_B range for AA5091 and below ΔK_B= 3.0 MPa√m for AA8022. a_{aff} decreased with decreasing ΔK_B and was significantly less than the overload plastic zone size calculated from Equation 2.3. N_d increased with increasing overload magnitude. This resulted from decreasing $(da/dN)_{min}$ and increasing a_{aff} with increasing OLR as shown in Figure 4.22.

The behavior of AA8022 and AA5091 for OLR=1.44 is compared in Figure 4.23. N_d was larger in AA8022 over the entire range of ΔK_B. a_{aff} was nearly equal in the two alloys. The difference in N_d was primarily a consequence of a lower baseline crack growth rate, $(da/dN)_B$, in AA8022 as shown in Figure 4.24, rather than differences in the magnitude of reduction in growth rates or differences in a_{aff}. A lower $(da/dN)_B$ yields a higher N_d all other factors being equal, because the crack is in the affected zone for a larger number of cycles.

The behavior of the alloys at OLR=1.66 is compared in Figure 4.25. N_d was approximately equal at ΔK_B= 3.0 MPa√m, higher in AA5091 at lower ΔK_B, and higher in AA8022 at higher ΔK_B. The reason for this behavior
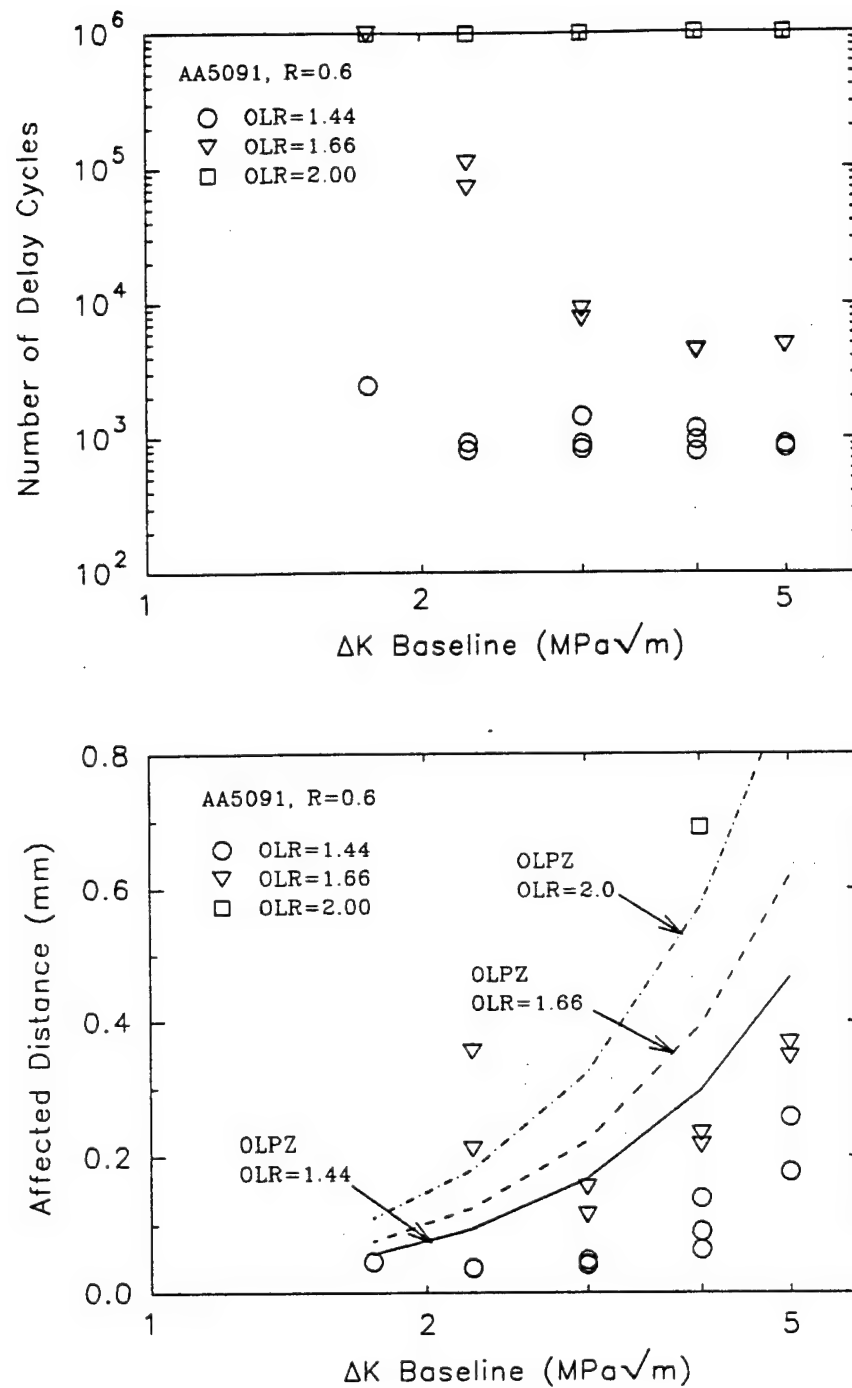
Figure 4.20. Magnitude of crack retardation in AA5091 at R=0.6 as a function of ΔK_B (OLPZ=calculated overload plastic zone size).
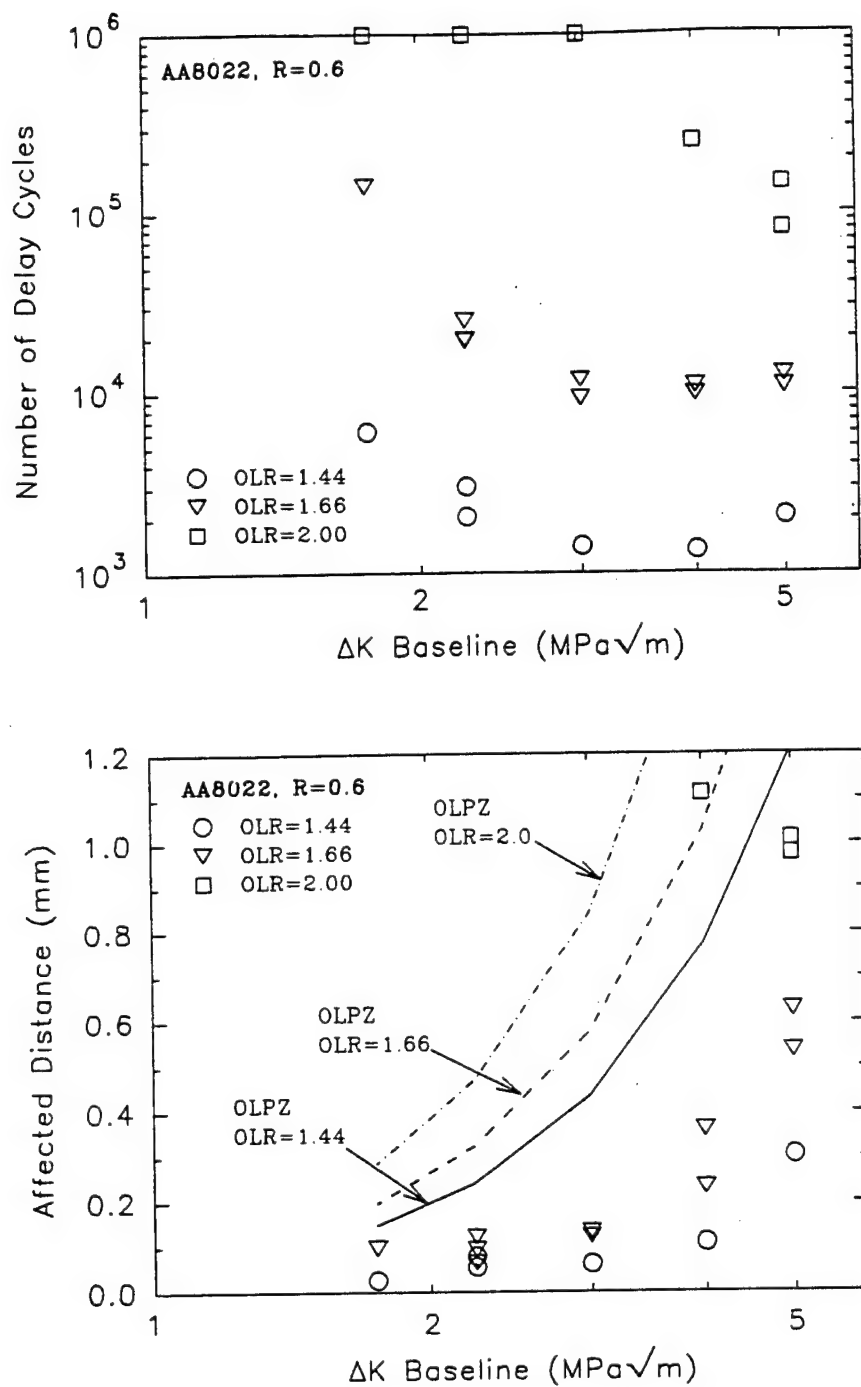
Figure 4.21. Magnitude of crack retardation in AA8022 at R=0.6 as a function of ΔK_B (OLPZ=calculated overload plastic zone size).
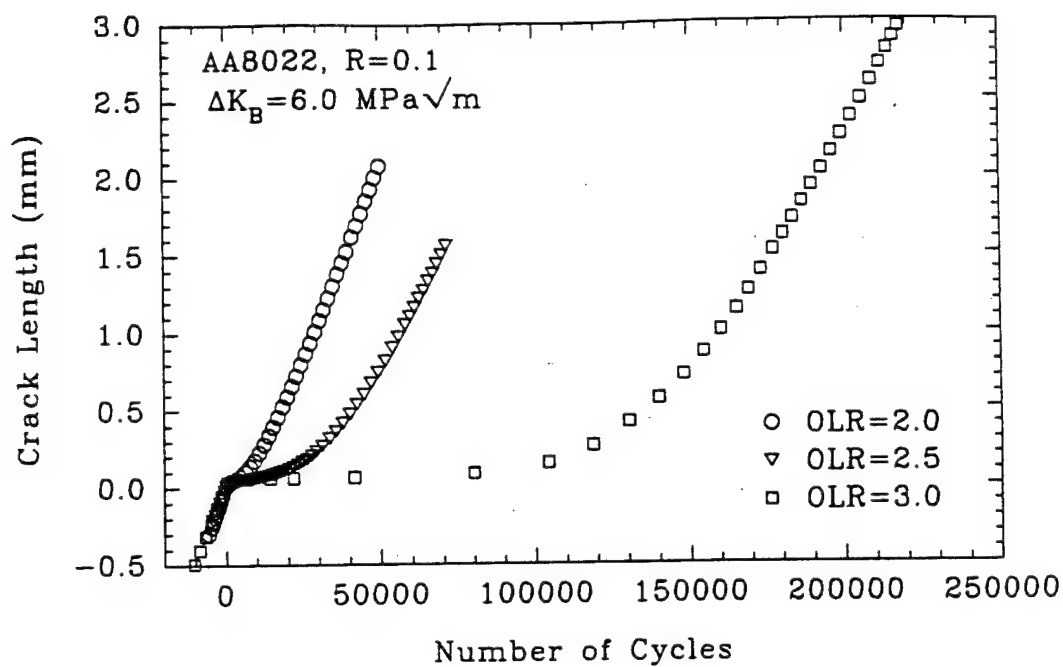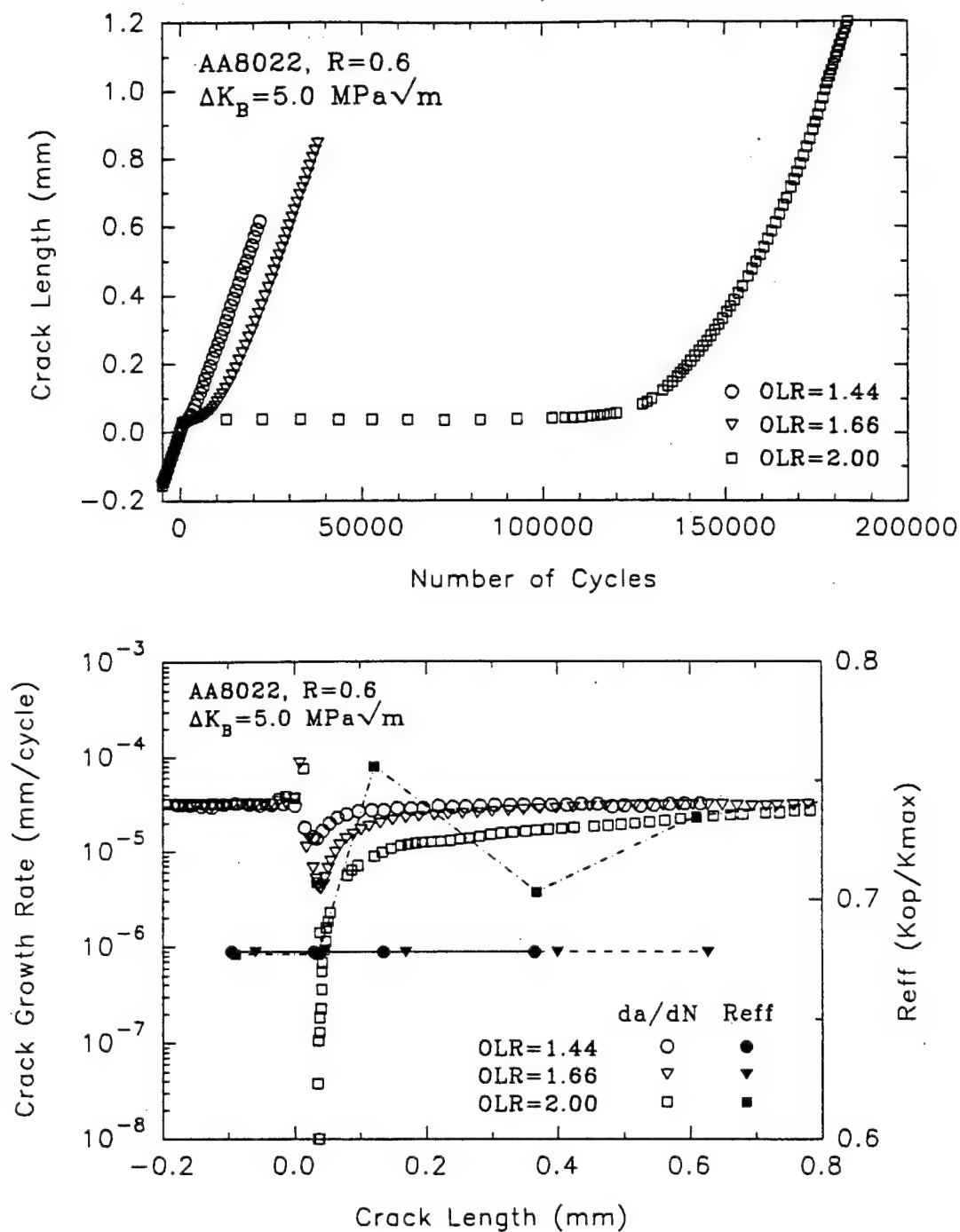
Figure 4.22. Effect of overload magnitude on overload response in AA8022 at ΔK_B=5 MPa$\sqrt{m}$, R=0.6.
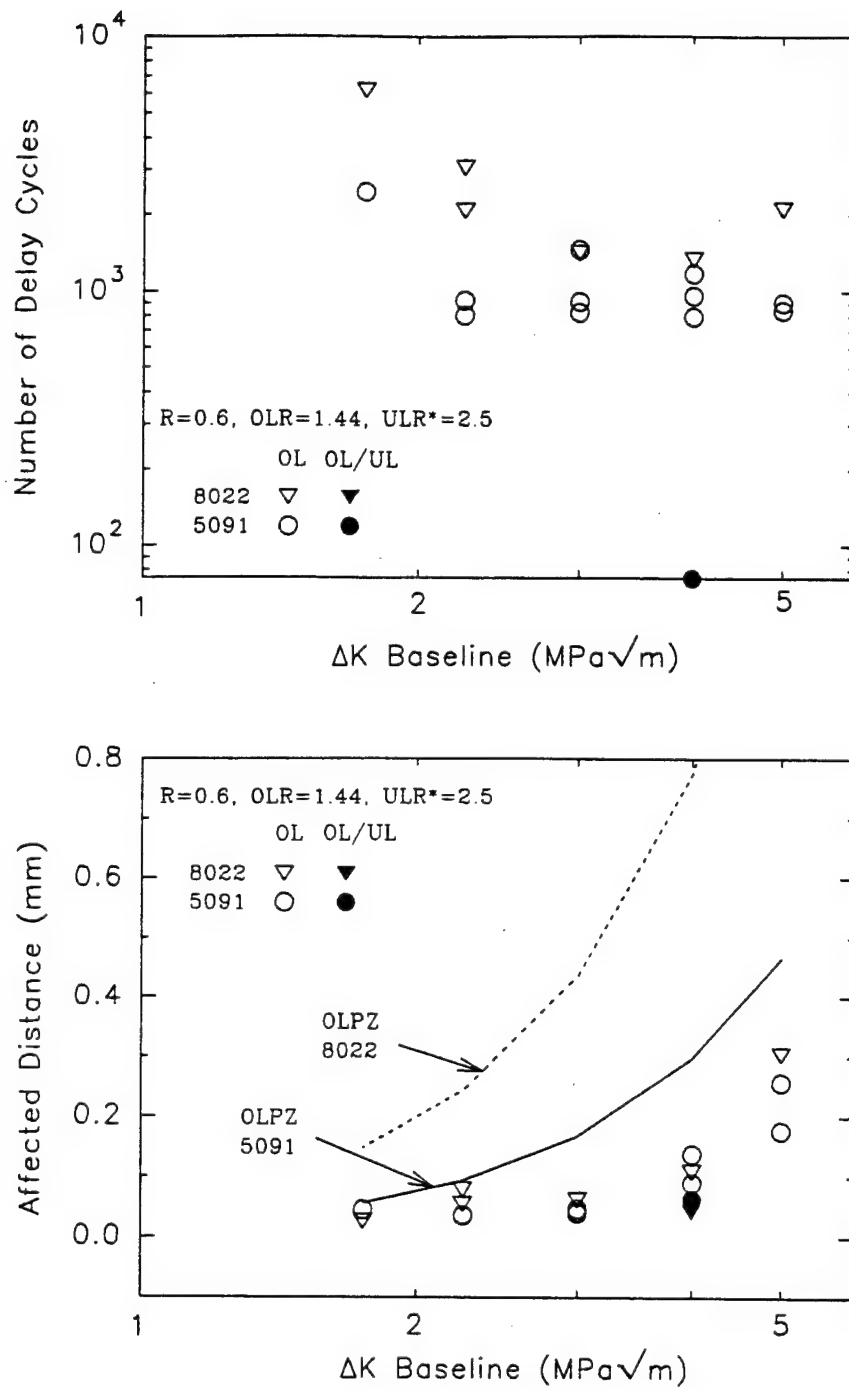
Figure 4.23. Comparison of retardation magnitude (OLR=1.44) in AA5091 and AA8022 at R=0.6 (OLPZ=calculated overload plastic zone size).
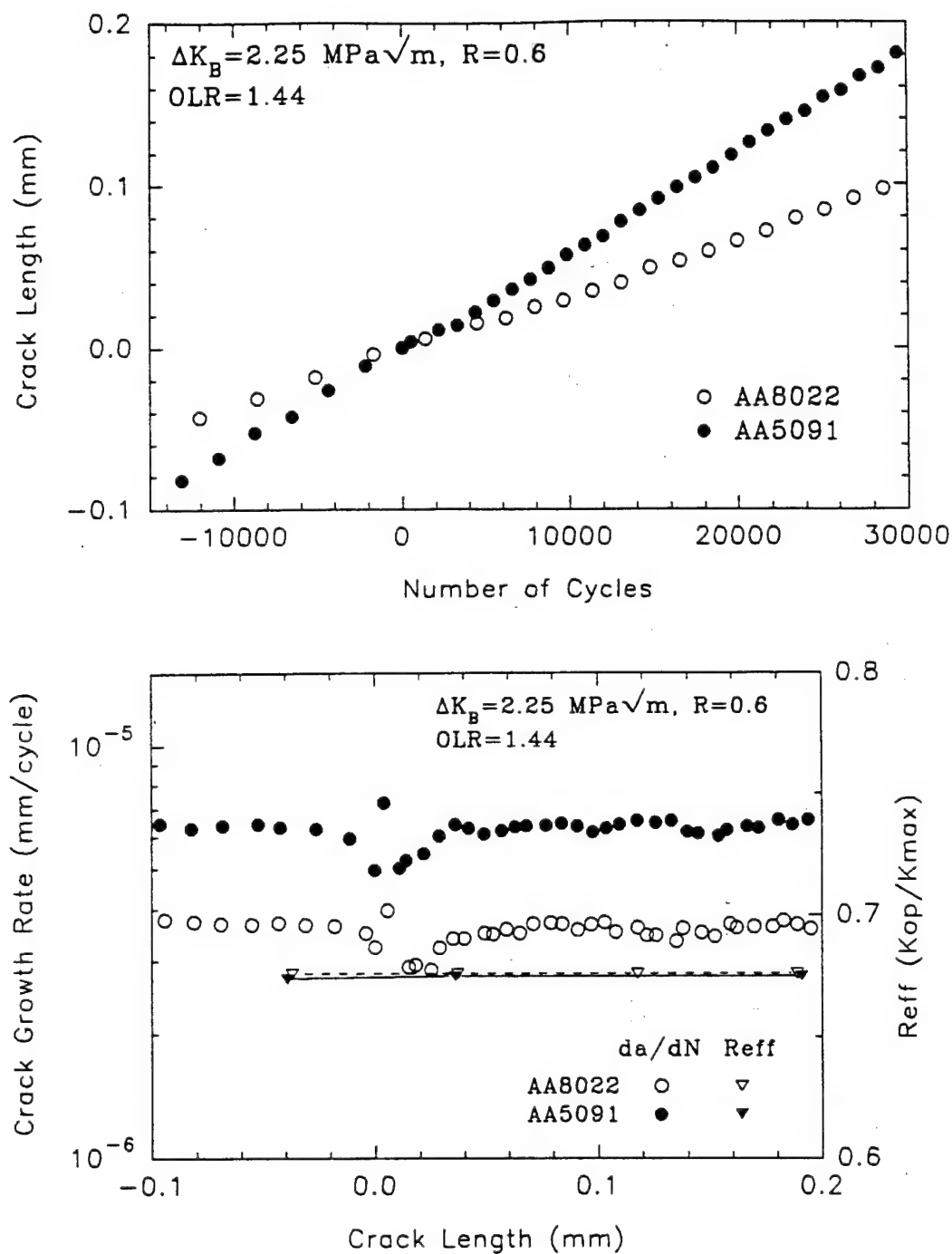
Figure 4.24. Comparison of overload response (OLR=1.44) of AA8022 and AA5091 at R=0.6 at ΔK_B= 2.25 MPa$\sqrt{m}$.
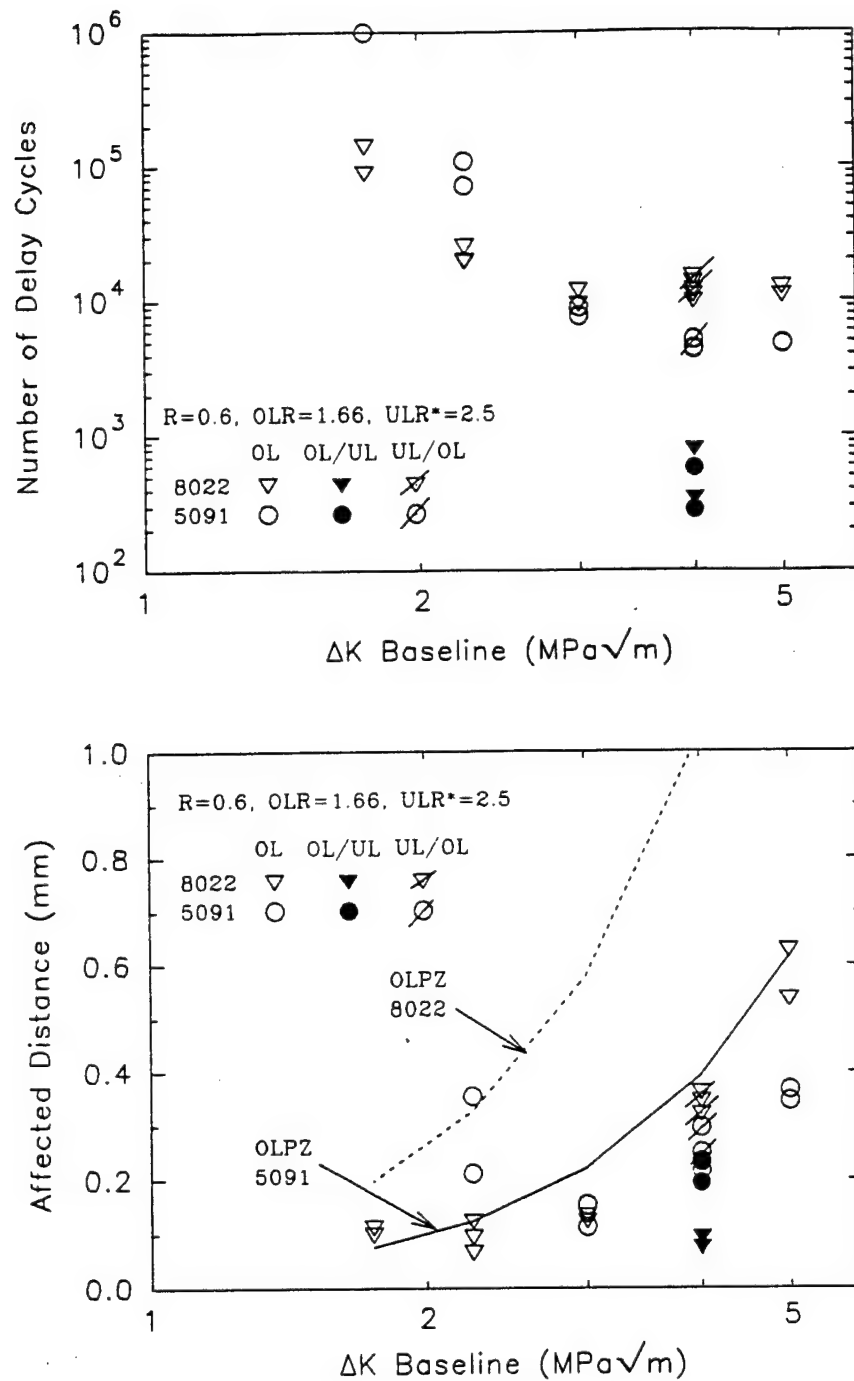
Figure 4.25. Comparison of retardation magnitude (OLR=1.66) in AA5091 and AA8022 at R=0.6 (OLPZ=calculated overload plastic zone size).

is not clear, but it is possibly the result of different contributions of baseline crack growth rate and minimum growth rate as ΔK_B varies. The lower $(da/dN)_B$ exhibited by AA8022 over the entire range of ΔK_B would tend to produce larger N_d in this alloy. However, the $(da/dN)_{min}$ exhibited by AA5091 would tend to produce larger N_d in this alloy. The results suggest that at low ΔK_B, shown in Figure 4.26(a), the effect of the $(da/dN)_{min}$ in AA5091 was greater than the effects of the lower $(da/dN)_B$ in AA8022, yielding a larger N_d in AA5091. At medium ΔK_B, shown in Figure 4.26(b), these two effects offset each other yielding a nearly equal N_d. At higher ΔK_B, shown in Figure 4.26(c), the effect of the lower $(da/dN)_B$ in AA8022 was greater than the effect of a lower $(da/dN)_{min}$ in AA5091 yielding a larger N_d in this alloy.

The behavior of the alloys at OLR=2.0 is compared in Figure 4.27. The alloys both exhibited crack arrest (i.e., $N_d > 1$ million) at $\Delta K_B = 3.0$ MPa√m and less. At higher ΔK_B, AA5091 continued to exhibit crack arrest, while N_d decreased with increasing ΔK_B in AA8022. The retardation behavior at $\Delta K_B = 5.0$ MPa√m is shown in Figure 4.28.

The effects of overload/underload and underload/overload combinations are also shown in Figures 4.23, 4.25, and 4.27. The retardation effect from an overload was nearly eliminated when it was followed by an underload, while preceding the overload by an underload had only a small effect on N_d. This occurred because the overload/underload combination produced a much smaller reduction in crack growth rates and smaller a_{aff} than either the overload alone or the underload/overload combination as shown in Figure 4.29. This behavior
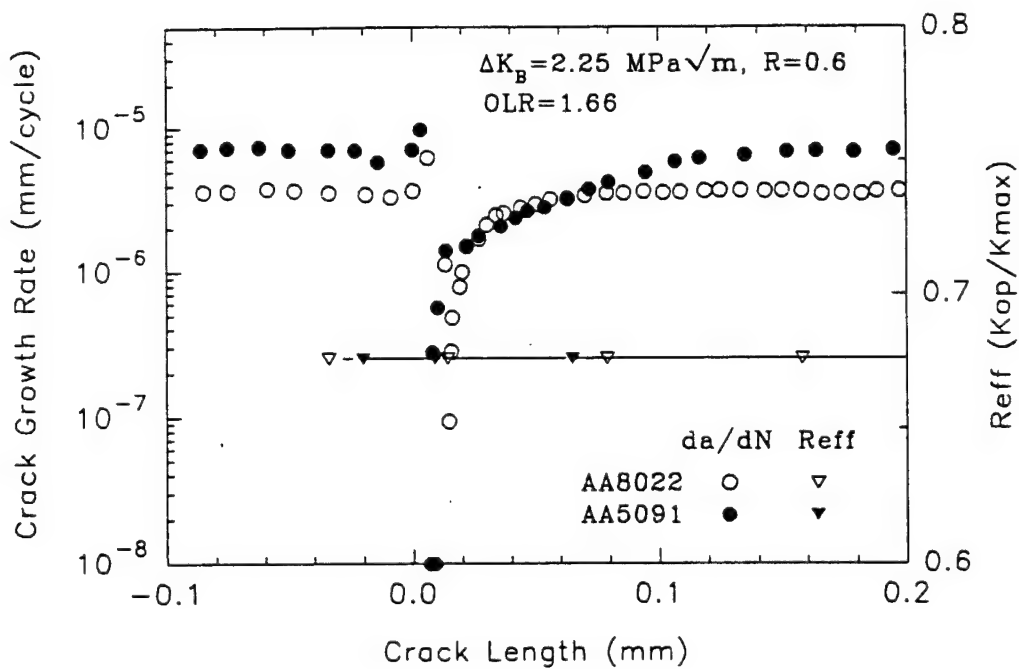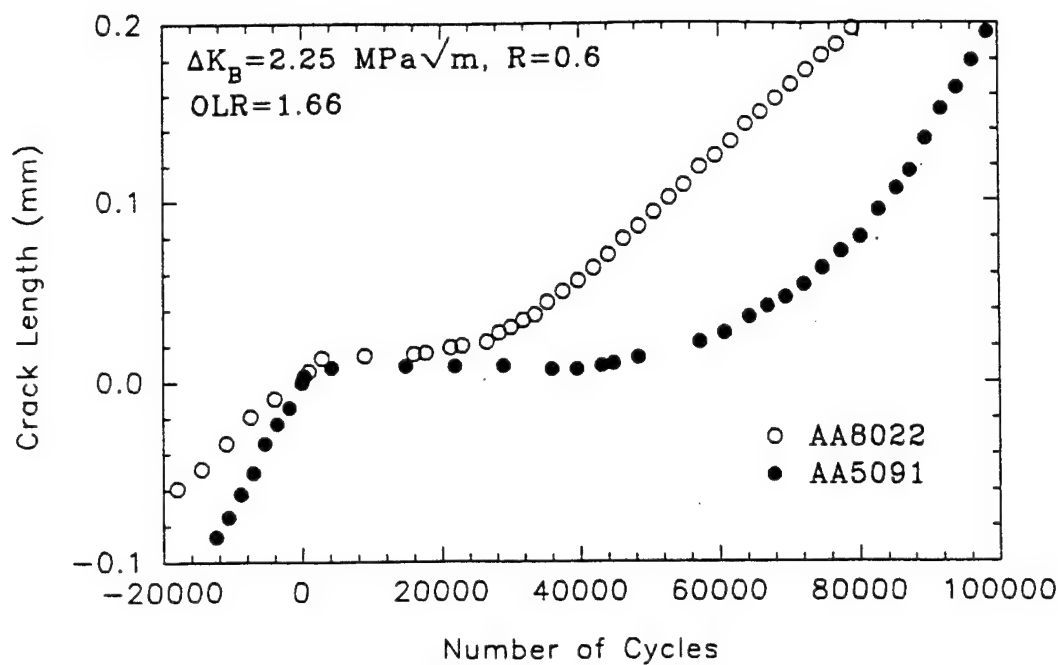
Figure 4.26. Comparison of overload response (OLR=1.66) in AA8022 and AA5091 at R=0.6: (a) ΔK_B=2.25 MPa$\sqrt{m}$;
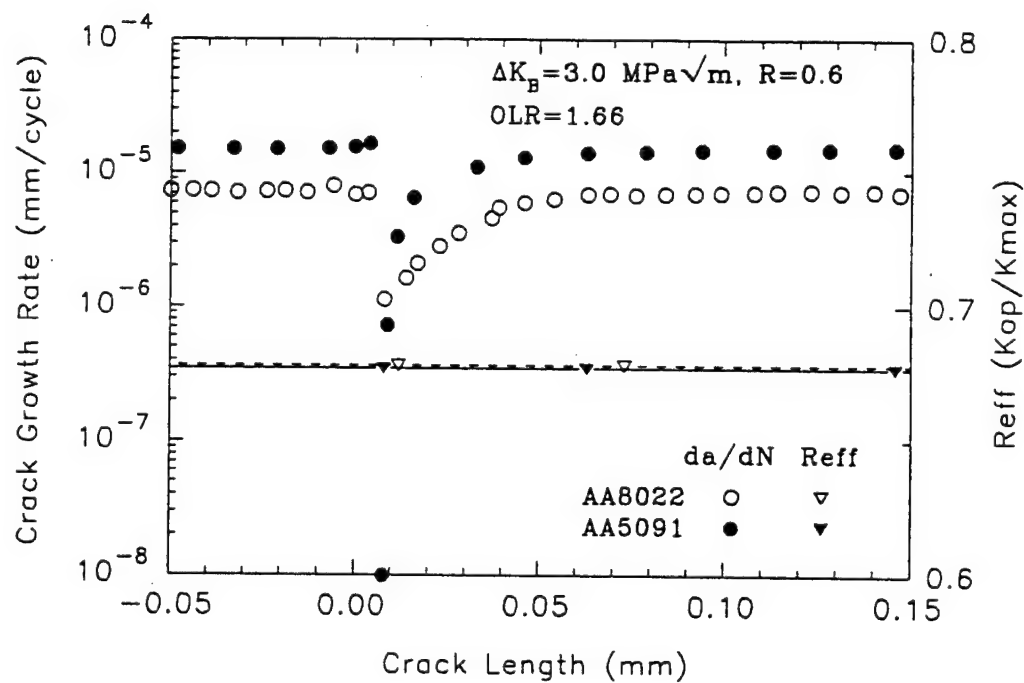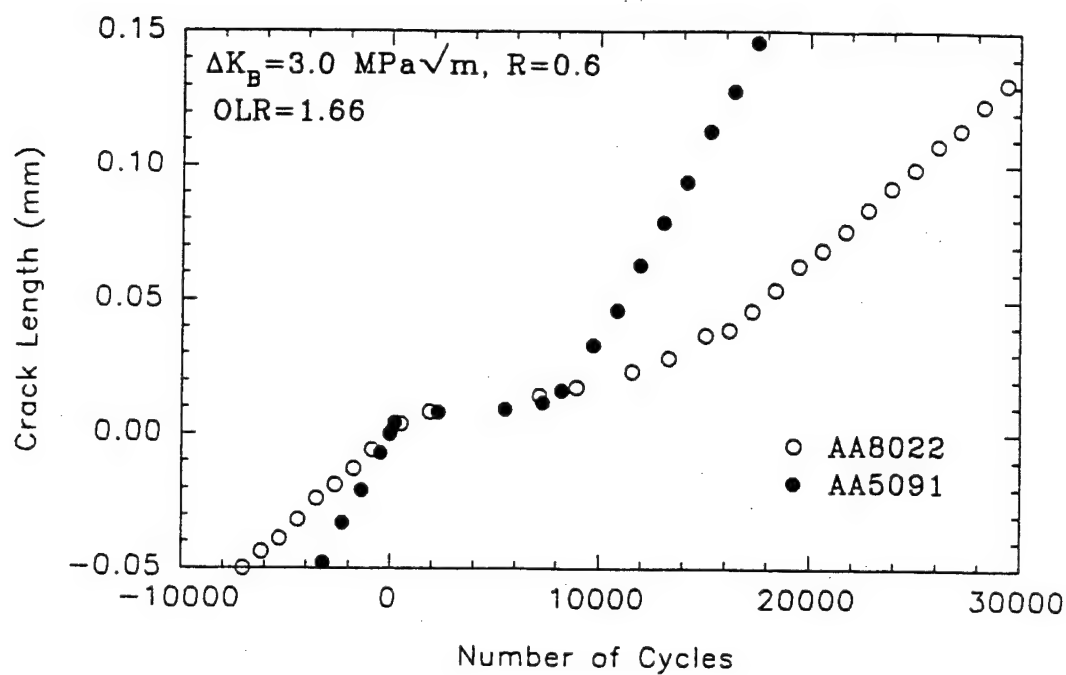
Figure 4.26 (cont'd). (b) ΔK_B=3 MPa$\sqrt{\text{m}}$;
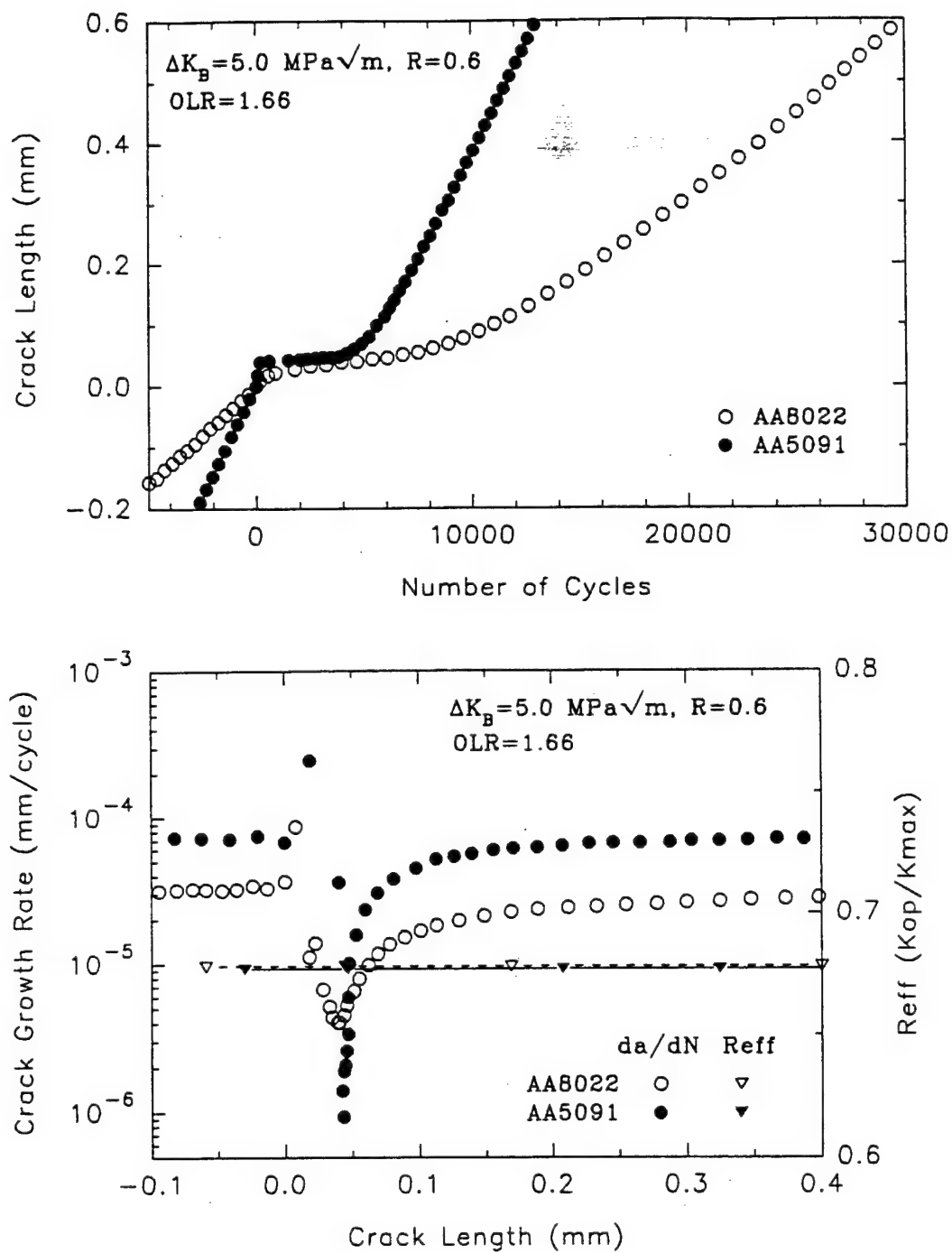
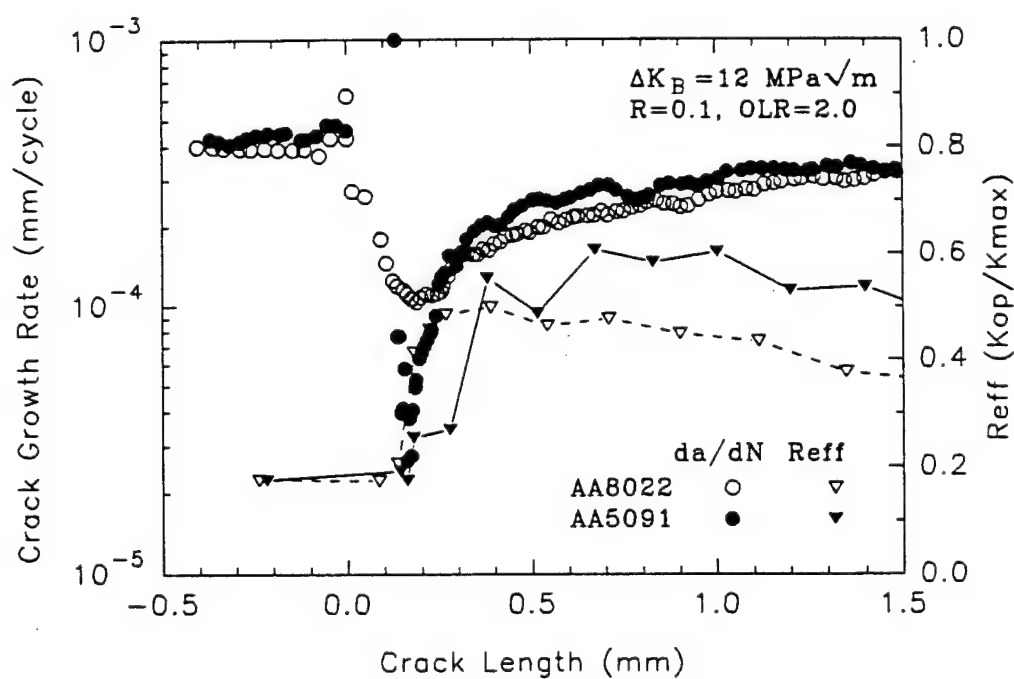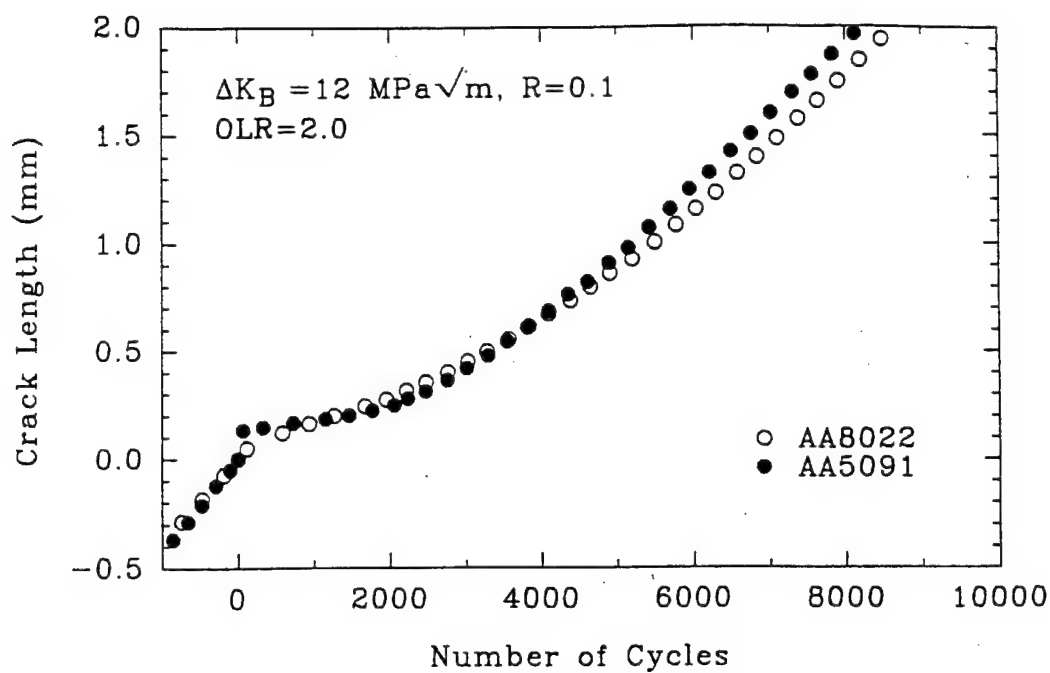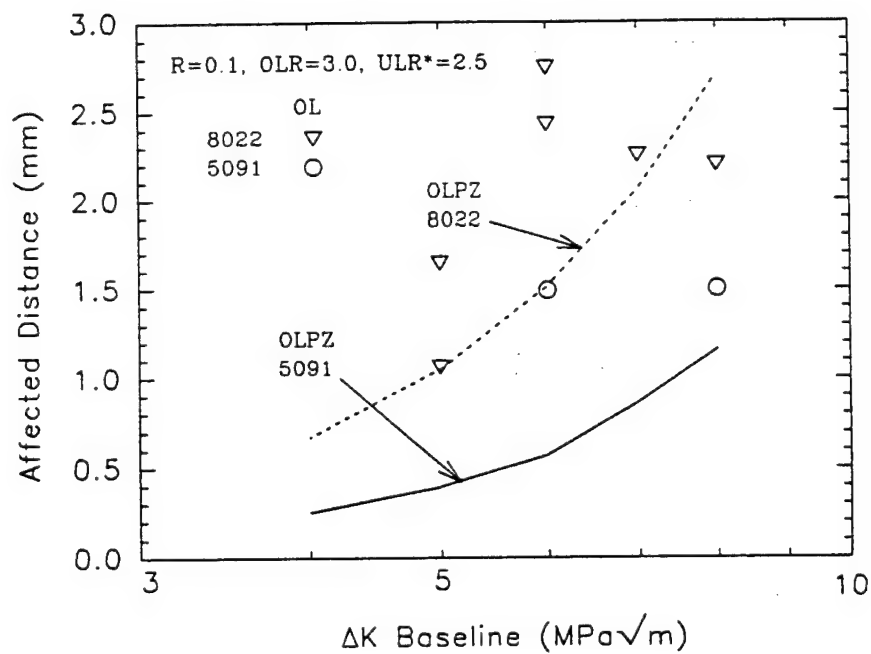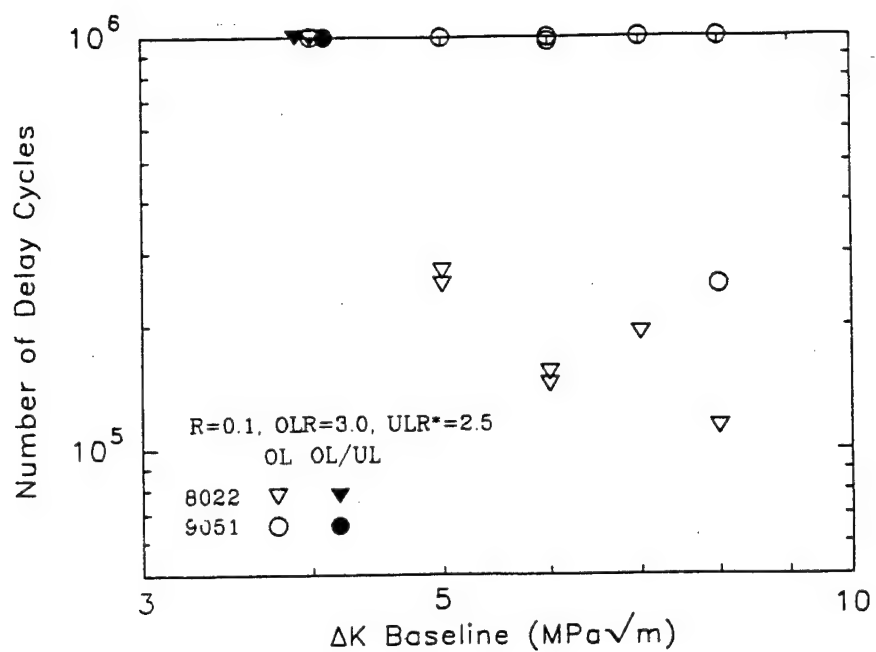Figure 4.26 (cont'd). (c) ΔK_B=5 MPa$\sqrt{m}$.
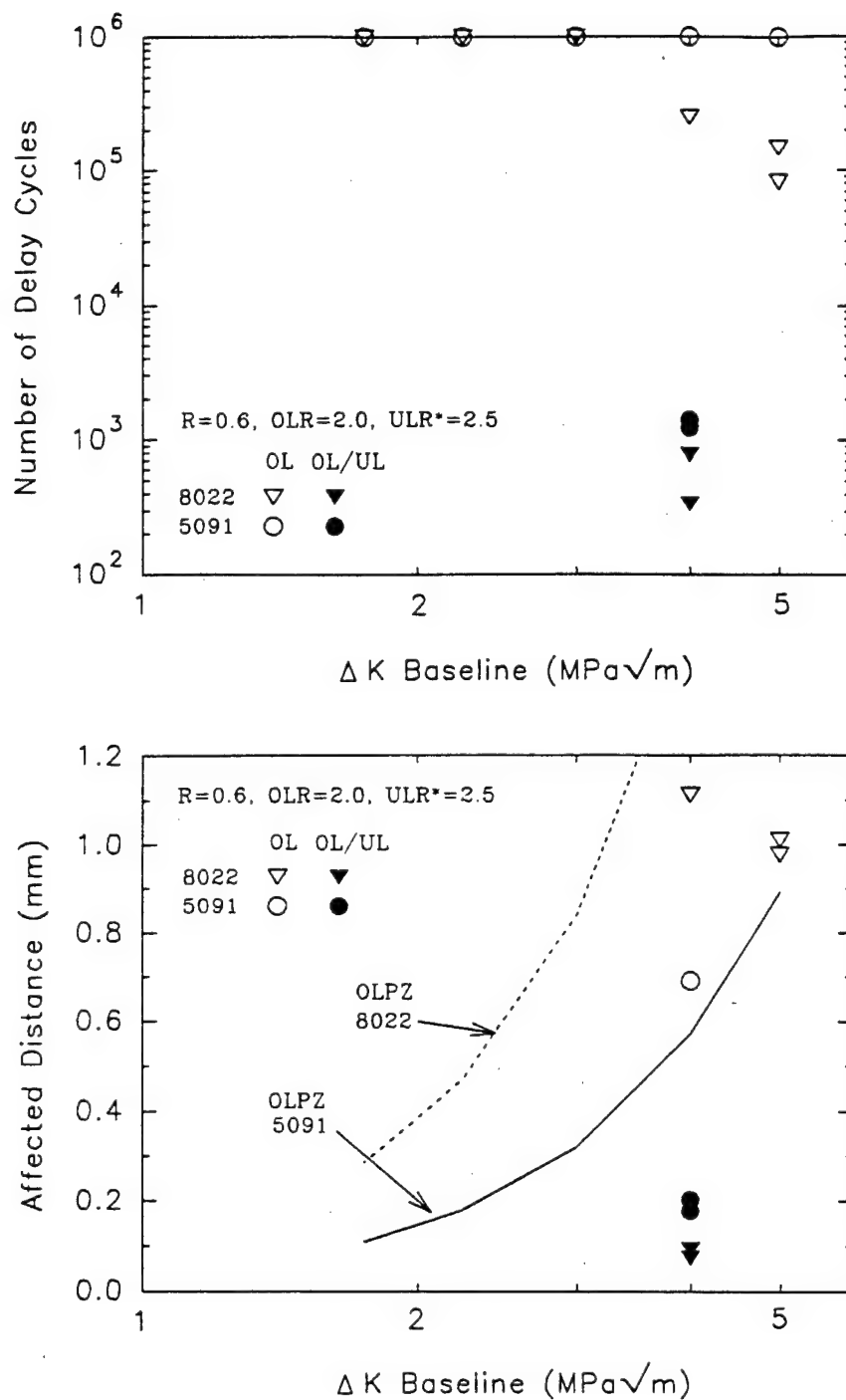
Figure 4.27. Comparison of retardation magnitude (OLR=2.0) in AA8022 and AA5091 at R=0.6 (OLPZ=calculated overload plastic zone size).
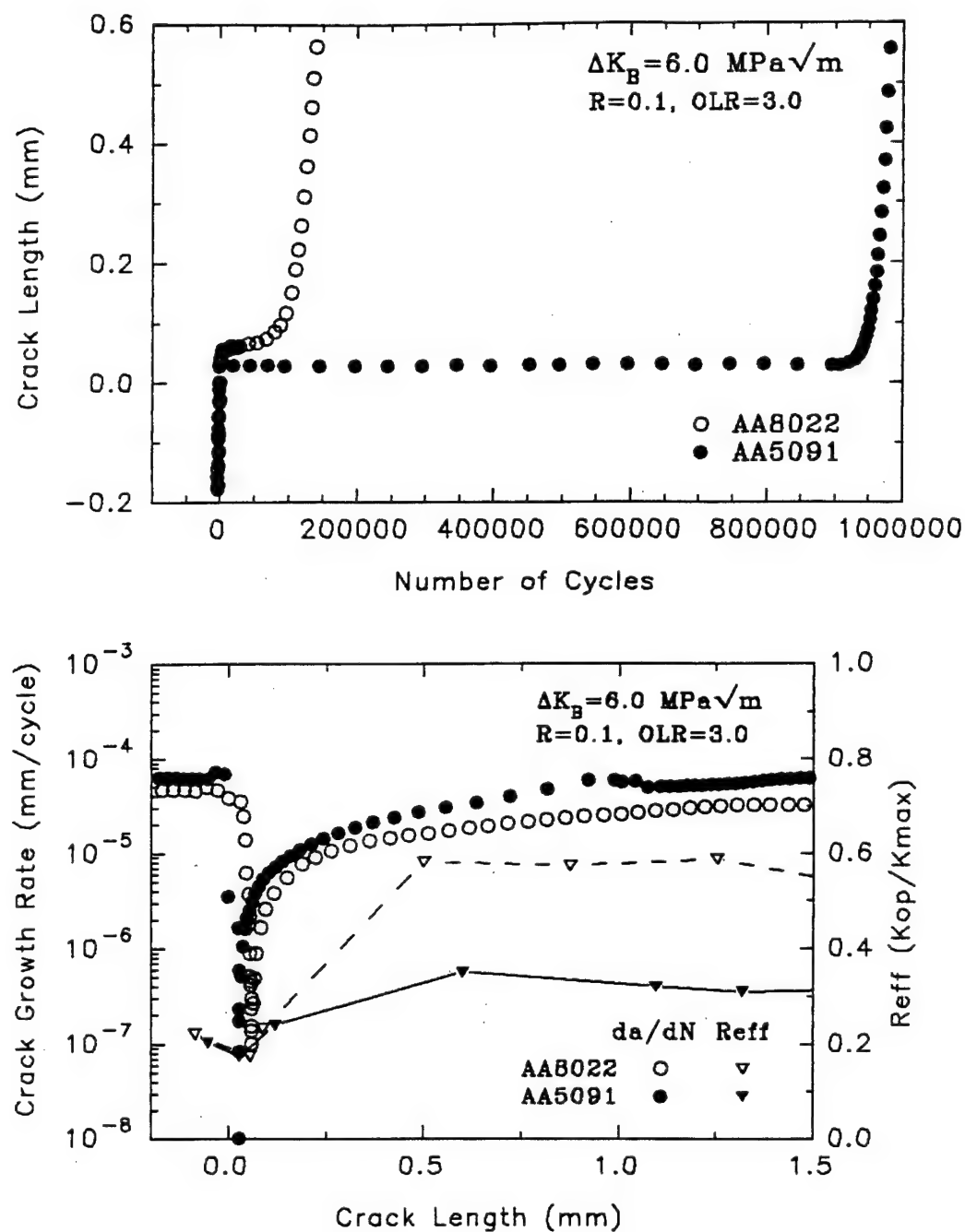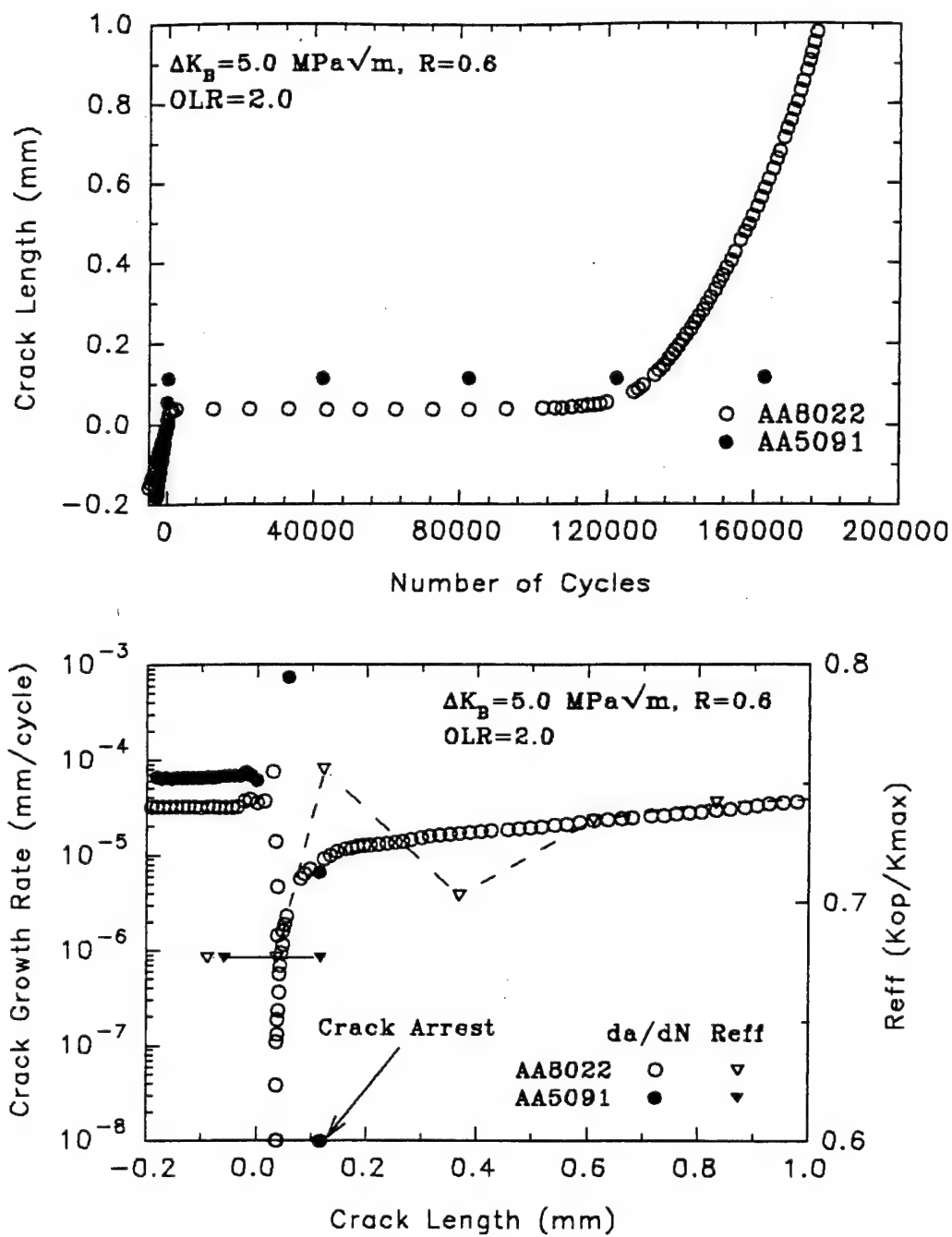
Figure 4.28. Comparison of overload response (OLR=2.0) in AA8022 and AA5091 at R=0.6, ΔK_B=5.0 MPa$\sqrt{m}$.
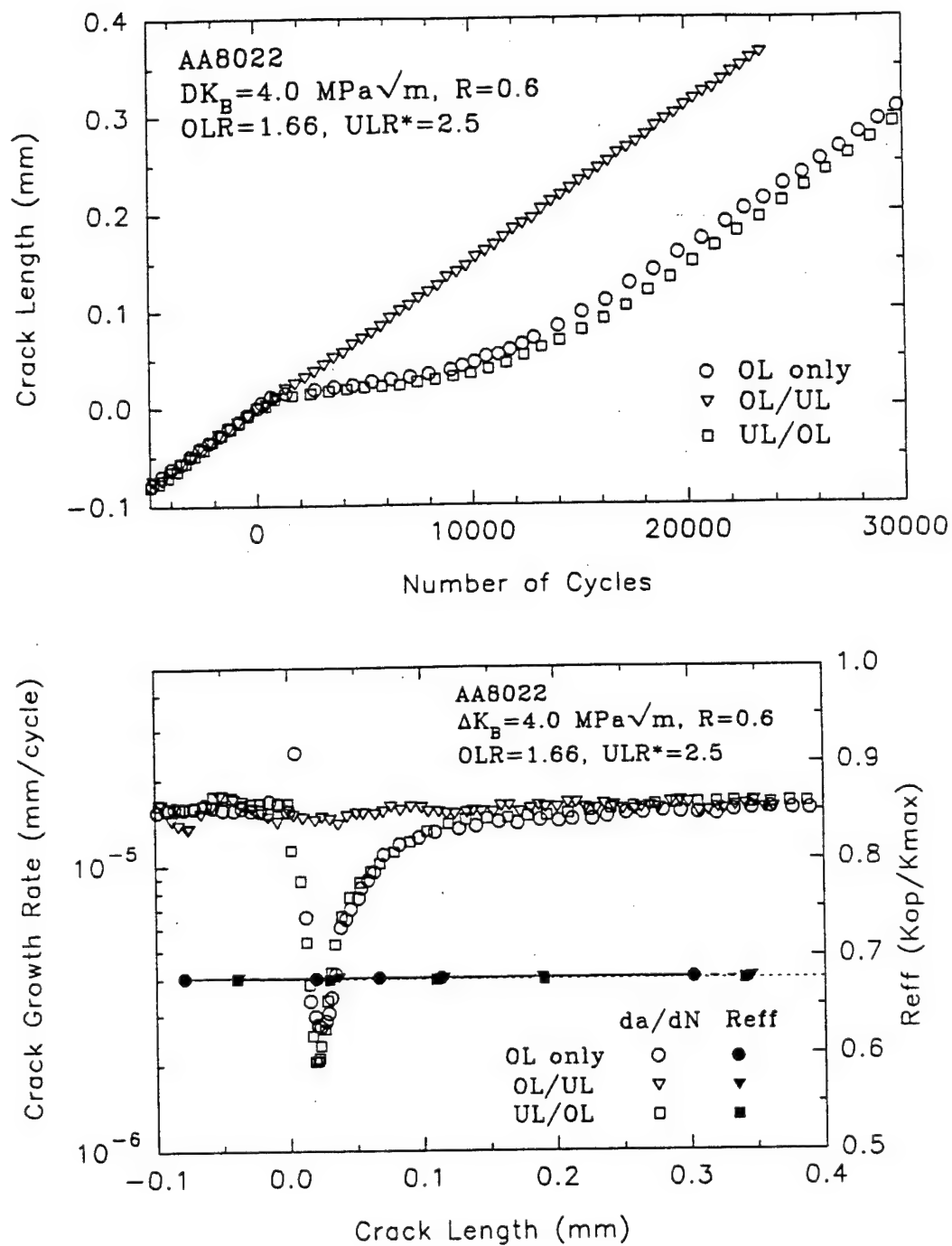
Figure 4.29. Effect of overload/underload combinations (OLR=1.66/ULR*=2.5) on the overload response of AA8022 at R=0.6.

is quite different from that at R=0.1 where neither the overload/underload or underload/overload combination had a significant effect on N_d.

The closure levels before and after overloads are also shown in Figures 4.24, 4.26(a)-(c), and 4.28. The closure level was $R_{eff}=0.67$ both before and after the overload in almost all the tests, indicating that no closure was detected. The only exceptions were the two tests in AA8022 at $\Delta K_B=5.0$ and OLR=2.0, one of which is shown in Figure 4.28. The closure level in these tests increased following the overload indicating that detectable closure occurred following the overload.

N_d was significantly larger following an overload of magnitude OLR=2.0 at R=0.6 than at R=0.1 at an equivalent ΔK_B as can be seen by comparing Figures 4.12 and 4.21, and 4.13 and 4.20. This resulted from a lower $(da/dN)_{min}$ and a larger a_{aff} at R=0.6 as shown in Figure 4.30.

The fatigue surfaces at the point of the overloads were examined in the SEM. At R=0.1, single tensile overloads in AA8022 produced a step on the fatigue surface consistent with crack tip blunting followed by a decrease in surface roughness. In cases where the crack did not arrest, the surface roughness gradually increased to the pre-overload or baseline roughness as the crack propagated through the affected zone. The affected zone was always larger at the surfaces than in the interior of the specimen. A typical example of this behavior is shown in Figure 4.31(a) and (b). In cases where the crack arrested (i.e., $N_d > 1$ million cycles), it did so after propagating only a short distance, and the surface roughness did not change appreciably over that distance. A typical example of this behavior is shown in Figure 4.31(c) and (d). The amount of post-overload growth in cases of crack arrest was always greater at
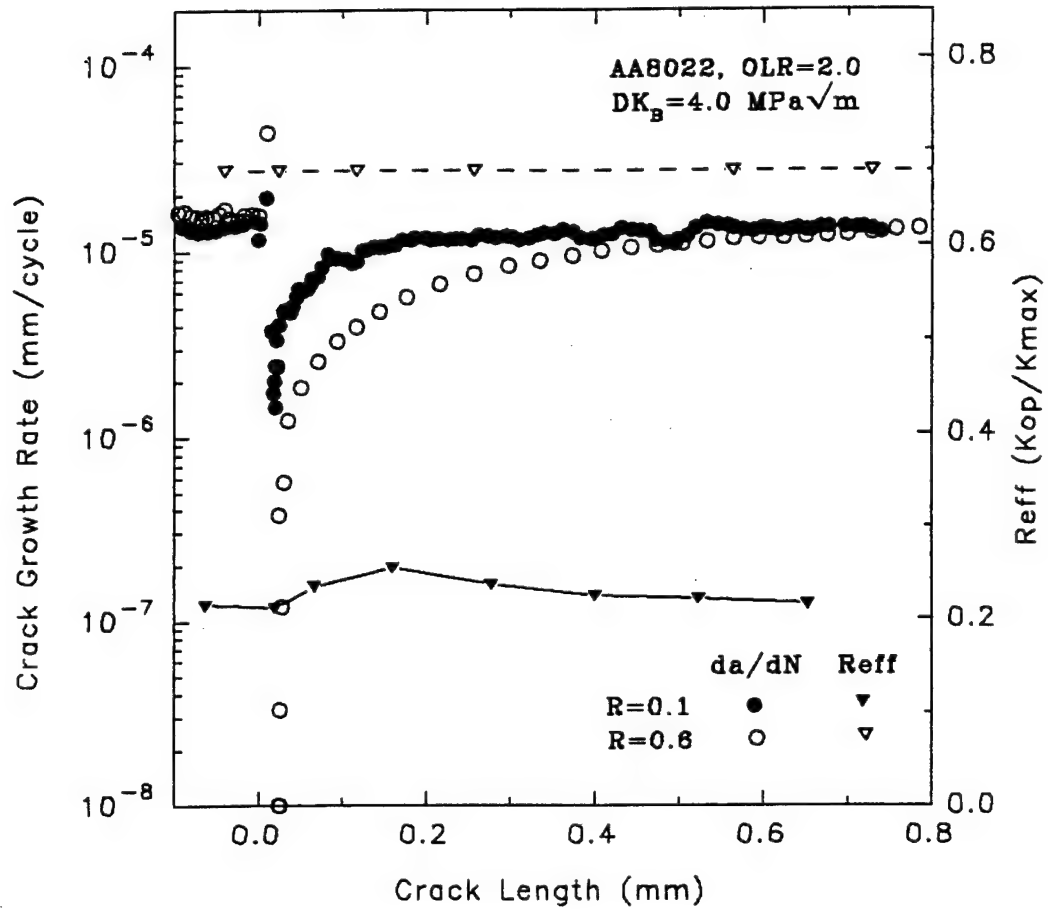
Figure 4.30. Comparison of overload response (OLR=2.0) in AA8022 at R=0.1 and 0.6.
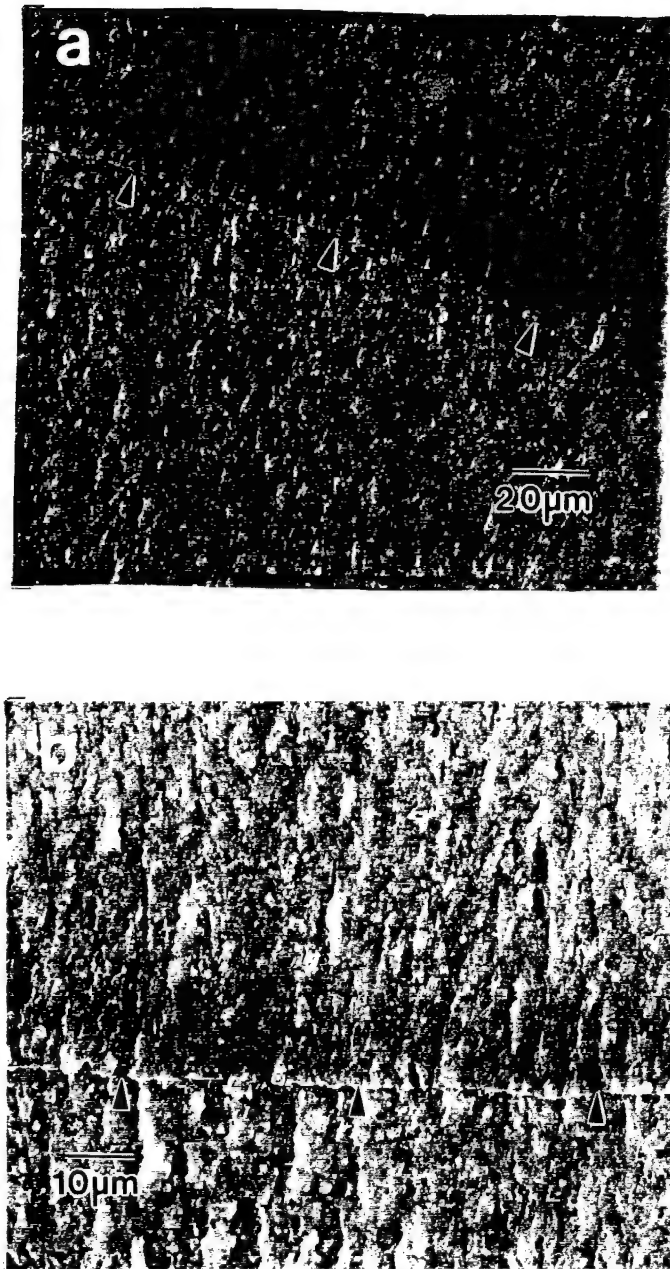
Figure 4.31. Fatigue crack surfaces in AA8022 at R=0.1 at point of overloads: OLR=2, ΔK_B=3 MPa√m in (a) surface region; and (b) interior region (arrows indicate crack front position at overload and direction of growth).
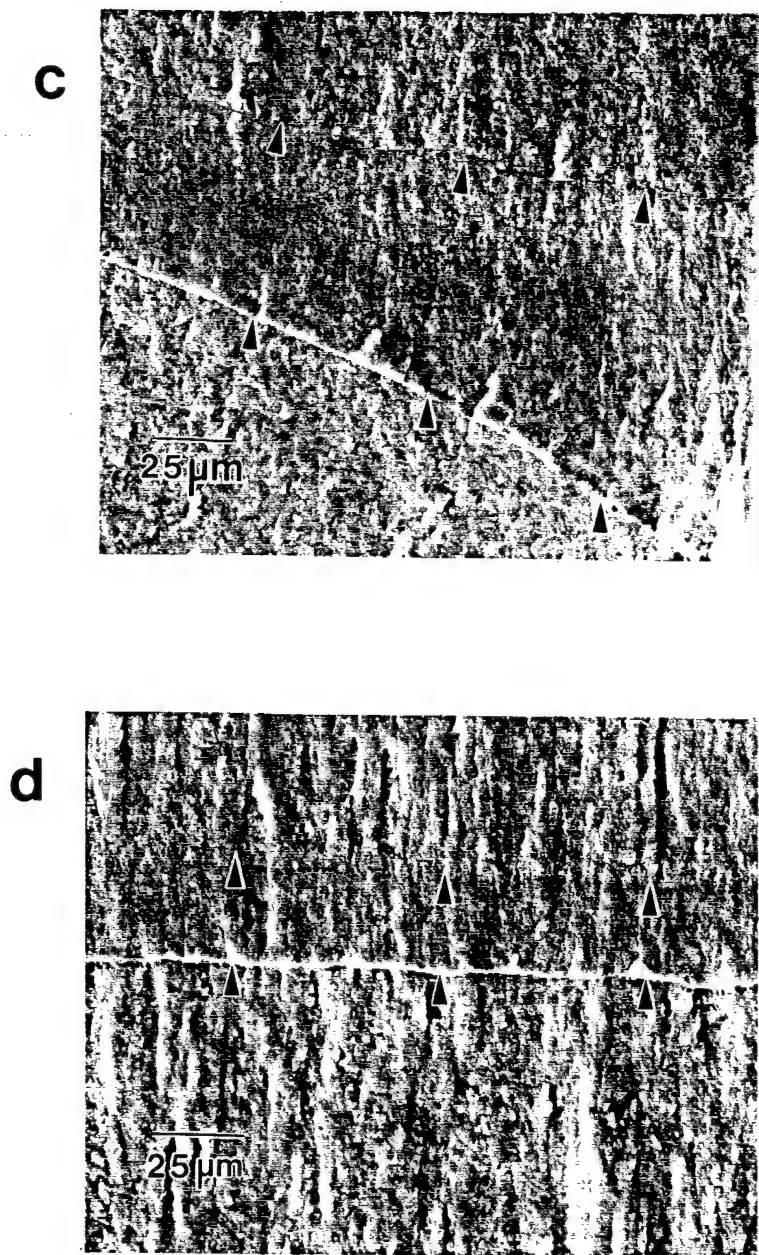
Figure 4.31 (cont'd). OLR=3, ΔK_B=4 MPa√m in (c) surface region; and (d) interior region (arrows indicate crack front position of point of overload and point of arrest).

the surfaces of the specimen than in the interior. The behavior at R=0.6 was nearly identical to that at R=0.1 as shown in Figure 4.32.

The fatigue surfaces in AA5091 were very similar in appearance to those in AA8022 at low ΔK_B for both R=0.1 and 0.6, except the affected zone was smaller for any given overload condition. However, at higher ΔK_B, the fatigue surfaces in AA5091 exhibited a region of unstable crack extension and crack deflection adjacent the specimen surface. The unstable crack growth occurred during the overload cycle as evidenced by an immediate increase in crack length following the overload (see Figure 4.16(c) and Figure 4.28). Only at the highest ΔK_B did K_{ol} approach the reported K_{Ic} of 30 MPa$\sqrt{m}$ for AA5091. A typical example of unstable crack growth is shown in Figure 4.33(a) and (b). Crack deflection in AA5091 is discussed in more detail in Section 4.3.3.

The greatest amount of unstable growth occurred at approximately mid-thickness. The surface roughness in this region of unstable growth was approximately R_a=3.5 µm which is significantly rougher than the roughness of the fatigue surface which ranged from R_a=0.1 to 0.7 µm. The amount of unstable growth increased with increasing ΔK_B and overload magnitude. The overload conditions which produced unstable growth and the amount of that growth are shown in Table 4.2. After the region of unstable growth, the crack again propagated by fatigue. The surface roughness initially decreased compared to the baseline roughness and then increased again, just as it did in the absence of unstable growth at low ΔK_B. In cases of crack arrest, the unstable growth was nearly always followed by fatigue crack growth as shown in Figure 4.33(c). The only exception was at R=0.1, ΔK_B=8.0 MPa$\sqrt{m}$, and OLR=3.0.
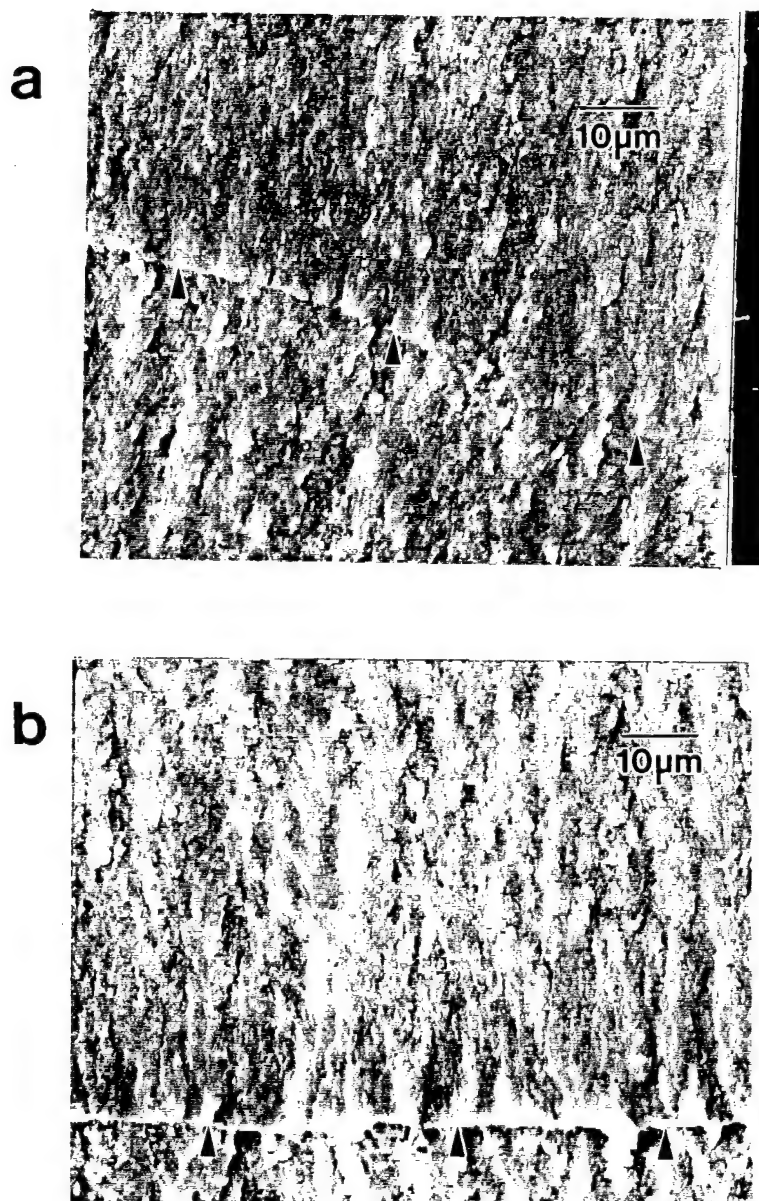
Figure 4.32. Fatigue crack surfaces in AA8022 at R=0.6 at point of overloads: OLR=1.66, ΔK_B=3 MPa$\sqrt{m}$ in (a) surface region; and (b) interior region (arrows indicate crack front position at point of overload and direction of growth).
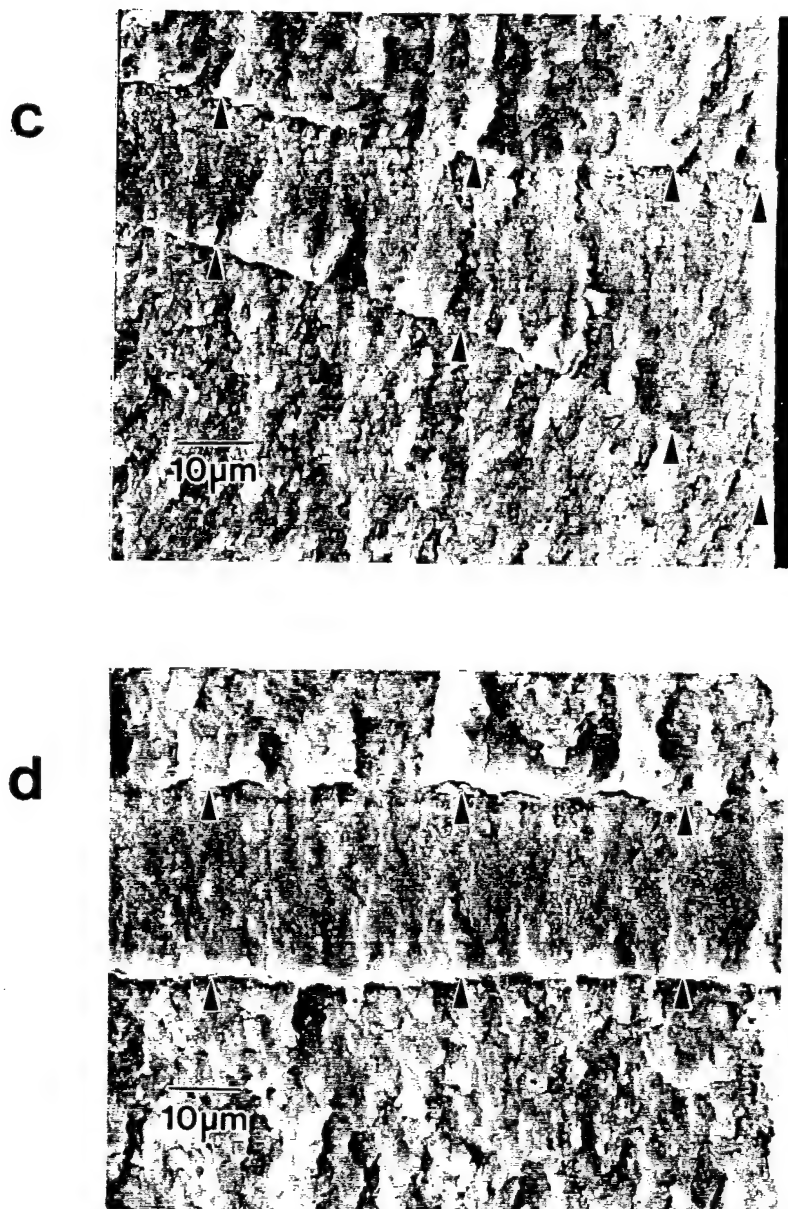
Figure 4.32 (cont'd). OLR=2, ΔK_B= 3 MPa√m in (c) surface region; and (d) interior region (arrows indicate crack front position at point of overload and point of arrest).

For this overload condition, post-overload fatigue crack growth occurred in the surface regions, but none was observed in the interior as shown in Figure 4.33(d). The amounts of post-overload growth for overload conditions producing crack arrest are shown for both AA8022 and AA5091 in Table 4.3. The amount of growth prior to arrest was greater at the surface than in the interior except at high ΔK_B where significant amounts of unstable growth had occurred at mid-thickness. Under identical overload conditions the amount of post-overload growth in AA5091 was approximately one-fourth to one-half that in AA8022.

Table 4.2   Extent of Unstable Growth in AA5091 Following Overloads

Stress Ratio	OLR	ΔK_B (MPa√m)	Unstable Extension at Center (B/2) (μm)
0.1	2.0	1.75 to 4.0 6.0 8.0 10.0 12.0	None 2 12 60 300
	3.0	4.0 5.0 6.0 7.0 8.0	None 6 13 52 430
0.6	1.44	1.75 to 4.0 5.0	None 8
	1.66	1.75 to 3.0 4.0 5.0	None 10 42
	2.0	1.75 to 2.25 3.0 4.0 5.0	None 5 26 140
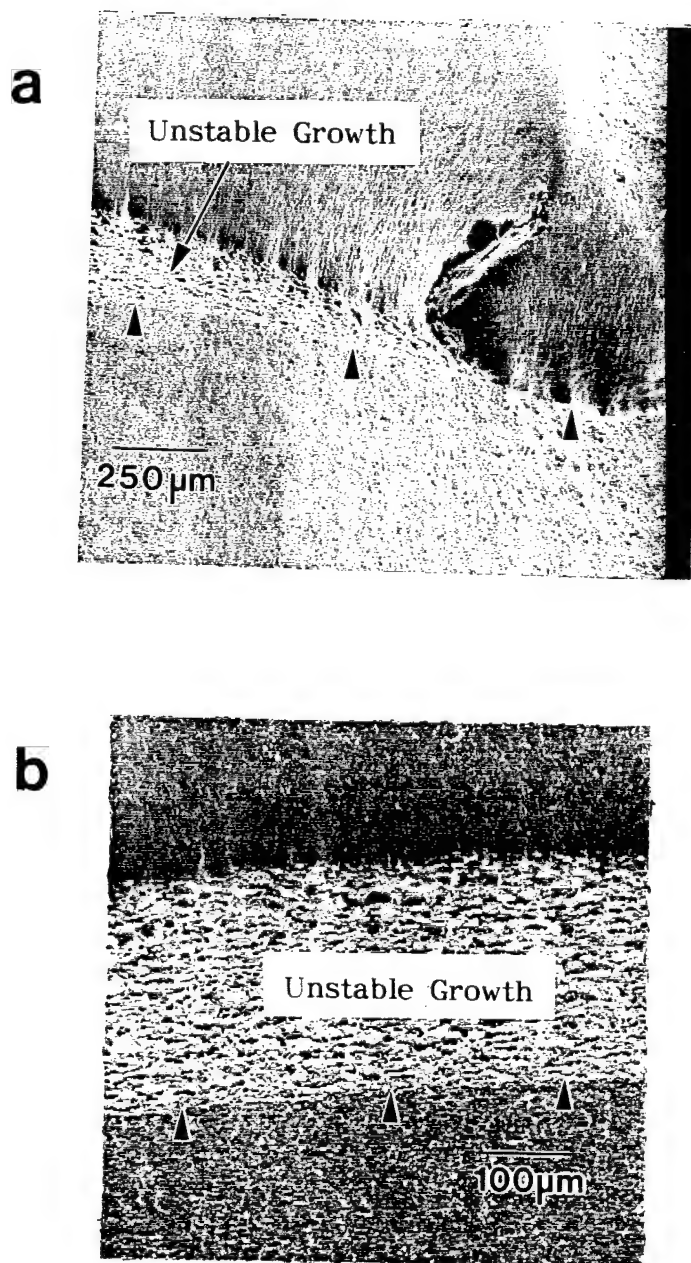
Figure 4.33. Fatigue crack surfaces in AA5091 at R=0.1 at point of overloads (OLR=2): ΔK_B=12 MPa√m in (a) surface region; and (b) interior region (arrows indicate crack front position at point of overload and direction of growth).
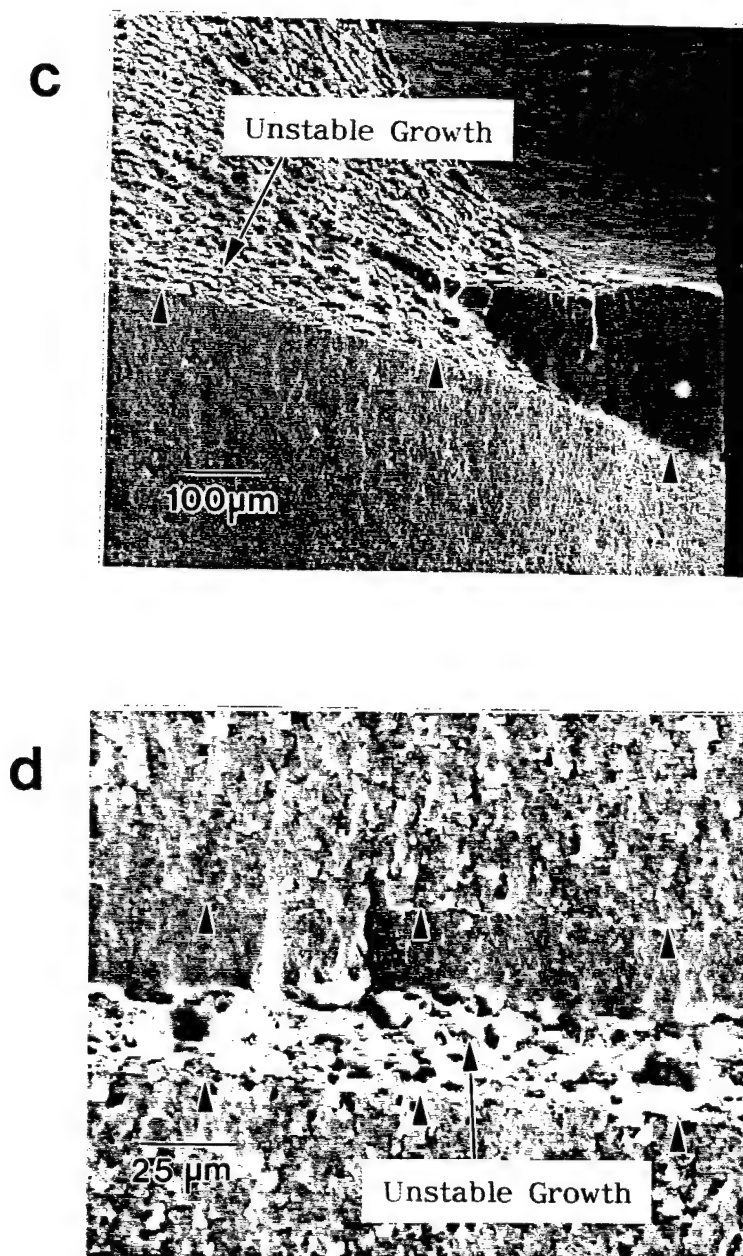
Figure 4.33 (cont'd). At R=0.6, ΔK_B=4 MPa√m in (c) surface region and (d) interior region (arrows indicate crack front position at point of overload).

The changes in surface roughness following overloads are consistent with the dependence of surface roughness on crack growth rates observed in the constant amplitude FCGR tests. In these tests the surface roughness decreased with decreasing crack growth rates as shown previously in Figures 4.9. Since crack growth rates are a function of ΔK_{eff} it can also be said that surface roughness decreases with decreasing ΔK_{eff}. Thus, a decrease in surface roughness following an overload should be expected in these alloys since ΔK_{eff} and the crack growth rate decreases. As ΔK_{eff} and the crack growth rate increases, the surface roughness increases. After the crack resumes growing at the baseline rate the surface roughness is equivalent to that prior to the overload.

The fatigue surfaces of both AA8022 and AA5091 showed evidence of crack surface rubbing at medium to high ΔK_B for both R=0.1 and 0.6. The rubbing occurred across the entire crack front but was most severe in the surface regions. A typical example of rubbing is shown in Figure 4.34(a) and (b). The fatigue surfaces in AA5091 also exhibited fretting products in the surface region in cases where the overload produced significant crack deflection in this region. A typical example of fretting products is shown in Figure 4.34(c). The rubbing and fretting indicate that crack surfaces were contacting each other following the overload at both R=0.1 and 0.6. The fatigue surfaces showed no evidence of secondary cracking.

Table 4.3.   Crack Extension From Point of Overload to Point of Arrest

Alloy	Stress Ratio	OLR	ΔK_B (MPa$\sqrt{m}$)	Crack Extension Prior to Arrest (μm)	
				Surface	Interior
AA8022	0.1	2.0	1.75	4	4
		3.0	4.0	11	33
	0.6	2.0	1.75	8	5
		2.0	2.25	17	8
		2.0	3.0	43	25
AA5091	0.1	2.0	1.75	1	1
		3.0	4.0	35	8
		3.0	5.0	48	14
		3.0	6.0	82	31
		3.0	7.0	127	67
		3.0	8.0	228	430
	0.6	2.0	1.75	2	2
		2.0	2.25	7	3
		2.0	3.0	12	9
		2.0	4.0	29	31
		2.0	5.0	60	152

4.3.3.   Crack Deflection Behavior

The crack profiles at the specimen surface were examined at the point of overloads for evidence of crack deflection, crack branching, and secondary cracking. The point of the overload was identified by the intense shear bands that formed on the surface as a result of the overloads. There was no evidence of secondary crack formation in either alloy. In AA5091, there was no deflection or branching at low ΔK_B, but at higher ΔK_B, the crack deflected and sometimes branched. This resulted from unstable crack propagation during the overload cycle along one or both of the overload shear bands. The severity of the deflection and the propensity for crack branching increased with increasing ΔK_B and
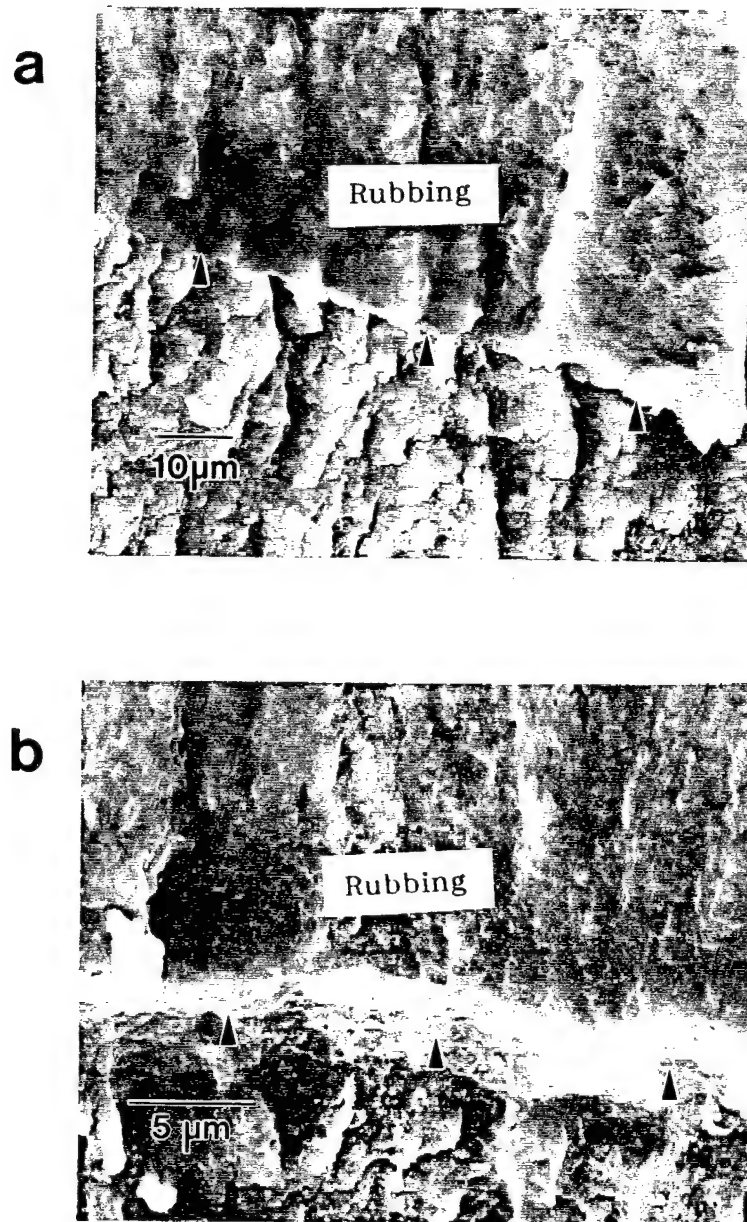
Figure 4.34. Fatigue crack surfaces at R=0.6 with evidence of rubbing at point of overload: AA8022, OLR=2, ΔK_B=5 MPa√m in (a) surface region; and (b) interior region (arrows indicate crack front position at point of overload);
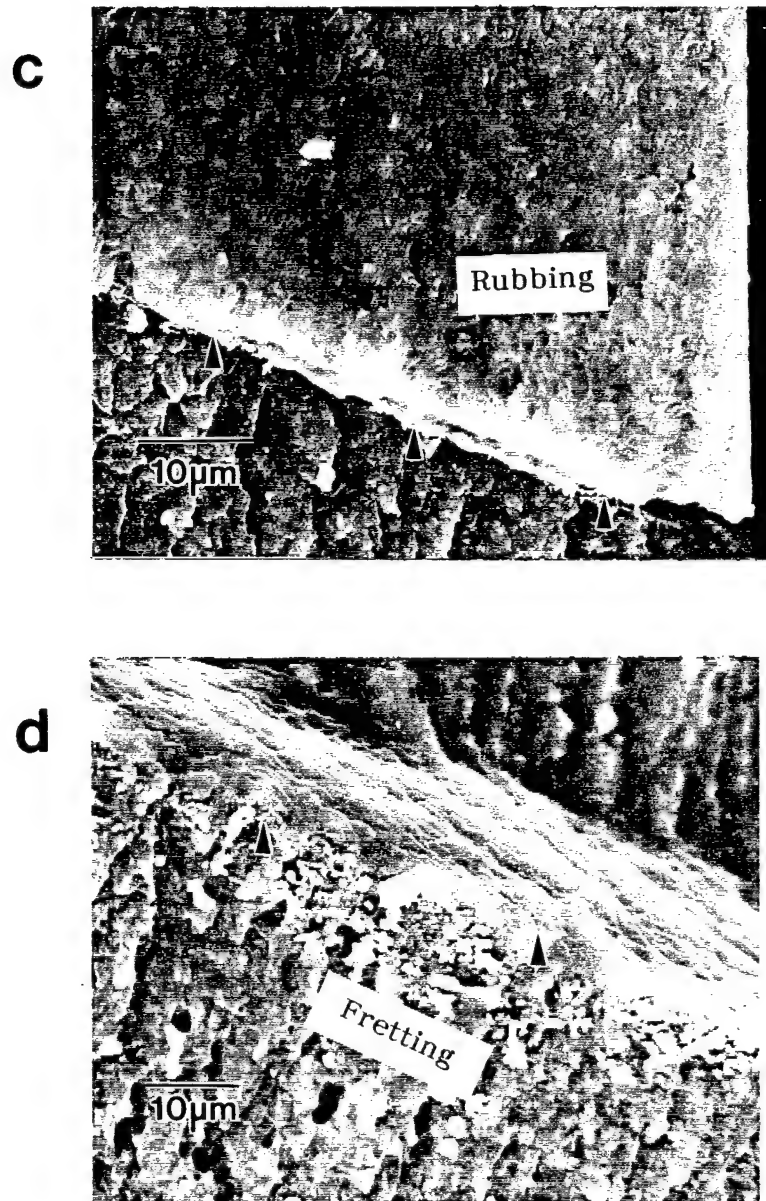
Figure 4.34 (cont'd). (c) AA5091, OLR=1.66, ΔK_B=5 MPa√m; (d) AA5091, OLR=2, ΔK_B=4 MPa√m (arrows indicate crack front position at point of overload).

overload magnitude. There was no noticeable difference in the crack deflection behavior of overloads, overload/underloads, or underload/overloads for a given overload condition. Typical examples of crack profiles in AA5091 are shown in Figure 4.35(a)-(c).

The shear bands are the boundary between the material behind the crack tip and that in front of the crack tip which has undergone greater through-thickness (z-direction) contraction as a consequence of the overload. This is evident in Figure 4.35(d). The crack deflects along this boundary during the overload cycle when the shear band strain exceeds the maximum strain which the material can withstand. The greatest amount of contraction occurs in the plane-stress surface region. The interior plane-strain region is prevented from contracting because of through-thickness constraint. Thus, crack deflection by this mechanism was limited to the surface regions. The depth of crack deflection for selected overload conditions was determined by successively removing material from the specimen surface and examining the crack profile. An example of this process is shown in Figure 4.36. The overload conditions which produced crack deflection and the depth of that deflection for selected tests are shown in Table 4.4. The results indicate the depth of deflection increased with increasing ΔK_B, increasing overload magnitude, and was greater at R=0.6 than at R=0.1 for a given ΔK_B and OLR.
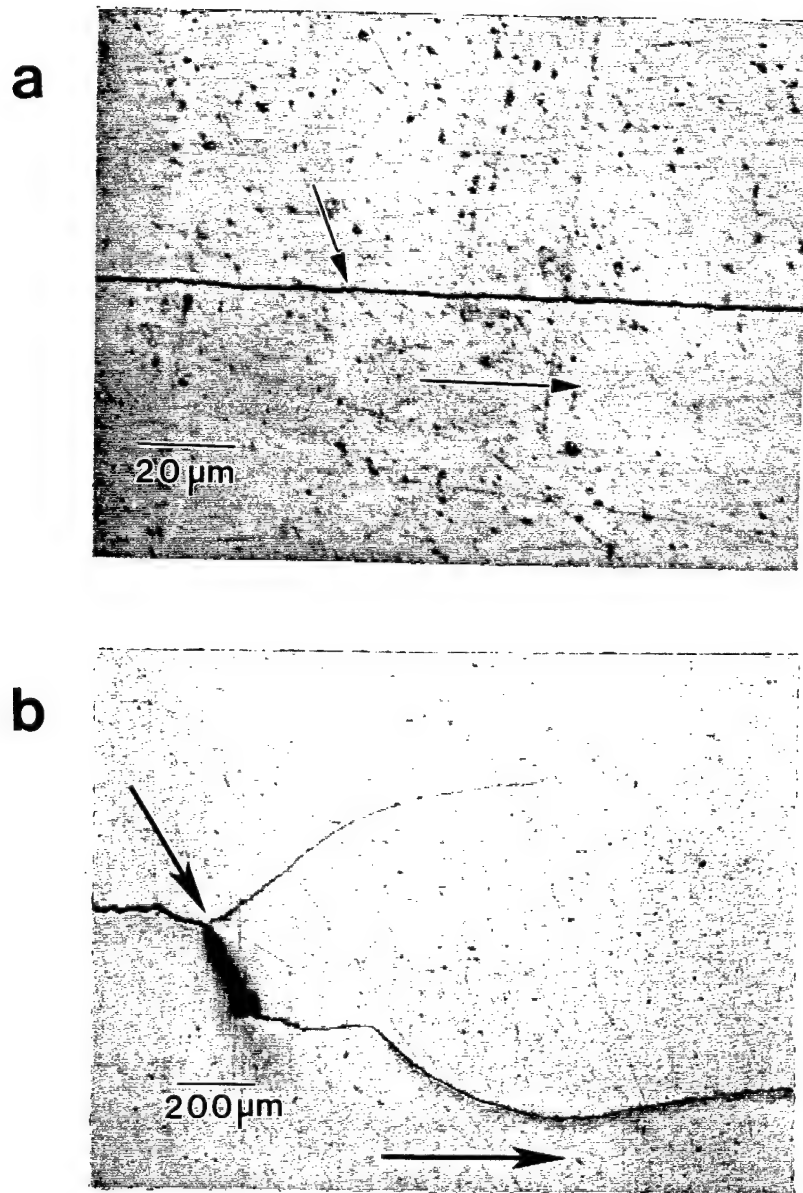
Figure 4.35. Crack profiles at point of overloads in AA5091 at R=0.1: (a) OLR=2, ΔK_B=2.25; (b) OLR=2, ΔK_B=12 (arrows indicate point of overload and direction of growth);
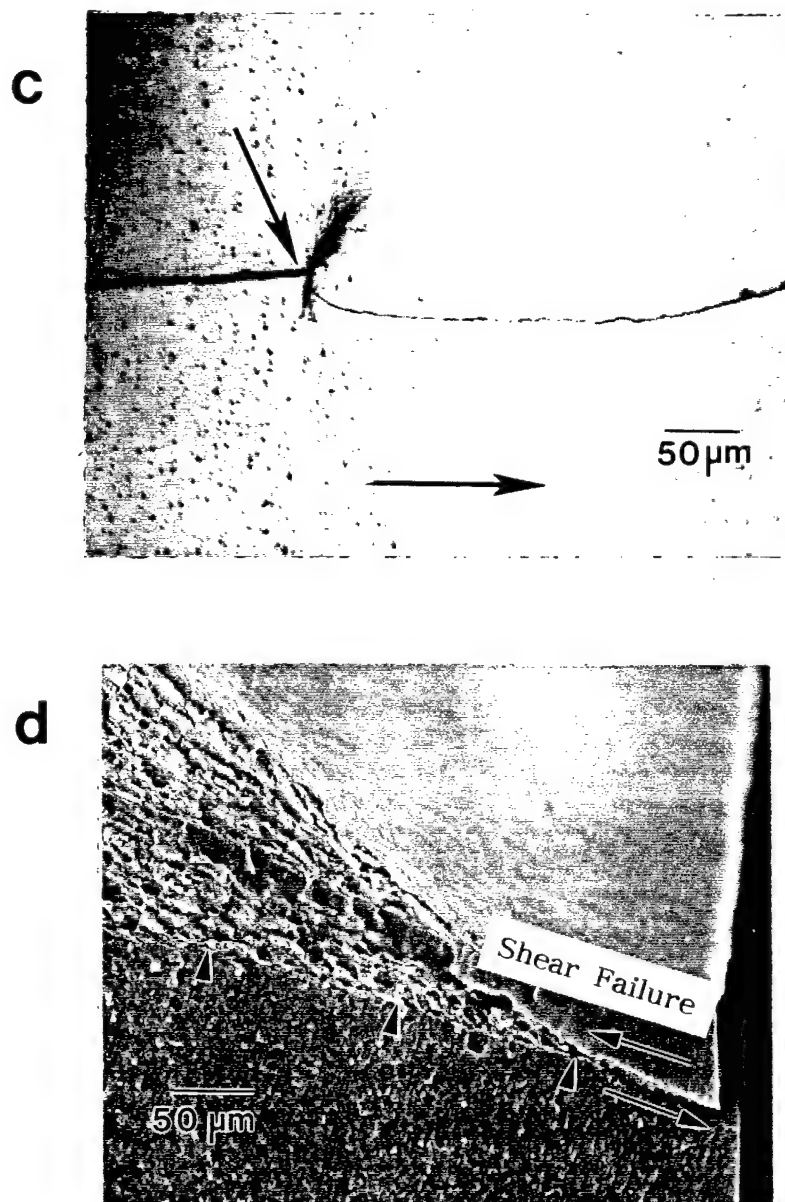
Figure 4.35 (cont'd). (c) OLR=3, ΔK_B=6 MPa$\sqrt{m}$ (arrows indicate point of overload and direction of growth). (d) Shear failure in AA5091 due to through-thickness contraction at R=0.6.
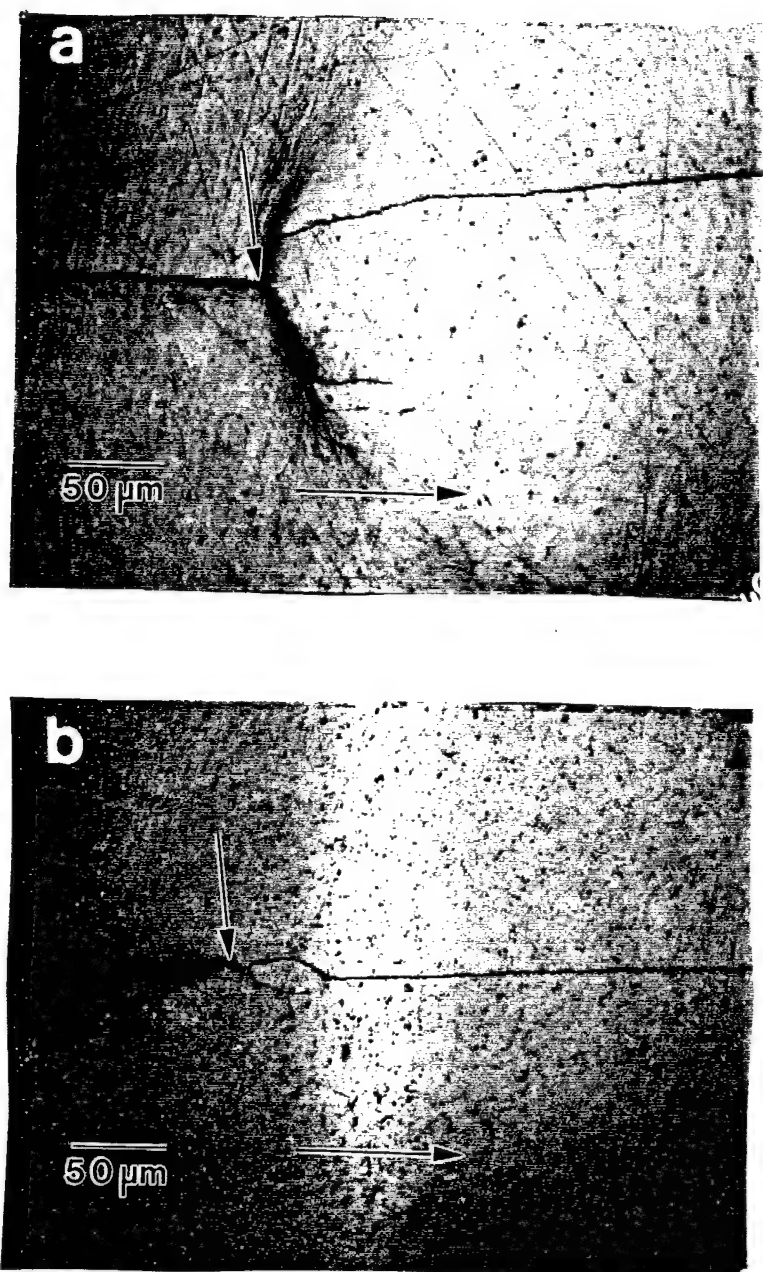
Figure 4.36. Crack profiles at point of overload (OLR=3) in AA5091 for $\Delta K_B=5$, R=0.6: (a) at surface; (b) with 0.125 mm removed (arrows indicate point of overload and direction of growth);
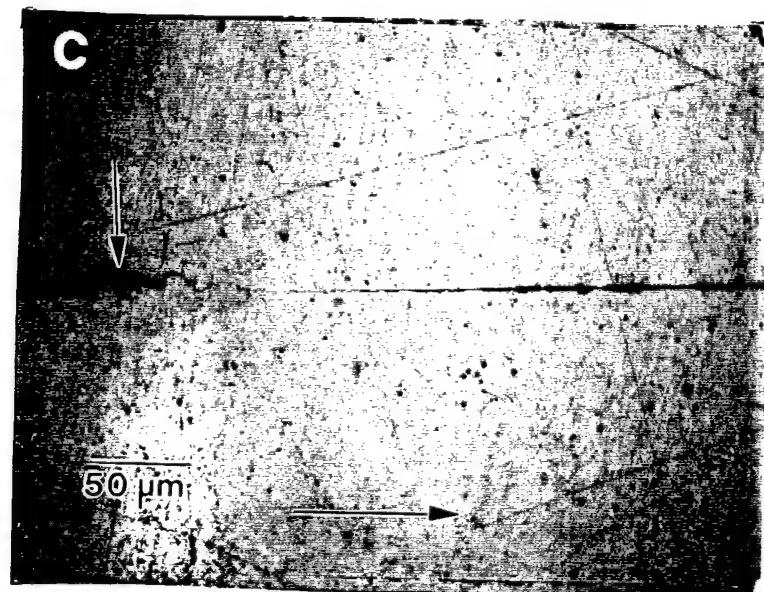
Figure 4.36 (cont'd) (c) with 0.25 mm removed (arrows indicate point of overload and direction of growth).

Table 4.4. Crack Deflection in AA5091

Stress Ratio	OLR	ΔK_B (MPa$\sqrt{m}$)	Deflection? (Yes/No)	Depth of Deflection (μm)
0.1	2.0	1.75 to 2.25 4.0 to 8.0 10.0 12.0	No Yes Yes Yes	0.0 <0.125 0.25-0.50 0.5-0.625
	2.5	3.0 4.0 to 8.0	No Yes	0.0 NM
	3.0	4.0 to 6.0 8.0	Yes Yes	<0.125 0.125-0.250
0.6	1.44	1.75 to 3.0 4.0 to 5.0	No Yes	0.0 NM
	1.66	1.75 to 3.0 4.0 to 5.0	No Yes	0.0 NM
	2.00	1.75 2.25 to 3.0 4.00 to 5.0	No Yes Yes	0.0 <0.125 0.125-0.250

NM= Depth of deflection not measured.

In AA8022, the behavior at low ΔK_B was similar to that in AA5091, i.e., the crack continued to propagate in the original crack plane without deflecting or branching along the shear bands as shown in Figure 4.37(a). At higher ΔK_B, the crack initially continued in the same crack plane without deflecting along the shear bands, but then it curved out-of-plane for some distance before returning to the original crack plane. A typical example of this behavior is shown in Figure 4.37(b). The severity of this behavior increased with increasing ΔK_B and overload magnitude, and was greater at R=0.6 than at R=0.1 for a given overload condition. There was no noticeable difference in the behavior of overload, overload/underload, or underload/overloads for a given overload condition. Examination of crack profiles following a small amount of surface removal revealed that
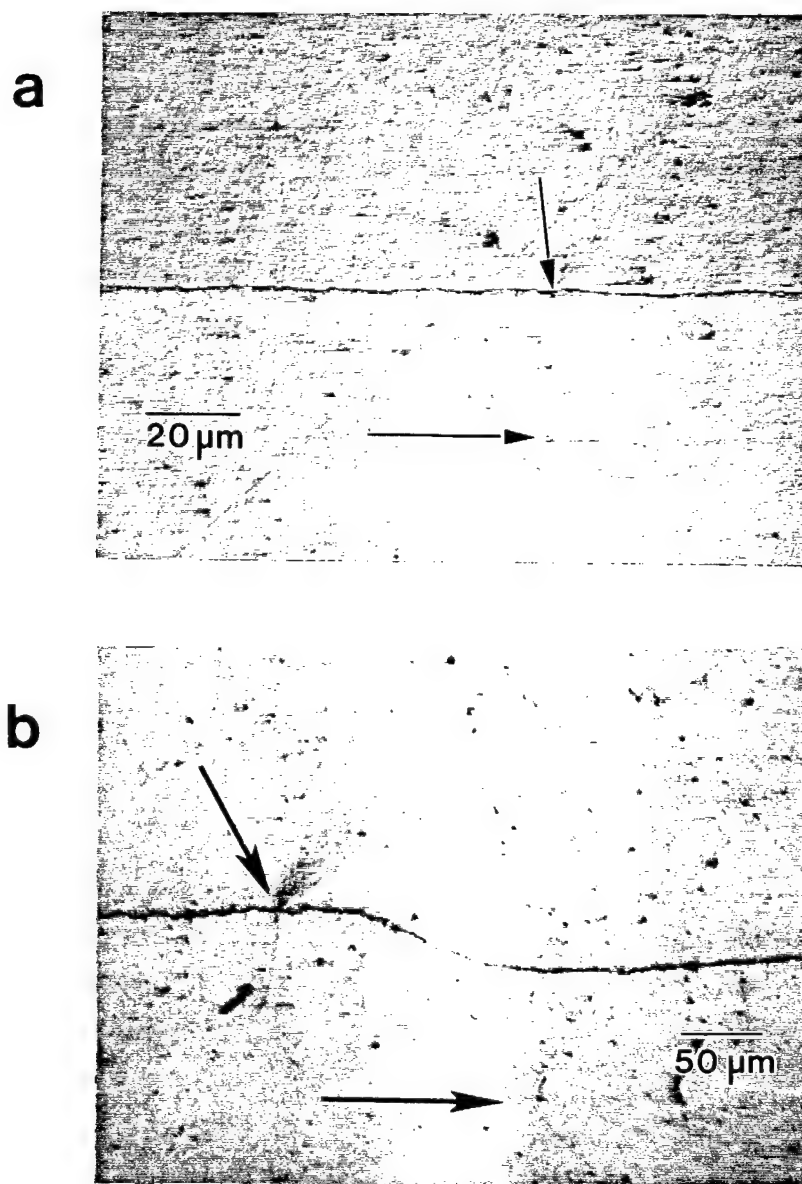
Figure 4.37. Crack profiles at point of overloads (OLR=2) in AA8022 at R=0.1: (a) ΔK_B=3 MPa√m; and (b) ΔK_B=6 MPa√m (arrows indicate point of overload and direction of growth).

shear failure had not occurred along the shear bands in AA8022 as it had in AA5091. Thus, no crack deflection or branching occurred along these bands as it did in AA5091. Surface removal also showed that the out-of-plane curvature was limited to the surface region. Examination of the crack surfaces showed that the curvature was due to an increase in the size of the shear lip at the specimen surfaces in the overload affected region.

4.3.4. Surface Crack Retardation Behavior

The results of the surface crack retardation study are shown in Figures 4.38 and 4.39 for AA8022 and AA5091, respectively. The crack growth rates in these figures were determined using the secant method from visual measurements taken directly from the specimen or from acetate replicas. The purpose of this study was to determine whether retardation at the surface was immediate (i.e., minimum growth rate occurred immediately) or delayed (i.e., minimum growth rate occurred after some increment of growth). The figures show that retardation in both alloys was delayed following all overloads including those that produced crack arrest. A typical example of crack arrest in AA5091 is shown in Figure 4.40. The crack continued to grow following the overload for the first 10,000 cycles as crack growth rates continually decreased. Following this growth, the crack remained virtually arrested for the remaining 1,990,000 cycles.
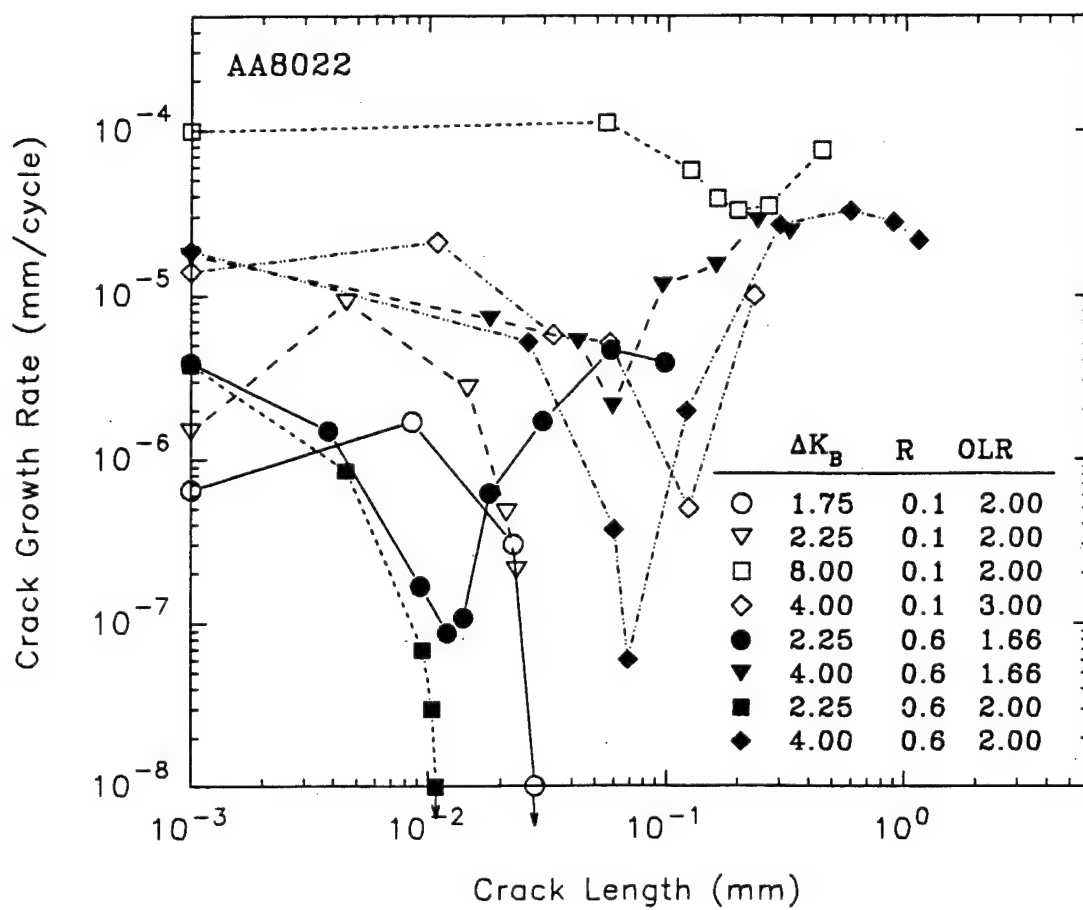
Figure 4.38. Overload response at surface in AA8022 at R=0.1 and 0.6 (overload applied at left axis)
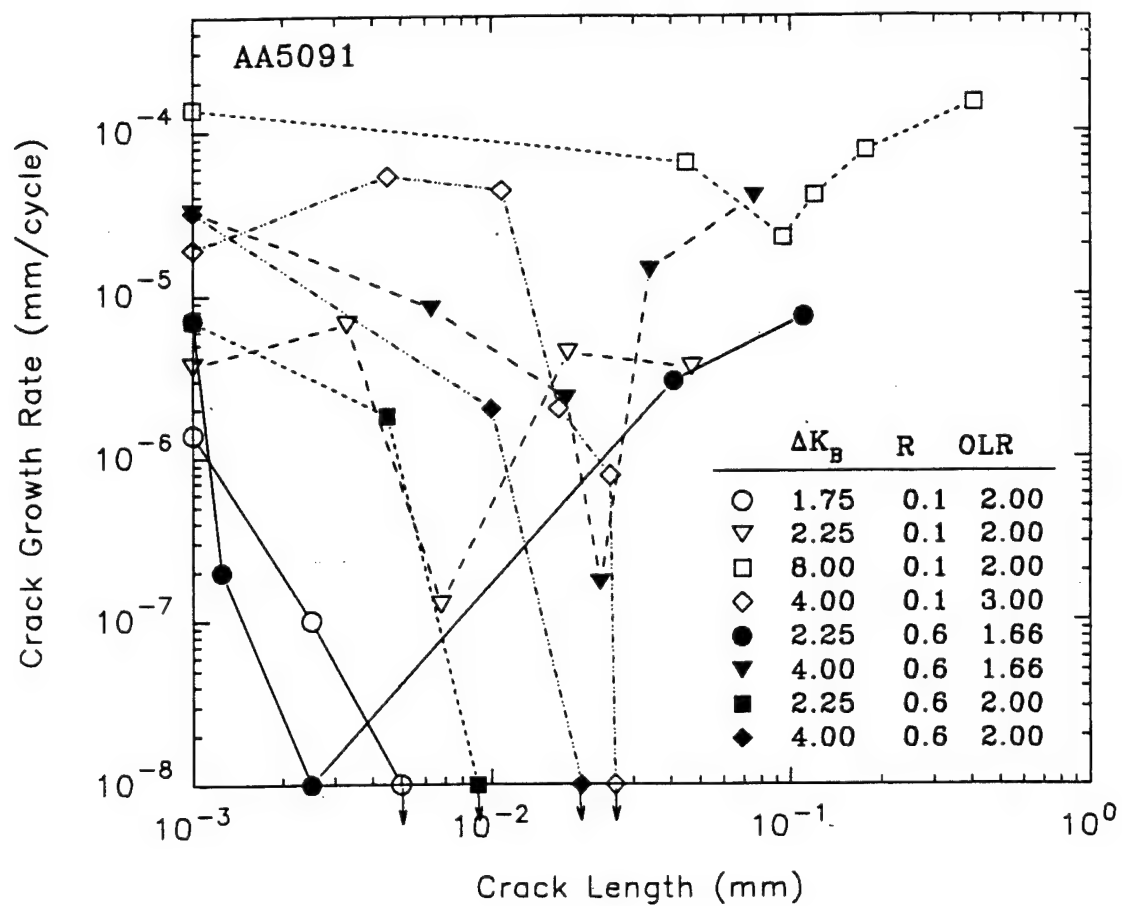
Figure 4.39. Overload response at surface in AA5091 at R=0.1 and 0.6
(overload applied at left axis).
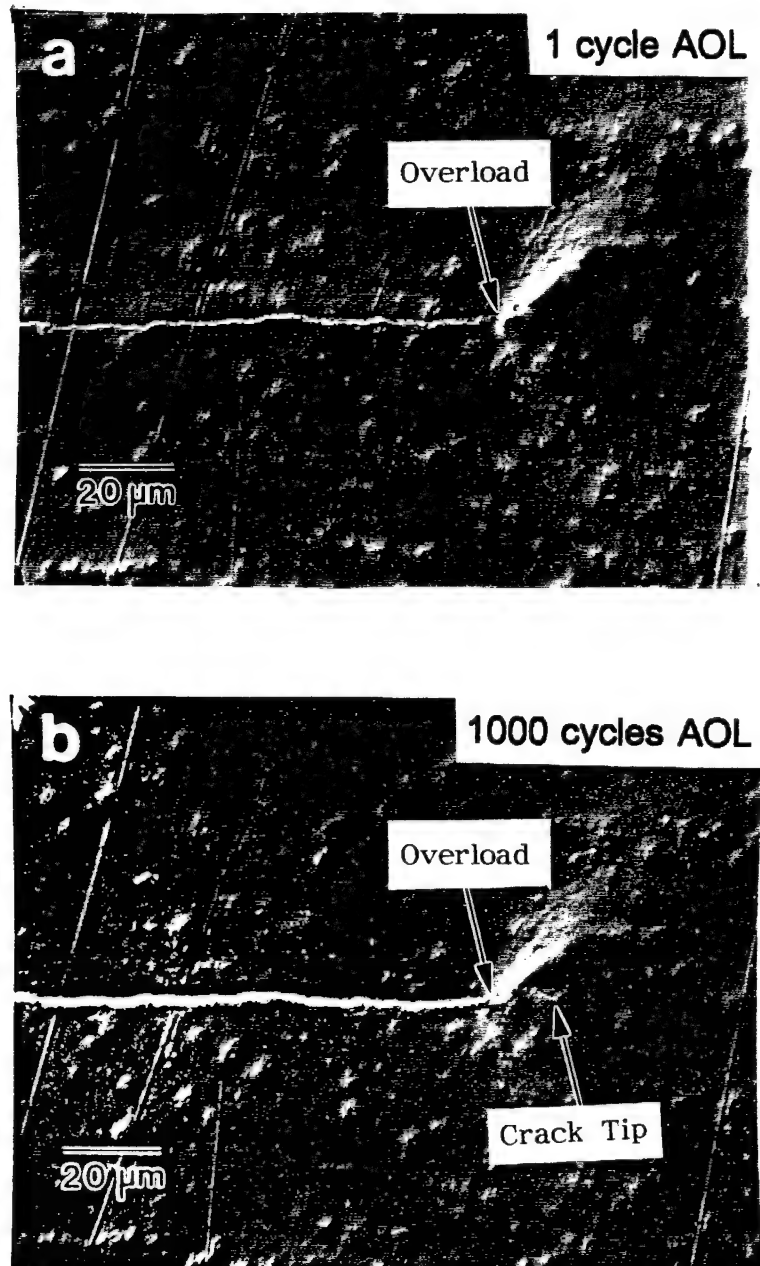
Figure 4.40. Crack profiles showing crack arrest in AA5091 for OLR=3 at $\Delta K_B=4$ MPa$\sqrt{m}$, R=0.1: (a) 1 cycle after overload; (b) 1000 cycles after overload (arrows indicate point of overload and current position of crack tip);
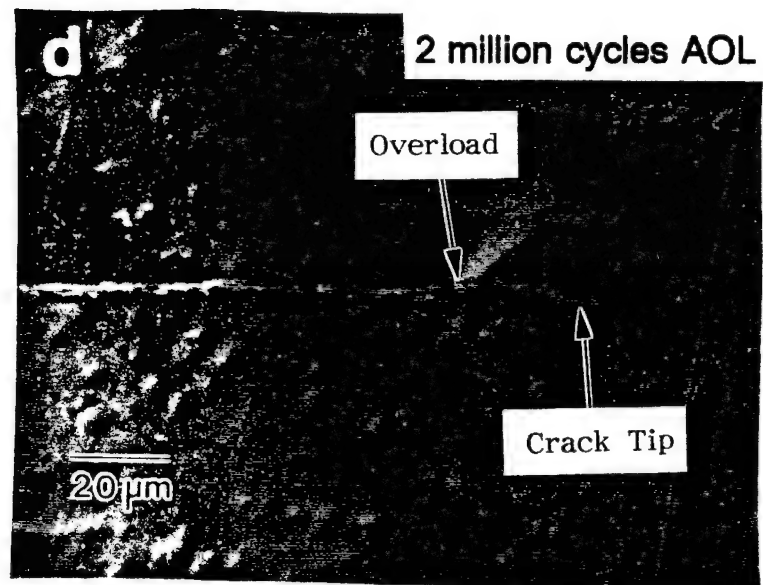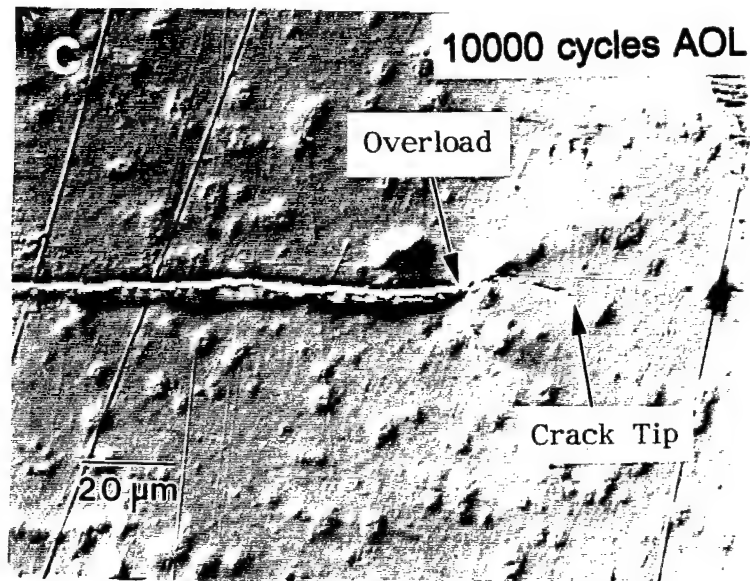
Figure 4.40 (cont'd) (c) 10,000 cycles after overload; and (d) 2 million cycles after overload (arrows indicate point of overload and current position of crack tip).

4.3.5. Effect of Surface Removal

The effect of surface removal immediately following an overload of magnitude OLR=2.0 on N_d and a_{aff} is shown in Table 4.5. In AA5091, N_d was reduced approximately 55% by surface removal at both ΔK_B=2.25 and 10 MPa$\sqrt{m}$. In AA8022, N_d was reduced approximately 90% at ΔK_B=2.25 MPa$\sqrt{m}$. The reduction in N_d in all three cases resulted from a decrease in a_{aff} and a higher $(da/dN)_{min}$ as illustrated by Figure 4.41.

These results indicate that the retardation effect was greater in the surface regions than in the interior region of the specimen. However, significant retardation still occurred in the interior region after the surface region was removed.

Table 4.5. Effect of Surface Removal on Retardation (OLR=2, R=0.1)

Alloy	ΔK_B (MPa$\sqrt{m}$)	No Removal		With Removal	
		N_d	a_{aff} (mm)	N_d	a_{aff} (mm)
AA5091	2.25	90100	0.34	38200	0.216
	10.0	1728	1.41	761	0.770
AA8022	2.25	126900	0.34	14250	0.048

4.3.6. Crack Front Progression Following Overloads

The manner in which the crack front progressed following an overload of magnitude OLR=2.0 at R=0.1 was very similar for both alloys and both ΔK_B. The crack front progression in AA8022 at ΔK_B=4.0 MPa$\sqrt{m}$ is shown in Figure 4.42. The crack front initially progressed faster at
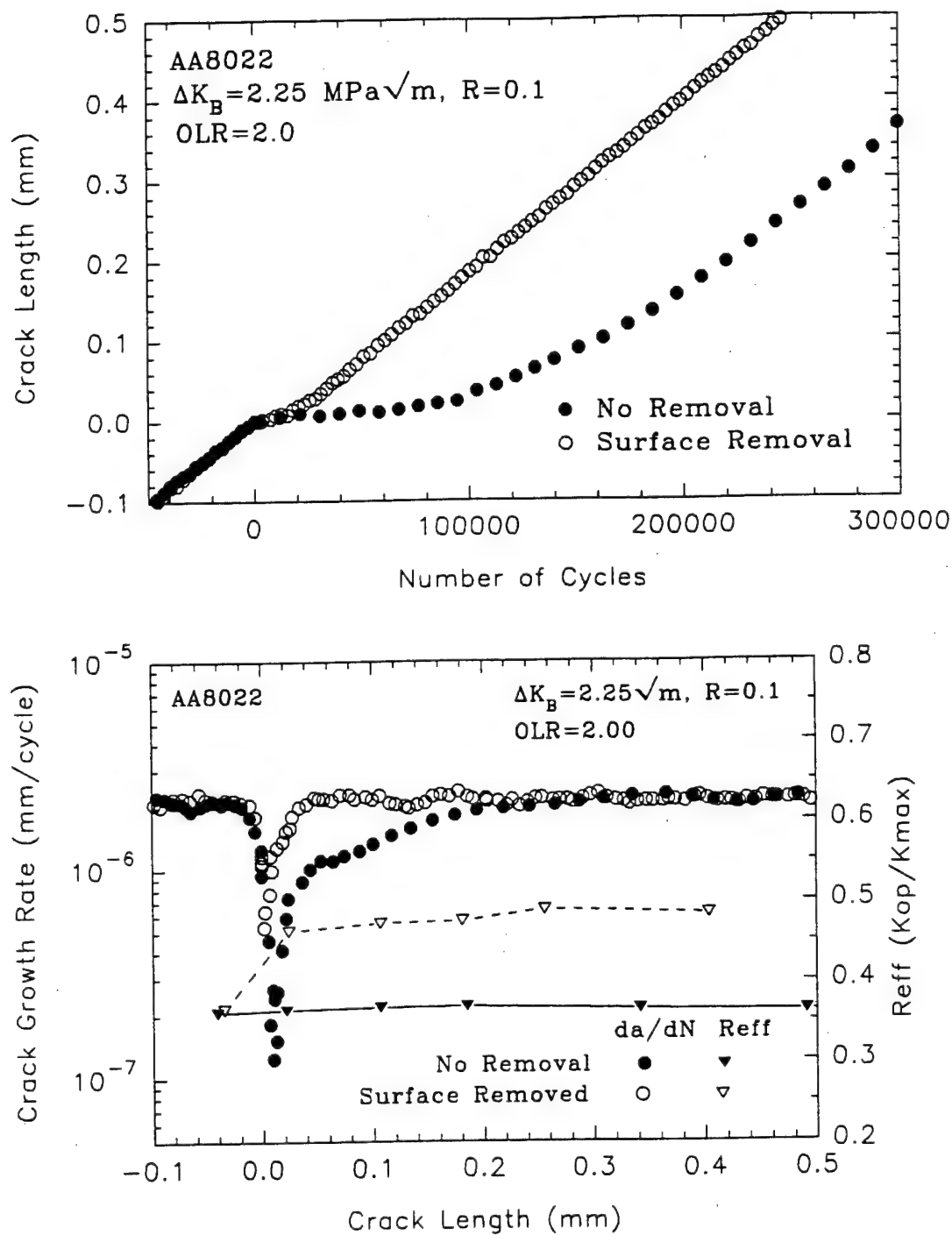
Figure 4.41. Effect of surface removal on overload response (OLR=2) at R=0.1: (a) AA8022 at ΔK_B=2.25 MPa√m;
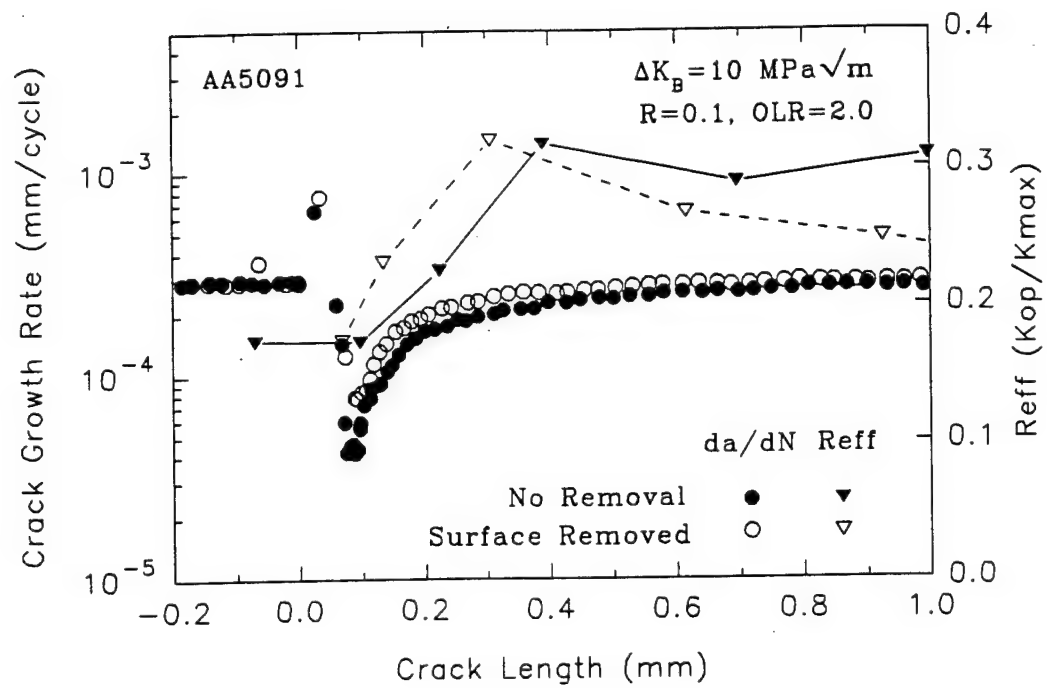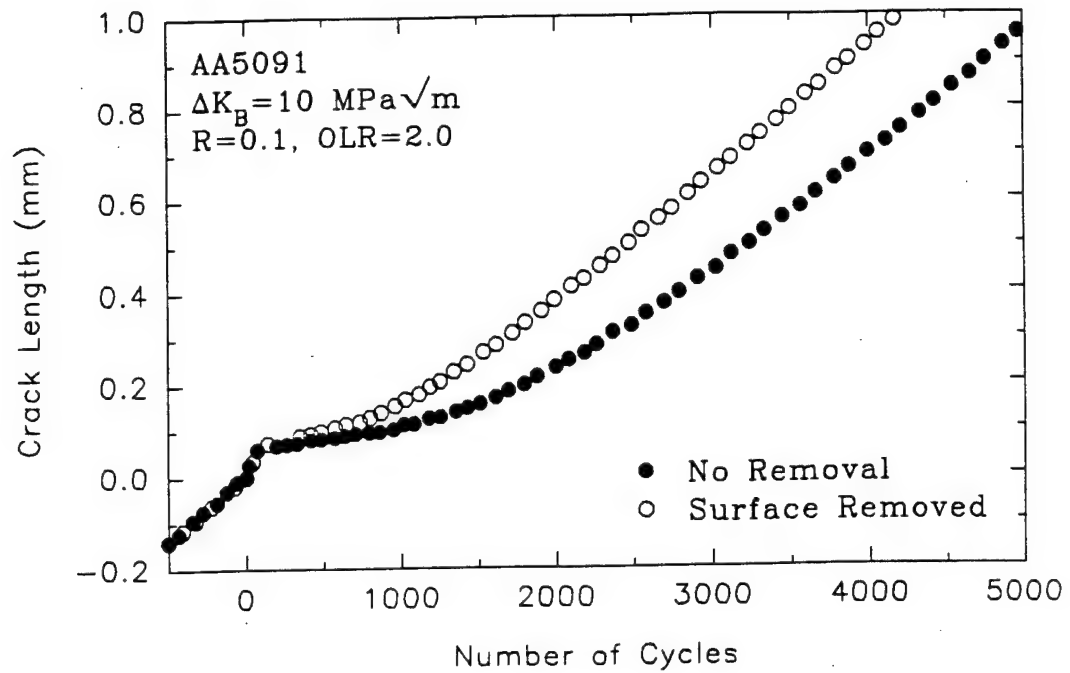
Figure 4.41 (cont'd). (b) AA5091 at ΔK_B=10 MPa$\sqrt{}$m.

the surface than in the interior producing a decrease in crack front curvature near the specimen surface as shown in Figure 4.42(a). The crack then progressed faster in the interior than at the surface producing an increase in crack front curvature (i.e., crack front tunneling) as shown in Figure 4.42(b) and (c). Finally, the crack front progressed faster at the surface than in the interior and eventually assumed the equilibrium baseline curvature as shown in Figure 4.42(d).

The results of all tests at R=0.1 are shown in Figure 4.43. These figures show the increment of post-overload crack extension (Δa) as a function of depth from the specimen surface rather than the absolute position and shape of the crack front. In these plots a straight line represents a crack front with baseline curvature. This method of plotting makes the relative rates of crack propagation in the surface and interior easier to visualize. Only that portion of the crack front from the surface to a depth of approximately B/4 is shown. The remainder of the crack front is not shown because Δa from B/4 to B/2 remained essentially constant, and across the mid-plane (B/2) the crack is approximately symmetric.

The results for OLR=1.66, ΔK_B=4 MPa$\sqrt{m}$ at R=0.6 are shown in Figure 4.44. The behavior was identical to that at R=0.1, except that crack front tunneling occurred to a greater degree. The results at both R=0.1 and 0.6 show that in most cases the equilibrium baseline curvature was not attained until Δa exceeded a_{aff}. In other words, the crack did not attain its equilibrium baseline curvature until some distance after the retardation effect had already ended. Once the baseline curvature was
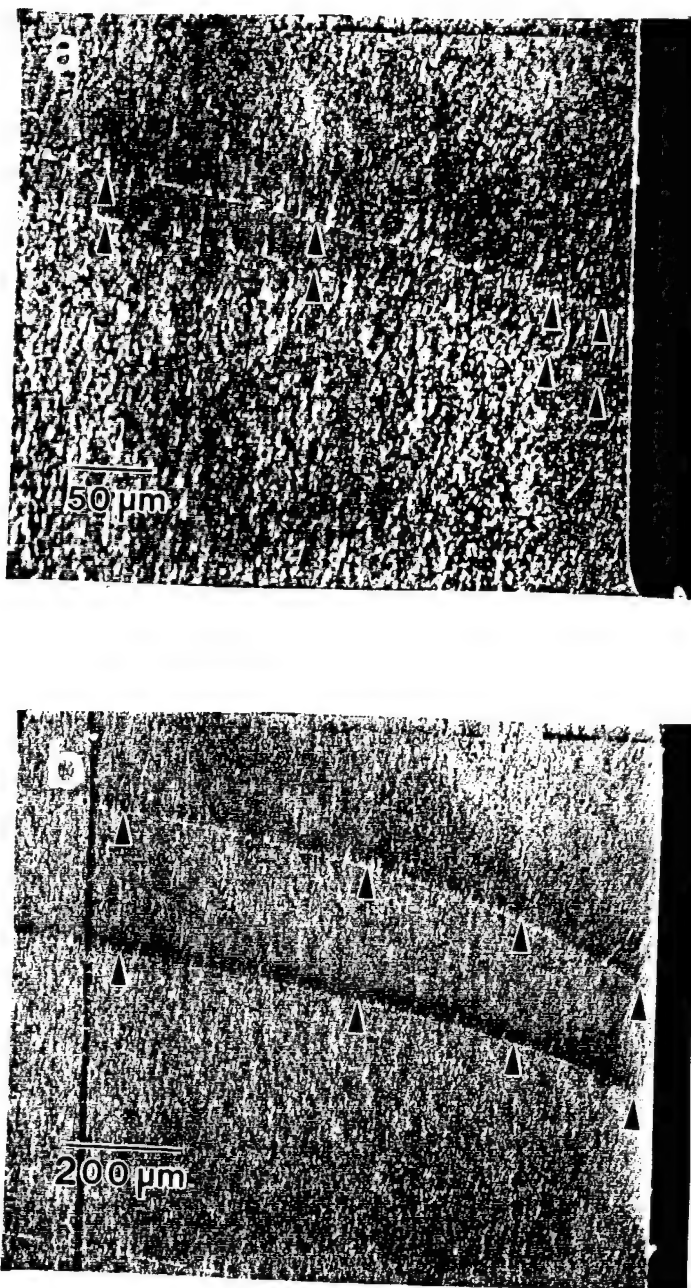
Figure 4.42. Fatigue crack surfaces at showing crack front progression in AA8022 following overload (OLR=2) at ΔK_B=4 MPa$\sqrt{m}$, R=0.1: (a) post-overload growth, Δa_{ol}=0.05a_{aff}; (b) Δa_{ol}=0.5 a_{aff} (arrows indicate crack front position at point of overload and current crack front position);
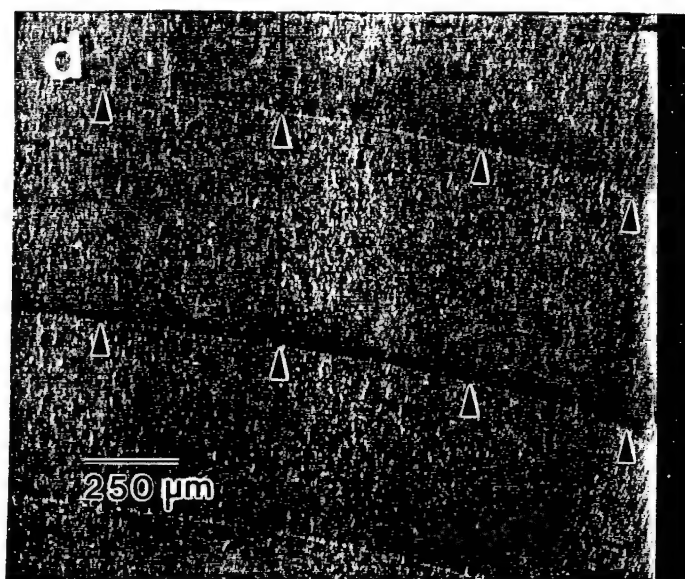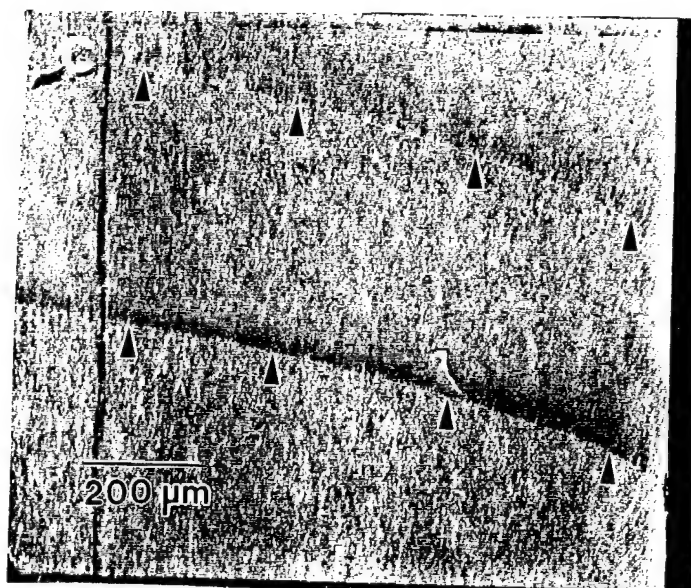
Figure 4.42 (cont'd). (c) $\Delta a_{ol} = a_{aff}$; (d) $\Delta a_{ol} = 1.35 a_{aff}$ (arrows indicate crack front position at point of overload and current crack front position).
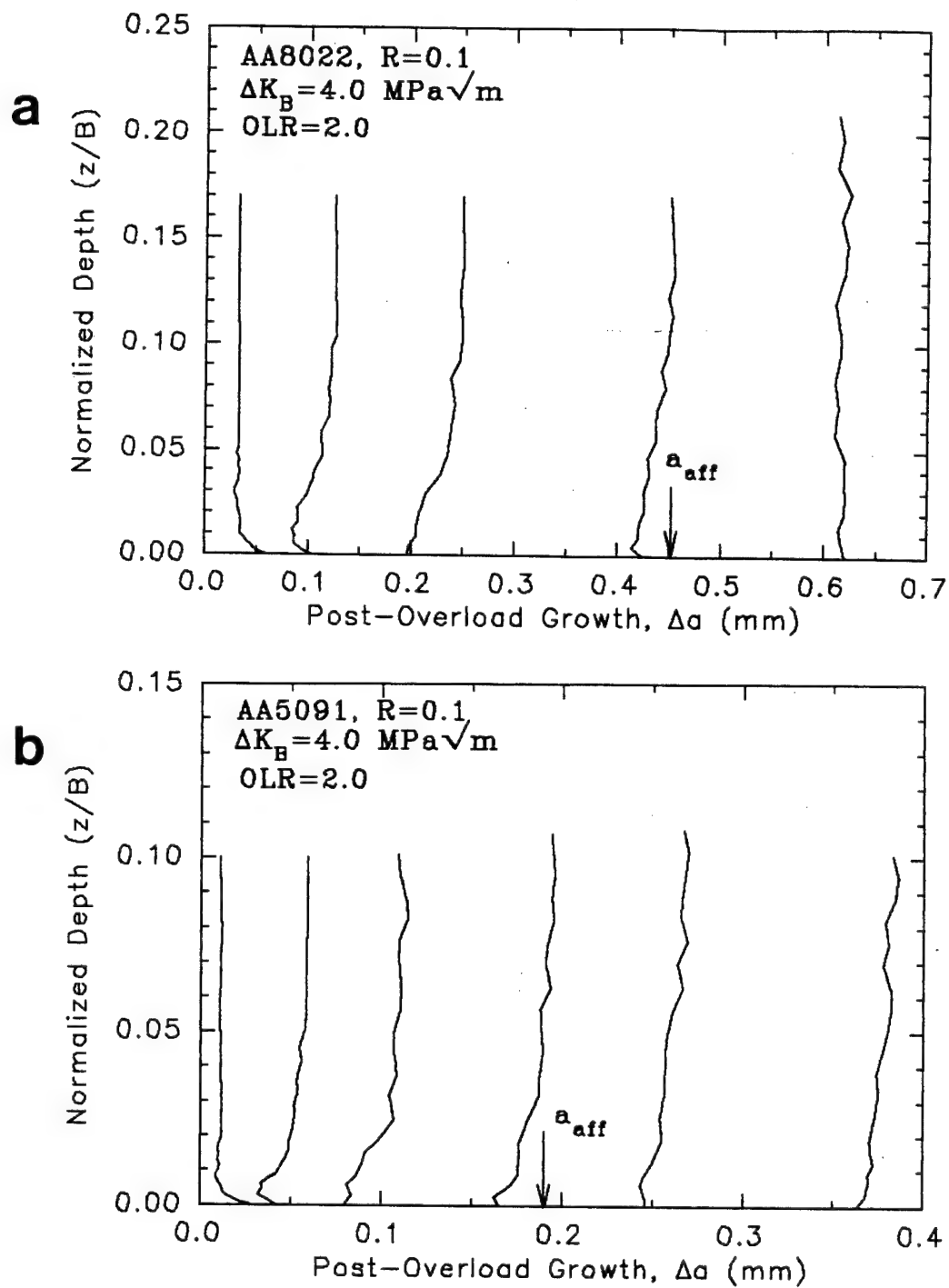
Figure 4.43. Crack front progression following overload (OLR=2) at R=0.1:
(a) AA8022, ΔK_B=4 MPa$\sqrt{m}$; (b) AA5091, ΔK_B=4 MPa$\sqrt{m}$;
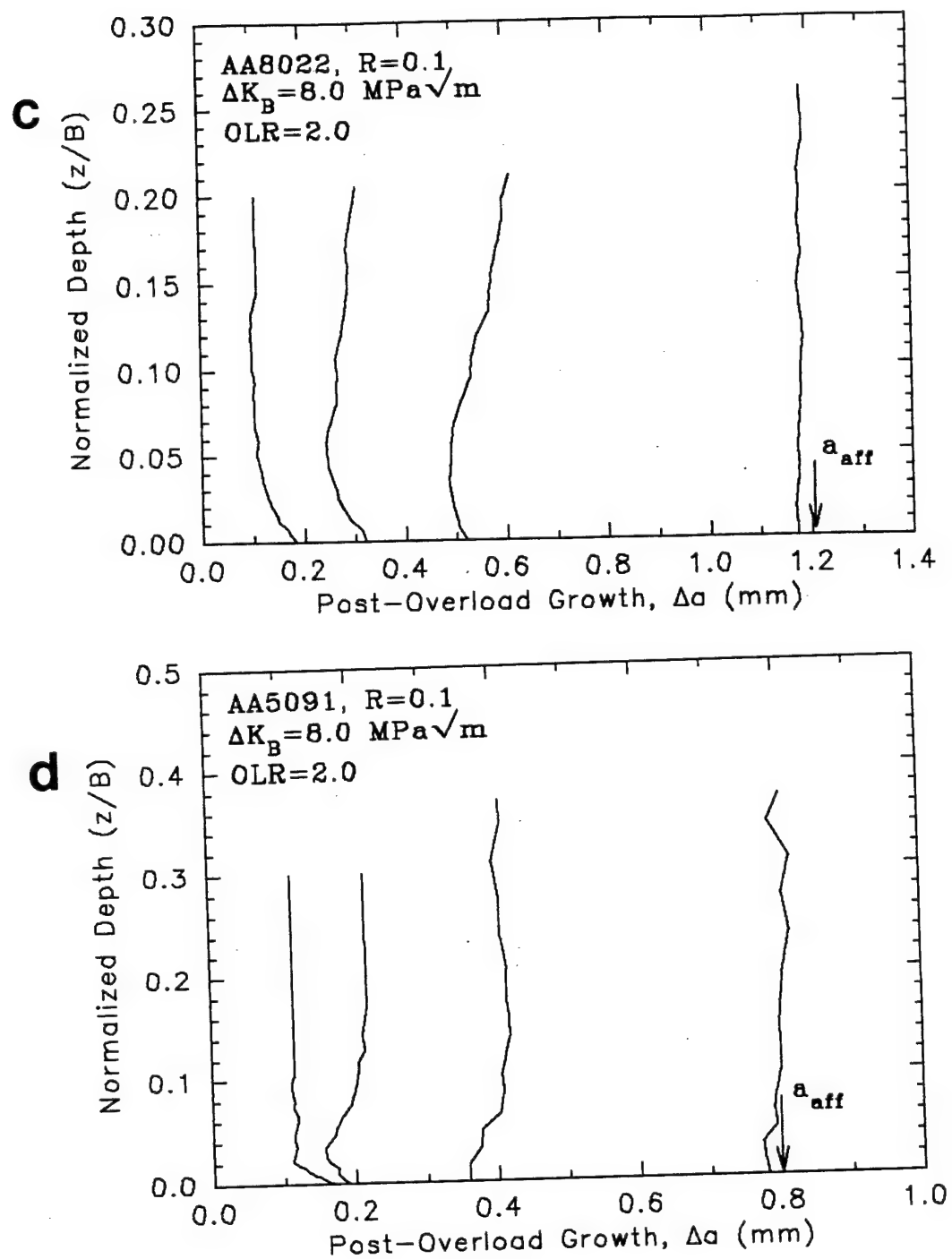
Figure 4.43 (cont'd)   (c) AA8022, ΔK_B=8 MPa√m; (d) AA5091, ΔK_B=8 MPa√m.
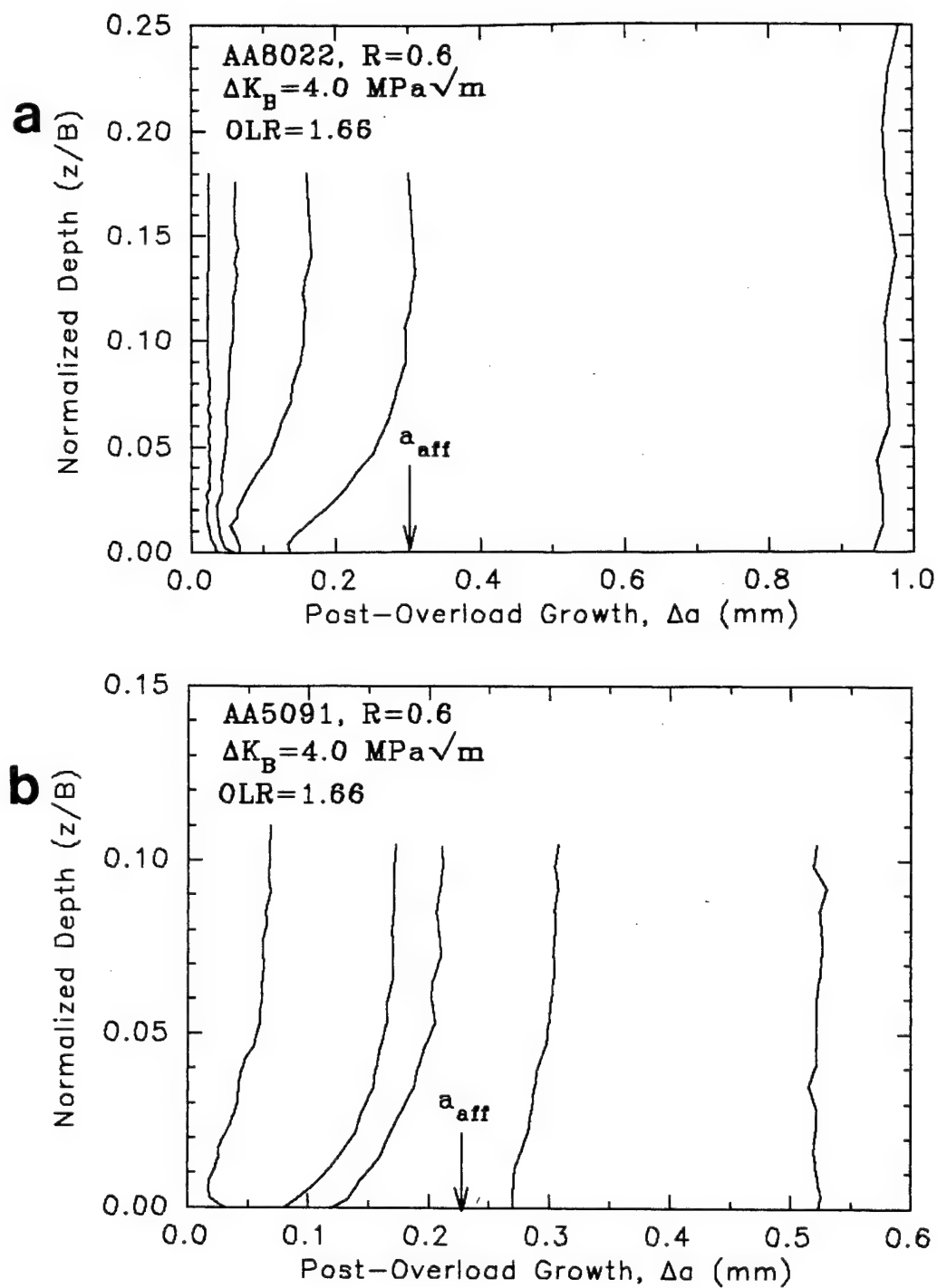
Figure 4.44. Crack front progression following overload (OLR=1.66) at ΔK_B=4 MPa$\sqrt{m}$, R=0.6: (a) AA8022; (b) AA5091.

achieved the crack growth rate was again constant across the entire crack front.

The observations in the crack front progression experiments are supported by compliance and surface crack length measurements obtained for OLR=1.66, ΔK_B=4 MPa$\sqrt{m}$, at R=0.6 shown in Figure 4.45. The compliance measurement represents the average through thickness crack length. In these thick specimens (B=8 mm) it is more representative of the behavior in the interior than at the surface since the interior comprises a greater portion of the crack front. The surface measurement reveals the behavior only at the specimen surface. After 5000 post-overload cycles the compliance measurement indicated the interior crack front was beginning to advance at a significant rate while the surface measurement indicated the surface crack front was still significantly retarded. After 10000 cycles the surface crack front began to grow at a significant rate. At this point the compliance measurement indicated that, on average, the crack front was already growing at the baseline rate. For the next 7000 cycles the surface crack front grew at a rate faster than the baseline rate. After 17000 post-overload cycles the surface and compliance measurements were in agreement indicating that the crack growth rate was again constant across the entire crack front.

4.3.7. Effect of Elevated Temperature Exposure

The effect of elevated temperature exposure immediately following overloads on the number of delay cycles is shown in Table 4.6. Overloads of magnitude OLR=3.0 at ΔK_B=4 MPa$\sqrt{m}$, R=0.1 without exposure produced
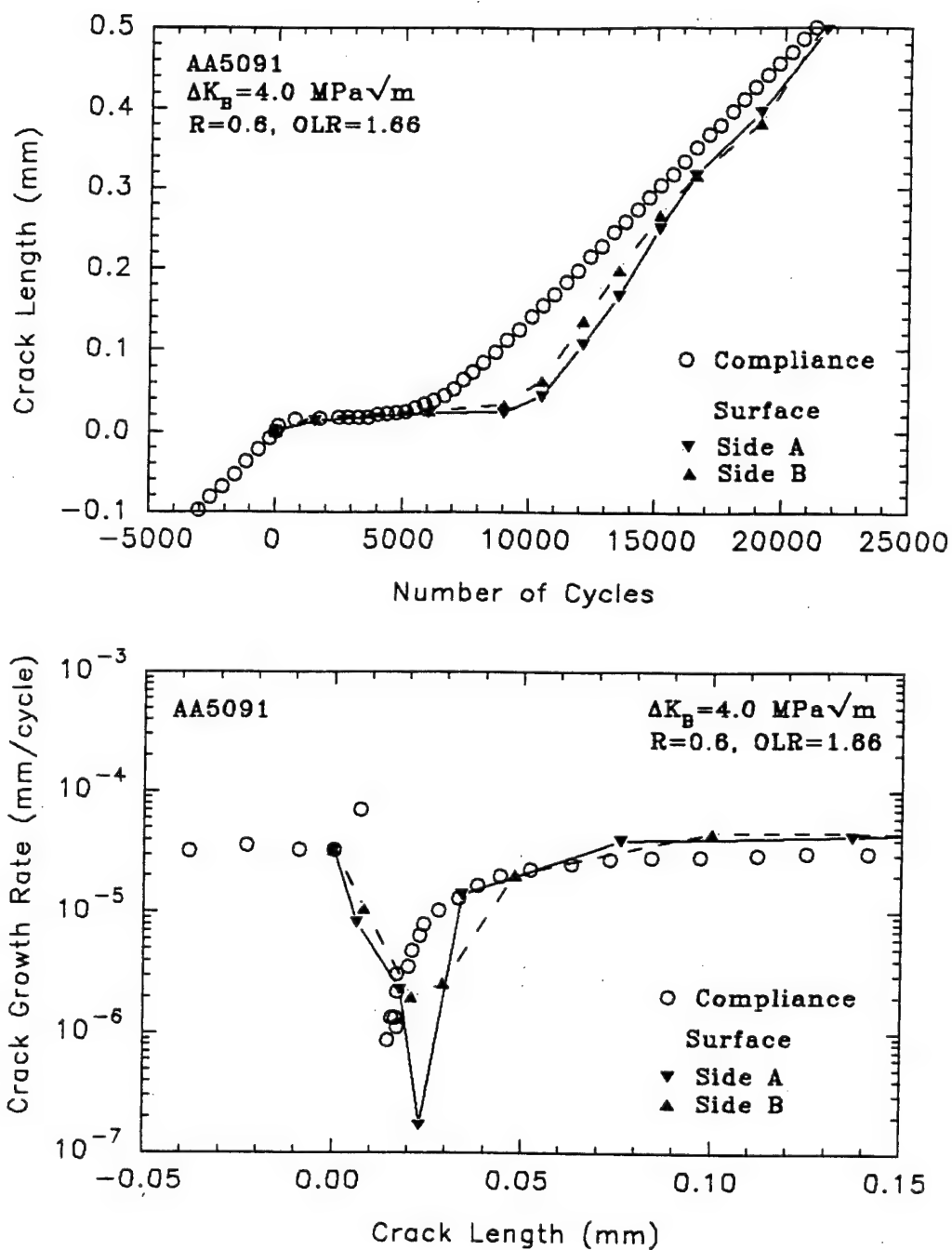
Figure 4.45. Comparison of overload response (OLR=1.66) at R=0.6 based on surface and compliance measurements.

complete crack arrest (i.e., $N_d > 10^6$). N_d was significantly reduced by subsequent elevated temperature exposure. The reduction resulted from an increase in $(da/dN)_{min}$ with increasing temperature and a decrease in a_{aff} as shown in Figure 4.46. The reduction in N_d was much larger in AA5091 than in AA8022. The retardation effect in AA5091 was nearly eliminated after exposure at 225°C, while a relatively small N_d still existed in AA8022 after exposure at 300°C.

For an overload of magnitude OLR=2.0 at ΔK_B=10 MPa√m, R=0.1 the retardation effect was completely eliminated following exposure at 275°C as shown in Figure 4.47. In this case, the overload had produced significant crack deflection extending to a depth of 0.25 to 0.5 mm.

Table 4.6. Effect of Elevated Temperature Exposure on Retardation

Alloy	ΔK_B (MPa√m)	OLR	Exposure Temp.(°C)	N_d	a_{aff} (mm)
AA8022	4.0	3.0	None 150 225 300	$>10^6$ 60200 28600 3320	Arrest 0.65 0.74 0.40
AA5091	4.0	3.0	None 100 150 225	$>10^6$ 6140 3210 135	Arrest 0.30 0.27 0.14
	10.0	2.0	None 250	2210 0	0.68 0
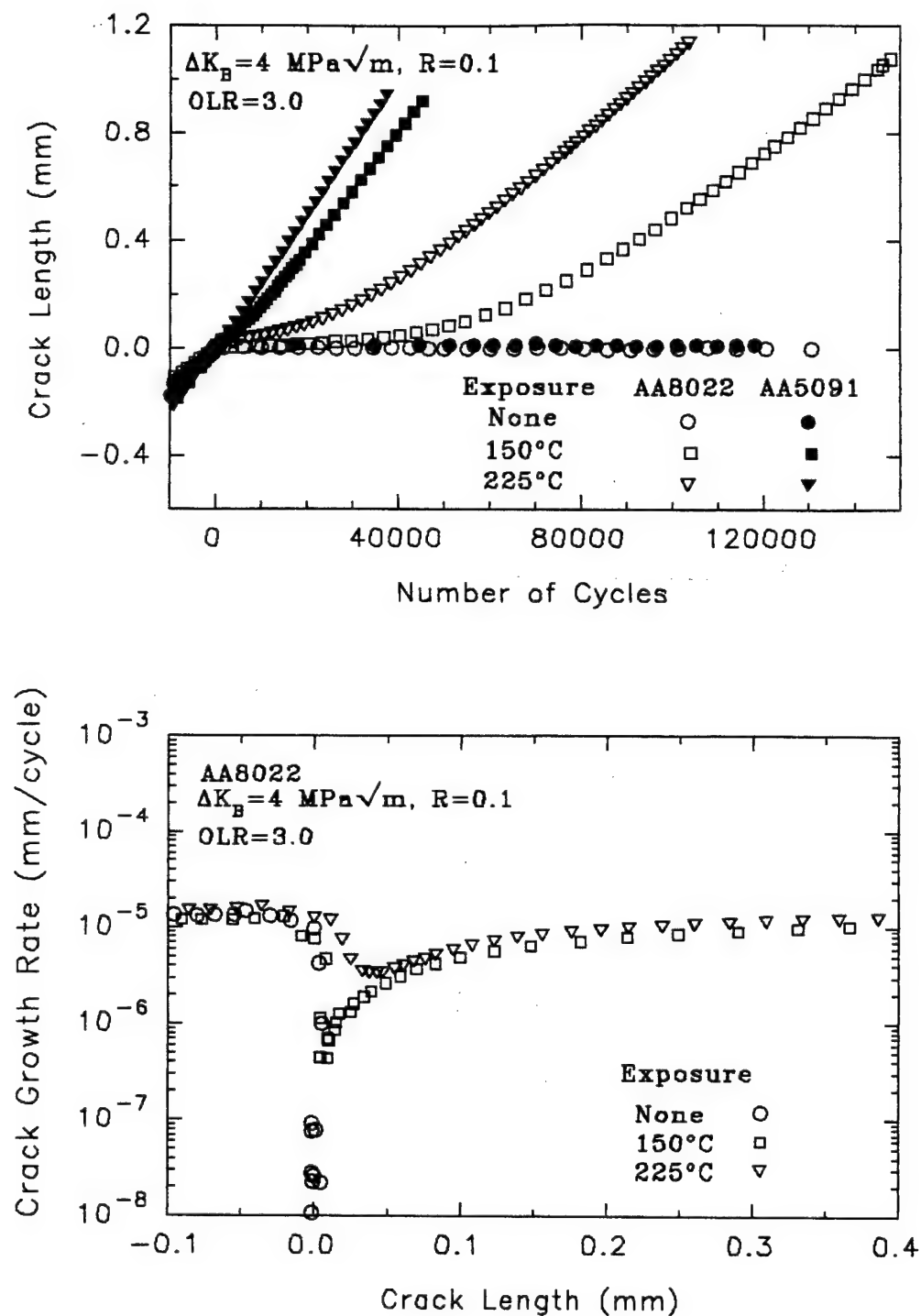
Figure 4.46. Effect of elevated temperature exposure on overload response (OLR=3) at R=0.1 of AA8022 and AA5091, ΔK_B=4 MPa√m.
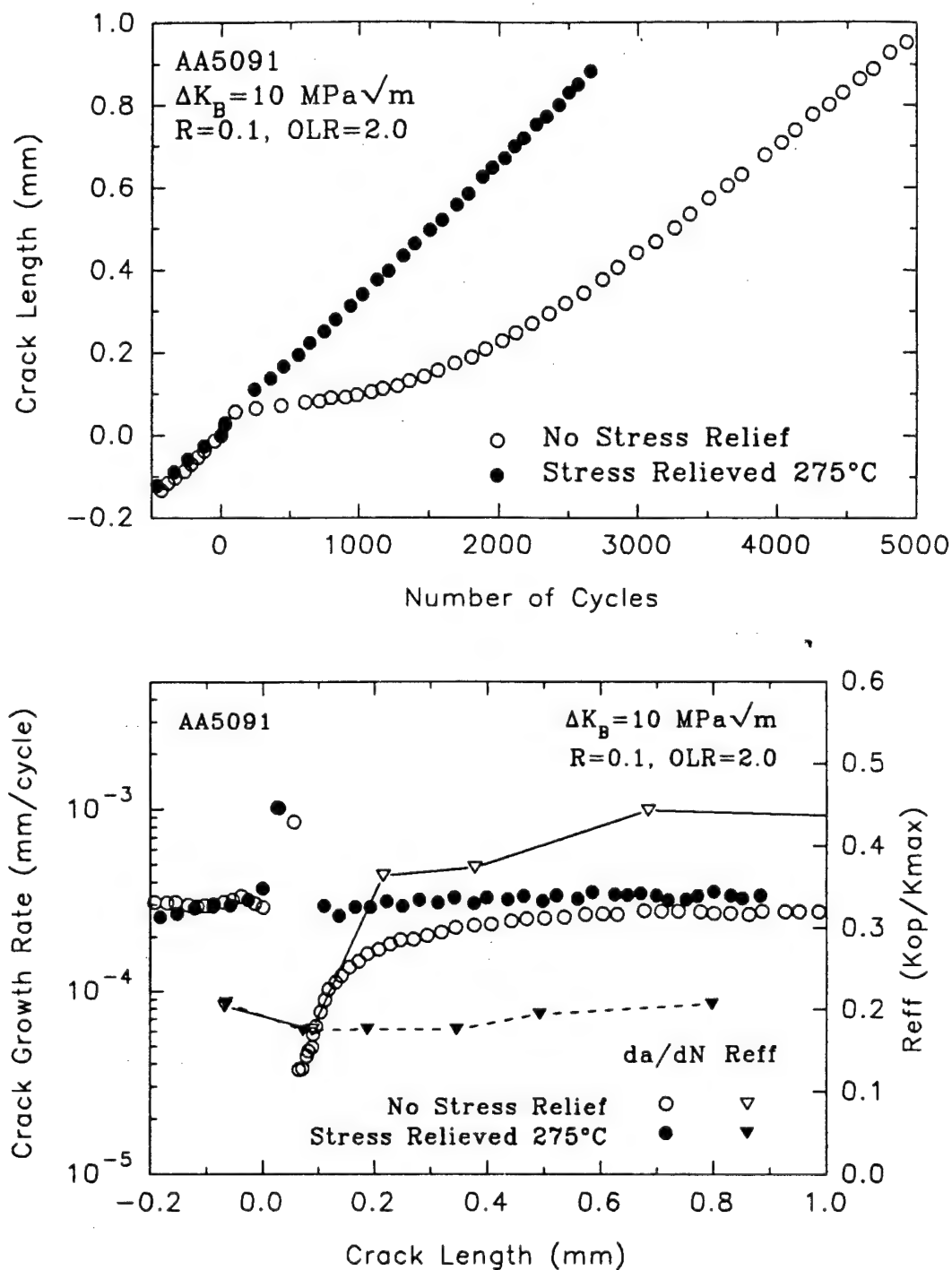
Figure 4.47. Effect of elevated temperature exposure on overload response (OLR=2) at R=0.1 of AA5091, ΔK_B=10 MPa√m.

4.3.8.   Residual Strains at the Crack Tip

The results of the residual crack tip strain experiment are shown in Table 4.7.   The strain was measured in the following sequence: K_{min}, K_{max}, K_{ol}, K_{min}, K_{ul}, and again at K_{min}.   This allowed the determination of the average residual strain within the strain gage at K_{min} following an overload and the change in residual strain resulting from a subsequent underload.   At R=0.1, an overload of magnitude OLR=3.0 at ΔK_B= 4.0 MPa$\sqrt{m}$ increased the strain measured at K_{min} 100% in AA5091 and 440% in AA8022. A subsequent underload of magnitude ULR*=2.5 produced only a small change in strain at K_{min} in both alloys.   At R=0.6, an overload of magnitude OLR=2.0 increased the strain measured at K_{min} approximately 40% in AA5091 and 90% in AA8022.   Following an underload of magnitude ULR=2.5*, the increase in strain resulting from the overload was reduced from 40% to 25% in AA5091 and from 90% to 75% in AA8022.   These results are qualitative since they represent the average strain across the gage area and not the strain directly at the crack tip.   However, they indicate that the overload produced a residual tensile strain in front of the crack tip at both R=0.1 and 0.6.   A subsequent underload did not significantly change the residual strain at R=0.1, but significantly reduced the residual strain at R=0.6.

Table 4.7. Results of Residual Strain Experiments

Baseline Conditions	OLR	Position in Sequence	Strain (µε)	
			AA5091	AA8022
R=0.1 ΔK_B=4.0 MPa√M	3.0	K_{min} K_{max} K_{ol} K_{min} K_{ul} K_{min}	13 320 969 26 -25 28	30 343 1240 132 107 125
R=0.6 ΔK_B=4.0 MPa√m	2.0	K_{min} K_{max} K_{ol} K_{min} K_{ul} K_{min}	471 815 1961 657 151 592	389 675 1803 737 246 678

The increase in residual strain following an overload occurs because the increase in plastic strain resulting from an overload is not totally reversible as discussed previously in Section 2.3.2.e. The increase in plastic strain ahead of the crack tip is evident in the crack profiles of Figure 4.35(b). The crack is more fully open behind than in front of the point of overload application due to the increase in plastic strain resulting from the overload. The increase in plastic strain also produces crack tip blunting. The strain readings indicate the residual plastic strain resulting from an overload is significantly reduced by a subsequent underload at R=0.6 but not at R=0.1.

4.3.9. FASTRAN Predictions

The FASTRAN-II program is a fatigue crack growth program based on plasticity-induced closure. Thus, the ability or inability of this program to model or predict the trends observed in the fatigue crack propagation overload tests provide an indicator of whether the plasticity-induced closure mechanism is contributing to retardation in these alloys. The experimental results and FASTRAN predictions for R=0.1 are compared in Figure 4.48. There is generally good agreement between trends in the FASTRAN predictions and those in the experimental results. FASTRAN predicts that N_d increases with decreasing ΔK_B, as was observed experimentally. FASTRAN also predicts that N_d increases with increasing OLR. This increase resulted from a decrease in $(da/dN)_{min}$ and an increase in a_{aff} as shown in Figure 4.49, just as it did experimentally (compare Figure 4.14). The quantitative agreement between the experimental results and FASTRAN predictions was better in AA8022 than in AA5091. The FASTRAN predictions for AA8022 generally agreed with the experimental results over the whole range of ΔK_B for all three overload ratios. For AA5091 at OLR=2.0, the agreement was good at low ΔK_B, but at higher ΔK_B, FASTRAN predicted a continued decrease in N_d, while experimentally N_d increased again at high ΔK_B. At OLR=3.0, FASTRAN significantly underestimated N_d in AA5091.

The experimental results and FASTRAN predictions at R=0.6 are compared in Figure 4.50. Again there is good agreement between the trends observed in the FASTRAN predictions and in the experimental results. N_d increases with decreasing ΔK_B and with increasing OLR. The
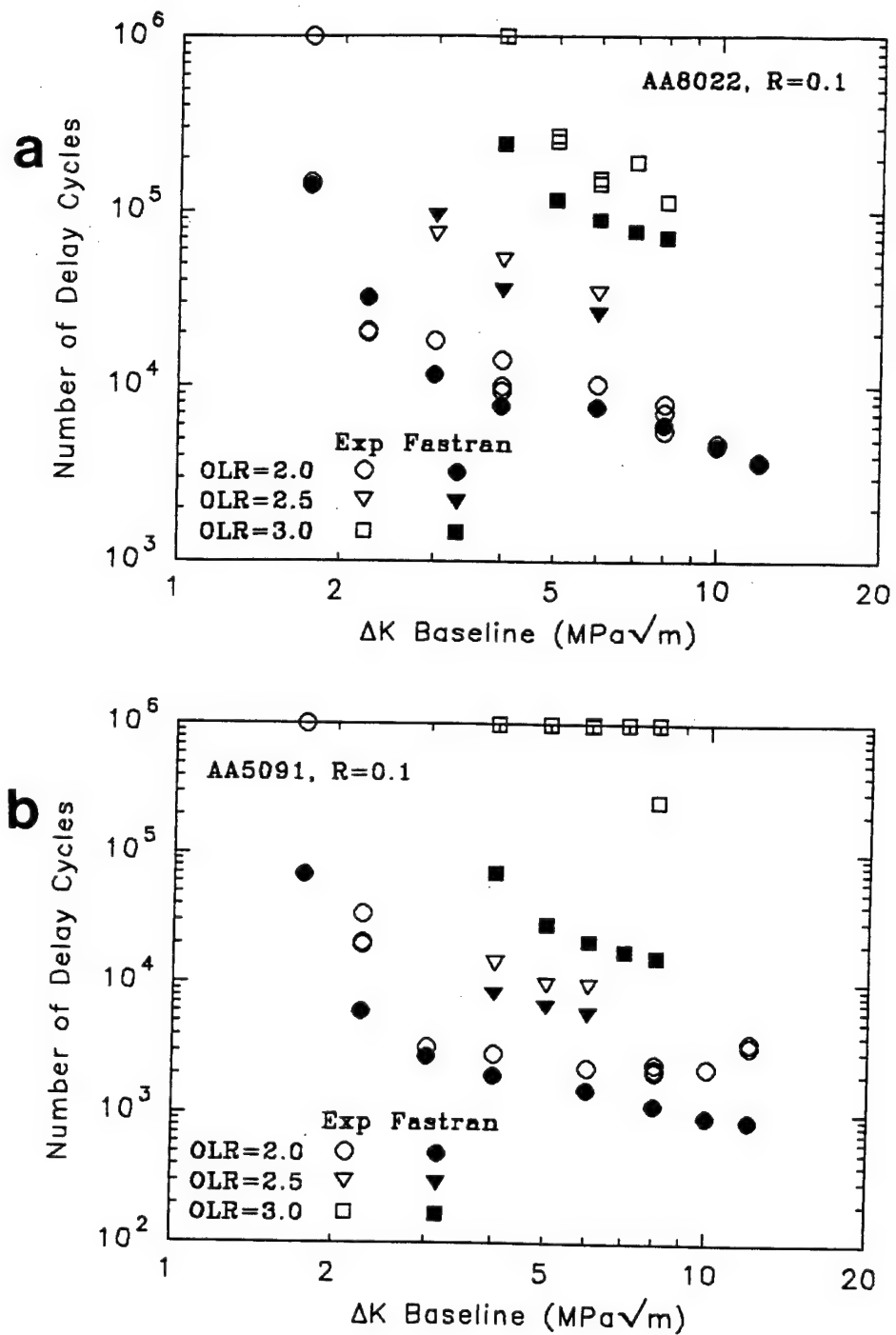
Figure 4.48. Comparison of FASTRAN prediction and experimental retardation magnitude at R=0.1: (a) AA8022; and (b) AA5091.
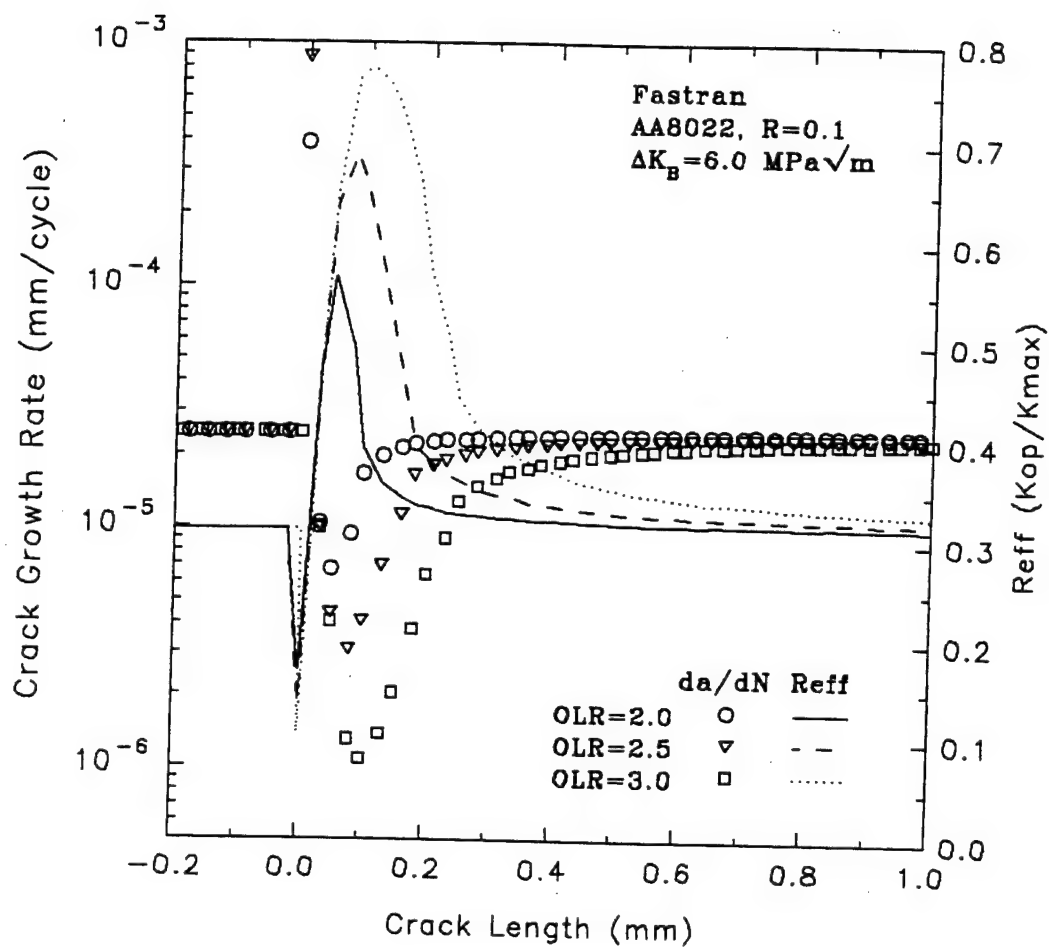
Figure 4.49. FASTRAN predicted effect of overload magnitude on overload response in AA8022 at ΔK_B=6 MPa$\sqrt{m}$, R=0.1.
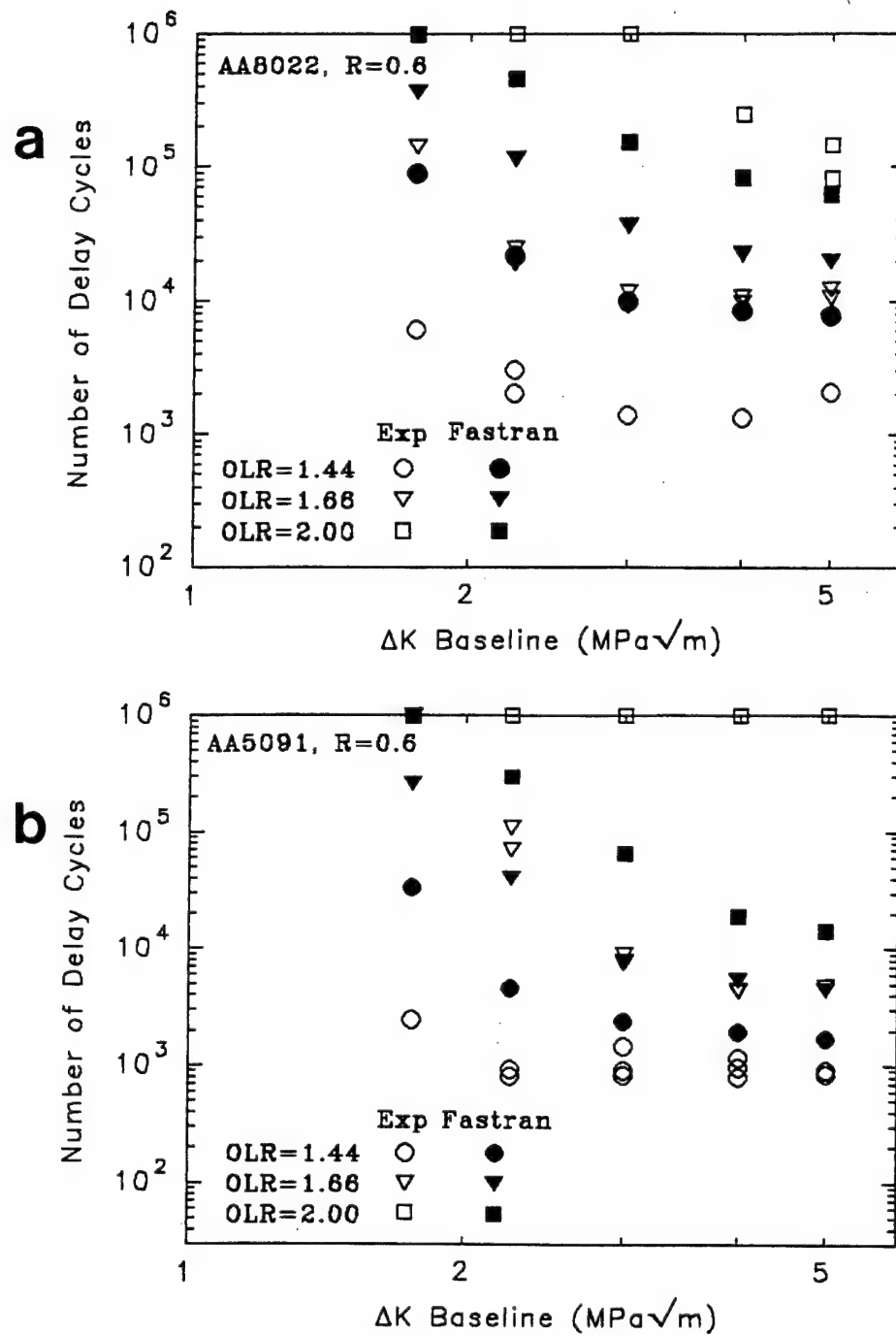
Figure 4.50. Comparison of FASTRAN prediction and experimental retardation magnitude at R=0.6: (a) AA8022; and (b) AA5091.

latter effect again results from a decrease in $(da/dN)_{min}$ and an increase in a_{aff}. However, the quantitative agreement was not as good as at R=0.1. FASTRAN significantly overestimates N_d at OLR=1.44 and underestimates N_d at OLR=2.0. Experimentally, it was observed that for an equivalent OLR, N_d was greater at R=0.6 than at R=0.1. This was a consequence of a lower $(da/dN)_{min}$ and a larger a_{aff} (see Figure 4.30). This same behavior was predicted by FASTRAN as shown in Figure 4.51.

The FASTRAN predictions for AA8022 and AA5091 at R=0.1 and 0.6 are compared in Figure 4.52. The predicted N_d is always larger in AA8022 than in AA5091 for a given ΔK_B and OLR. This results from a lower $(da/dN)_B$ and a larger a_{aff} as shown in Figure 4.53. FASTRAN predicts a larger a_{aff} for the lower strength AA8022 because a_{aff} is proportional to overload plastic zone size which increases with decreasing yield strength. FASTRAN predicts that yield strength does not have a significant effect on the maximum post-overload closure levels. Thus, FASTRAN predicts that yield strength most strongly influences N_d through its effect on a_{aff} not closure levels.

Experimentally, N_d was sometimes larger in AA8022 and sometimes larger in AA5091. For OLR=2.0 at R=0.1, N_d was approximately equivalent in the two alloys at low and high ΔK_B, but greater in AA8022 at medium ΔK_B (see Figure 4.15). For OLR=3.0, N_d was always greater in AA5091 (see Figure 4.17). For OLR=1.44 at R=0.6, N_d was always greater in AA8022. For OLR=1.66, N_d was higher in AA5091 at low ΔK_B and higher in AA8022 at high ΔK_B (see Figure 4.23). For OLR=2.0, N_d was higher in AA5091 (see Figure 4.27). These differences in N_d observed experimentally resulted from an interplay of $(da/dN)_B$, $(da/dN)_{min}$, and a_{aff} that FASTRAN was not
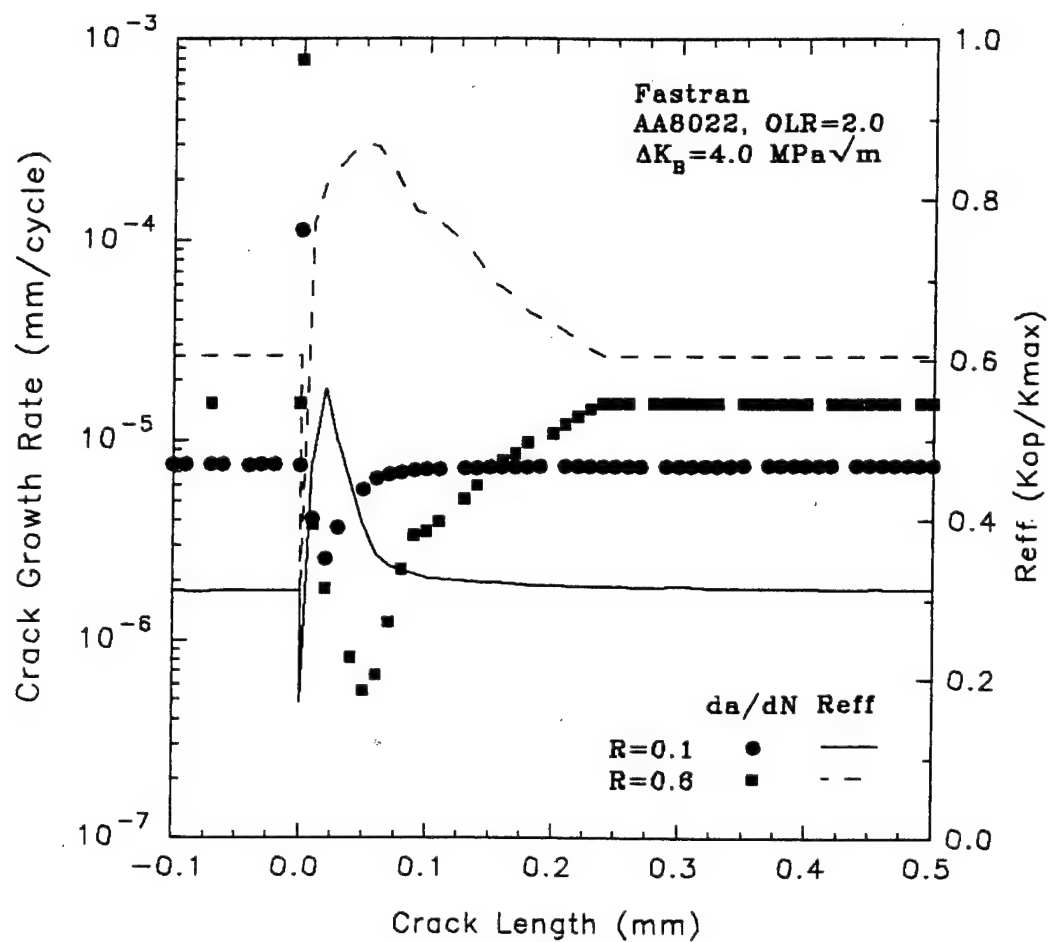
Figure 4.51. FASTRAN predicted overload response (OLR=2.0) in AA8022 at R=0.1 and 0.6.
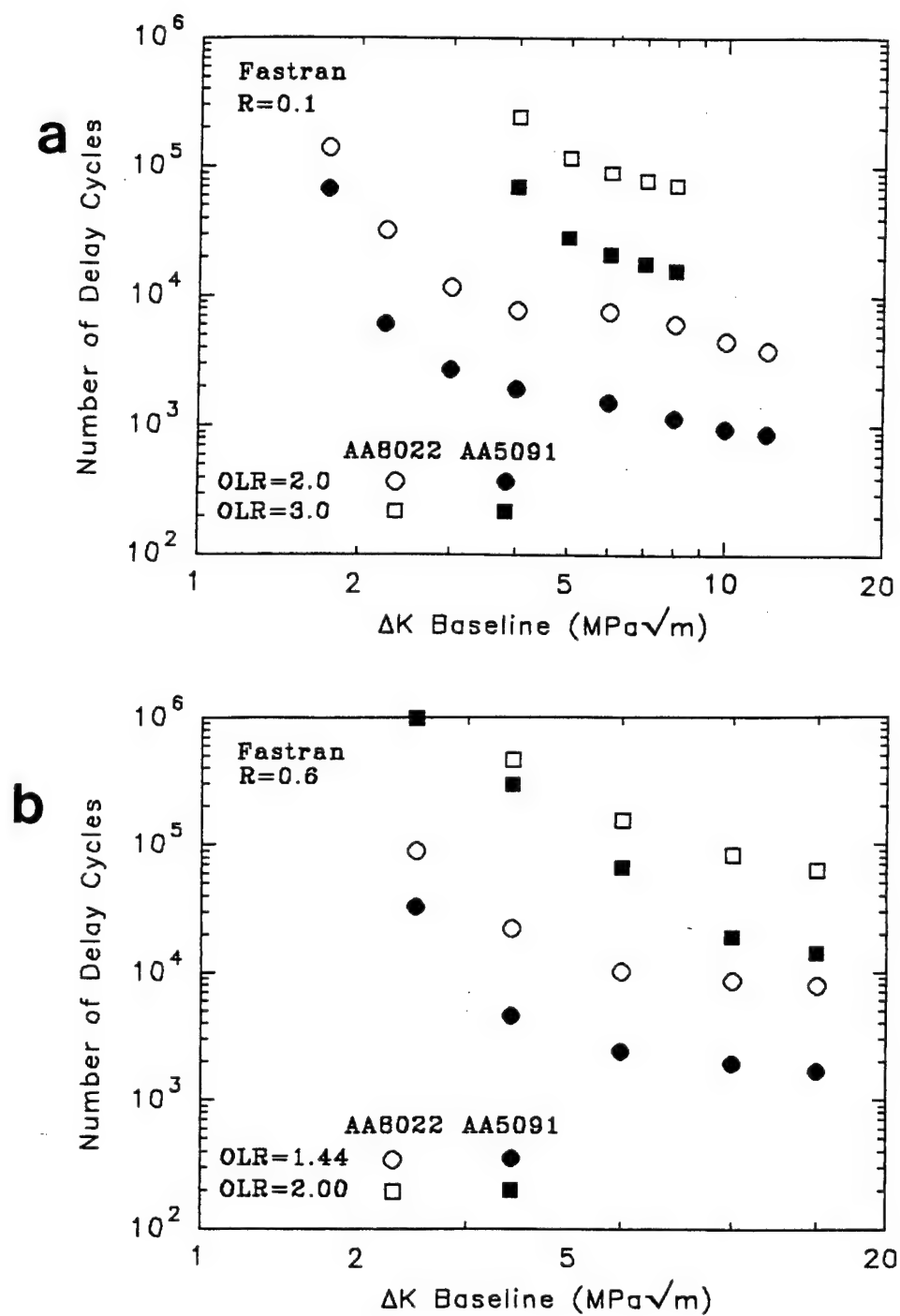
Figure 4.52. Comparison of FASTRAN predicted retardation magnitude of AA8022 and AA5091: (a) R=0.1; and (b) R=0.6.
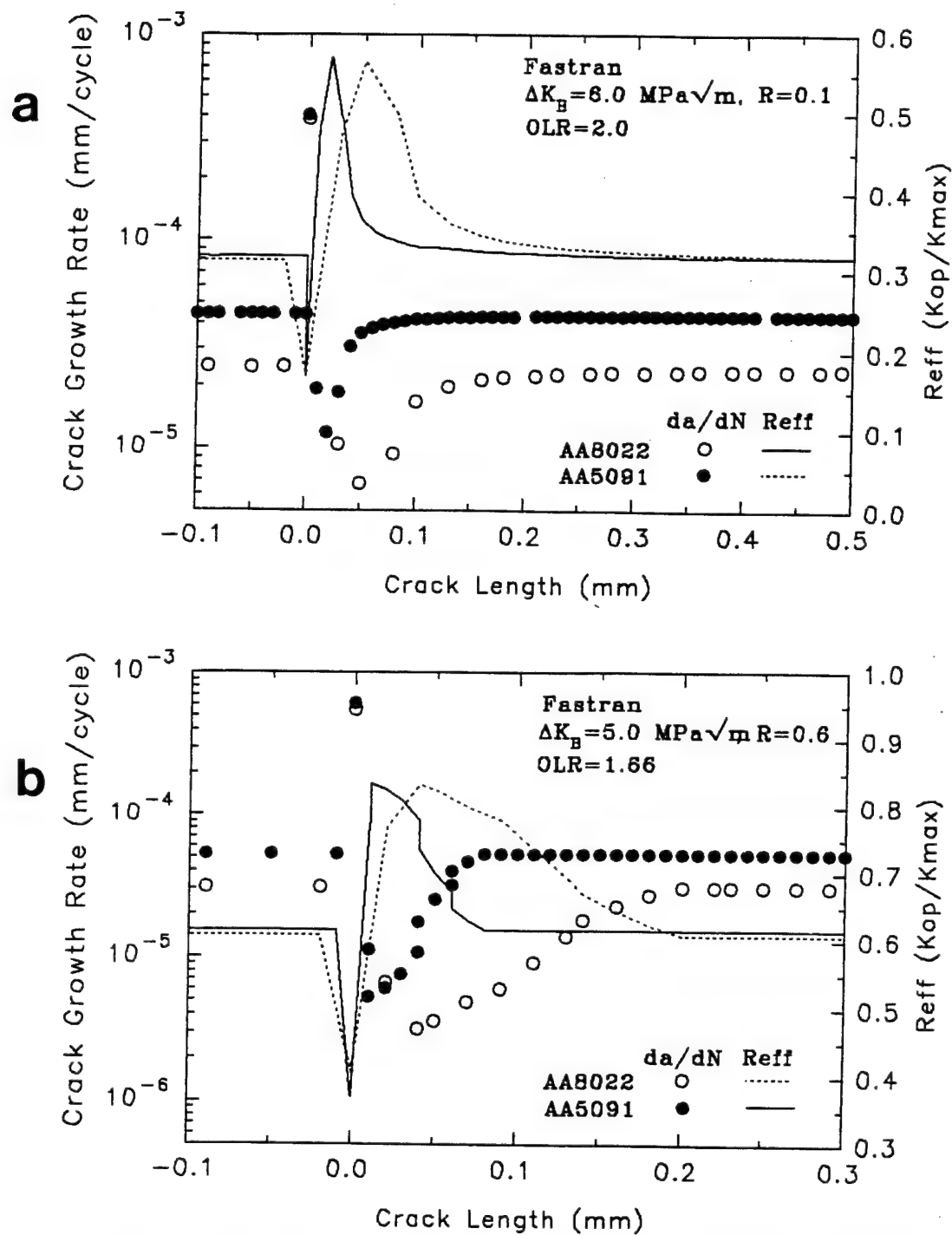
Figure 4.53. Comparison of FASTRAN predicted overload response in AA8022 and AA5091: (a) OLR=2, R=0.1, ΔK_B=6 MPa√m; (b) OLR=1.66, R=0.6, ΔK_B=5 MPa√m.

always able to predict purely on the basis of plasticity-induced closure.

Typical examples of predicted and experimental post-overload behavior at R=0.1 and 0.6 are shown in Figure 4.54. There are several notable differences which are typical of all such comparisons. First, $(da/dN)_{min}$ in the experimental data occurs after a shorter increment of growth, a_{min}, than in the predicted curve at both R=0.1 and 0.6. Second, a_{aff} is larger in the experimental curve than in the predicted curve. Third, there is exact correspondence between increased closure levels and decreased growth rates in FASTRAN, while experimentally at R=0.1 the increase in closure levels typically lagged behind the decrease in crack growth rates. At R=0.6, there was no increase in closure levels observed experimentally, with the exception of the two tests for OLR=2.0 at ΔK_B=5.0 MPa√m.

The predicted effects of overload/underload and underload/overload combinations on post-overload behavior are shown in Figure 4.55. FASTRAN predicts that at R=0.1 the post-overload behavior following these combinations is nearly identical to that following single tensile overloads. At R=0.6, FASTRAN predicts that following an overload by an underload significantly reduces the retardation effect while preceding the overload by an underload has little effect. This is exactly what was observed experimentally (compare Figures 4.19 and 4.29).
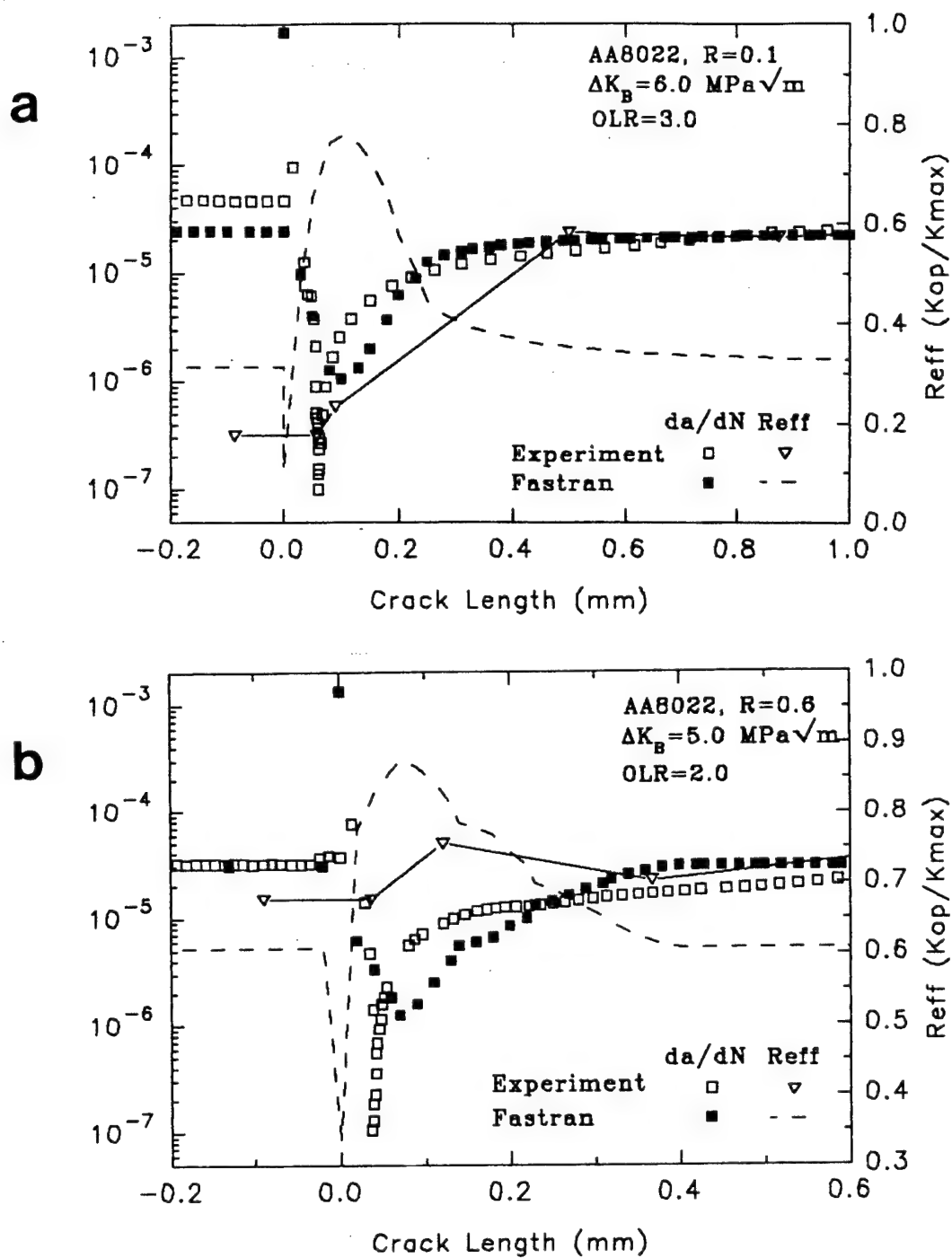
Figure 4.54. Comparison of FASTRAN predicted and experimental overload response in AA8022: (a) OLR=3, R=0.1, ΔK_B=6 MPa$\sqrt{m}$; (b) OLR=2, R=0.6, ΔK_B=5 MPa$\sqrt{m}$.
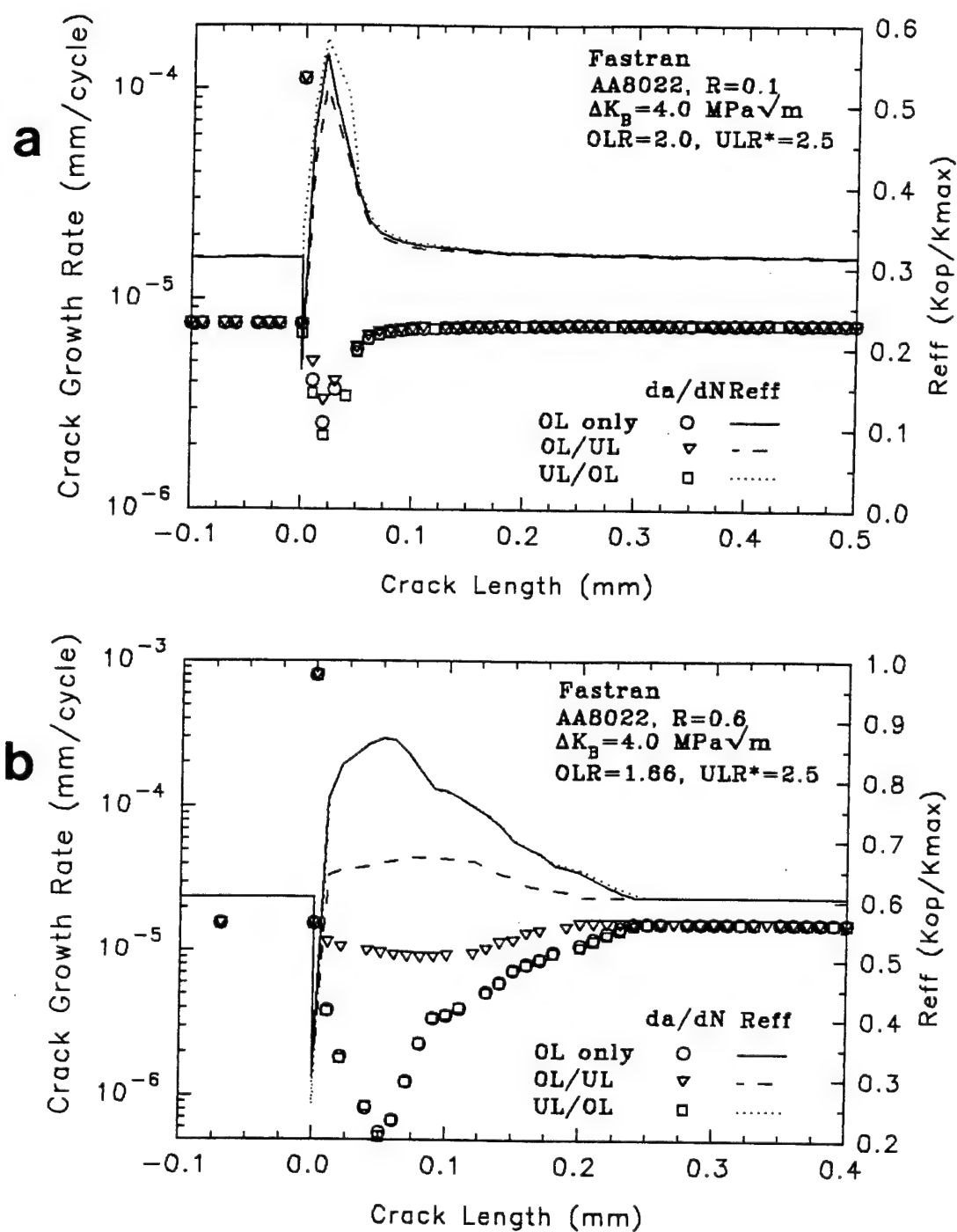
Figure 4.55. FASTRAN predicted effect of overload/underload combinations: (a) OLR=2/ULR*=2.5, R=0.1, ΔK_B=4 MPa√m; (b) OLR=1.66/ULR*=2.5, R=0.6, ΔK_B=4 MPa√m.

5. Discussion

5.1. Tensile Behavior

The strength in alloys similar to AA8022 and AA5091 is usually attributed to a combination of dispersion strengthening and grain boundary strengthening. In this case, the flow stress, τ_o, can be represented by:

$$\tau_o = \tau_p + \tau_{disp} + \tau_{gb} \tag{5.1}$$

where τ_p is the lattice friction or Peierls-Nabarro stress, τ_{gb} is the strength increase due to grain boundaries and τ_{disp} is the strength increase due to dispersoids.

The strength increase resulting from dispersoids is often attributed to Orowan hardening. In this mechanism, yield strength increases because dislocations must bypass the incoherent dispersoids before significant plastic deformation can occur. The stress necessary to loop the dispersoids and cause initial plastic deformation is given by the Orowan equation:

$$\tau_{loop} = Gb/\lambda \tag{5.2}$$

The flow stress necessary to produce additional plastic deformation is given by [70]:

$$\tau = \tau_{loop} + \tau_b + \tau_{LR} + \tau_{im} \tag{5.3}$$

where τ_b is the bowing stress which increases with strain due to the reduction in the effective gap between neighboring particles, τ_{LR} is a long-range stress from the accumulation of dislocation loops and τ_{im} is an "image stress" arising from differences in the elastic-plastic behavior of the matrix and dispersoid. The soft matrix deforms plastically while the hard particle deforms only elastically. This induces back stresses in the matrix which oppose further plastic deformation. τ_{im} differs from τ_{LR} and τ_b because it produces uni-directional or kinematic hardening, while they produce isotropic hardening. If the direction of plastic strain were reversed, τ_{im} would assist rather than oppose plastic deformation producing the Bauschinger effect. The magnitude of τ_b, τ_{LR}, and τ_{im} increase with increasing plastic strain to produce significant work hardening in dispersion-strengthened materials. A study by Hazzledine and Hirsch [70] in a copper alloy containing Al_2O_3 dispersoids suggests that τ_{im} is responsible for approximately 60% of the work hardening from dispersoids.

AA8022 and AA5091 exhibited an initial rate of work hardening consistent with this mechanism. The flow stress from the proportional limit ($\Delta\epsilon_p=0$) to a plastic strain of approximately $\Delta\epsilon=0.6\%$ increased approximately 75 MPa and 150 MPa in AA8022 and AA5091, respectively. However, beyond this point the rate of work hardening was very low. In AA8022, the flow stress from $\Delta\epsilon_p=0.6\%$ to the onset of necking at $\Delta\epsilon_p=1.5\%$ increased only 13 MPa. In AA5091, the flow stress increased only 15 MPa from $\epsilon_p=0.6\%$ to the onset of necking at $\Delta\epsilon_p=8.8\%$. This suggests that work hardening due to dispersoids saturates at a fairly small plastic strain in AA8022 and AA5091.

Beyond the point of necking, the work hardening behavior was not determined. However, the early necking in AA8022 suggests this alloy either ceased to work harden or possibly work softened.

The early saturation and subsequent low rate of work hardening or work softening is typical of fine-grained dispersion-strengthened alloys [23]. However, it may not be consistent with the Orowan mechanism leading Hawk et al. [71] and Hasagawa and Miura [72] to question whether the Orowan mechanism is the primary dispersion-strengthening mechanism in fine-grained PM alloys. Hasagawa and Miura proposed that dispersion strengthening in fine-grained PM alloys is controlled by the detachment or generation of dislocations from the dispersoid-matrix interface rather than Orowan looping. Kuhlmann-Wilsdorf and Wilsdorf [90] explained work softening in similar alloys on the basis of low energy dislocation structures (LEDS). They contend that unconventional manufacturing techniques such as mechanical alloying and melt spinning produce metastable LEDS with dislocation densities higher than conform to LEDS generated through conventional straining conditions. Work softening occurs because of a gradual change from an initial metastable LEDS structure to a LEDS structure with fewer nodes appropriate for the test conditions. The work in the current study was insufficient to resolve this issue, but the tensile behavior and low cycle fatigue behavior discussed in Section 5.2 suggests to this author that the Orowan mechanism is not the primary dispersion-strengthening mechanism in AA5091 and AA8022.

The contribution of grain boundaries to strength in many coarse-grained alloys can be represented by the Hall-Petch relationship:

$$\tau_{gb}=kd^{-1/2} \qquad\qquad (5.4)$$

The effect of grain size on strength in fine-grained alloys was investigated by Lloyd [73] in an Al-6% Ni alloy and more recently by Westengen [74] in an Al-2% Fe-0.8% Mn-0.16% Si alloy. The grain size was varied from 0.5 to 20 μm in the Al-6 Ni alloy and 0.5 to 10 μm in the Al-Fe-Mn-Si alloy. The yield strength in both alloys exhibited a d^{-1} dependency rather than the $d^{-1/2}$ dependency observed in coarse-grained alloys indicating that grain size strengthening is enhanced at finer grain sizes. This suggests that grain boundary strengthening may contribute significantly to the overall strength of AA8022 and AA5091.

Lloyd and Westengen also examined the effect of grain size on work hardening and found that the work hardening capability decreased significantly with decreasing grain size at grain sizes below about 10 μm. Lloyd proposed that dislocation accumulation and the resultant "forest" hardening occurs at a lower rate as grain size decreases because the mean free slip length approaches the grain size and there is less opportunity for dislocation interaction. He also suggested that the rate of dynamic recovery is higher in a fine-grained alloy. The low rate of work hardening in AA8022 and AA5091, beyond the initial part of the stress-strain curve and prior to necking is consistent with these studies. AA8022 and AA5091 had average grain diameters of 1.0 and 0.6 μm, respectively.

The nature of the grain boundaries in AA8022 and AA5091 was not determined in the current study, but has been determined by other investigators in similar alloys. Hawk et al. [89] used convergent beam electron diffraction to measure misorientation between grains in MA IN9052.

The composition of this alloy is similar to that of AA5091 except that it contains no lithium. They found misorientation angles between 20° and 45° indicating the boundaries were high angle. They concluded that the alloy possessed a genuine sub-micron grain size. Franck [90] used Kikuchi patterns to determine the misorientation between grains in FVS1212. This alloy is similar to AA8022 except that it contains a higher volume fraction of dispersoids (27%). The misorientations were typically greater than 15° indicating the boundaries were high angle.

Lloyd and Morris [75] compared the tensile behavior of Al-6% Ni and Al-6% Ni-0.3 Mg. The Mg containing alloy exhibited a higher rate of work hardening. Lloyd and Morris concluded that Mg enhanced dislocation interactions in these alloys leading to a higher rate of work hardening. AA5091 had a higher rate of work hardening and a greater uniform elongation prior to necking than AA8022 consistent with this study. AA5091 contains 4% Mg in solution. A more uniform distribution of dispersoids may also have contributed to the higher rate of work hardening in AA5091.

The Mg in AA5091 is probably also responsible for the observed serrated yielding. Serrated yielding is not uncommon in aluminum alloys. It is usually attributed to pinning of dislocations by solute atmospheres (i.e, Cottrell-Bilby mechanism). This effect is strongest in alloys containing Mg which has the greatest size differential (+12%) of the common alloying elements with aluminum. The Mg and Li in solution also contribute to the higher strength of AA5091 through solid solution strengthening.

The tensile deformation in AA5091 and AA8022 was homogeneous (see Figure 4.4). The homogeneous deformation is a consequence of their fine grain size, the absence of shearable precipitates, and the presence of non-

shearable dispersoids. A fine grain size promotes homogeneous deformation due to compatibility requirements. The deformation of a grain requires that its neighboring grains also deform. This effect is enhanced with decreasing grain size as a larger total volume of material must satisfy compatibility requirements. Grain boundaries are also effective barriers to slip, the more frequent the barriers, the more homogeneous the deformation. AA5091 and AA8022 also contain no shearable precipitates. Shearable precipitates tend to localize slip because once they have sheared on a slip plane it is easier for slip to continue in that plane. Non-shearable dispersoids have the opposite effect. Once slip has occurred on a plane containing dispersoids, further slip is more difficult on that plane due to localized work hardening.

5.2. Constant Amplitude Low Cycle Fatigue Behavior

The cyclic response in particle-hardened alloys is often explained on the basis of precipitate shearability [76,77]. Shearable particles (e.g., coherent precipitates) tend to produce cyclic softening because their contribution to strength is progressively lost as they are sheared by dislocations. Non-shearable particles (e.g., incoherent precipitates or dispersoids) tend to produce cyclic hardening due to the accumulation of dislocation loops around the particles and the resulting "forest" and Orowan hardening.

However, the monotonic tensile behavior in AA8022 and AA5091 suggests that Orowan looping may not contribute significantly to work hardening in these alloys. This is further supported by their cyclic

response. Both alloys exhibited significant cyclic softening over about the first 10 cycles (see Figure 4.6). One possible explanation for this initial softening is that there is an initial shortage of mobile dislocations in these alloys. Once mobile dislocations are generated through the operation of sources the peak stress temporarily decreases. After the initial softening, AA5091 gradually hardened to the onset of failure. This hardening probably resulted from "forest" hardening. On the other hand, AA8022 continued to gradually soften until the onset of failure. The maximum plastic strain at all three total strain amplitudes in AA5091 and for the two lower strain amplitudes in AA8022 was less than the plastic strain at necking in the tensile tests, so it is unlikely that necking contributed to this behavior. The relative behavior of AA8022 and AA5091 reflects a greater cyclic work hardening capacity in AA5091. The behavior is consistent with the monotonic loading behavior discussed previously in Section 5.1.

5.3. Constant Amplitude Fatigue Crack Growth Behavior

The constant amplitude fatigue crack growth behavior of AA5091 and AA8022 (see Figure 4.7) is a consequence of the homogenizing effects of their fine grain size and incoherent dispersoids on deformation. As deformation becomes more homogeneous the influence of microstructure on crack path diminishes and the material behaves more like a perfect continuum. The result is a smoother fatigue surface, less tortuous crack path, and a smaller contribution of roughness-induced closure to fatigue crack propagation resistance. This is reflected in the lower closure levels

and higher crack growth rates in AA8022 and AA5091 at R=0.1 in comparison to IM aluminum alloys. The crack growth resistance of these alloys approaches that of IM alloys at R=0.6 because the effects of roughness-induced closure diminish with increasing stress ratio.

There was no evidence in these alloys of a change to a crystallographic mode of cracking in the near threshold region like that which is often observed in IM alloys [4]. This change in mode is usually accompanied by an increase in surface roughness which enhances roughness-induced closure effects. The transition to this mode typically occurs when the cyclic plastic zone is approximately equal to the mean free slip length between microstructural barriers to slip. It is believed to result from a change in deformation character from homogeneous deformation involving multiple slip systems to localized deformation on a single slip system [78]. The mean free slip length in AA8022 and AA5091 cannot possibly be any larger than the grain size and may be smaller. The cyclic plastic zone size in AA8022 and AA5091 is equal to their grain size at approximately ΔK= 1.3 MPa$\sqrt{m}$ and 1.0 MPa$\sqrt{m}$, respectively, so it is possible that a change to a crystallographic mode of cracking does occur. However, even if it did occur, the change in surface roughness from cracking along crystallographic slip planes would be insignificant compared to that which occurs in an IM alloy because of the very fine grain size.

The fact that AA8022 and AA5091 with their novel microstructures and many other aluminum alloys have similar intrinsic resistance to fatigue crack growth is remarkable considering the wide range of microstructures and deformation modes represented in IM and PM aluminum alloys. Differences in intrinsic resistance are often more pronounced in vacuum

suggesting that environmental effects dominate any microstructural influence on fatigue crack propagation resistance in air.

5.4. Overload Behavior

5.4.1 Intrinsic Material Response to an Overload

The purpose of the low cycle fatigue (LCF) overstrain tests was to determine the intrinsic material response of AA5091 and AA8022 to a strain history simulating that experienced by material at the tip of a crack subjected to an overload. The results of these tests indicate that an overload produces kinematic hardening and isotropic softening. The overall effect on yield strength is to increase the tensile yield strength and decrease the compressive yield strength. The magnitude of this effect is probably greater at the tip of a crack subjected to an overload, since the overstrain in this case is greater than that which can be simulated in an LCF tests. The results also indicate that the effects of an overload on the intrinsic behavior of AA5091 and AA8022 are short-lived.

The kinematic hardening produced by an overstrain (see Figures 4.10 and 4.11) most likely results from an increase in τ_{im}, the "image" stress component in Equation 5.3. These image stresses arise from the difference in the elastic-plastic behavior of the matrix and dispersoid as previously discussed in Section 5.1. The additional "image" or back stress induced by a tensile overstrain increases the peak tensile stress and reduces the peak compressive stress necessary to achieve a total strain range of $\Delta\epsilon_t$=2% following the overstrain. An understrain has the opposite effect.

The rapid diminution of this effect with subsequent cycling is probably a consequence of plastic relaxation processes.

The magnitude of the kinematic hardening was reduced significantly when the overstrain was followed by a partial understrain. This occurs because the additional reversed plastic strain from the understrain reduces the magnitude of the back stresses available to oppose tensile deformation and assist compressive deformation during subsequent cycling. The elimination of this overstrain effect by annealing indicates annealing eliminates the internal stress system between the precipitate and matrix, probably by local recovery and rearrangement of the dislocations around the precipitates [76].

The isotropic softening following an overstrain indicates that the isotropic hardening mechanisms represented by τ_b and τ_{LR} in Equation 5.3 were not active. The absence of isotropic hardening by these mechanisms suggests that the Orowan hardening mechanism may not be the primary dispersion-strengthening mechanisms in these alloys.

5.4.2. Mechanisms Contributing to Crack Retardation in AA8022 and AA5091

The possible contributions of each of the seven crack retardation mechanisms described previously in Section 2.3.2. to crack retardation in AA8022 and AA5091 are considered in this section:

a. **Crack tip strain hardening–** Crack retardation by this mechanism requires that the material isotropically harden from the application of an overload. The isotropic hardening reduces the cyclic plastic strain range

in subsequent baseline cycles to produce crack retardation (see Figure 2.18). This mechanism cannot contribute to crack retardation in AA8022 and AA5091 since the LCF overstrain experiments indicate an overload produces isotropic softening rather than hardening. Isotropic softening would produce crack acceleration rather than retardation according to this mechanism.

The LCF overstrain tests also indicates an overload produces kinematic hardening. This probably also makes no contribution to retardation, since it will equally reduce the maximum strain and minimum strain at the crack tip relative to a non-kinematic hardening material, producing no change in the cyclic plastic strain range as shown in Figure 5.1. In any event, the intrinsic response to an overstrain was short-lived (<100 cycles) compared to the number of delay cycles following an overload, suggesting that the crack tip strain hardening mechanism, or any other possible mechanism relying on intrinsic material response, make little or no contribution to crack retardation in AA8022 or AA5091.

The kinematic hardening in AA8022 and AA5091 may actually reduce crack retardation stemming from the plasticity-induced closure mechanism. Work hardening from K_{min} to K_{ol} should lead to a reduction in the size of the overload plastic zone and strain increase resulting from K_{ol}, and the strain should be more reversible on unloading from K_{ol} to K_{min} due to the decrease in compressive yield strength. The final effect would be a smaller overload plastic zone and smaller residual plastic strain relative to a non-kinematic hardening material, which would result in a smaller increase in closure levels as the crack propagated through the overload plastic zone, and less retardation.
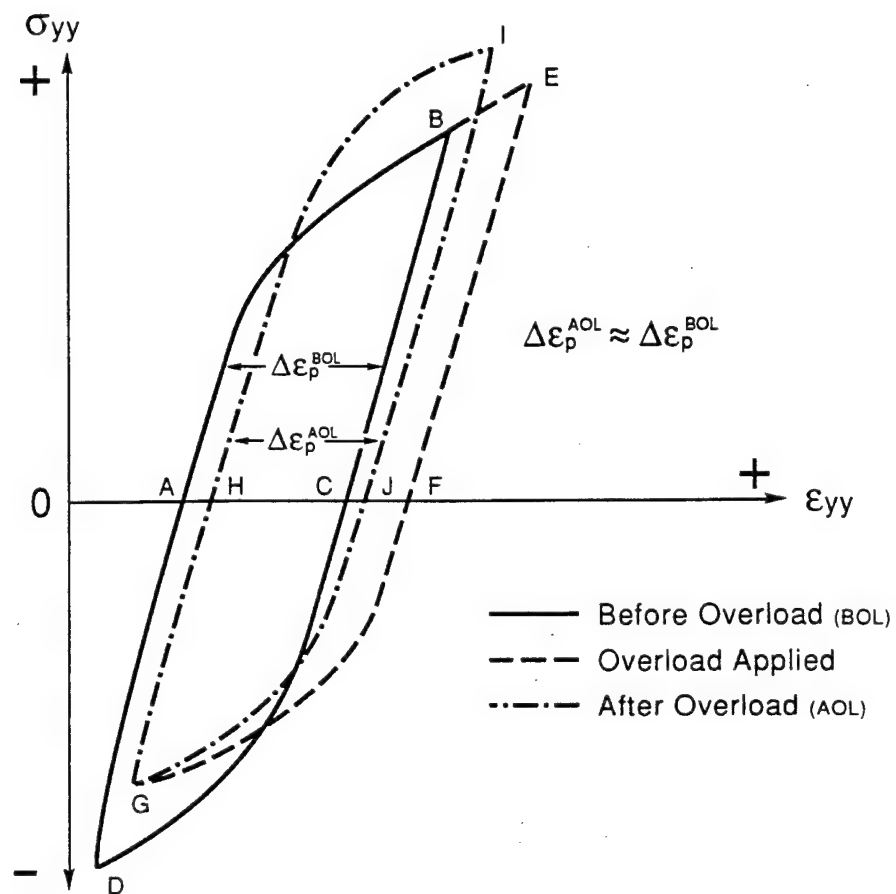
Figure 5.1. Schematic showing effect of kinematic hardening from an overload on stress-strain behavior of crack tip element.

b. Crack tip blunting- Crack tip blunting, resulting from an increase in plastic strain ahead of the crack tip during the overload cycle, can lead to a reduction in the cyclic plastic strain range at the crack tip. The strain gage experiments confirm that overloads in AA8022 and AA5091 did produce an increase in residual plastic strain (see Table 4.7). However, several experimental observations indicate that crack tip blunting was not the primary cause of retardation in these alloys. First, this mechanism predicts that largest reduction in growth rate should occur immediately (i.e., immediate retardation). Second, this mechanism can produce crack retardation only until the fatigue crack reinitiates. However, the surface crack retardation experiments revealed that the crack reinitiated almost immediately following an overload (see Figure 4.40). The crack also reinitiated at the surfaces and interior even in cases of crack arrest (see Table 4.3). The unstable crack growth in the interior, and the crack deflection at the specimen surface in AA5091 at higher ΔK_B, would also act to resharpen the crack and render this mechanism ineffective.

The potential of this mechanism to make any contribution to retardation can be explored using Equation 2.12. The root radii after overloads were not measured, so the root radii were estimated to be one eighth the crack tip opening displacement (CTOD) at K_{ol} using the Irwin equation for CTOD under plane-strain conditions [10]:

$$\rho = \frac{1}{8} CTOD_{ol} = \frac{1}{2\pi} \left(\frac{K_{ol}^2 (1-v^2)}{E\sigma_{ys}} \right) \tag{5.5}$$

This estimate recognizes that most of the increase in crack tip strain (i.e., blunting) resulting from K_{ol} is reversed on unloading to K_{min}, as shown in the strain gage experiments.

The estimated values of ρ and ΔK_{notch} obtained by substituting ρ into Equation 2.12 are shown in Table 5.1 for a range of overload conditions. Also shown are the predicted percent reduction from ΔK_B, the ΔK_{eff} corresponding to the actual minimum growth rate following the overload obtained from the R=0.6 FCGR curve, and the actual percent reduction in ΔK_B. The predicted percent reduction in ΔK due to blunting primarily depended on OLR and baseline stress ratio. In AA5091, the predicted percent reduction at R=0.1 was 3% and 6% for OLR=2 and OLR=3, respectively. The required reductions in ΔK to achieve the actual minimum growth rates following the overloads ranged from 50% to 90%. At R=0.6, the predicted percent reduction was approximately 7% and 15% for OLR=1.44 and OLR=2.0, respectively. The required reduction at OLR=1.44 was 10% to 25%, while that at OLR=2 was 50 to 77%. Similar results were obtained for AA8022. These results suggest that crack tip blunting contributed very little to crack retardation in AA8022 and AA5091, except possibly at R=0.6, OLR=1.44.

Table 5.1. Predicted Effect of Crack Blunting on ΔK

Alloy	R	OLR	ΔK_B	$\rho(\mu m)$	Predicted		Actual	
					ΔK_{notch}	$\Delta\%$	ΔK_{eff}	$\Delta\%$
AA5091	0.1	2.0	1.75	0.06	1.70	-2.8	<0.9	-49
			4.00	0.30	3.89	-2.7	1.51	-62
			8.00	1.21	7.79	-2.6	3.91	-51
			12.0	2.73	11.7	-2.5	3.55	-70
		3.0	4.00	0.68	3.76	-6.0	<0.9	-77
			8.00	2.73	7.51	-6.0	<0.9	-88
	0.6	1.44	1.75	0.15	1.62	-7.4	1.58	-9
			4.00	0.79	3.71	-7.2	2.97	-25
		2.0	1.75	0.29	1.50	-14.3	<0.9	-48
			4.00	1.53	3.42	-14.5	<0.9	-77
AA8022	0.1	2.0	1.75	0.09	1.72	-1.7	<0.9	-48
			4.00	0.50	3.93	-1.7	1.62	-59
			8.00	2.01	7.86	-1.7	4.90	-39
			12.0	4.52	11.8	-1.7	7.20	-40
		3.0	4.00	1.13	3.85	-3.7	<0.9	-77
			8.00	4.52	7.69	-3.9	1.20	-85
	0.6	1.44	1.75	0.25	1.67	-4.6	1.52	-13
			4.00	1.32	3.82	-4.5	3.44	-14
		2.0	1.75	0.48	1.59	-9.1	<0.9	-48
			4.00	2.54	3.65	-8.7	<0.9	-77

c.   **Crack deflection/branching and secondary cracking–** The crack deflection/branching mechanism cannot contribute to retardation in AA8022 because little or no crack deflection occurred following an overload in this alloy. Crack deflection/branching also did not occur in AA5091 at ΔK_B= 4.0 MPA$\sqrt{m}$ so it can be eliminated as a cause of retardation at low ΔK_B in this alloy. Crack deflection/branching did occur in AA5091 at ΔK_B> 4.0 MPa$\sqrt{m}$. Suresh [4] calculated that crack deflection at an angle of 45° reduces the stress intensity factor by 15% while crack branching reduces the effective stress intensity by approximately 35%. The ΔK due to deflection or

branching and the percent reduction from ΔK_B for several overload conditions are shown in Table 5.2. The table also shows the ΔK_{eff} corresponding to the actual minimum growth rates observed following an overload and the percent reduction from ΔK_B. The required reductions in ΔK to achieve the actual minimum growth rates following the overloads was approximately 50% in the two overloads producing deflection, and 65% to 88% in the overloads producing branching. This analysis suggests that crack deflection/branching may contribute significantly to crack retardation at high ΔK_B.

However, the stress relief experiments and overload/underload experiments suggest that this analysis greatly overestimates the effect of crack deflection/branching. An overload of magnitude OLR=2.0 at baseline conditions ΔK_B=10 MPa√m, R=0.1 produced significant crack branching. However, a subsequent stress relief completely eliminated the retardation effect (see Figure 4.47). Similarly, an overload of magnitude OLR=2.00 at baseline conditions ΔK_B=4 MPa√m, R=0.6 produced significant crack branching, but the retardation effect was almost eliminated by a subsequent underload (See Figure 4.27). A subsequent stress relief or underload did not act to "unbranch" the crack, but both nearly eliminated the retardation effect. The discrepancy between the analysis and the experimental results probably occur because the analysis assumed the crack was deflected/branched along the entire crack front, when, in fact, the maximum depth of deflection in any test did not exceed 0.62 mm. This causes the effects of crack deflection/branching to be overestimated. The stress relief and underload experiments suggest that any contribution to crack retardation in AA5091 from deflection/branching is minimal.

Table 5.2. Predicted Effect of Crack Deflection/Branching on ΔK

R	OLR	ΔK_B	Predicted		Actual	
			ΔK_{eff}	$\Delta\%$	ΔK_{eff}	$\Delta\%$
0.1	2.0	4	3.4	-15	1.8	-54
		8	6.8	-15	4.2	-47
		12	7.8	-35	4.1	-65
	3.0	4	2.6	-35	<0.9	-77
		8	5.2	-35	<0.9	-88
0.6	2.0	5	2.6	-35	<0.9	-82

There was no evidence of secondary cracking in either AA8022 or AA5091 indicating this mechanism makes no contribution to crack retardation in these alloys. Secondary cracking in IM alloys is promoted by inhomogeneous deformation due to planar slip [7] and by the presence of large constituent particles [5]. AA8022 and AA5091 deform homogeneously and contain no large constituent phases.

d. Compressive residual stresses– Proponents of the compressive residual stress mechanism believe that compressive residual stresses can cause retardation in the complete absence of any crack closure effects. The reduction or elimination of the crack retardation effect by stress relieving following an overload is offered as experimental support for this mechanism [46-48]. This same behavior was observed in AA8022 and AA5091 (see Table 4.6 and Figure 4.47). However, stress relief experiments are actually inconclusive because crack closure mechanisms also rely on compressive residual stresses both ahead of and behind the crack tip. Thus, stress relieving will also eliminate any contribution to crack retardation from

crack closure mechanisms. A mechanism by which this can occur is described in Section 5.4.3.a.

A crack retardation mechanism must be capable of reducing ΔK_{eff} or the cyclic plastic strain range ahead of the crack tip. The ability of compressive residual stresses to do this in the absence of closure will now be considered. The first part of the discussion will be on the basis of the Rice analysis which assumes an infinitely sharp crack tip and immediate yielding on load reversal (see Section 2.2.1). Then the finite element study of Sun and Sehitoglu [31,45] which accounts for a finite crack tip radius will be considered.

The general effect of a compressive residual stress field on the load history and the stress-strain history of a crack tip element are shown in Figure 5.2. By the principle of superposition, the compressive residual stress reduces the applied K_{max} and K_{min} equally, producing a reduction in the stress ratio R, but no net change in ΔK. Similarly, ϵ_{max} and ϵ_{min} are reduced producing a reduction in ϵ_{mean}, but no net change in the cyclic plastic strain range, $\Delta \epsilon_p$. The element experiences the same stress range ($-\sigma_o$ to σ_o) with or without the compressive residual stress field. Thus, the effects of a compressive residual stress field are the same as a decrease in R in the absence of a residual compressive stress field (see Figure 2.8), i.e, the mean strain is reduced, but there is no change in the cyclic plastic strain range. Conversely, a residual tensile stress field has the same effect as an increase in R.

The question that now must be addressed is whether there is an R-ratio (i.e., mean strain) effect on fatigue crack growth rates in the absence of crack closure. McEvily and Minikawa [79] observed virtually no effect
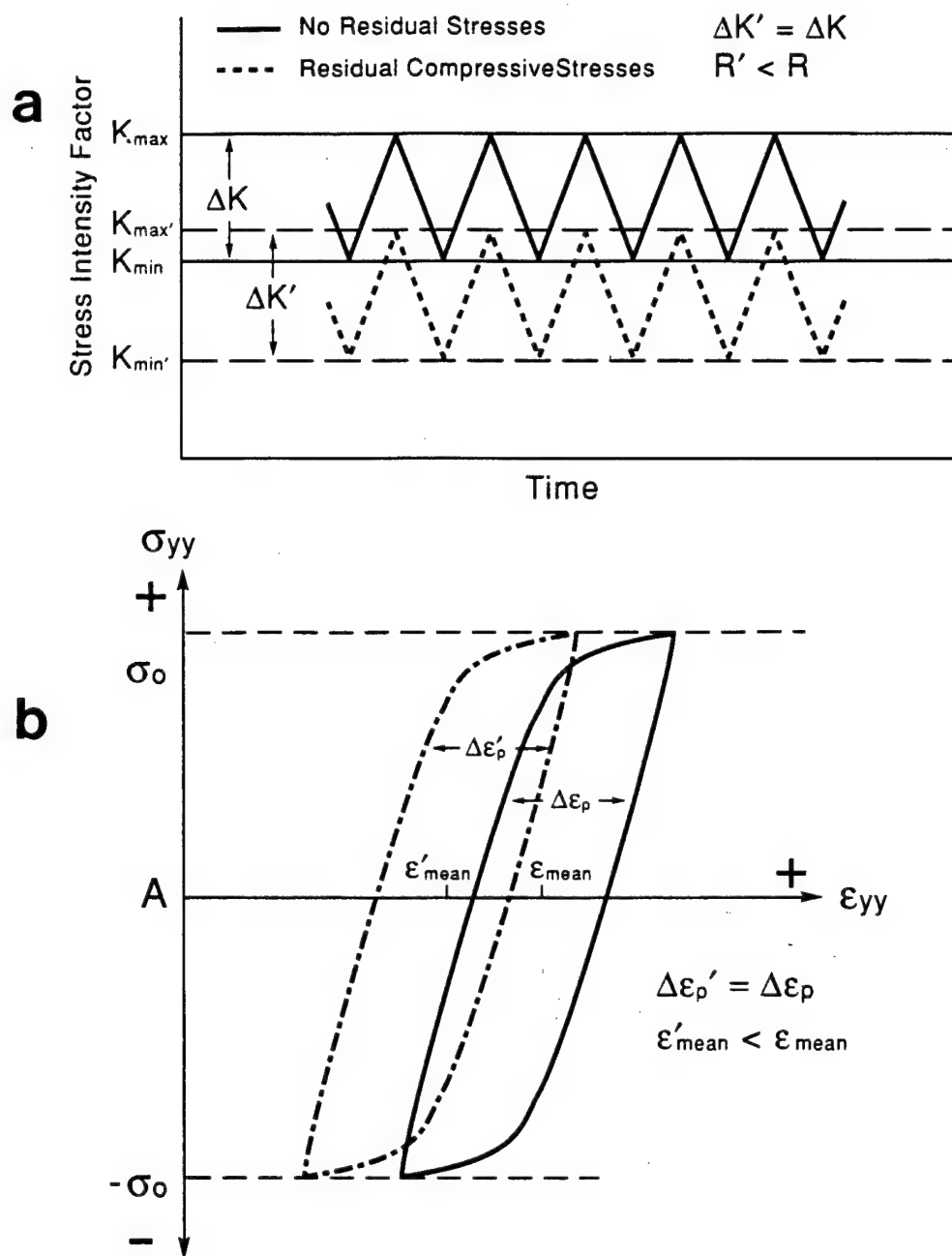
Figure 5.2. Schematic showing effect of compressive residual stresses on: (a) load history; and (b) stress-strain history of crack tip element.

of stress ratio on fatigue crack growth rates in MA aluminum alloy IN-9025 over a range of stress ratio from R=0.05 to 0.8 until static failure modes were activated at high ΔK. This alloy had very little closure due to its extremely smooth fatigue crack surfaces. Ohta et al. [80] studied fatigue cracks propagating in welded plates. The welds contained high residual tensile stresses (60 MPa) which increased the effective stress ratio and eliminated crack closure. The applied stress ratio was varied from R=0.5 to 1.15 (i.e, K_{min} and K_{max} both negative) while holding applied ΔK constant at 5.7 MPa$\sqrt{m}$. The fatigue crack growth rates remained essentially constant with decreasing R until R approached 1. They concluded that in the absence of closure, crack growth rates are independent of R even under fully compressive loading. The lack of a stress ratio effect under constant amplitude loading conditions suggests that a reduction in R (i.e., mean strain) resulting from compressive residual stresses has little effect on crack growth rates and cannot contribute to crack retardation.

The previous description of the effects of compressive residual stresses on stress and strain of a crack tip element (Figure 5.2) assumed an infinitely sharp crack. The finite element model of Sun and Sehitoglu [31,45] indicates that compressive residual stresses acting on a crack tip with a finite radius can reduce the cyclic plastic strain range. Since an overload enlarges the zone of compressive residual stresses ahead of a crack tip it is reasonable to believe that crack retardation may result. However, another implication of this model, suggested by the authors themselves, is that there should be a stress ratio effect under constant amplitude loading conditions even in the absence of closure. The absence of one suggests that this model overestimates the effect of residual

compressive stresses and finite crack tip radii on cyclic plastic strain ranges.

Nayeb-Hashemi, McClintock, and Ritchie [55] investigated the effects of overloads under Mode III loading conditions. Shear overloads were applied to A469 rotor steel under Mode III loading conditions and tensile overloads under Mode I loading conditions. Mode III loading differs from Mode I in that there is no possibility of crack closure since there is no residual tensile deformation in the crack wake. However, an overload in Mode III should produce residual shear stresses ahead of the crack tip just as an overload in Mode I produces residual compressive stresses. The residual shear stresses will act to reduce K_{III} just as compressive residual stresses reduce K_I. No retardation occurred in Mode III suggesting that residual stresses resulting from an overload cannot produce crack retardation. Typical retardation behavior occurred in Mode I which the investigators contributed to crack closure mechanisms.

The above discussion suggests that the compressive residual stress mechanism probably contributes very little to crack retardation in AA8022, AA5091, or any other ductile material where fatigue crack growth rates are controlled by the cyclic plastic strain range. However, compressive residual stresses are an important component of crack closure mechanisms.

e. Crack Closure- The delayed retardation observed under all overload conditions (see Figures 4.38 and 4.39), the crack growth preceding crack arrest (see Figures 4.31 and 4.32) at R=0.1 and 0.6, the crack surface rubbing observed at high ΔK_B at R=0.1 and 0.6 (see Figure 4.34), and the inability of any of the previous mechanisms to explain retardation in

AA8022 and AA5091, suggest that crack closure mechanisms are the primary cause of crack retardation in AA8022 and AA5091. The effects of surface removal, the observed crack front progression following an overload, and the effects of stress relieving, which will be discussed in Sections 5.4.3.a. and 5.4.3.d., are also consistent with closure mechanisms.

The significant retardation effect in AA8022 under all conditions and in AA5091 at low ΔK_B, despite a decrease in surface roughness following an overload (see Figures 4.31 and 4.32), suggests that the plasticity-induced closure mechanism, rather than the roughness-induced closure mechanism, is the primary cause of retardation under these conditions. The significant increase in surface roughness due to unstable crack growth in the interior of AA5091 at medium and high ΔK_B (see Figure 4.33), and the presence of fretting products associated with crack deflection at the surfaces (see Figure 4.34(d)) suggest that the roughness-induced closure mechanism may contribute to retardation in AA5091 at medium to high ΔK_B. However, in this case the increase in surface roughness in AA5091 is not due to change to a Stage I crystallographic mode of cracking which often occurs in IM alloys, but rather due to unstable crack extension.

The ability of FASTRAN-II, which is based on plasticity-induced closure, to successfully predict the following experimental trends is also an indication that the plasticity-induced closure mechanism is a primary cause of retardation in these alloys: (1) the increase in N_d with decreasing ΔK_B and increasing OLR (see Figures 4.48 and 4.50); (2) the increase in N_d with increasing stress ratio (see Figure 4.54); and the effects of overload/underload combinations at both R=0.1 and 0.6 (see Figure 4.55).

However, FASTRAN-II was not always successful in predicting the relative behavior of AA5091 and AA8022. The model predicts that the N_d will always be larger in AA8022 than in AA5091 under any given overload condition (see Figure 4.52). This is a consequence of the lower yield strength in AA8022 which produces a larger a_{aff}. In fact, N_d in AA5091 was equal to or larger than that in AA8022 at high ΔK_B and/or OLR. These are the conditions that produced the most extensive crack branching and unstable crack growth in AA5091, suggesting that in these cases roughness-induced closure was contributing significantly to crack retardation. Since FASTRAN-II does not include roughness-induced closure effects, it fails to predict the relative behavior of AA8022 and AA5091 under these conditions.

However, the following experimental results seemed inconsistent with crack closure mechanisms: (1) measured crack closure levels did not always increase following overloads at R=0.1 at low ΔK_B and in cases of crack arrest, and the increase at medium to high ΔK_B was generally not sufficient to produce the observed reduction in growth rates; (2) the position of the maximum closure level typically occurred after a_{min}, the position of the minimum growth rate; (3) the measured crack closure levels did not increase following overloads at R=0.6 except in AA8022 at the highest ΔK_B and overload magnitude; (4) a_{aff} was in some cases larger than the calculated overload plastic zone at R=0.1; (5) a_{aff} was significantly smaller than the calculated plane-stress overload plastic zone size at R=0.6. Since the previous discussion suggests that non-closure mechanisms contribute little to crack retardation in AA8022 and AA5091, these discrepancies need

to be examined to determine if explanations consistent with crack closure mechanisms can be found.

There are several factors which may have contributed to the discrepancy between measured crack closure levels and post-overload crack growth rates. Closure measurements in this study were made by the compliance method using a front-face COD gage as previously described in Section 3.3.3. This method is frequently referred to as a "far-field" method since the measuring device is remote from the crack tip. In Donald's opinion [66] the method utilized in the current study should be used only for constant amplitude loading conditions, since the near-tip closure increase following an overload may not be detectable using a far-field technique. This is supported by the analytical study of Nakamura and Kobayashi [81]. They used a modified Dugdale model to investigate the effects of residual stretch in the crack wake on the actual K_{cl} at the crack tip and the K_{cl} that would be measured by a far-field compliance technique. Their results indicate that far-field closure measurements underestimate the actual closure levels when the residual stretch is adjacent the crack tip. This is the situation immediately following an overload.

Another factor which almost certainly contributed to the discrepancy between closure levels and post-overload fatigue crack growth rates in this study was the analysis method by which the closure levels were determined by the software program utilized to perform the overload tests. This program calculates an average closure level over an increment of crack growth. The increment of growth in the overload tests ranged from $\Delta a=0.08$ mm in the low ΔK_B to $\Delta a=0.2$ mm in the high ΔK_B tests. The averaging

would tend to reduce the maximum closure level obtained following an overload. This effect would be largest at low ΔK_B where in many cases the increment of growth over which closure was averaged was larger than a_{aff}. Unfortunately, it was not possible to use a smaller Δa increment in these tests, because doing so produced an unacceptable level of imprecision in crack length measurements.

The discrepancy between a_{min} and the maximum closure levels probably result from three-dimensional effects. Dexter et al. [8] proposed that discrepancy occurs because growth rates are controlled by the average through-thickness closure levels, while measured closure levels reflect the closure levels in the plane-stress surface regions. Three dimensional effects are discussed in more detail in Section 5.4.3.d.

The fracture surface rubbing and fretting is strong evidence that crack closure occurred following overloads at both R=0.1 and R=0.6. For a given ΔK_B and overload magnitude, N_d was larger at R=0.6 than at R=0.1 indicating there should be a higher increase in closure levels at R=0.6. Why then was no closure detected following overloads at R=0.6, except in AA8022 at the highest ΔK_B and overload magnitude? One explanation is that crack closure occurs over too small a distance at high R to be detected by a "far-field" method. McEvily and Minikawa [82] used optical microscopy to measure the distance over which cracks were closed at K_{min} at R=0.05 and 0.5 in the near threshold region (da/dN=3E-6 mm/cycle). They found that the crack closed 20 μm behind the crack tip at R=0.5 compared to 1 cm at R=0.05. These observations were made at the specimen surface where the material is in plane stress. A finite element study by McClung et al. [26] indicates the amount of crack length closed under plane-strain is even

smaller than that under plane stress. Plane stress cracks were closed over much of their crack length. Plane strain cracks under minimum load at R=0 were closed over only about ten percent of their crack length and at R=0.1 the amount of closed crack was only 2 percent of the total crack length. The result of the smaller amount of closed crack at high R is that there is a much smaller change in specimen compliance. The far-field compliance method used in the present investigation may simply have been too insensitive to detect the compliance change resulting from crack closure at R=0.6. Bertel et al. [59] were able to detect an increase in closure levels following overloads in 2124-T351 at R=0.5 using a "near-tip" compliance gage.

The general absence of an increase in closure in cases of crack arrest at R=0.1 can be explained in the same manner. The cracks in these tests propagated 60 μm or less prior to crack arrest. The compliance change resulting from increased closure levels over such a small distance was probably not detectable by the far-field method utilized in this study.

Now consider the discrepancy between a_{aff} and the overload plastic zone size at R=0.1. Overloads of magnitude OLR=2.0 at medium and high ΔK_B generally produced a_{aff} that were approximately equal to the plane stress overload plastic zone. This seems reasonable for plasticity-induced closure since increased closure levels and the accompanying retardation might be expected to decrease rapidly after the crack has propagated through the overload plastic zone. The apparent discrepancy arises at low ΔK_B for OLR=2.0 and at OLR=3.0 where a_{aff} was typically larger than the overload plastic zone size (see Figures 4.15 and 4.17).

Similar behavior in IM aluminum and titanium alloys has been observed by Ritchie and coworkers [7,57]. They proposed that an increase in surface roughness due to a change to a crystallographic mode of cracking prolonged the effect of an overload beyond the overload plastic zone size. This mechanism should have its greatest effect at low ΔK_B because roughness-induced closure effects are greatest when CTOD is small. This is a reasonable mechanism for IM alloys that exhibit an increase in surface roughness following an overload. However, in AA8022 and AA5091 surface roughness decreased following an overload at low ΔK_B. Therefore, this mechanism cannot be responsible for this behavior. An alternative mechanism based on plasticity-induced closure has been proposed by Fleck [41]. He contends that the contact of the plastic hump (i.e., the region of increased residual tensile deformation) produced by the overload can prevent the fatigue crack from closing thereby reducing ΔK_{eff} even after the crack has grown beyond the overload plastic zone. This mechanism, which Fleck calls discontinuous closure, was previously shown in Figure 2.22. The analytical study of Beevers et al [83] suggests this is a viable mechanism. This work examined the effect of a surface asperity in the crack wake on crack closure. The analysis showed that an asperity in the crack wake can have a significant effect on K_{cl} and that the magnitude of this effect depends on the height of the asperity, its distance from the crack tip and rigidity. This same analysis is applicable in this case since the effects of an asperity in the crack wake on crack closure must be the same regardless of whether the asperity is due to an oxide particle, shim, or a plastic hump resulting from an overload. The disparity between a_{aff} and the overload plastic zone size increases with decreasing

ΔK_B and increasing OLR because the effectiveness of the discontinuous closure mechanism increases with decreasing crack tip opening displacements and increasing height of the plastic hump.

In contrast, a_{aff} values at R=0.6 were typically <u>less</u> than the calculated overload plastic zone sizes. Discontinuous closure is much less likely to occur at R=0.6 than at R=0.1 because crack tip opening displacements are higher and much more of the total crack remains open at K_{min}. One possible for the explanation for the discrepancy is that K_{cl} at R=0.6 under baseline condition is slightly less than K_{min} rather than equal to it as suggested by crack closure models (see Figure 2.12) [18,20-22]. The effect of this on a_{aff} is shown schematically in Figure 5.3. Both the experimental results and FASTRAN suggest that K_{cl} increases rapidly immediately following an overload and then asymptotically approaches its baseline value. If the baseline K_{cl} is greater than or equal to K_{min}, which is typically the case at low stress ratios below R_{cr}, then the increase in K_{cl} should retard crack growth rates for the entire distance where K_{cl} is elevated. However, if the baseline K_{cl} is even slightly less than K_{min}, which could possibly occur at R=0.6, then a_{aff} will be significantly less than the distance over which K_{cl} is elevated. Since the distance over which K_{cl} is elevated is equal to the overload plastic zone size in the absence of discontinuous closure, it is quite reasonable to have a_{aff} less than the overload plastic zone size at R=0.6. The crack front progression experiments indicate that three-dimensional effects may have also contributed to this discrepancy. How this might occur is discussed in more detail in Section 5.4.3.d.
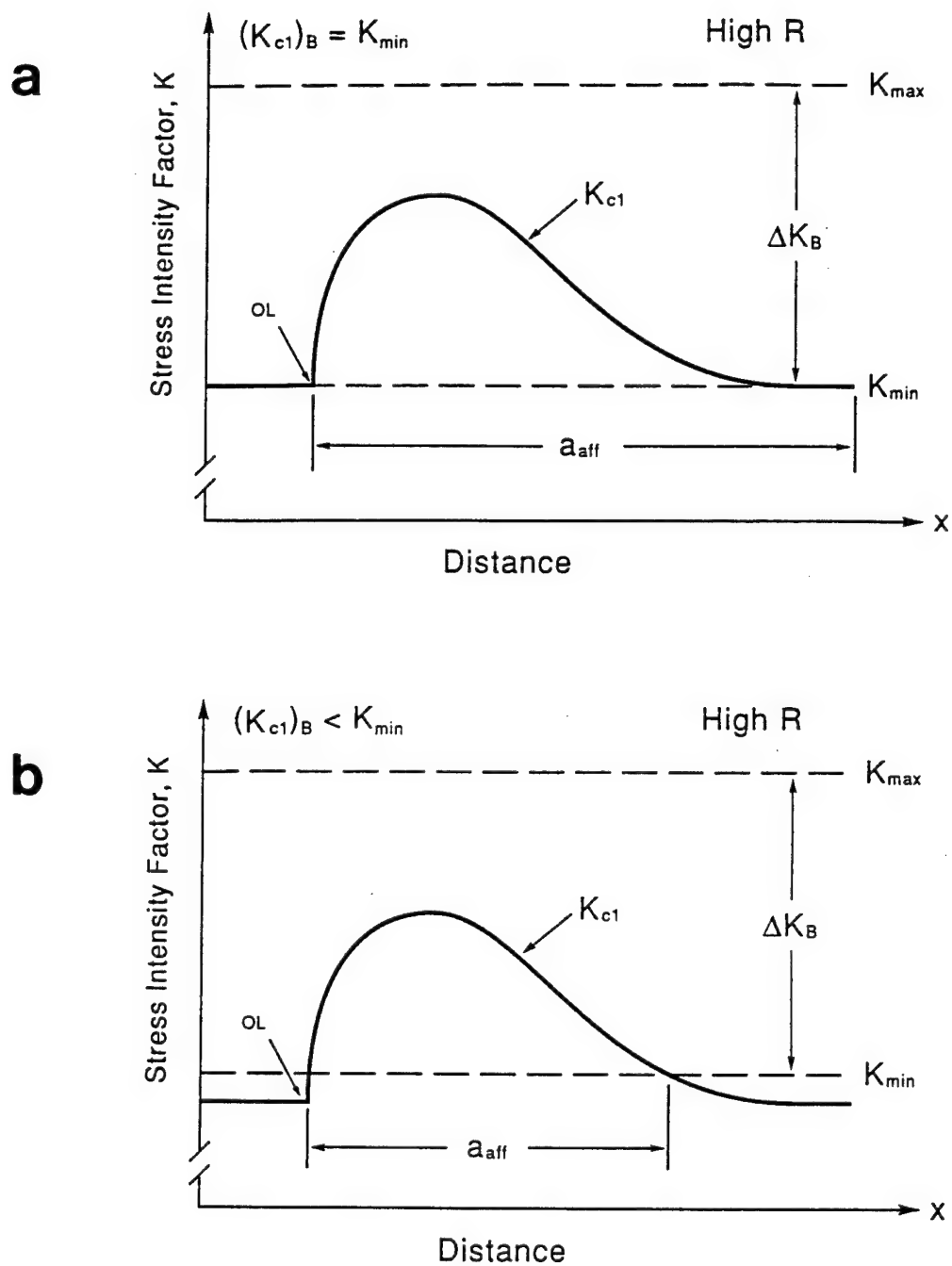
Figure 5.3. Schematic showing one possible explanation for a_{aff} less than overload plastic zone size at R=0.6: (a) $(K_{c1})_B = K_{min}$; (b)$(K_{c1})_B < K_{min}$.

The above discrepancies have led many investigators to conclude that crack closure mechanisms are not responsible for or cannot fully account for crack retardation effects. This is particularly true at high R where often no increase in measured closure levels occurs. They then conclude by default that retardation is due to compressive residual stresses, crack tip blunting or some other mechanism without providing direct evidence or analysis that this is the case. The previous discussion suggests that these discrepancies may often result from detection methods which are too insensitive to measure changes in closure levels following overloads. This is particular true at high R due to the small length of closed crack. These discrepancies also arise from three-dimensional effects which are generally not considered by investigators.

5.4.3. Special Topics

The discussion in this section is intended to shed light on the current areas of disagreement and confusion that exist regarding crack retardation mechanisms previously described in Section 2.3.3.

a. The role of residual compressive stresses and the effect of elevated temperature exposure- The residual compressive stress mechanism was rejected as a cause of retardation in Section 5.4.2.e. because it is theoretically unsound and inconsistent with constant amplitude FCGR experiments which show there is no stress ratio effect (i.e., mean strain effect) on crack growth rates in the absence of crack closure. The elimination of retardation by stress relieving is often used as proof that

the residual stress mechanism is responsible for retardation. The question will now be addressed as to whether this behavior can also be explained on the basis of crack closure mechanisms since the results suggest that these are the primary causes of retardation in AA8022 and AA5091.

The stress and strain distribution at a crack tip at zero load immediately before and after an overload are shown in Figure 5.4(a). As the crack grows into the overload plastic zone, the increased residual tensile deformation in the crack wake and the enlarged zone of compressive residual stresses ahead of the crack tip combine to increase closure levels and cause crack retardation. The underlying cause of the crack closure mechanism is the increased plastic strain at the crack tip which is responsible for both the changes in the stress distribution and the increase in residual tensile deformations in the crack wake.

The possible changes to the stress and strain distribution resulting from elevated temperature exposure are shown in Figure 5.4(b). The compressive yield strength is reduced at elevated temperature. The material in the compressive region directly in front of the crack tip, which has residual stresses greater in magnitude than the elevated temperature yield stress, yields in compression producing a concurrent reduction in the plastic strain ahead of the crack tip and the magnitude of the residual compressive stresses. The residual tensile stresses further in front of the crack tip are also possibly reduced by tensile yielding. The decrease in plastic strain resulting from the elevated temperature exposure reduces the magnitude of the compressive residual stress ahead of the crack tip and leads to smaller tensile deformations in the crack wake as the crack propagates into the overload plastic zone. The result is a reduction in N_d.
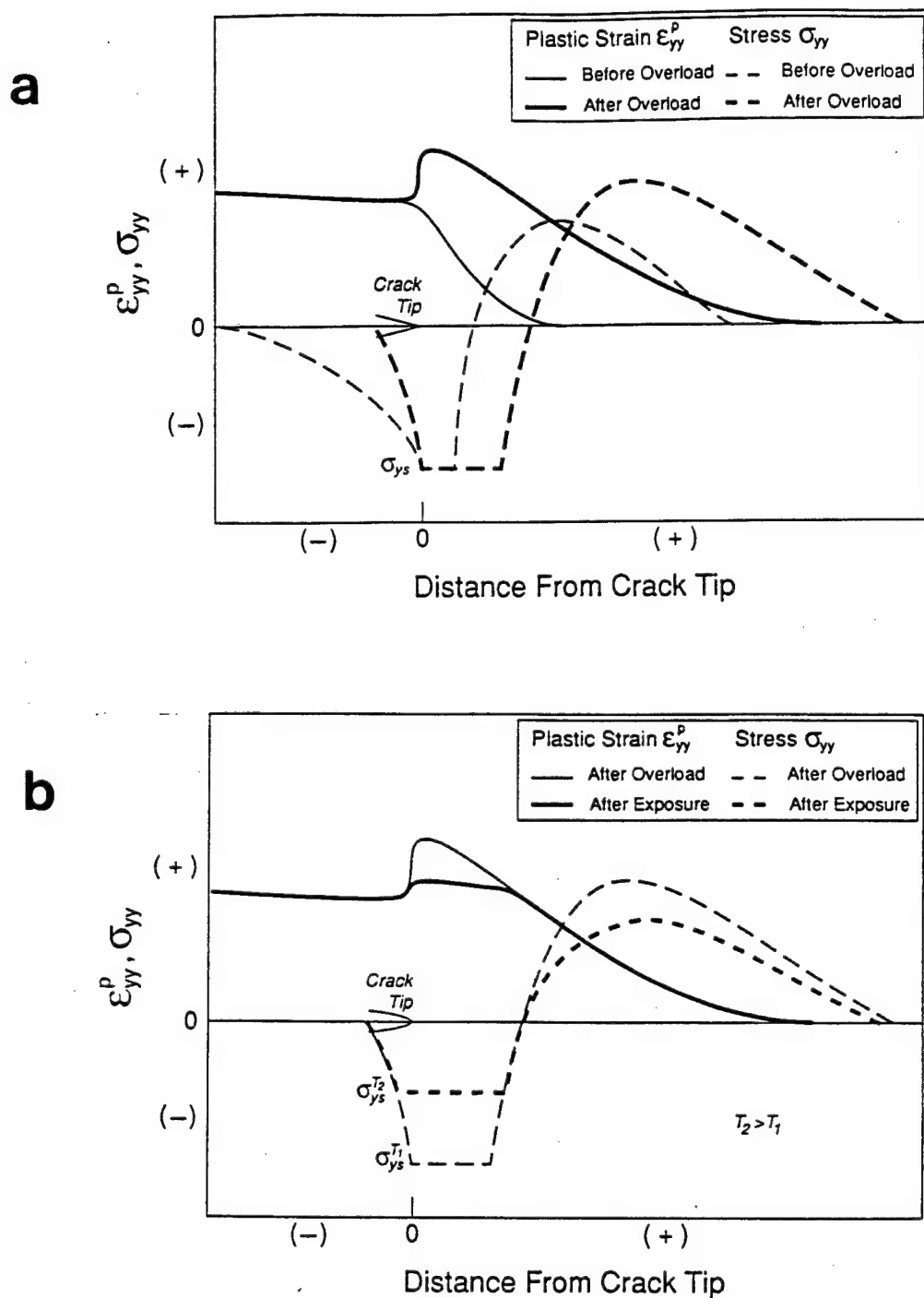
Figure 5.4. Schematics showing proposed effect of elevated temperature exposure on stress and strain distribution at the crack tip: (a) immediately before and after overload; (b) after overload and after elevated temperature exposure.

The greater reduction in N_d in AA5091 at equivalent exposure temperatures can be explained by considering the yield strength versus temperature in the two alloys shown in Figure 5.5. The AA5091 actually has a higher yield strength until about 200°C. On this basis, one might expect AA5091 to experience a smaller reduction in N_d at 150°C and a larger reduction at 225°C. However, it is not the absolute value of the yield strength which controls the magnitude of the reduction in N_d, but the magnitude of the change in yield strength. This becomes readily apparent by considering an alloy that experiences no loss in yield strength with increasing temperature. In this case, elevated temperature exposure would produce no change in the stress and strain distribution and no reduction in the number of delay cycles.

b. Mechanisms of Crack Retardation at High Stress Ratios– Since crack closure effects decrease with increasing stress ratio under constant amplitude loading conditions, it seems reasonable that crack retardation resulting from crack closure mechanisms should also diminish with increasing stress ratio. However, several studies have shown that the magnitude of retardation is as large or larger at high R as it is at low R. This same behavior was exhibited by AA8022 and AA5091 (see Figure 4.30). This apparent discrepancy and the fact that no closure is measured has led several investigators to conclude that the crack tip blunting or the compressive residual stress mechanism is responsible for crack retardation at high R.

However, the similarity of post-overload behavior in AA8022 and AA5091 at R=0.1 and R=0.6 suggests that crack closure mechanisms were
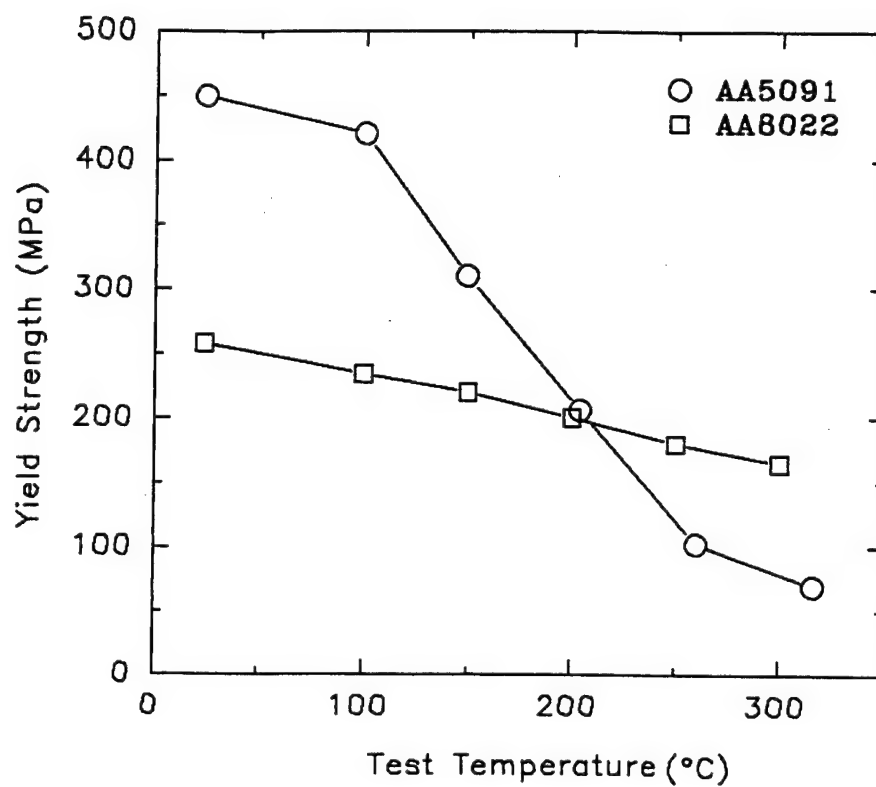
Figure 5.5. Yield strength in AA8022 and AA5091 as a function of temperature.

responsible for retardation at both low and high stress ratios. The occurrence of plasticity-induced closure following overloads at high R is quite reasonable. First, consider constant amplitude loading conditions. Plasticity-induced closure models [18,20-22] predict that even above R_{cr}, the critical stress ratio above which closure occurs, K_{cl} is still approximately equal to K_{min}. This is supported by an experimental study performed by McEvily and Yang [84] on a steel alloy tested in vacuum at 538°C. At this temperature, no closure was detected and there was very little R dependency on crack growth rate over the range of R from R=0.05 to 0.5. However, when R was decreased from R=0.5 to 0.05 at a constant applied ΔK there was a significant reduction in crack growth rate. McEvily concluded that before the change in R, K_{cl} was approximately equal to K_{min} (i.e., ΔK_{eff} was equal to the applied ΔK). Retardation occurred when R was reduced because K_{cl} remained unchanged and was now significantly greater than the new applied K_{min} producing a significant reduction in ΔK_{eff}. The retardation effect ended as the crack propagated away from the point of the R change and K_{cl} decreased to the new K_{min} at the new stress ratio. Phillips [85] examined the effects of 6, 18, and 30% load step reductions on ΔK_{th} in 2024-T3 at R=0.7. The crack was grown 0.5 mm between load steps. The 6% load reduction experiment yielded a ΔK_{th}=1.7 MPa√m which was equivalent to that obtained under constant K_{max}-decreasing ΔK test conditions. Closure measurements taken while unloading to zero load showed that K_{cl} was approximately equal to K_{min}. Crack arrest occurred following a 30% load reduction at ΔK_B=5 MPa√m. Closure measurements showed that K_{cl} following the load reduction was almost equal to the new

K_{max}. Since the ΔK_{eff} value was below the ΔK^{th}_{eff} determined in the constant K_{max} test the crack arrested.

Now consider overloads. Closure models and experimental results both agree that under baseline loading conditions $Kcl \approx K_{min}$ above R_{cr}. In this case, a retardation effect following an overload is quite reasonable, since the increased residual tensile deformation in the crack wake as the crack grows into the overload plastic zone combine with the enlarged zone of compressive residual stresses ahead of the crack tip to increase K_{cl}. This situation was shown previously in Figure 5.3.

The situation following an overload is actually very similar to that following a load reduction. The crack is propagating into a residual stress field corresponding to the higher K_{max} that existed prior to the load stepdown. This zone is larger than that which would exists at the new lower K_{max} under constant amplitude loading condition (i.e., without a load step down). The residual tensile deformation in the crack wake corresponding to the old K_{max} is also greater than that which would exist at the new K_{max} under constant amplitude loading conditions. The only difference between an overload and a load step down is that for a load step down the residual tensile deformation corresponding to the old K_{max} already exists in the crack wake. This leads to immediate retardation following a load stepdown. Immediately following an overload, the residual tensile deformations in the crack wake correspond to the baseline K_{max}. The increase in residual tensile deformations from K_{ol} can only occur after the crack propagates into the overload plastic zone, so retardation is delayed.

Since AA8022 and AA5091 exhibit very little crack closure at R=0.1 under constant amplitude loading conditions (see Figure 4.7), the situation prior to the overload is almost identical to that at R=0.6 at ΔK_B of 3 MPa$\sqrt{m}$ and higher. That is, $K_{cl} \approx K_{min}$. This being the case, the larger N_d in AA8022 and AA5091 at R=0.6 compared to that at R=0.1 at an equivalent ΔK_B can be readily explained. It is the consequence of two factors. First, a_{aff} is significantly larger at R=0.6 due to the much larger overload plastic zone (K_{ol}@R=0.6 > K_{ol}@R=0.1). Second, the larger K_{ol} at R=0.6 results in a larger increase in K_{cl} and a greater reduction in growth rates (see Figures 4.30 and 4.51). In alloys with high levels of crack closure at R=0.1, the difference in N_d will be smaller and N_d may even be larger at R=0.1. This is a result of significantly lower baseline crack growth rates at R=0.1.

The lack of an increase in measured closure levels following overloads at high R in this and many other investigations [48,58] is most likely a consequence of insensitive measurement techniques. Closure measurement at high R is especially difficult due to the small length of closed crack as discussed previously. Near-tip methods which are more sensitive have detected increases in closure levels at high R [59].

c. **The "U"-shaped curve-** The increase in N_d with decreasing ΔK_B observed in AA8022 and AA5091 is also commonly observed in IM alloys [7,36,57,60]. The two mechanisms proposed to explain this behavior were previously described in Section 2.3.3.c. Briefly, Rao and Ritchie (7) propose that the increase in N_d at low ΔK_B is the result of roughness-induced closure. They argue that plasticity-induced closure cannot produce this effect since the size of the overload plastic zone decreases

with decreasing ΔK_B. McEvily and Yang [60] propose that this behavior is a consequence of plasticity-induced closure. They argue that the increase in N_d as ΔK_B approaches threshold is due to the high sensitivity of crack growth rates to small changes in ΔK_{eff} in this range.

The increase in N_d with decreasing ΔK_B in AA8022, despite the absence of crack deflection, and a decrease in surface roughness indicates that plasticity-induced closure is capable of producing this behavior. This is supported by the FASTRAN predictions which show the same trend. The FASTRAN simulations also provide support for the proposal of McEvily and Yang [60] that the increase in N_d is due to the greater sensitivity of crack growth rates to small changes in ΔK_{eff} as ΔK_B approaches threshold. For example, FASTRAN predicts that overloads of magnitude OLR=2.0 in AA8022 at R=0.1 will reduce ΔK_{eff} a maximum of 0.5 MPa$\sqrt{m}$ at ΔK_B= 2 MPa$\sqrt{m}$ and 2.8 MPa$\sqrt{m}$ at ΔK_B=10 MPa$\sqrt{m}$, respectively for OLR=2.0. The effect of these reductions in ΔK_{eff} is shown in Figure 5.6. In spite of the much smaller change in ΔK_{eff} at ΔK_B=2.0 MPa$\sqrt{m}$, the minimum growth rate is 15 times slower than the baseline rate, while at ΔK_B=10 MPa$\sqrt{m}$ the minimum growth rate is only 5 times slower. The greater reduction in growth rates at low ΔK_B produces the increase in N_d. This is readily apparent if a crack propagating just above threshold is considered. In this case, only a small reduction in ΔK_{eff} from an overload is required to produce complete crack arrest and an infinite number of delay cycles.

The overload plastic zone size does decrease significantly with decreasing ΔK_B as noted by Rao and Ritchie [7]. The overload plastic zone at ΔK_B= 2.0 MPa$\sqrt{m}$ is only 1/25 the size of that at ΔK_B= 10 MPa$\sqrt{m}$. However, this in itself does not lead to a decrease in N_d as assumed by Rao
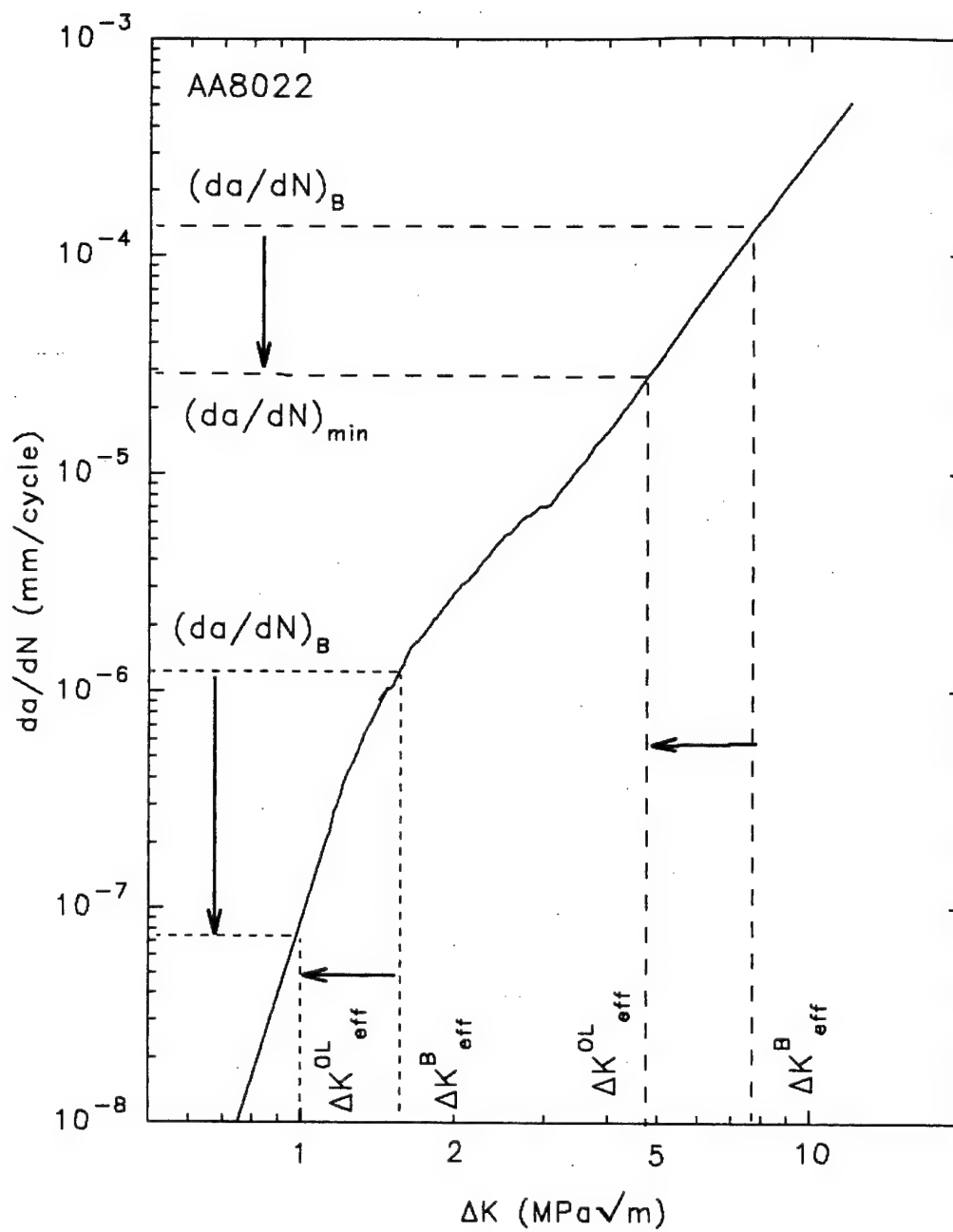
Figure 5.6. Origin of "U"-shaped curve in AA8022 (ΔK_{eff}^{B} and ΔK_{eff}^{OL} predicted by FASTRAN).

and Ritchie because the baseline crack growth rate is also decreasing. The size of the plastic zone at different ΔK_B must be related to baseline crack growth by some method before comparison is meaningful. This can be accomplished simply by normalizing the overload plastic zone size by the baseline crack growth rate. On this basis the relative "size" of the overload plastic zone at $\Delta K_B = 2.0$ MPa$\sqrt{m}$ is 4 times larger than that at $\Delta K_B = 10$ MPa$\sqrt{m}$.

d.   Three-Dimensional Effects on Retardation- The retardation effect at R=0.1 was significantly reduced by removal of 0.5 mm from the specimen surfaces immediately following the overload as discussed in Section 4.3.5. These results indicate that the retardation effect is greater in the surface region than in the interior region of the specimen. Several mechanisms have been proposed to explain this effect. Rao and Ritchie [7] proposed a mechanism based on roughness-induced closure. They contend that the reduction in retardation effect after surface removal occurs because machining away the surface layers removes the portion of the crack front adjacent to the surface where the crack has deflected along the intense shear bands caused by the overload. Since crack deflection enhances roughness-induced closure, removal of the surface reduces the retardation effect.

McEvily and Yang [60] proposed a mechanism based on plasticity-induced closure. They contend that retardation is entirely controlled by the plane-stress surface regions, and that the closure level in the surface region increases following an overload to produce the retardation effect, while that in the interior actually decreases following an overload.

Although closure levels decrease in the interior region (ΔK_{eff} increases), the crack front in this region also experiences retardation because it is restrained by the pinning of the crack front at the surfaces. Fleck [41], on the other hand, proposed that the plasticity-induced closure mechanism is responsible for retardation in both the surface and interior regions.

The roughness-induced closure mechanism of Rao and Ritchie could not have produced the surface removal effect in AA8022 or AA5091 at ΔK_B=2.25 MPa√m (see Figure 4.41), because there was no crack deflection at the surface following the overload under these conditions. This mechanism possibly contributed to the surface removal effect in AA5091 at ΔK_B=10.0 MPa√m where significant crack deflection occurred.

If crack retardation is entirely due to plasticity-induced closure in the surface regions as proposed by McEvily and Yang, then surface removal at ΔK_B=2.25 MPa√m should have entirely eliminated the retardation effect. However, the results show that there was still a significant retardation effect following surface removal (see Figure 4.41). This indicates that the plasticity-induced closure mechanism operates in both the plane-stress surface regions and the plane-strain interior as proposed by Fleck. This is further supported by the work of Bray, Reynolds, and Starke [86] in which they compared the effects of overloads on standard and side-grooved specimens. The results of their study are shown in Figure 5.7. Side grooving acts to constrain the material at the specimen surface suppressing plane-stress deformation. There was still a significant retardation effect in the side-grooved specimens over the entire range of ΔK_B even though the plane-stress deformation mode was suppressed at the specimen surface.
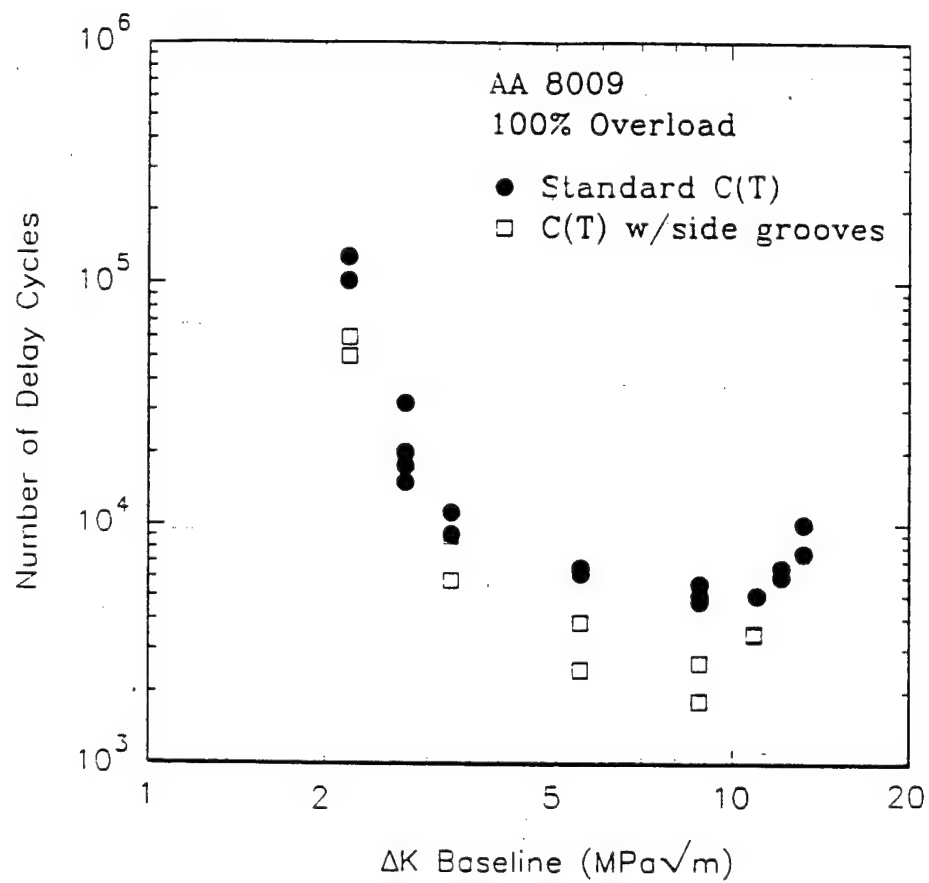
Figure 5.7. Effect of side grooves on retardation magnitude in PM alloy AA8009 (after Bray, Reynolds, and Starke [85]).

The reason the retardation effect is greater in the plane-stress surface region is apparent in Figure 5.8(a) which shows a FASTRAN simulation for an overload of magnitude OLR=2.0 at ΔK_B= 4.0 MPa$\sqrt{m}$ under plane-stress and plane-strain conditions. Under plane stress conditions, there is a greater reduction in growth rates resulting from higher closure levels, and a larger a_{aff} resulting from a larger overload plastic zone (see Equations 2.4 and 2.5). McEvily [60] and many other researchers contend that plasticity-induced closure cannot occur under plane strain conditions because there is no through-thickness contraction (ϵ_z=0) to act as a source of material for the residual tensile deformation in the crack wake. However, it follows from this same argument that the formation of a crack tip plastic zone is not possible under plane-strain conditions since the tensile plastic deformation in this zone under constant-volume deformation also requires a source of material. The fact that a plastic zone does form indicates that material is transferred from somewhere. The transferred material that forms the plastic zone also forms the residual material in the wake of the advancing crack. The recent finite element studies of McClung et al. [26] using finite element analysis indicate that residual plastic stretch in plane strain results from a transfer of material in the in-plane transverse direction (x-direction).

The results of crack front progression experiments, discussed in Section 4.3.6., also indicate that plasticity-induced closure produces retardation in both the plane-stress surface regions and the plane-strain interior regions. They also serve to further elucidate the three-dimensional behavior of the crack front following an overload. These experiments showed that the crack front initially progressed faster at the
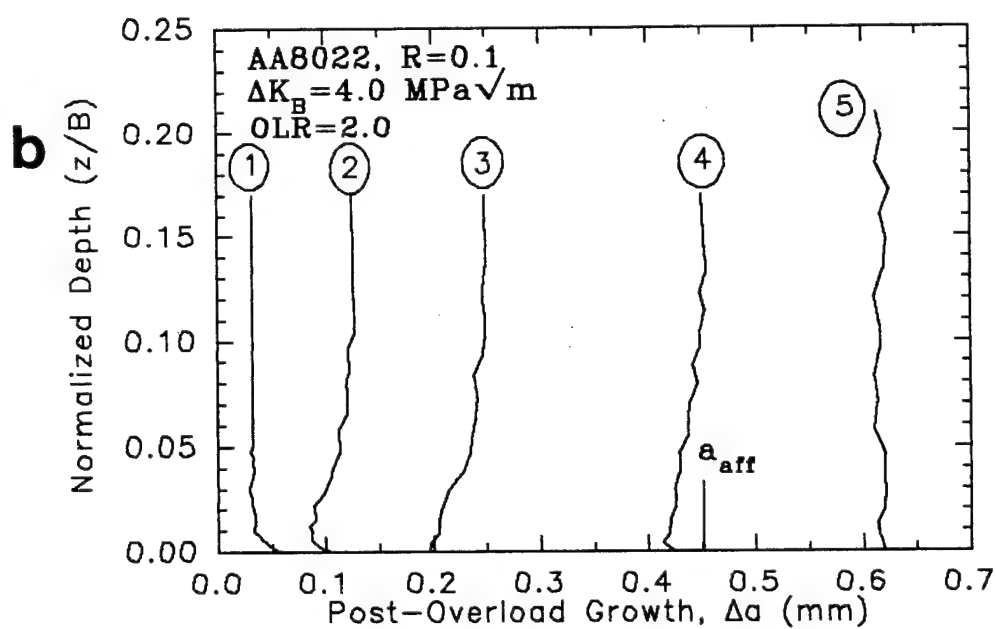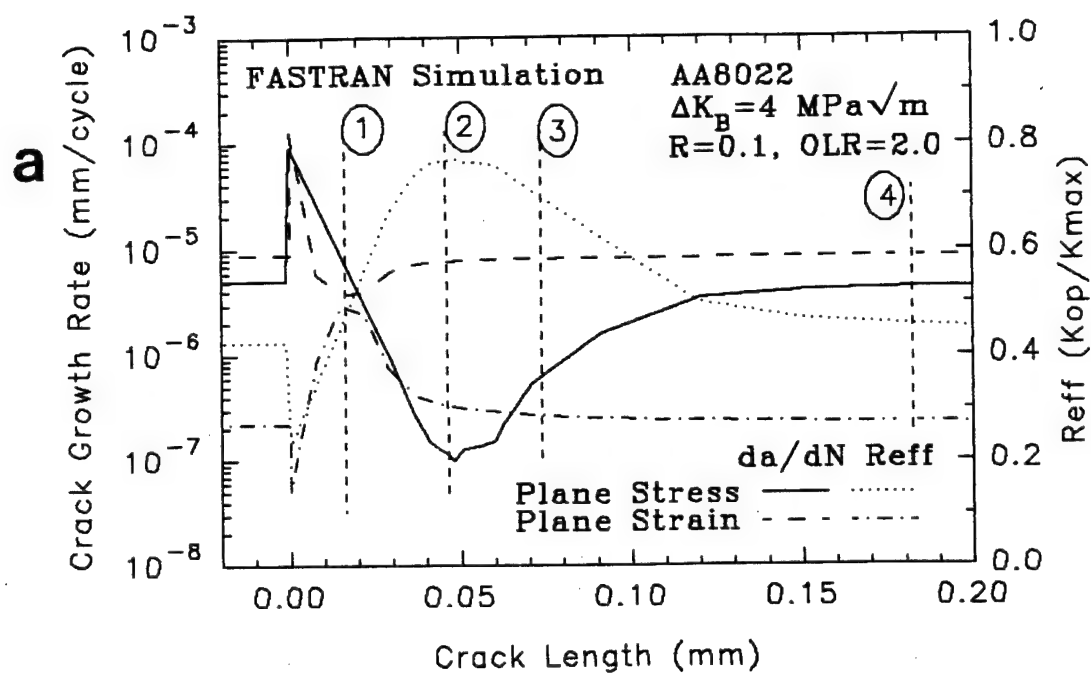
Figure 5.8. Three dimensional behavior following overloads: (a) FASTRAN prediction for plane stress and plane strain; (b) Crack front progression following overload.

surface than in the interior producing a decrease in crack front curvature near the specimen surface. The crack then progressed faster in the interior than at the surface producing an increase in crack front curvature (i.e., crack front tunneling). Finally, the crack front progressed faster at the surface than in the interior and eventually assumed the baseline curvature. This behavior seems quite unusual at first appearance, but actually it is quite consistent with the occurrence of plasticity-induced closure across the entire crack front. This will now be demonstrated using Figure 5.8(b) which shows the results of the crack front progression experiment at R=0.1 for ΔK_B=4.0 MPa√m and the FASTRAN simulation for plane stress and plane strain for the same conditions.

The crack initially grows faster at the surface than in the interior because closure levels increase more slowly and crack growth rates decrease less rapidly under plane stress than under plane strain as shown in Figure 5.8(a). At this point (position 1), the crack front is retarded by plasticity-induced closure in both the surface and interior regions. However, the crack front grows out of the overload plastic zone in fewer cycles in the interior due to the smaller reduction in growth rates and the smaller overload plastic zone size under plane strain conditions. Once this occurs, the crack grows significantly faster in the interior producing tunneling. At this point (positions 2 and 3) the crack front at the surface is still significantly retarded by plasticity-induced closure. The interior crack front is no longer retarded by plasticity-induced closure, but is now retarded (or restrained) by crack front tunneling which acts to decrease ΔK_{eff} in the interior and increase it at the surface [87]. Once the surface crack front progresses beyond the plane stress overload plastic zone (or

at low ΔK_B, beyond the point at which discontinuous closure no longer occurs) the retardation effect is over, i.e., the average growth rate across the thickness is equal to the baseline rate. However, at this point (position 4) the crack front still has a greater curvature than the equilibrium baseline curvature. The excess curvature is removed by the crack front at the surfaces and interior growing at rates slightly greater than and less than baseline rate, respectively. Once the equilibrium curvature is achieved, ΔK_{eff} and the growth rate are again constant across the entire crack front (position 5).

In Section 5.4.2.e. it was suggested that three-dimensional effects may contribute to several apparent discrepancies that often lead investigators to conclude that crack closure mechanisms are not responsible for or cannot fully account for crack retardation effects. These will now be considered in greater detail in light of the preceding discussion. First, consider the discrepancy between calculated overload plastic zone size and a_{aff} at R=0.6. At R=0.1, a_{aff} was typically equal to or greater than the calculated plane stress overload plastic zone size as expected, while at R=0.6, a_{aff} was typically much smaller. Two possible contributing factors have already been identified in Section 5.4.2.e. Discontinuous closure is much less likely to occur at R=0.6, and K_{cl} maybe slightly less than K_{min} at high R under baseline loading conditions. However, comparison of crack front progression at R=0.1 and R=0.6 following an overload at ΔK_B=4 MPa√m (compare Figure 4.43(a) with 4.44(a) and 4.43(b) with 4.44(a)) suggests that three-dimensional effects may also contribute to these differences. This comparison shows that crack front tunneling is much more severe at R=0.6 than at R=0.1 for the same baseline ΔK. Crack front tunneling leads to an

increase in ΔK_{eff} in the surface region due to crack front curvature effects. If the increase is large enough that ΔK_{eff}(surface) approaches ΔK_{eff} under baseline conditions, the retardation effect could effectively end at an a_{aff} smaller than the overload plastic zone size.

Now, consider the lack of correspondence between closure levels and crack growth rates following an overload. More specifically, the increase in closure levels often lags behind the decrease in crack growth rates, and $(da/dN)_{min}$ and the maximum closure level do not correspond [e.g., 50]. This same behavior was observed in AA8022 and AA5091 (see Figure 4.54) Dexter et al. [8] proposed that this discrepancy occurs because growth rates are controlled by the average through-thickness closure levels, while measured closure levels reflect the closure levels in the plane-stress surface regions. This explanation is consistent with the three-dimensional behavior observed in the current study. The crack growth rate in these experiments represented the average crack growth rate across the entire crack front since it is based on the compliance of the specimen above the load where closure occurs. The average growth rate depends on the average through-thickness closure level. The closure level, on the other hand, is based on the load where the slope of load-displacement curve deviates from that in the closure free region by 1%. Since closure is higher under plane-stress than in plane-strain, the measured closure level is probably more representative of the closure level in the surface regions. The point where the minimum crack growth occurred corresponded approximately to point where the maximum closure level occurred under plane-strain conditions in the interior of the specimen (position 1). The maximum measured closure level, on the other hand, corresponded to the

point of maximum closure in the surface regions. The minimum crack growth rate did not occur at this point because the retardation effect had already diminished in the interior region and crack front tunneling had begun. The preceding discussion points out that investigators need to be aware of three-dimensional effects following overloads when comparing post-overload closure levels to fatigue crack growth rates.

The magnitude of the retardation effect typically decreases with increasing thickness as shown previously in Figure 2.17. While only a single thickness (B=8 mm) was utilized in the current investigation, the three-dimensional retardation behavior exhibited by AA8022 and AA5091 sheds some light on the thickness effect. The results indicate that the retardation effect is larger in the plane-stress surface regions than in the interior regions. Since the proportion of the crack front experiencing plane stress increases with decreasing thickness it is quite reasonable that N_d should increase with decreasing thickness. This can be explained on the basis of crack front curvature effects. Once the interior crack front grows beyond the point of plasticity-induced closure effects (i.e., crack front tunneling begins) it is retarded only by crack front curvature effects. As thickness increases, the proportion of the plane-stress surface region to overall thickness decreases and the surface region becomes less effective at restraining the interior regions. Since the surface region is primarily responsible for the retardation effect, N_d decreases with increasing thickness.

5.4.4. Comments on FASTRAN-II

The ability of FASTRAN-II to predict the trends in AA8022 and AA5091 was quite remarkable. FASTRAN predicted the effects of decreasing ΔK_B, increasing OLR, increasing R, and overload/underload combinations. However, the behaviors that FASTRAN failed to predict are noteworthy because they reveal some of the limitations of a 2-dimensional plasticity-induced closure model.

FASTRAN underpredicted N_d in both AA5091 and AA8022 at R=0.1 (see Figure 4.48). The underprediction in AA5091 was most severe for OLR=3.0. FASTRAN always predicted a larger N_d in AA8022 than in AA5091. This was the case experimentally at OLR=2.0, but at OLR=3.0, N_d was larger in AA5091. At R=0.6, FASTRAN overpredicted N_d for OLR=1.44, but underpredicted N_d at OLR=2.0 (see Figure 4.50). Again FASTRAN always predicted a larger N_d in AA8022. This was the case for OLR=1.44, but not OLR=2.00.

These predictions were made using a single constraint factor $\alpha=2.4$. This constraint factor was chosen using the original method described by Newman [62] which relies on constant amplitude FCGR curves. The constraint factor that was chosen gave the "best fit". However, the choice was somewhat arbitrary. An equally "good fit" could have been obtained with $\alpha=2.3$ or 2.5. The lower value would have improved the quantitative predictions. More recent studies by Newman and Dawicke [64] have also shown that better quantitative predictions can be obtained by using an α that varies as a function of crack growth rate (i.e., ΔK_{eff}) The use of other α's and varying α would have been quite reasonable in some cases

and probably improved the quantitative predictions considerably. For example, at R=0.6 it is reasonable to believe that the through-thickness constraint following an overload is greater for OLR=1.44 than OLR=2.00 since K_{ol} at a given ΔK_B is larger for OLR=2.0. Thus, it would have been reasonable to increase α for OLR=1.44 and decrease α for OLR=2.0. This would have improved the quantitative predictions at R=0.6.

On the other hand, the α's that would have been necessary to correctly predict the relative magnitude of the retardation behavior in AA8022 and AA5091 do not always make sense on the basis of plasticity-induced closure. For example, α would need to be smaller in AA5091 than in AA8022 to correctly predict the behavior at R=0.1, OLR=3.0 and R=0.6, OLR=2.0. This is not reasonable because the through-thickness constraint should always be less in a lower yield strength material. These inconsistencies arise because FASTRAN does not account for the contribution of the roughness-induced closure mechanism to retardation.

Quantitative agreement can always be obtained even when roughness-induced closure effects are present if α is employed as a "fitting parameter", but it then loses its theoretical meaning as a measure of through-thickness constraint. However, use of α as a "fitting parameter" to account for roughness-induced closure mechanisms can cause other problems. For example, decreasing α will increase a_{aff} when in fact roughness-induced closure mechanism may have little or no effect on a_{aff}.

FASTRAN also did not correctly predict the position of minimum crack growth rate and underpredicted a_{aff} (see Figure 4.54). These are a consequence of using a 2-D model to model a 3-D phenomena. FASTRAN cannot accurately model the complex three-dimensional behavior observed

in thick specimens in a single simulation. Thus, the selected α must represent an average through-thickness constraint. Since the position of the minimum crack growth rate was controlled primarily by the interior plane-strain region of the specimen where the constraint was greater than the chosen α, FASTRAN predicted that $(da/dN)_{min}$ occurs after a larger increment of crack extension than it actually did. Similarly, since a_{aff} was controlled to a large extent by the plane-stress surface regions where the constraint is less than α, FASTRAN underpredicted a_{aff}.

FASTRAN has proven itself to be a very effective tool in examining overload effects and predicting fatigue life in the current study and many others [8,18,63,64] in spite of these minor shortcomings.

6. Conclusions

(1)   The primary cause of crack growth retardation in AA8022 is plasticity-induced closure at both R=0.1 and 0.6. The primary cause of crack retardation in AA5091 at low ΔK_B and low overload magnitudes is plasticity-induced closure. At high ΔK_B and larger overload magnitudes the crack retardation in AA5091 is due to a combination of plasticity and roughness-induced closure. At low ΔK_B and low overload magnitudes, where plasticity-induced closure is the dominant closure mechanism in both alloys, the number of delay cycles is larger in AA8022. The larger delay in AA8022 under these conditions is due to its lower yield strength which results in a larger overload plastic zone (i.e., larger a_{aff}). At high ΔK_B and larger overload magnitude, where roughness-induced closure effects become significant in AA5091, the number of delay cycles is larger in AA5091. The larger delay in AA5091 under these conditions is due to a lower minimum growth rate (i.e., greater reduction in ΔK_{eff}). The crack tip strain hardening, crack tip blunting, crack deflection/branching, secondary cracking, and the compressive residual stress mechanisms make either a minimal or no contribution to crack retardation in AA8022 and AA5091. However, compressive residual stresses are an important component of the plasticity-induced closure mechanism and crack deflection enhances roughness-induced closure effects.

(2)   The magnitude of the retardation effect is significantly reduced by elevated temperature exposure due to a reduction in plastic strain and a reduction in the magnitude of the compressive residual stresses ahead of the crack. These changes significantly reduce the contribution of closure mechanisms to crack retardation. The reduction in the number of delay cycles is controlled by the magnitude of the change in yield strength from room temperature to the elevated temperature, rather than the absolute value of the yield strength at the elevated temperature.

(3)   The increase in the number of delay cycles with decreasing ΔK_B is consistent with the plasticity-induced closure mechanism. Two factors contribute to this behavior: (1) the high sensitivity of crack growth rates to small changes in ΔK_{eff} as ΔK_B approaches threshold; and (2) an increase in the size of the overload plastic zone normalized by the baseline crack growth rate with decreasing ΔK_B.

(4)   The plasticity-induced closure mechanism is through-thickness in nature, occurring in both the interior region and surface regions. However, the magnitude of the retardation effect is greater in the surface regions than in the interior region, because the increase in plastic strain and the overload plastic zone are larger in the plane-stress surface regions than in the interior region. The progression of the crack front following an overload is consistent with plasticity-induced closure and crack front curvature effects.

(5)   FASTRAN-II is a useful tool for studying overload effects and predicting fatigue life as evidenced by its ability to accurately predict the effects of ΔK_B, overload ratio, stress ratio, yield strength, and overload/underload combinations on crack retardation behavior. FASTRAN-II is most applicable to alloys such as AA8022 where plasticity-induced closure is the dominant retardation mechanism. In alloys such as AA5091, where two or more mechanisms contribute significantly to retardation, FASTRAN-II is less applicable, but can still be successfully utilized by empirically determining the proper choice of the constraint factor, α.

References

1. W. Elber: in *Damage Tolerance in Aircraft Structures, ASTM STP 486,* American Society for Testing and Materials, Philadelphia, PA, 1971, pp. 230-42.

2. J.F. Knott and A.C. Pickard: *Met. Sci.,* Aug./Sept., 1977, pp. 399-404.

3. J.R. Rice: in *Fatigue Crack Propagation, ASTM STP 415,* American Society for Testing and Materials, Philadelphia, PA, 1967, pp. 247-309.

4. S. Suresh: *Eng. Fract. Mech.,* 1983, vol. 18, pp. 577-93.

5. R.J. Bucci, A.B. Thakker, T.H. Sanders, R.R. Sawtell, and J.T. Staley: in *Effect of Load Spectrum Variables on Fatigue Crack Initiation and Propagation, ASTM 714,* D.F. Bryan and J.M. Potter, eds., American Society for Testing and Materials, Philadelphia, PA, 1980, pp. 41-78.

6. O.E. Wheeler: *J. of Basic Eng.,* Trans. of the ASME, 1972, vol. 4, pp. 181-6.

7. K.T.V. Rao and R.O. Ritchie: *Acta Metall.,* 1988, vol. 36, pp. 2849-62.

8. R.J. Dexter, S.J. Hudak, Jr. and D.L. Davidson: *Eng. Fract. Mech.,* 1989, vol. 33, pp. 855-70.

9. P.C. Paris, P.C. Gomez, and W.E. Anderson: *The Trend in Engineering,* University of Washington, 1961, vol. 13, pp. 9-14.

10. H.L. Ewalds and R.J.H. Wanhill: *Fracture Mechanics,* Edward Arnold (Publishers) Ltd., London, England, 1984, pp. 56-74.

11. R.C. McClung: *Fat. Fract. Eng. Mater. Struct.,* 1991, vol. 14, pp. 455-68.

12. J. Lankford, D.L. Davidson, and T.S. Cook: in *Cyclic Stress-Strain and Plastic Deformation Aspects of Fatigue Crack Growth, ASTM STP 637,* American Society for Testing and Materials, Philadelphia, PA, 1977, pp. 36-55.

13. G. Nicoletto: in *Advances in Fracture Research (ICF7),* vol.2, K. Salama, K. Ravi-chandar, D.M.R. Taplin, P. Rama Rao, eds., Pergamon Press, United Kingdom, 1989, pp. 1279-87.

14. D. Broek: *The Practical Use of Fracture Mechanics,* Kluwer Academic Publishers, The Netherlands, 1989, pp. 136-45.

15. D.L. Davidson and J. Lankford in: *Fatigue Mechanisms: Advances in Quantitative Measurement and Physical Damage, ASTM STP 811,* J. Lankford, D.L. Davidson, W.L. Morris, and R.P. Wei, eds., American Society for Testing and Materials, Philadelphia, PA, 1983, pp. 371-99.

16. W. Elber: *Eng. Fract. Mech.*, 1970, vol. 2, pp. 37-45.

17. R.C. McClung and D.L. Davidson: *Eng. Fract. Mech.*, 1991, vol. 39, pp. 113-30.

18. J.C. Newman, Jr: in *Methods and Models for Predicting Fatigue Crack Growth Under Random Loading, ASTM STP 748*, J.B. Chang and C.M. Hudson, eds., American Society for Testing and Materials, Philadelphia, PA, 1981, pp. 53-84.

19. H. Fuhring and T. Seeger: *Eng. Fract. Mech.*, 1979, vol. 11, pp. 99-122.

20. B. Budiansky and J.W. Hutchinson: *J. of App. Mech.*, Trans. of the ASME, 1978, vol. 45, pp. 267-75.

21. H. Kobayashi and H. Nakamura: in *Current Research in Fatigue Cracks, Current Japanese Materials Research*, vol. 1, T. Tanaka, M. Jono, and K. Komai, eds., Elsevier Applied Science, London, England, 1987, pp. 229-45.

22. F.K Ibrahim, J.C. Thompson, and T.H. Topper: *Int. J. Fatigue*, 1986, vol. 8, pp. 135-42.

23. H.G.F. Wilsdorf, F.E. Wawner,Jr., and J.A. Wert: Report No. WL-TR-91-4022, Wright Laboratory, Wright-Patterson Air Force Base, OH, May 1991.

24. S.J. Hudak, Jr. and D.L. Davidson: in *Mechanics of Fatigue Crack Closure, ASTM STP 982*, J.C. Newman, Jr. and W. Elber, eds., American Society for Testing and Materials, Philadelphia, PA, 1988, pp. 121-38.

25. T.G.F. Gray and P.M. MacKenzie: *Int. J. Fatigue*, 1990, vol.12, pp. 417-23.

26. R.C. McClung, B.H. Thacker, and S. Roy: *Int. J. Fracture*, 1991, vol. 50, pp. 27-49.

27. R.G. Chermahini, K.N. Shivakumar, and J.C. Newman, Jr.: in *Mechanics of Fatigue Crack Closure, ASTM STP 982*, J.C. Newman, Jr. and W. Elber, eds., American Society for Testing and Materials, Philadelphia, PA, 1988, pp. 398-413.

28. H.L. Ewalds and R.T. Furnee: *Int. J. Fracture*, 1978, vol. 14, pp. R53-R55.

29. D.S. Dawicke: *Three-Dimensional Fatigue Crack Closure Behavior of Metals*, Ph.D. Thesis, Purdue University, 1989.

30. A.J. McEvily: *Fat. Fract. Eng. Mater.*, 1989, vol. 12, pp. 71-72.

31. H. Sehitoglu and W. Sun: *J. Eng. Mater. Tech.*, Trans. of the ASME, 1991, vol. 113, pp. 31-40.

32. S. Suresh and R.O. Ritchie: in *Fatigue Crack Growth Threshold Concepts*, S. Suresh and D.L. Davidson, eds., The Metallurgical Society, Warrendale, PA, 1984, pp. 227-61.

33. G.S. Booth and S.J. Maddox: in *Mechanics of Fatigue Crack Closure, ASTM STP 982*, J.C. Newman, Jr. and W. Elber, eds., American Society for Testing and Materials, Philadelphia, PA, 1988, pp. 516-27.

34. P.K. Liaw: *Materials Research Society Bulletin*, Aug. 1989, pp. 25-35.

35. R.D. Carter, E.W. Lee, E.A. Starke, Jr., and C.J. Beevers: *Metall. Trans. A*, 1984, vol. 15A, pp. 555-63.

36. R.S. Vecchio, R.W. Hertzberg, and J.C. Jaccard: *Scripta Metall.*, 1983, vol. 17, pp. 343-6.

37. W.J. Mills and R.W. Hertzberg: *Eng. Fract. Mech.*, 1975, vol. 7, pp. 705-11.

38. J.J. Kleek and T. Nicholas: in *Effects of Load and Thermal Histories on Mechanical Behavior of Materials*, P.K. Liaw and T. Nicholas, eds., The Metallurgical Society, Warrendale, PA, 1987, pp. 27-47.

39. J. Schijve: in *Fatigue '87*, vol. 1, R.O. Ritchie and E.A. Starke, Jr., eds., Engineering Materials Advisory Services Ltd., United Kingdom, 1987, pp. 1685-1721.

40. A.P. Reynolds: *Fat. Fract. Eng. Mater. Struct.*, 1992, vol. 15, pp. 551-62.

41. N.A. Fleck: in *Basic Questions in Fatigue: Volume 1, ASTM STP 924*, J.T. Fong and R.J. Fields, eds., American Society for Testing and Materials, Philadelphia, PA, 1988, pp. 157-83.

42. D. Taylor, I.A.N. Staniaszek, and J.F. Knott: *Int. J. Fatigue*, 1990, vol. 12, pp. 397-402.

43. S. Suresh and A.K. Vasudevan: in *Fatigue Thresholds-Fundamentals and Engineering Applications*, vol. 1, Engineering Materials Advisory Services, Ltd., United Kingdom, 1987, pp. 361-77.

44. L.R.F. Rose: *Int. J. Fracture*, 1986, vol. 31, pp. 233-42.

45. W. Sun and H. Sehitoglu: *Fat. Fract. Eng. Mater. Struct.*, 1992, vol. 15, pp. 115-28.

46. M. Drew, K.R.L. Thompson, and L.H. Keys: in *Strength of Metals and Alloys (ICSMA6)*, vol. 2, R.C. Gifkins, ed., Pergamon Press, United Kingdom, 1982, pp. 867-73.

47. D. Damri and J.F. Knott: in *Fatigue '90*, vol. 3, H. Kitigawa and T. Tanaka, eds., Materials and Components Engineering Publications, Ltd, United Kingdom, 1990, pp. 1505-10.

48. M.R. Ling and J. Schijve: *Fat. Fract. Eng. Mater. Struct.*, 1992, vol. 15, pp. 421-30.

49. R.D. Brown and J. Weertman: *Eng. Fract. Mech.*, 1978, vol. 10, pp. 867-78.

50. J. Lankford and D.L. Davidson: in *Advances in Fracture Research (Fracture 81)*, vol. 2, D. Francois, ed., Pergamon Press, United Kingdom, 1981, pp. 899-906.

51. G. Nicoletto: *Int. J. Fatigue*, 1989, vol. 11, pp. 107-15.

52. G. Nicoletto: in *Basic Mechanisms in Fatigue in Metals*, P. Lukas and J. Polak, eds., Academia, Prague, Czechoslovakia, 1988, pp. 281-88.

53. D.L. Davidson and S.J. Hudak: in *Fracture Mechanics: 18th Symp.*, *ASTM STP 945*, D.T. Read and R.P. Reed, eds., American Society for Testing and Materials, Philadelphia, PA, 1988, pp. 934-54.

54. V.W. Trebules, Jr., R. Roberts, and R.W. Hertzberg: in *Progress in Flaw Growth and Fracture Toughness Testing, ASTM STP 536*, American Society for Testing and Materials, Philadelphia, PA, 1973, pp. 115-46.

55. H. Nayeb-Hashemi and F.A. McClintock, and R.O. Ritchie: *Eng. Fract. Mech.*, 1983, vol. 18, pp. 763-83.

56. E.P. Phillips: NASA Technical Memorandum 101601, Langley Research Center, Hampton, VA, 1989.

57. C.M. Ward-Close and R.O. Ritchie: in *Mechanics of Fatigue Crack Closure, ASTM STP 982*, J.C. Newman, Jr. and W. Elber, eds., American Society for Testing and Materials, Philadelphia, PA, 1988, pp. 93-111.

58. C.C. Turner, C.D Carman, and B.M. Hillberry: in *Mechanics of Fatigue Crack Closure, ASTM STP 982*, J.C. Newman, Jr. and W. Elber, eds., American Society for Testing and Materials, Philadelphia, PA, 1988, pp. 529-35.

59. J.D. Bertel, A. Clerivet, and C. Bathias: in *Advances in Fracture Research (Fracture 81)*, vol. 2, D. Francois, ed., Pergamon Press, United Kingdom, 1981, pp. 943-51.

60. A.J. McEvily and Z. Yang: *Metall. Trans. A,* 1990, vol. 21A, pp. 2717-27.

61. J.C. Newman, Jr.: NASA Technical Memorandum 104159, Langley Research Center, Hampton, VA, 1992.

62. J.C. Newman, Jr.: *Int. J. Fract.,* 1984, vol. 24, pp. R131-35.

63. J.C. Newman, Jr.: in *Design of Fatigue and Fracture Resistant Structures, ASTM STP 761,* P.R. Abelkis and C.M Hudson, eds., American Society for Testing and Materials, Philadelphia, PA, 1982, pp. 255-77.

64. J.C. Newman, Jr. and D.S. Dawicke: in *Advances in Fracture Research (ICF7),* vol.2, K. Salama, K. Ravi-chandar, D.M.R. Taplin, P. Rama Rao, eds., Pergamon Press, United Kingdom, 1989, pp. 945-52.

65. A. F. Blom and D.K. Holm: *Eng. Fract. Mech.,* 1985, vol. 22, pp. 997-1011.

66. J.K. Donald: in *Mechanics of Fatigue Crack Closure, ASTM STP 982,* J.C. Newman, Jr. and W. Elber, eds., American Society for Testing and Materials, Philadelphia, PA, 1988, pp. 222-9.

67. *IncoMAP alloy AL-905XL,* Inco Alloys International, Huntingtion, WV, 1988.

68. P.S. Gilman: in *Proceedings- First Thermal Structures Conference,* University of Virginia, Charlottesville, VA, 1990, pp. 111-28.

69. Y.-W. Kim, W.M. Griffith, and F.H. Froes: *J. Metals,* 1985, vol. 32, pp. 27-33.

70. J.W. Martin: *Micromechanisms in Particle Hardened Alloys,* Cambridge University Press, United Kingdom, 1980, pp. 79-83.

71. J.A. Hawk, P.K. Mirchandani, R.C. Benn, and H.G.F. Wilsdorf: in *Dispersion Strengthened Aluminum Alloys,* Y-W. Kim and W.M. Griffith, eds., The Metallurgical Society, Warrendale, PA, 1988, pp. 517-537.

72. T. Hasagawa and T. Miura: in *Structural Applications of Mechanical Alloying,* F.H. Froes and J.J. DeBarbadillo, eds., ASM International, Metals Park, OH, 1991, pp. 213-19.

73. D.J. Lloyd: *Met. Sci.,* 1980, vol. 14, pp. 193-98.

74. H. Westengen: in *Strength of Metals and Alloys (ICSMA 6),* vol. 1, R.C. Gifkins, ed., Pergamon Press, United Kingdom, 1982, pp. 461-66.

75. D.J. Lloyd and L.R. Morris: *Acta Metall.,* 1977, vol. 25, pp. 857-61.

76. R.E. Stoltz and R.M. Pelloux: *Met. Trans.*, 1976, vol. 7A, pp. 1295-1306.

77. T.S. Srivatsan: *Int. J. Fatigue*, 1991, vol. 13, pp. 313-321.

78. E.A. Starke, Jr. and J.C. Williams: in *Fracture Mechanics: Perspectives and Directions, ASTM STP 1020*, R.P. Wei and R.P. Gangloff, eds., American Society for Testing and Materials, Philadelphia, PA, 1989, pp. 184-205.

79. A.J. McEvily and K. Minikawa: in *Fatigue Crack Growth Threshold Concepts*, D.L. Davidson and S. Suresh, eds., The Metallurgical Society, Warrendale, PA, 1984, pp. 227-61.

80. A. Ohta, M. Kosuge and S. Nishijima: *Int. J. Fatigue*, 1988, vol. 10, pp. 237-42.

81. H. Nakamura and H. Kobayashi: in *Mechanics of Fatigue Crack Closure ASTM STP 982*, J.C. Newman, Jr. and W. Elber, eds., American Society for Testing and Materials, Philadelphia, PA, 1988, pp. 459-74.

82. A.J. McEvily and K. Minikawa: in *Strength of Metals and Alloys (ICSMA 6)*, vol. 2, R.C. Gifkins, ed. Pergamon Press, United Kingdom, 1982, pp. 845-50.

83. C.J. Beevers, K. Bell, R.L. Carlson, and E.A. Starke: *Eng. Fract. Mech.*, 1984, vol. 19, pp. 93-100.

84. A.J. McEvily and Z. Yang: *Scripta Met.*, 1986, vol. 20, pp. 1781-84.

85. E.P. Phillips: in *Mechanics of Fatigue Crack Closure, ASTM STP 982*, J.C. Newman, Jr. and W. Elber, eds., American Society for Testing and Materials, Philadelphia, PA, 1988, pp. 505-15.

86. G.H. Bray, A.P. Reynolds, and E.A. Starke, Jr.: *Metall. Trans. A*, 1992, vol. 23A, pp. 3055-66.

87. M.L. Lucci and S. Rizutti: *Int. J. Fract.*, 1987, vol. 34, pp. 23-40.

88. D. Kuhlmann-Wilsdorf and H.G.F. Wilsdorf: *Phys. Stat. Sol.*, 1992, b172, pp. 235-248.

89. J.A. Hawk, W. Ruch, and H.G.F. Wilsdorf: in *Dispersion Strengthened PM Aluminum Alloys*, Y-W. Kim and W.M. Griffith, eds., The Metallurgical Society, Warrendale, PA, 1988, pp. 603-618.

90. Rich Franck: *An Al-Fe-V-Si Alloy for Elevated Temperature Applications: Microstructural Stability and Mechanical Properties*, M.S. Thesis, University of Virginia, 1989.